NON-DESTRUCTIVE QUANTITATIVE ASSESSMENT OF OXIDATION IN AGED AND REJUVENATED ASPHALT CONCRETE PAVEMENTS USING A NON-COLLINEAR WAVE MIXING APPROACH

BY

MEGAN E. MCGOVERN

DISSERTATION

Submitted in partial fulfillment of the requirements
for the degree of Doctor of Philosophy in Systems and Entrepreneurial Engineering
in the Graduate College of the
University of Illinois at Urbana-Champaign, 2016

Urbana, Illinois

Doctoral Committee:

Professor Henrique Reis, Chair
Professor William G. Buttlar
Professor Emeritus William D. O'Brien, Jr.
Associate Professor Ramavarapu S. Sreenivas
Professor Emeritus Marshall R. Thompson

Abstract

Oxidative aging in asphalt concrete pavements is one of the chief contributors to pavement degradation. Oxidation contributes to the formation of a diffuse micro-flaw population in the mastic. This damage is primarily concentrated at the top (surface) of the pavement, where exposure to oxygen is the greatest. These flaws serve as the nuclei to crack formation and propagation, and adversely affect the pavement's structural integrity. It is more cost effective to perform maintenance when the pavement contains relatively little damage, than it is to defer maintenance until more drastic measures must be taken. Currently, engineers lack the proper tools for non-destructive, quick, and reliable inspection.

The work in this report addresses this need by employing non-collinear wave mixing, a nonlinear acoustic technique, to evaluate the level of oxidation of the pavement. To implement the nonlinear technique, the linear acoustic parameters, *i.e.*, dilatational and shear velocities and attenuations, of asphalt concrete specimens with various levels of oxidative aging were characterized. In non-collinear wave mixing, two waves are propagated so that they cross paths. Under the right conditions, these two waves will interact to produce a third wave.

Taking advantage of critically refracted longitudinal waves enabled the non-collinear wave mixing measurements to be taken from the pavement surface. Two nonlinear parameters were measured as a function of oxidative aging: the efficiency of interaction, $\frac{\beta}{\beta_0}$, and the frequency at which the interaction takes place, $\frac{f_2}{f_1}$. A nonlinear damage characterization curve was introduced, which is generated for a particular mixture under laboratory conditions, by plotting $\frac{\beta}{\beta_0}$ versus $\frac{f_2}{f_1}$ for various levels of oxidative aging. Field pavement measurements of $\left(\frac{\beta}{\beta_0}, \frac{f_2}{f_1}\right)$ can then be referenced against the nonlinear damage characterization curve to evaluate the state of the pavement. The testing set-up was configured to be one-sided, hence truly non-destructive, via the use of these subsurface waves. Two data-collection approaches are presented, which can be used even if the linear acoustic properties are unknown *a priori*, for practical field implementation. The efficacy of an asphalt rejuvenation product was also studied using this technique. Pavement engineers can thus continuously monitor the pavement and make decisions (such as the application of rejuvenators) to prolong its service life.

For Marco.

Acknowledgments

Success and accomplishments are in part due to perseverance, a solid support system, and sometimes a little luck. I have had the good fortune in working under an excellent adviser; without whom my accomplishments throughout my graduate studies would have been impossible. So, first and foremost, I would like to thank my adviser, Professor Henrique Reis, for allowing me to work in his lab and offering his truly invaluable guidance. I would also like to thank the members of my dissertation committee for their constructive ideas and time commitments: Professor William Buttlar, Professor William O'Brien, Professor R.S. Sreenivas, and Professor Marshall Thompson.

I am very grateful to the Department of Industrial and Enterprise Systems Engineering (which is made up of many wonderful people) at the University of Illinois Urbana-Champaign for providing me with this amazing opportunity, along with financial assistance towards achieving my goals. This research was made possible by the support of the National Cooperative Highway Research Program (Ideas Deserving Exploratory Analysis program); the Federal Aviation Administration, with technical support from: Dr. David Brill, Dr. Hao Wang, Dr. Charles Ishee and Mr. Don Barbagallo; the US Airforce Civil Engineering Center, with technical support of Dr. George Vansteenburg. I am also grateful for the technical support of Mr. Jeb S. Tingle (ERDC-RDE-GSL-MS). The rejuvenation products were donated by the Heritage Group, with technical support of Mr. Anthony J. Kriech, Mr. Gerald A. Huber, and Mr. Herb Wissel.

I have been very fortunate to work in the lab with brilliant, talented, and amiable individuals, who I hope will all be life-long friends: Dr. Adam Senalik, Dr. Behzad Behnia, Thomas Suchy, Nathan Price, Alex Haser, Nick Farace, Jake Arnold, Zhe Sun, and Jeb Conway. Thank you all for your intellectually stimulating conversations, research support, jokes, and general camaraderie. I will not even endeavor to write how each one of you has made graduate school an enjoyable and unforgettable experience.

Thank you to my family and friends for keeping me sane and offering unconditional love and support: My parents: Mike and Shari, brother Steven, grandparents, mi suegra Silvia, and Maria ("sis").

Finally, to my husband Marco: You have dedicated nearly as much as I have to this dissertation (but not as much as El Gato, of course). Thank you for putting everything on hold while I've pursued my goals.

Table of Contents

Chapter 1

Introduction to Oxidative Aging in Asphalt Concrete Pavements

Asphalt concrete is one of the most heavily used composite materials in transportation infrastructure [1]. Asphalt concrete (AC) pavements suffer a number of harsh, damaging environmental elements during service-life, such as moisture infiltration, temperature fluctuations, oxygen, and traffic loadings. Environmental exposure causes the pavement to undergo an aging process, which can adversely alter its material properties. Oxidative aging, due to oxygen exposure, is one of the chief contributors of pavement degradation [2]. High amounts of oxidative aging can significantly reduce the performance of the pavement, consequently shortening the service life.

Asphalt is a highly temperature susceptible material. In cold temperatures, it behaves stiff, brittle, and elastic; whereas in warmer temperatures, it exhibits soft, ductile, and viscoelastic behavior. This temperature susceptibility poses a challenge for transportation engineers, especially in climates with variable temperatures, because they must ensure that the pavement does not suffer excessive cracking the colder winter months, nor rutting (*i.e.*, excessive deformation) in the summer months. The Superpave Performance Grading (PG) system [**?**] was put in place to aid pavement engineers in selecting the appropriate binder. Asphalt binders graded with this system are denoted in the following format: PG $XX\pm XX$, where the first number denotes the average seven-day maximum pavement temperature that the pavement is expected to withstand. The second number denotes the minimum pavement temperature that the pavement is expected to withstand. Both temperatures denote pavement (not air) temperatures and are in degrees Celcius (°C). For example, a PG 64-22 binder is expected to perform adequately in climates where the minimum pavement temperature is -22°C, and the average seven-day pavement temperature does not exceed 64°C.

Oxidative aging reduces the low temperature performance properties of asphalt, hence, raising the low-temperature performance grade number. As the degraded pavement is subjected to the conditions for which it was initially designed (with its original, unaged properties), it sustains damage. In the Midwest, one common manifestation of this damage is in the form of potholes (see

Figure 1.1: Damage manifested in the form of a potholes. Extracted from [3].

Figure 1.1). Aged pavements experience a reduction in crack resistance and self-healing capabilities compared to their unaged counterparts. As a result, aged pavements accumulate damage at accelerated rates. Once the pavement damage has reached a severe state, expensive maintenance measures must be taken for repair. It is much less expensive to perform preventative maintenance for structural integrity preservation, than it is to defer maintenance until damage becomes severe, and more drastic corrective maintenance or rehabilitation efforts are required.

Pavement engineers face the difficult task of predicting the long-term behavior of AC pavements subjected to field conditions and must make decisions regarding treatments or rehabilitation in order to ensure proper performance and length of service life. Empirical data provides the foundation to understanding the material behavior under various conditions. Currently, engineers rely in part on visual inspection techniques, at which point the damage may be either undetectable (although present) or severe enough to require expensive repair efforts. They also rely on destructive mechanical tests, which can either be performed on a portion of the batch of the AC mixture or on cores from the in-place design. However, there are no truly non-destructive techniques in place for the accurate, *in-situ*, and early damage detection and assessment of AC pavements.

In this chapter, a brief description of various aspects of the problem of oxidative aging in AC pavements will be presented. First, a general description of oxidative aging in AC pavements will be presented. Then, discussions on the implications of aging and current pavement inspection techniques will be described. This chapter will conclude with an overview of the investigations in this report and summary of how the report has been organized.

1.1 Terminology

Some terminology which will be used throughout this report will now be clarified. Some terminology related to AC:

- **Asphalt concrete** will be used to refer to the composite material, *i.e.*, asphalt binder + stone aggregates. In the literature, this is often referred to as hot mix asphalt (HMA).
- **Asphalt** will be used to denote the asphalt cement, *i.e.*, bitumen.
- **Binder** will be used interchangeably with the term asphalt (see above bullet).
- **Mastic** will refer to the binder plus the fines.

Some terminology related to acoustics:

- **Dilatational Waves** will be used to describe compressional waves (polarized in the direction of propagation).
- **Longitudinal Waves** will be used interchangeably with dilatational waves (see above bullet) to describe compressional waves.
- **Shear Waves** will be used to refer to waves polarized 90° to the direction of propagation. Also known as **transverse waves**.

1.2 Oxidative Aging in Asphalt Concrete Pavements

In the early stages, damage via oxidative aging takes the form of diffuse micro-flaws. These micro-flaws, under continual subjection to the damage-causing conditions, grow and eventually coalesce to form cracks. Thus, micro-flaws serve as the nuclei to the fracture process, and significantly limit the strength of the pavement. Most of the damage is concentrated at the top (surface) of the pavement, where exposure to the oxygen is highest. Deeper portions of the pavement are more protected, and consequently, may have material properties very similar to that of the unaged, virgin mix. This is evidenced by Figure 1.2, which shows the complex modulus as a function of pavement depth after 8 years of service in Illinois. Notice that the stiffest portions are located near the top.

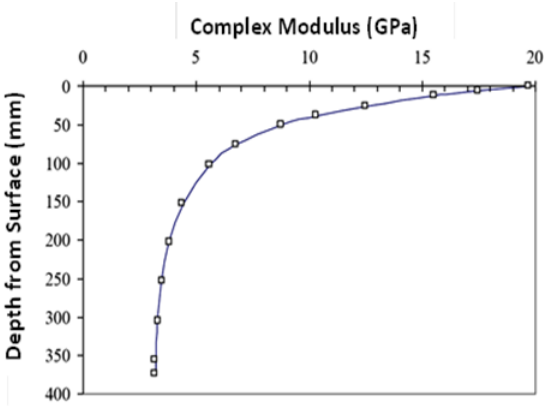

Figure 1.2: Complex modulus as a function of the pavement depth after 8 years of service in Illinois. Extracted from [4].

As the aging level in the AC increases, the binder stiffness increases and the cohesive strength of the mastic decreases. These two mechanisms have competing effects on the overall composite asphalt concrete stiffness. This complicates the pattern of the global stiffness as a function of the level of oxidative aging, which will be discussed in more detail in Chapter 2.

1.3 Implications of Oxidative Aging in Pavements

It is more cost effective to maintain a pavement in an acceptable state than it is to defer maintenance until the damage becomes so severe that more drastic maintenance rehabilitation or reconstruction measures are required. This is especially true for pavements which must withstand heavy traffic loadings. In comparison to timely preventative maintenance, deferred maintenance has negative implications, such as higher construction efforts, cost consequences, and negative effects on traffic. Deferred maintenance increases the quantity and severity of defects; consequently, the cost of repair increases. Thus, the ability to identify proper maintenance time is crucial for pavement preservation and ultimately cost savings.

Brown et al. [5] provides a nice discussion on the compounding effect of deferred maintanence on cost. Figure 1.3 contains a schematic of the quality of the pavement as a function of the years in service. Quality is a subjective term which relates to the condition of the pavement. Notice that deterioration (aging level) accelerates with time. For 75% of the pavement's life, it remains in a "fair" to "very good" state. The "fair" condition corresponds to a 40% drop in the quality

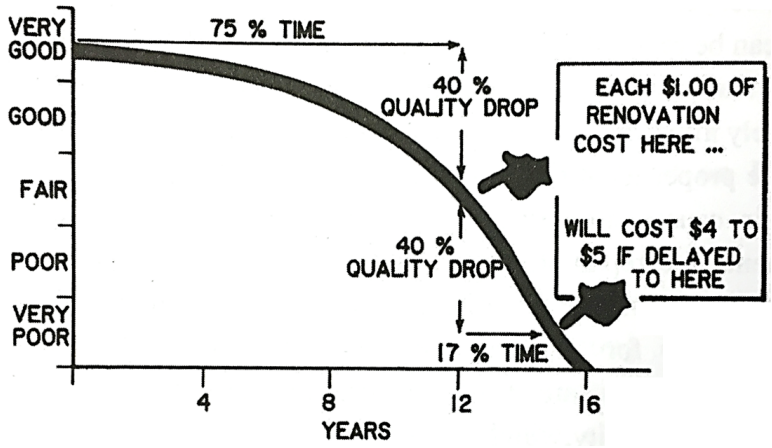

Figure 1.3: Pavement degradation for years in service. Extracted from [5].

(compared to the "very good" state). An 80% drop in quality corresponds to a "very poor" condition pavement. It costs $4 to $5 to repair a "very poor" condition pavement for every $1 it costs to repair a "fair" condition pavement. Clearly, cost conscious decisions hinge on the engineers' ability to detect when the pavement is in the fair condition so that proper maintenance can be executed at the appropriate time.

1.4 Current Pavement Inspection Techniques

Visual inspection remains the primary tool for pavement assessment and determining the appropriate corrective action to perform on the pavement. Using this technique, practitioners identify the damage, the source of the damage, and select the appropriate maintenance treatments and repair strategies. Of course, it is possible (and even probable) that by the time damage has reached the point where it can be visually detected, the pavement has surpassed that of the "fair" condition (Figure 1.3), rendering any decisions less cost effective. Also, this technique relies on the experience and discretion of the person executing the inspection, and as such is highly subjective. Less subjective pavement inspection techniques are also sometimes employed, such as deflection based nondestructive pavement analyses, dynamic cone penetration (DCP) test, and ground penetrating radar (GPR). None of these methods, however, has the ability to detect the presence of diffuse micro-flaws.

1.5 Outline of the Investigation

The primary goal of this report is to develop a tool for pavement engineers to quickly, accurately, and non-destructively make an assessment of the AC pavement to aid in the maintenance decision making. A nonlinear acoustic technique is proposed, specifically non-collinear wave mixing, as a way to assess the oxidative aging level in AC pavements when there is still time to take preemptive measures. The following investigations follow a natural trajectory of events. First, the linear acoustic properties (velocities and attuations) of asphalt concrete specimens subjected to various levels of oxidative aging were characterized. Linear characterization was necessary to carry out non-collinear wave mixing. Next, non-collinear wave mixing was used to assess the level of oxidative aging. The non-collinear wave mixing testing set-up was then configured so that it could be performed with all of the testing apparatus on one side, *i.e.*, the top surface of the pavement. The final investigation covered the efficacy of a commercial rejuvenation product, which aims to restore the aged binder to its original properties. The following subsections will briefly introduce these major investigations in the order that they appear in this report.

The appendices of this report contain important theory for the reader who wishes a more in-depth background on the derivations and theory of various aspects important to the theoretical considerations of the investigations. Appendix A contains a brief outline on the oxidative aging process in asphalt. The function of Appendices B through D is to provide a thorough reference to nonlinear acoustics, specifically nonlinear elastic interaction. Appendix B contains the fundamental linear acoustic theory prerequisite to nonlinear elasticity. A complete and in-depth discussion on the theory and derivation of nonlinear interaction of elastic wave mixing is presented in Appendix C. For completeness, Appendix D contains a discussion on self-interaction and harmonic generation of a single propagating acoustic wave.

1.5.1 Linear Acoustic Characterization

The complex moduli can be measured for asphalt concrete specimens subjected to various amounts of aging in order to understand the effect aging has on the properties. In Chapter 2, it will be shown that the change in mechanical properties due to aging can be detected via ultrasonic

measurements, *e.g.*, velocity and attenuation. The results from ultrasonic tests can be utilized to determine the complex moduli in a quick, repeatable, and low-cost manner. Current conventional mechanical techniques for the determination of complex moduli in asphalt concrete are costly and time-consuming. The correlation in conjunction with the fact that ultrasonic tests are quick to run, demonstrate the potential of ultrasonic methods for characterizing the amount of aging.

Previous studies [6–8] have successfully correlated complex modulus results from ultrasonic tests to the results from conventional mechanical tests; however, either the velocities were assumed to be constant across frequencies, or the unknown Poisson's ratio was assumed. This study assumes neither. Furthermore, the lack of frequency-dependent ultrasonic measurements leads to uncertainties in the construction of the master curve. When velocities are taken at multiple temperatures, they must be shifted using time-temperature superposition [1, 9]. If the velocity is not frequency dependent (only a single reported value at each temperature), the amount at which it should be shifted (*i.e.* the shift factor) is unknown. When the shift factor is unknown, comparisons must be made between the ultrasonic data and the data obtained via mechanical testing; consequently, the need for mechanical testing is not eliminated. The techniques in Chapter 2 address these deficiencies.

1.5.2 Nonlinear Acoustic Characterization

Asphalt concrete, even in its unaged, undamaged state, is a nonlinear material. This is because it belongs to a class of materials known as nonlinear mesoscopic materials, which are materials with a brick and mortar type structure. As asphalt concrete ages via oxidation, it displays increasingly strong nonlinear behavior. This nonlinear behavior can be characterized via a nonlinear acoustic method, specifically the non-collinear wave-mixing technique. In the non-collinear wave-mixing technique, two ultrasonic bulk waves are propagated through the medium in such a manner which they cross paths at a certain angle and set of frequencies. For a material which displays nonlinear behavior, the higher-order terms in the nonlinear wave equation are not insignificant, and these two waves can interact to produce a third nonlinear scattered wave. In Chapter 3, it will be shown that the level of oxidative aging of the AC can be assessed by monitoring the characteristics of this nonlinear scattered wave (*i.e.*, frequency and amplitude).

In Chapter 4, the non-collinear wave mixing technique is modified so that it can be applied readily and practically in the field to monitor AC pavements. Specifically, the technique is modified so that it can be employed when there is only access to one side, the top, of the pavement.

1.5.3 Asphalt Rejuvenation Products

The importance of taking corrective actions to prolong the service life of a pavement was discussed in Section 1.3. One such corrective action is through the use of asphalt rejuvenation products, or rejuvenators. Rejuvenators are products that aim to restore the aged asphalt binder back to its original state by replacing volatile components lost during the aging process.

The efficacy of these products has been debated. In Chapter 5, the efficacy of the commercial asphalt rejuvenator, *Reclamite*, is tested using the non-collinear wave mixing technique. The use of the non-collinear wave mixing technique, in conjunction with rejuvenators, would allow engineers to continuously monitor the pavement, even after corrective actions have been taken, to significantly prolong the life of the pavement.

Chapter 2

Assessment using Linear Acoustics

Prior to implementing any nonlinear characterization techniques, it is necessary to characterize the linear acoustic properties. Thus, the primary goal of this portion of the study is to assess the effects of laboratory induced oxidative aging on the linear ultrasonic parameters (ultrasonic velocities and corresponding attenuations) of asphalt concrete mixtures. Ultrasonic dilatational and shear velocity and attenuation measurements were taken on six different asphalt concrete specimens subjected to different amounts of laboratory oven-aging (0 hours, 12 hours, 24 hours, 28 hours, 32 hours, and 36 hours). Also, using these ultrasonic measurements, the dynamic uniaxial and shear complex moduli were computed.

2.1 Complex Moduli

Asphalt concrete is a viscoelastic material, as its material properties are dependent on both time and temperature. Accordingly, its moduli are complex. The complex Young's (uniaxial) modulus is given by [9],

$$E^* = E' + iE'' \tag{2.1}$$

where,

$$E' = |E^*| \cos\phi, \quad E'' = |E^*| \sin\phi \tag{2.2}$$

and,

$$|E^*| = \sqrt{(E')^2 + (E'')^2} = \frac{\sigma_0}{\varepsilon_0} \tag{2.3}$$

The magnitude of the complex Young's modulus $|E^*|$ is commonly referred to as the dynamic modulus. From Equation 2.2, the phase angle can be found as follows,

$$\phi = \tan^{-1} \frac{\mathrm{Im}\,[E^*]}{\mathrm{Re}\,[E^*]} = \tan^{-1} \frac{E''}{E'} \tag{2.4}$$

The storage modulus (the real component) is denoted by E', the loss modulus (the imaginary component) is denoted by E'', and ϕ is the phase angle. Please refer to Figure 2.1 for a graphical

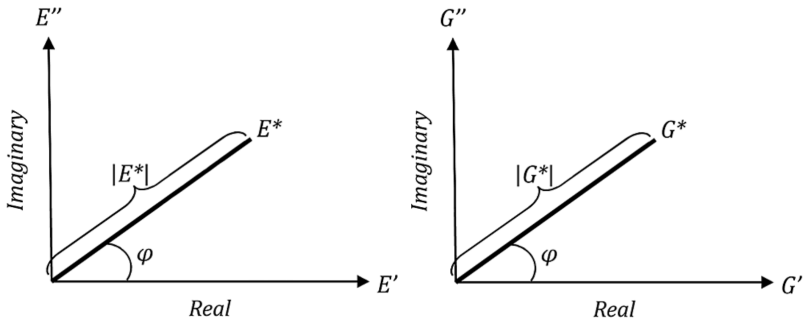

Figure 2.1: Graphical representation of complex Young's modulus. The naming conventions are as follows: $|E^*| \equiv$ dynamic modulus, $E^* \equiv$ complex modulus, $E' \equiv$ storage modulus, $E'' \equiv$ loss modulus, and $\phi \equiv$ phase angle.

representation. The complex shear moduli relationships are analogous to the uniaxial modulus by substituting the uniaxial moduli parameters for the shear moduli parameters G^*, G', G'', and $|G^*|$ in the above equations.

2.1.1 Mechanical Complex Modulus Test

Conventional techniques for measuring the dynamic modulus of AC involve mechanical tests such as the compressive dynamic modulus test and the indirect tension test [1]. Here, the focus will be on the compressive dynamic modulus test. AASHTO T342-11 [10] details the compressive dynamic modulus test procedures for determining the dynamic modulus and phase angle of the AC over a range of frequencies and temperatures. The set-up consists of a servo-hydraulic loading frame with the capability of applying a sinusoidal compressive loading at a specified frequency (for the range of 0.1 to 0.25 Hz). The system contains an environmental chamber, which is used to control the temperature of the AC specimen during testing. The AC specimen is the core from a cylindrical gyratory compacted specimen (150 mm tall, 102 ± 2 mm diameter). Linear variable differential transformers (LVDT) are used to measure the average axial deformation. The LVDTs are placed at four locations around the circumference of the AC specimen at a distance of 90 degrees apart. A load cell measures the applied load. In order to properly construct the master curve, tests should be conducted at temperatures of -10, 4.4, 21.1, 37.8, and 54°C for sinusoidal loading at frequencies of 0.1, 0.5, 1.0, 5, 10, and 25 Hz for each temperature. Figure 2.2 shows a schematic of this test-setup.

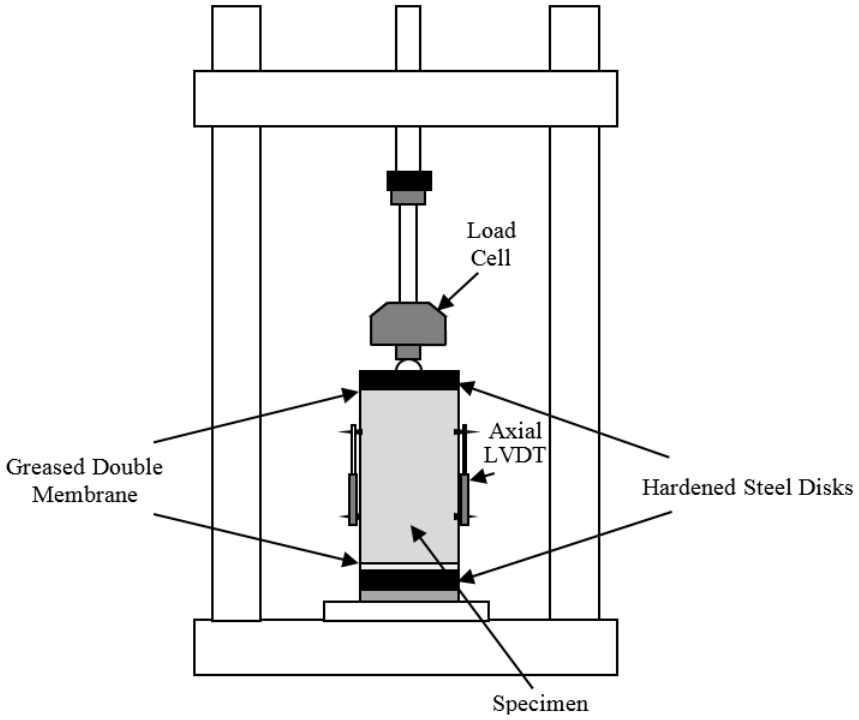

Figure 2.2: Schematic of the dynamic modulus test (replicated from AASHTO T342-11 [10]).

2.1.2 Ultrasonic Parameters and the Complex Moduli

The complex moduli can be related to the ultrasonic parameters via the dilatational and shear phase velocities and attenuations. The group velocities and attenuations can also be used to calculate the complex moduli; however, the group velocity is a meaningless concept when there is high attenuation, as the "wave packet" does not maintain its shape. The complex Poisson's ratio is a function of the shear to dilatational complex velocity ratio,

$$\mu^* = \frac{1 - 2\left(\frac{c_S^*}{c_L^*}\right)^2}{2\left[1 - \left(\frac{c_S^*}{c_L^*}\right)^2\right]} \tag{2.5}$$

where c_L^* and c_S^* are the complex dilatational and shear phase velocities, respectively. Thus, in order to obtain the complex moduli, it is necessary to have the dilatational ultrasonic parameters (velocity and attenuation), and either the Poisson's ratio or the shear ultrasonic parameters.

The elastic-viscoelastic correspondence principle [9] makes it possible to use complex material properties in the solution of the elastic wave equation. The one-dimensional, linear, complex wave equation is then written as follows [9, 11],

$$\frac{\mathrm{d}^2 u}{\mathrm{d}x} = \frac{1}{c^*(i\omega)^2}\frac{\mathrm{d}^2 u}{\mathrm{d}t^2} \tag{2.6}$$

where $c^*(i\omega)$ is the complex phase velocity, ω is the angular frequency, t is time, x is the propagation direction, and $u(x,t)$ is the particle motion. The solution to the equation (in terms of real and imaginary components) is,

$$u(x,t) = u_0 e^{i(\omega t - k^* x)} \tag{2.7}$$

And k^* can be separated into storage and loss components as,

$$u(x,t) = u_0 e^{k'' x} e^{i(\omega t - k' x)} \tag{2.8}$$

The second exponential term in the above equation is the familiar term describing the wave propagation in the x-direction, while the first exponential term is a decay (attenuation) term. The real and imaginary components of the complex wave number are as follows [11],

$$\begin{aligned} k' &= \mathrm{Re}[k^*] = \frac{\omega}{c(\omega)} \\ k'' &= \mathrm{Im}[k^*] = -\alpha(\omega) \end{aligned} \tag{2.9}$$

The complex phase velocity is related to the complex wave number as,

$$c^*(\omega) = \frac{\omega}{k' + ik''} = \left[\frac{1}{c(\omega)} - i\frac{\alpha(\omega)}{\omega}\right]^{-1} \tag{2.10}$$

Note, $c(\omega)$ is the real phase velocity, $\alpha(\omega)$ is the real attenuation, and both quantities are measurable via conventional ultrasonic techniques. If the attenuation coefficient approaches zero, then the complex phase velocity is simply the real portion (measured) of the phase velocity. In other words, the phase velocity is only complex in the presence of attenuation.

The complex Young's modulus E^* can be related to the complex velocities as follows [12],

$$E^* = \rho(c_S^*)^2 \left(\frac{3(c_L^*)^2 - 4(c_S^*)^2}{(c_L^*)^2 - (c_S^*)^2} \right) \tag{2.11}$$

where ρ is the material density. The complex shear modulus G^* can be written as follows,

$$G^* = \rho(c_S^*)^2 \tag{2.12}$$

2.2 Experimental Set-Up and Procedures

Due to the complex nature of wave propagation through asphalt concrete, some considerations must be made when devising the test set-up. First, the preparation of the specimens will be detailed. A detailed focus on the considerations for the experimental set-up and data processing will be provided. Finally, the experimental set-up and data collection procedures will be presented.

2.2.1 Sample Preparation

Six asphalt concrete specimens with the same mix design were prepared following Superpave guidelines. A 9.5 mm nominal maximum aggregate size (NMAS) with a target asphalt content of 5.9% by weight of the total mixture was selected for this study. The binder was performance grade (PG) 64-22. The aggregate blend consisted of limestone aggregates from four different stockpiles: 65.3% coarse aggregate (CM16), 23% manufactured sand (FM20), 10.5% natural sand (FM02), and 1.2%

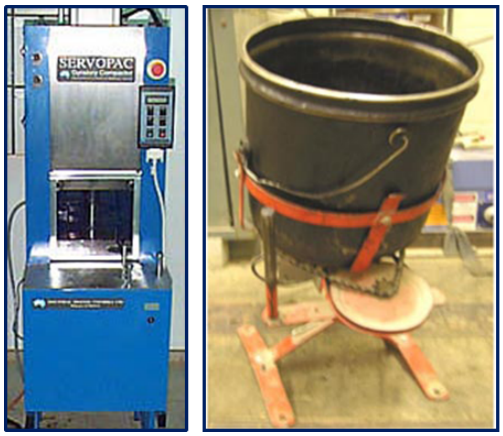

Figure 2.3: Asphalt concrete specimens prepared using a standard bucket mixing procedure (right) and gyratory compaction (left).

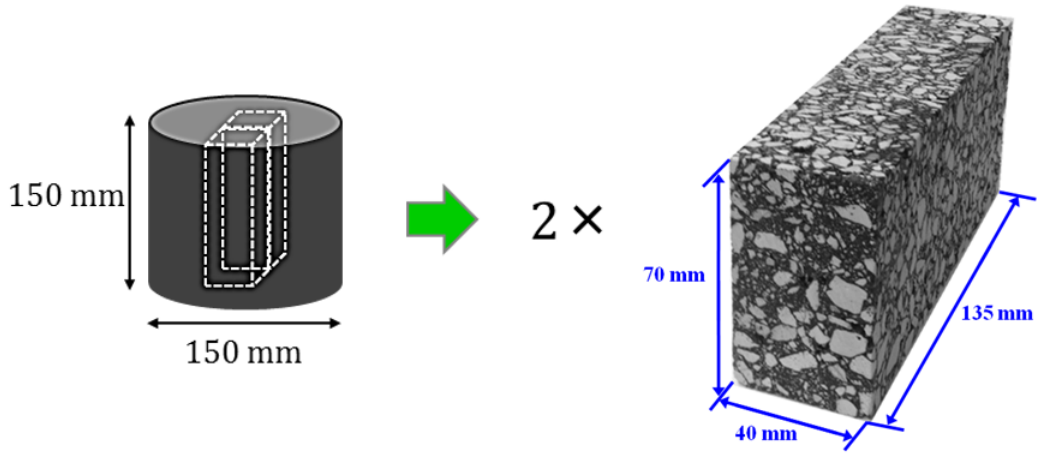

Figure 2.4: Preparation of tests samples along with their dimensions for ultrasonic and acoustic emission tests.

mineral filler (MF).

Mixing of the asphalt concrete mixtures was conducted at 155°C using a standard bucket mixing procedure. See Figure 2.3. The six uncompacted loose AC mixtures were each laboratory aged for a respective amount of time of 0, 12, 24, 28, 32, and 36 hours. Laboratory aging of the asphalt mixtures was performed by placing loose mixtures in the force draft oven (at 135°C) for the appropriate amount of time (0 - 36 hours). To achieve uniform aging (uniform exposure to oxygen) throughout the sample, the mixtures were hand-stirred every 12 hours. Once aged, the mixtures were compacted into cylinders (150 mm height, 150 mm diameter) at 155°C using a servo-controlled gyratory compactor (IPC Servopac, Figure 2.3). The compacted gyratory specimens were then cut to obtain two $40 \times 70 \times 135$ mm^3 rectangular specimens for ultrasonic testing. See Figure 2.4. During cutting, at least the last 5 mm of each side of the compacted samples was trimmed off to avoid any end-effects induced during compaction and to obtain a smooth surface for sensor placement. Ultrasonic measurements were only performed on specimens aged up to (and including) 36 hours, because the rough, cratered surfaces of specimens aged passed 36 hours caused coupling issues with the sensors. See Figure 2.5, which shows a specimen aged passed 36 hours, at 48 hours. Notice the very rough, cratered surface.

Figure 2.5: Asphalt concrete specimen oven-aged for 48 hours. Notice the very rough and cratered surface, which made for unacceptable couplant conditions with the transducers.

2.2.2 Considerations in Choosing Experimental Set-up

Prior to choosing and implementing an experimental set-up, some important considerations must be made. The complex wave propagation and finite dimensions of the AC samples complicate what might initially appear to be a straightforward measurement. This section will address some important considerations.

Wave Propagation through Asphalt Concrete

The structure of asphalt concrete is that of a brick and mortar type. As a dilatational wave propagates through the material, most of the wave passes through the limestone aggregate (≈94% of the composite is aggregate). There is a significant difference in the moduli between the brick, *i.e*, aggregate, and the mortar, *i.e.*, binder. As the wave propagates through the asphalt medium, it becomes scattered and distorted. As the wave propagation distance increases, the effect of scatter (hence, the wave shape distortion) also increases.

It was observed that across the height of the specimen (≈ 70 mm), the waveform becomes distorted and difficult to analyze at higher frequencies. Across the width of the specimen (≈ 40 mm), the wavelength is longer than the specimen dimensions at lower frequencies, which can lead to erroneous calculations due to phase interference effects. When the wavelength is shorter than the specimen dimension and longer than the NMAS, the signal propagates through the medium

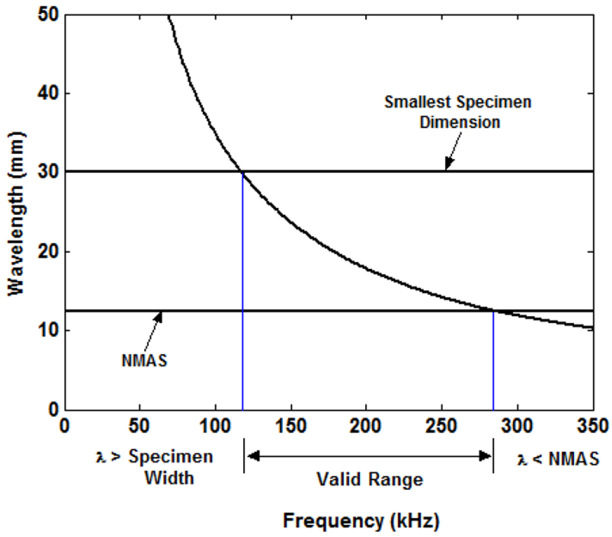

Figure 2.6: The wavelength (obtained via the velocity) as a function of frequency for the virgin specimen. The "valid range," *i.e.*, NMAS $< \lambda <$ specimen dimension, is the range at which ultrasonic measurements can be taken in a conventional through-transmission format (*e.g.*, without the use of a waveguide). Extracted from McGovern et al. [13]

with relatively little distortion. This range will be termed the "valid range," and is depicted in Figure 2.6.

As the shear wave propagates through the medium, a portion of the energy may mode convert to dilatational waves via scattering. Since shear waves travel slower than dilatational waves, the multiple modes may arrive at the same time; thus, the obtained signal may be a superposition of these multiple modes. The dilatational portion can be isolated by partitioning (windowing) the beginning of the signal in time, because it is the fastest, thus first, arriving wave. For shear wave measurements, partitioning out the shear portion should not be attempted, because it is difficult to isolate. To circumvent this difficulty, a pulse train can be used to "force" a majority of the wave energy to propagate as shear. Even with a pulse train, it is likely that the received wave is not entirely shear due to scatter induced mode conversion effects; however, a majority of the energy should be shear.

Delay Line

To overcome the difficulties that arise from the wavelength at lower frequencies being longer than the specimen dimension, a delay line can be used. By using a delay line, the transmitted waveform will

be fully formed, *i.e.*, not suffer from near field effects, before it propagates through the specimen. A block made of ultra-high molecular weight polyethylene (UHMWPE) was chosen as the delay line, because its acoustic impedance relative to the acoustic impedance of virgin asphalt was close enough such that there was not too much loss at the UHMWPE/asphalt interface. The block dimensions ($\approx 72 \times 57 \times 116$ mm^3) were chosen to allow the transmitted waves to propagate through the specimen without much interference from the boundaries.

Ultrasonic Velocity

Many velocity methods (*e.g.*, threshold-crossing [14], cross-correlation [15], overlap [16], etc.) require that the signal retain its shape as it propagates through the medium; however, in asphalt, the waveform does not retain its shape. The phase comparison method [17] was the method of choice, because it is insensitive to waveform distortion; however, this method can break down when there is a low signal-to-noise ratio and/or multiple waves with different paths arriving simultaneously. The phase velocity can be obtained by comparing the phases of the signals measured through the delay line and the delay line/asphalt set-up as follows [17],

$$c(\omega) = \frac{\omega d_{asphalt}}{\phi_{asphalt}(\omega) - \phi_{UHMWPE}(\omega)} \tag{2.13}$$

where $\phi_{asphalt}$ denotes the phase for the signal passed through the UHMWPE/asphalt set-up, ϕ_{UHMWPE} denotes the phase of the signal obtained from just the UHMWPE delay line, $d_{asphalt}$ is the distance traveled through the asphalt specimen, and ω is the angular frequency.

Ultrasonic Attenuation

The attenuation coefficient can be determined by comparing the amplitude of the signal passed through the delay line/specimen set-up to the amplitude of the signal passed through the delay line alone (the reference signal). At the delay line/specimen and transducer/specimen interfaces, signal loss will occur due to impedance mismatch and imperfect couplant conditions. If this loss is not accounted for, the attenuation will be overestimated. The loss can be accounted for by measuring the attenuation in the "valid range" (see Figure 2.6) via the conventional through-transmission technique (*i.e.* no delay line), and then translating the attenuation measured via the delay line

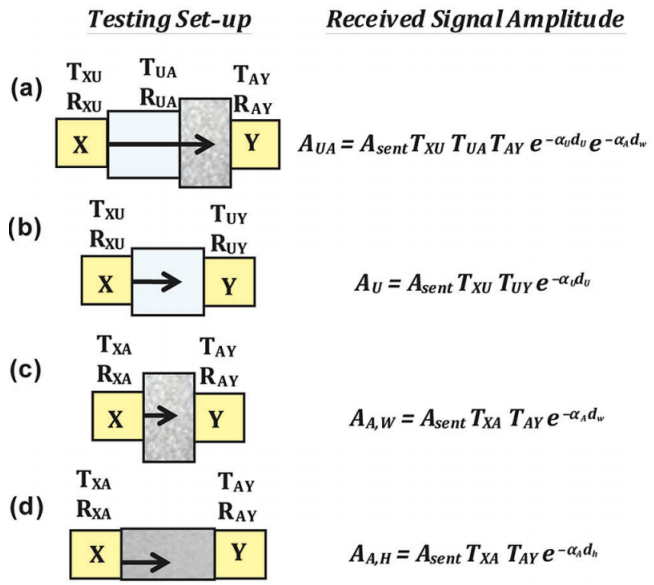

Figure 2.7: Method to find attenuation coefficients of asphalt specimens with correction for signal loss at the boundaries. A_{sent} is the signal sent by transducer X, Y is the receiving transducer, and subscripts A and U denote asphalt and UHMWPE, respectively.

configuration to coincide.

Please reference Figure 2.7, which contains the setups and the corresponding amplitude of the received signals. The data acquisition procedure will now be outlined. First the signal is recorded through the smallest (width) dimension of the specimen coupled to the delay line (see Figure 2.7 (a)). A signal is then recorded through only the delay line (Figure 2.7 (b)). Next, signals are obtained through the width and height dimensions of the specimen without the wave guide (Figures 2.7 (c) and (d), respectively). All recorded signals are appropriately windowed to isolate the dilatational portion of the signal. The window sizes may change based on frequency. Shear signals are not windowed.

The uncorrected attenuation $\alpha_{uncorrected}$ is determined across all frequencies based on the signals obtained for the set-up with the delay line. Recall, this attenuation is an overestimate of the attenuation in the asphalt concrete, because it contains the loss from the transducer/asphalt and delay line/asphalt interfaces. Equation 2.14 shows this uncorrected attenuation, where A_{UA} denotes the amplitude received through the delay line/asphalt set-up, and A_U denotes the amplitude received

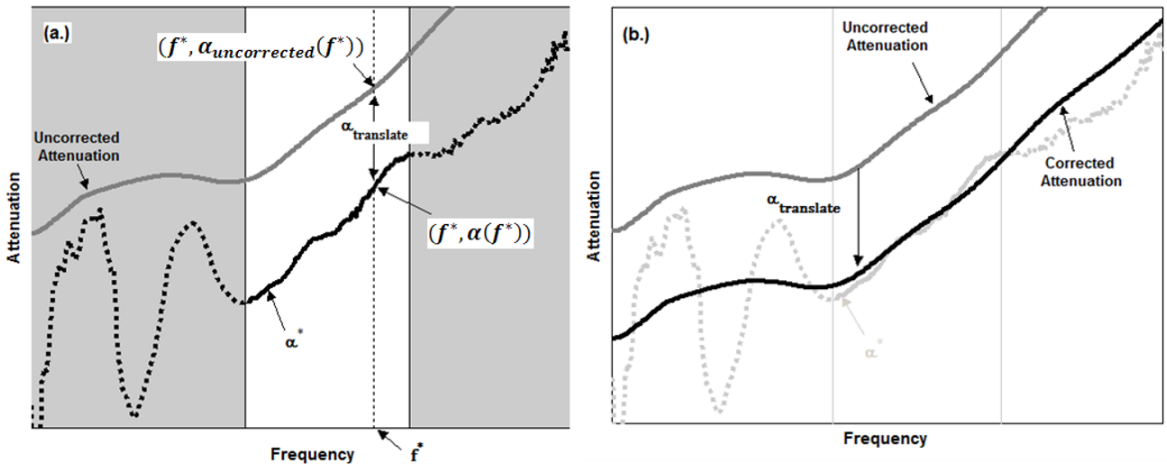

Figure 2.8: Correction of the attenuation obtained via the delay line technique in order to account for the loss at the interfaces. (a.) Arbitrarily choose f^* from the valid range and determine the corresponding $\alpha^*(f^*)$ and $\alpha_{uncorrected}(f^*)$ to obtain translate. The shaded gray regions denote the invalid regions for choosing f^*. The black data is α^*. The dark gray data is $\alpha_{uncorrected}$. (b.) Translate the uncorrected by $\alpha_{translate}$. The attenuation α^* is shown in a very light gray for comparison purposes.

through only the delay line.

$$\alpha_{uncorrected}(f) = -\frac{1}{d_w} \ln\left(\left|\frac{A_{UA}(f)}{A_U(f)}\right|\right) \tag{2.14}$$

The attenuation is then calculated using windowed signals obtained from the set-up without the delay line over the valid region (Figures 2.6 and 2.7 (c),(d)). This attenuation is denoted as α^*. Due to the manner in which α^* is found, it is independent of the loss at the transducer/asphalt boundaries (assuming consistent couplant conditions).

$$\alpha^*(f) = -\frac{1}{d_h - d_w} \ln\left(\left|\frac{A_{A,Height}(f)}{A_{A,Width}(f)}\right|\right) \tag{2.15}$$

It is worth emphasizing that if there were no phase interference or lossy signal issues, α^* could be used to fully characterize over entirety of the desired frequency range. However, in the presence of these issues, α^* can only be obtained for the "valid range," and extra measurements must be taken. To find the amount that $\alpha_{uncorrected}$ is to be translated (corrected), a frequency f^* should be chosen at which to evaluate α^*. This frequency f^* should be chosen from the "valid range" (see Figure 2.6), such that the wavelength is shorter than the specimen dimension and longer than the aggregates ($\lambda >$ NMAS $= 9.5$ mm). The difference is found between $\alpha_{uncorrected}$ and α^* at f^*; this

difference is denoted as $\alpha_{translate}$. See Figure 2.8 (a) for a graphical representation of these last few procedures.

$$\alpha_{translate} = \alpha_{uncorrected}(f^*) - \alpha^*(f^*) \tag{2.16}$$

Next, $\alpha_{uncorrected}$ is translated by $\alpha_{translate}$. The uncorrected attenuation coefficient should be translated down, such that the resulting attenuation coefficient is less in magnitude. See Figure 2.8 (b) for a graphical representation. Equation 2.17 describes the culmination of the procedures outlined above. An example of the attenuation described by Equation 2.17 is shown as the solid black data in Figure 2.8 (b).

$$\begin{aligned} \alpha(f) &= \alpha_{uncorrected}(f) - \alpha_{translate} \\ &= \frac{1}{d_w} \ln\left(\left|\frac{A_{UA}(f^*)A_U(f)}{A_U(f^*)A_{UA}(f)}\right|\right) - \frac{1}{d_h - d_w} \ln\left(\left|\frac{A_{A,Height}(f^*)}{A_{A,Width}(f^*)}\right|\right) \end{aligned} \tag{2.17}$$

2.2.3 Experimental Set-Up

Two longitudinal transducers (Panametrics V101) with a center frequency of 500 kHz were used for sending and receiving in a through-transmission setup. For more information regarding ultrasonic transducers, the reader is referred to the text by Bray and Stanley [18]. The sending transducer was coupled to a delay line (ultra high molecular weight polyethylene, UHMWP), and the receiving transducer was coupled to the opposite side of the AC specimen. A function generator (Krohn-Hite

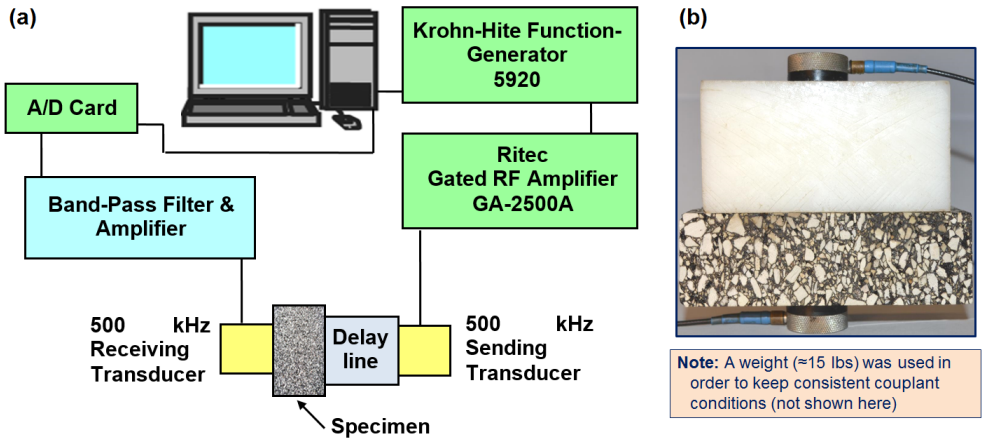

Figure 2.9: Schematic diagram (a) of experimental set-up and (b) actual set-up for measurements across both the width and the height of the asphalt specimens. Extracted from McGovern et al. [13]

model 5920) was used to generate a 5 cycle sinewave toneburst, which swept between 10 kHz and 500 kHz in 5 kHz increments. The number of cycles was chosen in order to force the transducer to operate at each frequency (even away from its center frequency). The generated signal was amplified by a gated amplifier (Ritec GA-2500A) and used as the input for the sending transducer. Measurements were taken at 10 different locations on each specimen. The data was sampled at ≈17 MHz and averaged 25 times to mitigate effects from scatter. Refer to Figure 2.9 for a schematic of the experimental setup. All specimens were tested at room temperature (≈23°C).

The received signals obtained from the swept frequency input were averaged to obtain one signal comprised of all the swept frequencies. Ultrasonic velocities and attenuations were determined based on a comparison of the signal traversing through the delay line/sample configuration and the signal obtained in the same manner through only the delay line (as described in Section 2.2.2).

2.3 Experimental Results

Using the experimental setup and techniques as described in Section 2.2, the ultrasonic velocities and attenuations were obtained for the asphalt specimens subjected to different amounts of aging. These results will now be presented and discussed. Then, the velocities and attenuations will be used to obtain the complex moduli. Refer to Figure 2.10, which contains representative examples of the (windowed) data collected in the time and frequency domains (Figure 2.10 (a) and (b), respectively).

2.3.1 Ultrasonic Velocity and Attenuations

Figure 2.11 shows the velocities and corresponding attenuations for the dilatational and shear measurements of each aged specimen as a function of the frequency. Figure 2.12 also shows the ultrasonic dilatational and shear measurements; however, presented as a function of both aging time and frequency. Referring to Figures 2.11 (a) and 2.12 (a), there is an increase in the dilatational velocity from 30 kHz to ≈100 kHz for all of the specimens. After ≈100 kHz, the velocity starts to plateau. For the specimens aged 32 and 36 hours, the velocity for frequencies above 250 kHz (*i.e.*, point A from Figure 2.11) were difficult to calculate because of the low signal-to-noise ratio caused

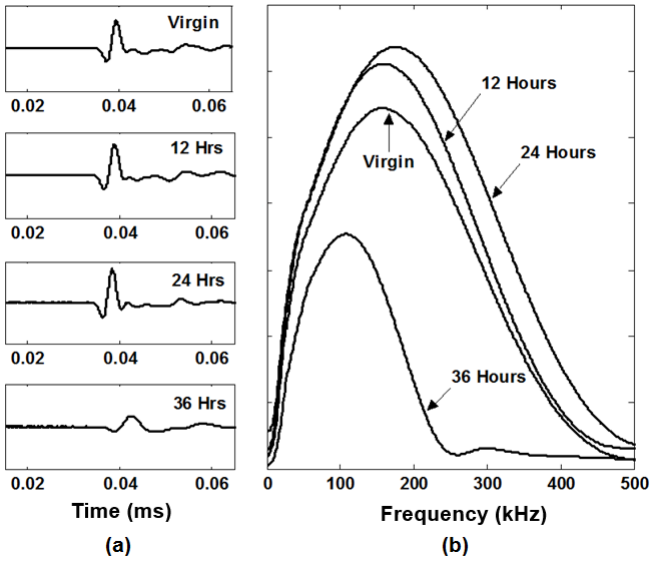

Figure 2.10: Representative data for dilatational measurements in the (a) time domain and (b) frequency domain obtained from asphalt concrete aged from 0 hours to 36 hours.

by increased attenuation.

Figure 2.13 shows the average of each ultrasonic parameter across frequency as a function of aging. From 0 to 24 hours, the velocity (across all frequencies) increases; however, from 24 to 36 hours, the velocity (across all frequencies) decreases (see Figure 2.13 (a)). As the binder ages, its stiffness increases, thus accounting for the increase in velocity for the specimens aged 0 to 24 hours. However, after 24 hours of aging, the cohesive strength loss suffered by the mastic begins to result in the development of a diffuse micro-flaw population. The presence of these micro-flaws effectively decreases the overall (composite) elastic modulus, which results in a much lower velocity.

The shear velocities tend to increase with increasing frequency (Figures 2.11 (c) and 2.12 (b)). One potential explanation for the increase in velocity with frequency is that as the frequency increases, an increase in both the shear attenuation and mode conversion (from shear to dilatational) causes the dilatational components of the signals to become more dominant. Under this explanation, the two velocities (dilatational and shear) will eventually converge as the frequency continues to increase. This hypothesis is supported by the fact that the shear velocities could not be measured through the larger specimen dimensions. In fact, when shear and dilatational velocity measurements were taken across the larger specimen dimensions, the dilatational and shear velocities were nearly

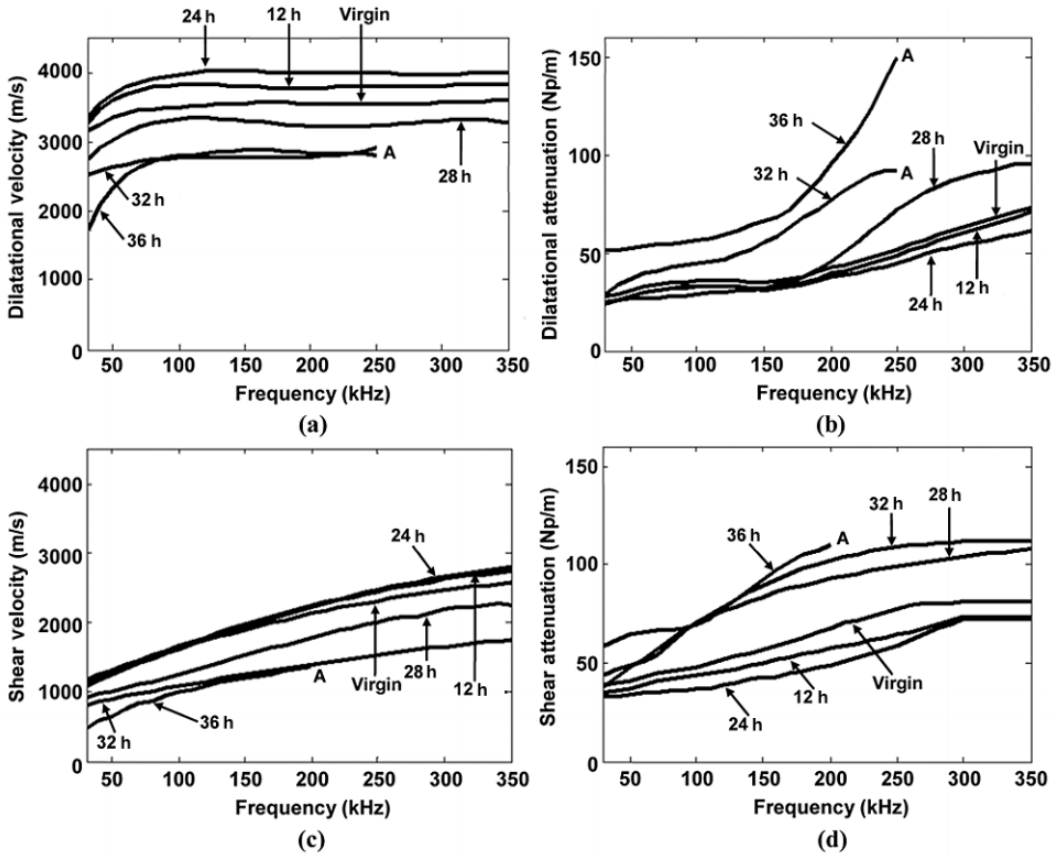

Figure 2.11: Dilatational (a.) velocities (m/s) and (b.) attenuations (Np/m) for asphalt concrete aged 0 to 36 hours. Shear (c.) velocities (m/s) and (d.) attenuations (Np/m) for asphalt concrete aged 0 to 36 hours. Some velocities and attenuations were only calculated up to a limited frequency, *e.g.*, point A, because of the low signal-to-noise ratio caused by the increased attenuation. Extracted from McGovern et al. [13]

identical. This is because, as the dimension of the specimen increases, the shear components of the signal become more attenuated, leaving the dilatational components to become dominant. Also, mode conversion from shear to dilatational waves will be more prevalent over larger distances. As a function of aging, the shear velocities exhibit a similar trend to the dilatational velocities: they increase from 0 to 24 hours and decrease from 24 to 36 hours (Figure 2.13 (b)).

Figures 2.11 (b) and 2.12 (a) show the magnitude of the dilatational attenuation coefficients as a function of frequency for the different specimens. It is observed that as the frequency increases, the attenuation also increases. For all the specimens, there looks to be an inflection point around 175 kHz, where the slope of the attenuation changes and the attenuation drastically increases. For the specimens aged 32 and 36 hours, the attenuation above 250 kHz was difficult to calculate because of the low signal-to-noise ratio. This implies that the attenuation continues to increase

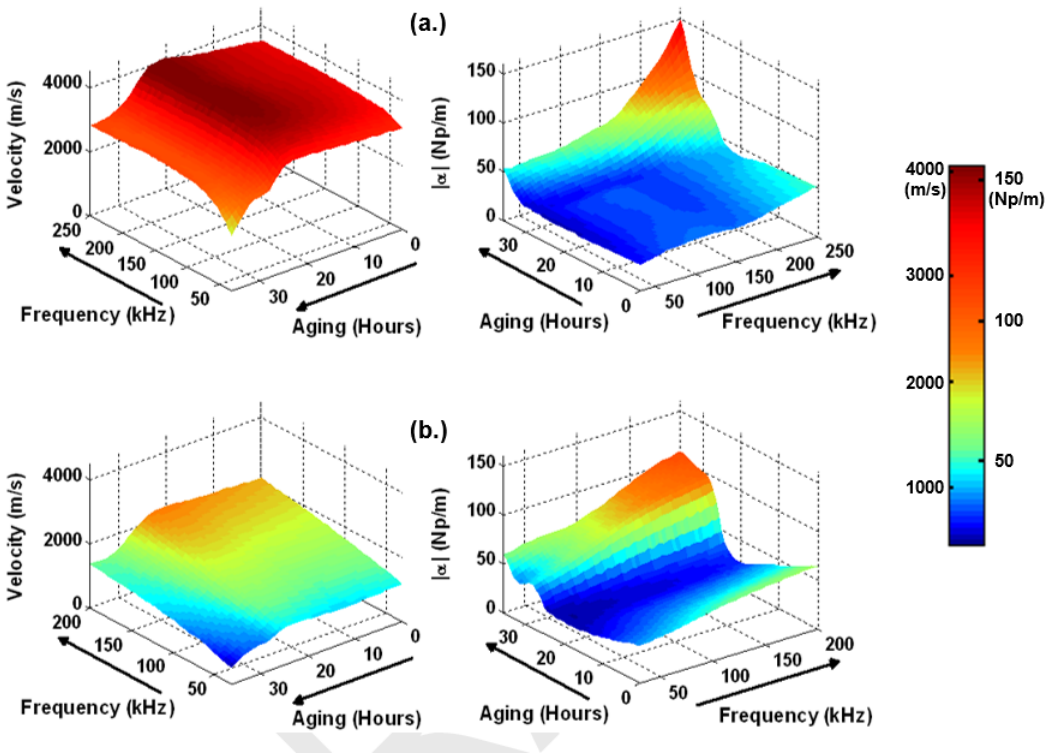

Figure 2.12: (Left column) Velocities (m/s) and (Right column) attenuations (Np/m) of asphalt concrete for (a.) dilatational waves and (b.) shear waves as a function of aging (hours) and frequency (kHz). The surface was fitted using cubic spline interpolation. Since interpolation was used to construct the surfaces, the R-squared value as a measure of goodness of fit is unity. Extracted from McGovern et al. [13]

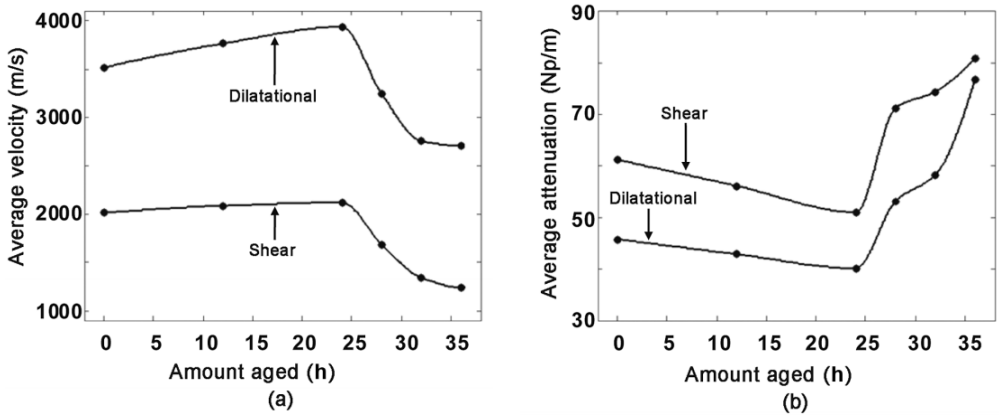

Figure 2.13: Average across frequency of (a.) velocities (m/s) and (b.) attenuations (Np/m) for asphalt concrete aged 0 to 36 hours. Extracted from McGovern et al. [13]

for frequencies above 250 kHz. The magnitude of the shear attenuation coefficients increase with frequency (see Figure 2.11 (d) and 2.12 (b)). The dilatational and shear attenuations as a function of aging (Figure 2.13 (b)) follow a similar trend to the velocity, where there is a decrease in the attenuation from 0 to 24 hours, and an increase from 24 to 36 hours.

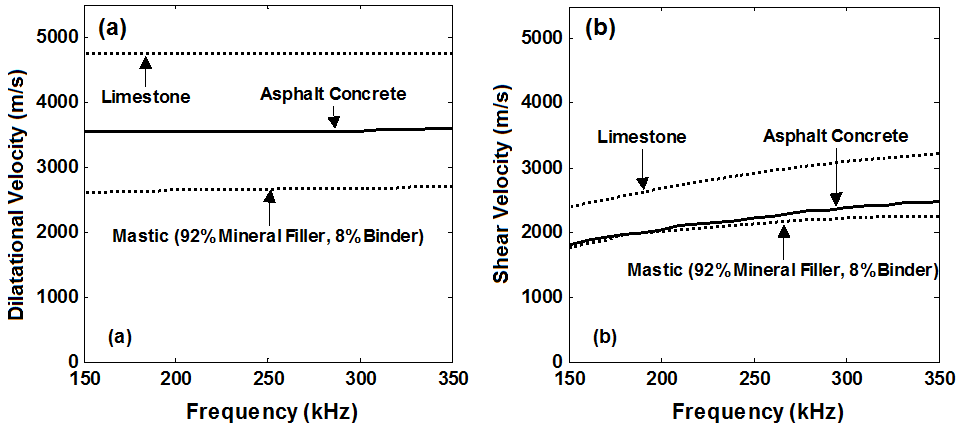

Figure 2.14: Dilatational (a) and shear (b) velocities (m/s) for virgin asphalt concrete, limestone, and mastic (92% mineral filler and 8% binder).

In order to gain a stronger understanding of the trends observed (with respect to frequency) in the asphalt concrete, ultrasonic measurements on the constituent materials (mastic and limestone) were carried out. The mastic sample was created with 92% mineral filler and 8% binder. This binder to fines proportion was chosen so that measurements could be carried out at room temperature (and the specimen did not loose its shape). For both dilatational and shear measurements, it was observed that the phase velocity of the asphalt concrete was slower than the phase velocity in the limestone, and faster than the phase velocity in the mastic. See Figure 2.14. The dilatational attenuation of the mastic was observed to be higher (but not by much) than that of the asphalt concrete; whereas, the shear attenuation of the mastic was much higher than that of the asphalt concrete. See Figure 2.15. For both dilatational and shear measurements, the limestone attenuation was found to be much lower than the virgin asphalt concrete sample.

Based on these results, it can be concluded that as the wave propagates through asphalt concrete, its attenuation is not dominated by the inherent damping of the binder/mastic. This makes sense when realizing that only $\approx$5% of the asphalt concrete is actually binder. Rather, much of the attenuation is due to scattering and the inherent damping of the limestone. This claim is supported since the attenuation in the limestone is lower than the attenuation in the asphalt concrete. The structure of the asphalt concrete might also play a role in the attenuation. The structure is a brick and mortar type, which may facilitate wave propagation (for dilatational waves) and actually lessen the attenuation.

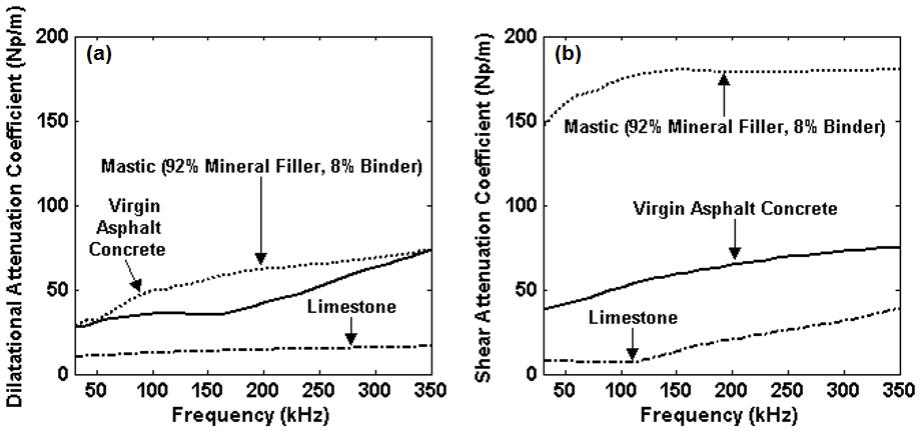

Figure 2.15: Dilatational (a) and shear (b) attenuations (Np/m) for virgin asphalt concrete, limestone, and mastic (92% mineral filler and 8% binder).

2.3.2 Complex Moduli

The complex moduli were calculated using the ultrasonic results (Figure 2.11) in the equations from Section 2.1.2. Comparisons were made between the complex moduli obtained via the ultrasonic technique to those obtained from the conventional mechanical technique [10]. Figure 2.16 contains the dynamic uniaxial modulus $|E^*|$ and the dynamic shear modulus $|G^*|$ as a function of frequency for different amounts of aging. From this point forward, the dynamic modulus will be called

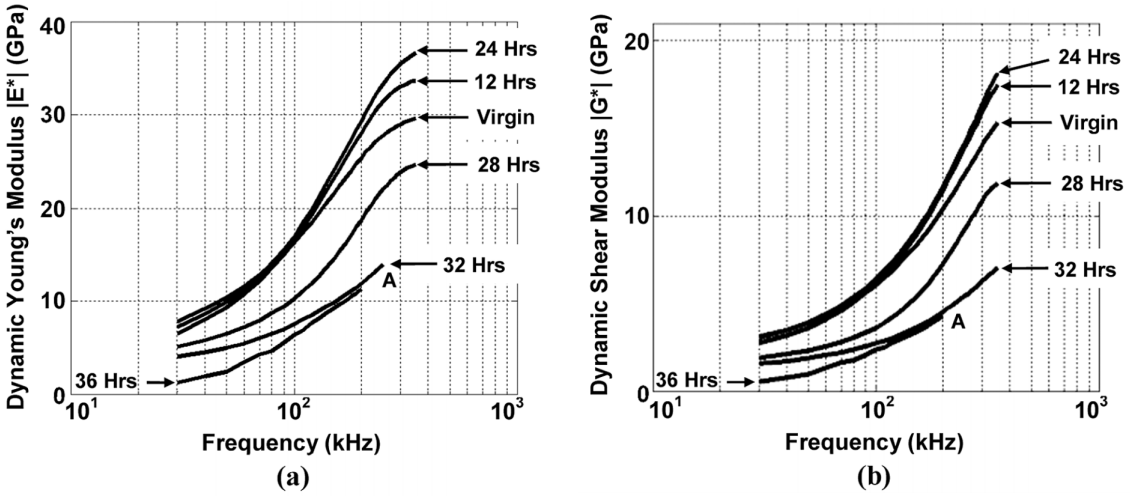

Figure 2.16: (a.) Dynamic Young's modulus $|E^*|$ and (b.) dynamic shear modulus $|G^*|$ as a function of frequency for specimens subjected to various amounts of aging computed using ultrasonic measurements. For 32 and 36 hours aged, measurements at higher frequencies, *e.g.* point A, were difficult to calculate because of the low signal-to-noise ratio caused by the increased attenuation. Extracted from McGovern et al. [19]

$|E^*|_{age}$, where the subscript denotes the specimen according to the amount of aging to which it was subjected. As the frequency increases, $|E^*|$ increases for all specimens. For example, for the frequency range of 30 kHz to 350 kHz, $|E^*|_0$ increases from ≈5 GPa to ≈28 GPa. This increase in $|E^*|_0$ is sharper than what would be obtained from a corresponding mechanical test. This discrepancy can be attributed to scattering and will be discussed in following text.

As expected, $|E^*|$ follows the same trend as the velocities with respect to the amount of aging: $|E^*|$ increases from 0 to 24 hours and decreases from 24 to 36 hours. The complex shear modulus G^* follows similar trends to E^*. The phase angle decreases with increasing frequency for all specimens. See Figure 2.17. This same trend is typically also seen in mechanical testing; however, discrepancies still exist. In mechanical testing, the phase angle is larger at low frequencies, and approaches zero with increasing frequencies. Via ultrasonic testing, the phase angle decreases with increasing frequencies; however, it seems to reach an asymptote at approximately 14°. There is no discernible trend with respect to aging.

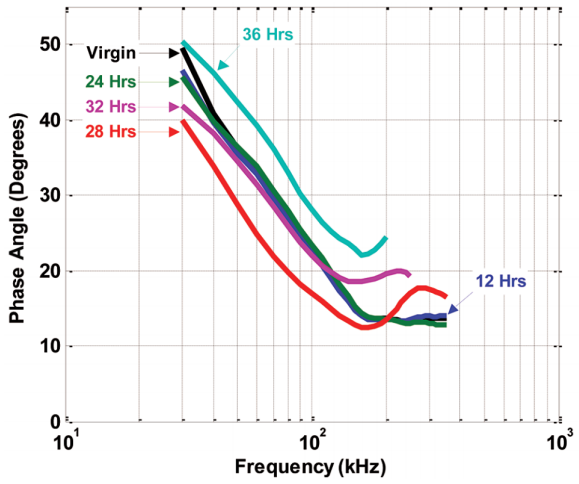

Figure 2.17: Phase angle (degrees) as a function of frequency for specimens subjected to various amounts of oven-aging (0 hours to 36 hours). Extracted from McGovern et al. [19]

Figure 2.18 contains the complex Poisson's ratio as a function of frequency. The real component of the Poisson's ratio decreases with increasing frequency. The imaginary component decreases with increasing frequency from 30 kHz to 190 kHz; above 190 kHz, it increases with increasing frequency.

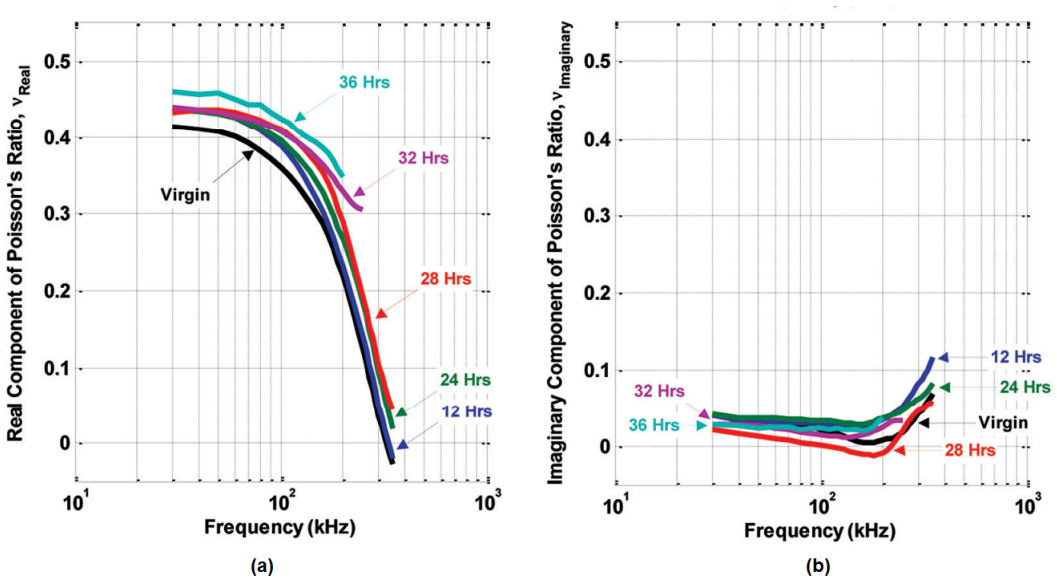

Figure 2.18: The real component (a.) and imaginary component (b.) of Poisson's ratio as a function of frequency for specimens subjected to various amounts of oven-aging (0 hours to 36 hours). Extracted from McGovern et al. [19]

2.3.3 Comparison with Mechanical Tests

Please refer to AASHTO T 342-11 [10], which details the compressive dynamic modulus test procedures for determining the dynamic modulus and phase angle of the AC over a range of frequencies and temperatures. The complex moduli results via the ultrasonic method do not coincide with typical results obtained from conventional mechanical tests (see Figure 2.19); however, this does not imply that there is no correlation. The results obtained via measuring ultrasonic parameters via wave propagation are affected by scattering. Conventional mechanical E^* tests out put the macroscopic properties of the AC specimen; thus, local scattering of mechanical waves by the aggregate structure will not affect the results. Scattering of the waves in ultrasonic testing will cause discrepancies between the ultrasonic and mechanical tests for two major reasons: 1. it will increase the measured attenuation, 2. the measured shear velocity will be dependent on frequency, which corresponds to a change in the Poisson's ratio. If scattering were not present during ultrasonic wave propagation, the attenuation would be lower and the shear velocity would not be heavily frequency dependent (corresponding to a nearly constant Poisson's ratio).

To illustrate the above point, $|E^*|$ can be computed for the case of constant shear velocity and lower attenuation (for both shear and dilatational). Note, this is done for illustration purposes only. Figure 2.19 (a) shows the dynamic modulus $|E^*|$ obtained via the conventional mechanical testing method (see Section 2.1.1) and the ultrasonic method (see Section 2.1.2). For the ultrasonic method, only the raw ultrasonic data was used, and no assumptions were made. Previously, it was mentioned that the discrepancies between the two tests are caused by scattering affects. If this is the case, lowering the attenuation and forcing the Poisson's ratio to be constant (thus forcing the shear velocity to be constant) should allow for the two methods to coincide. Figure 2.19 (b) shows the mechanical data along with the ultrasonic data with these major assumptions. Specifically, these assumptions are: 1. the shear velocity was forced to remain constant, and 2. the attenuation was arbitrarily decreased by 20 Np/m. In practice, it could be possible to characterize how the attenuation should shift (*e.g.*, based on scattering affects); however, the uncertainty in choosing a proper shear velocity value (at the appropriate frequency) would still exist. Since the dilatational velocities are nearly constant, the first assumption corresponds to a constant Poisson's ratio (see Equation 2.5). This is a big assumption, as evidenced by Figure 2.20, which shows the shear velocity dependence on Poisson's ratio for the mean value (across 100 - 350 kHz) of dilatational velocity. The second assumption does not have a strong effect on the results. Figure 2.19 (b) shows the

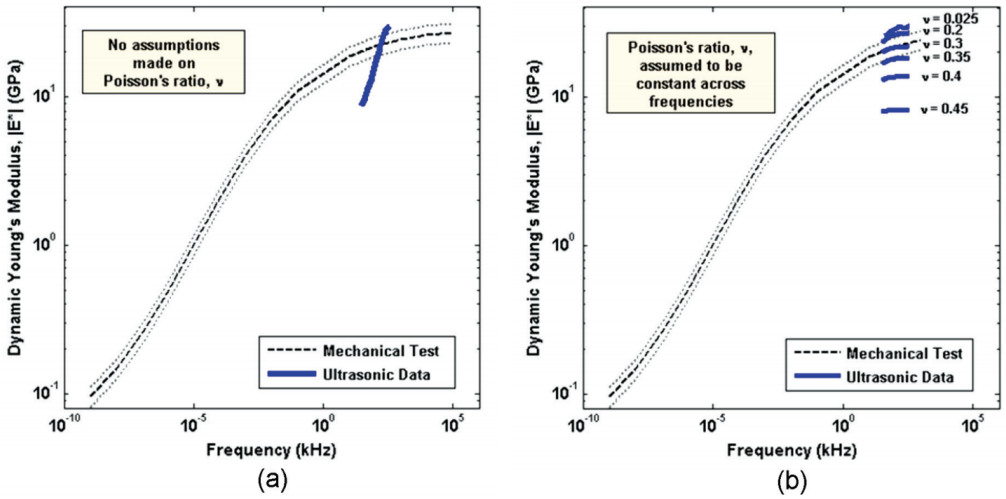

Figure 2.19: The dynamic modulus $|E^*|$ (GPa) obtained via conventional mechanical testing (gray dashed line) compared with the $|E^*|$ obtained via the ultrasonic method based on: (a.) no assumptions, (b.) the assumption that Poisson's ratio, μ, is constant and an arbitrary decrease in attenuation (for both dilatational and shear) of 20 Np/m. Results from the mechanical dynamic modulus test were provided by Brian Hill. Extracted from McGovern et al. [19]

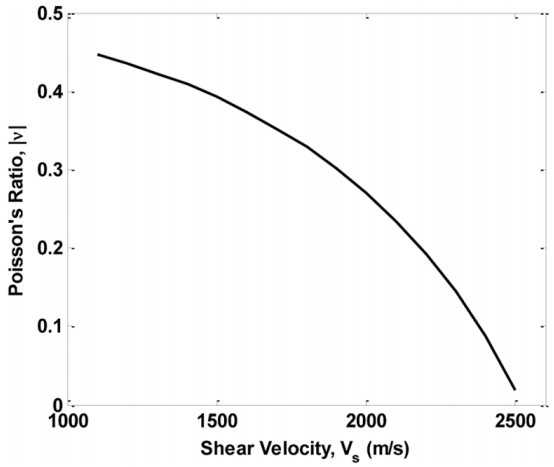

Figure 2.20: The mean Poisson's ratio as a function of shear velocity in virgin binder for higher frequencies (where the dilatational velocity does not change much with frequency)

ultrasonic results with an arbitrary reduction in attenuation of 20 Np/m for multiple assumptions of the shear velocity (within the measured range). It was observed that attenuation does not play a large role in the determination of these curves. This can be realized by recognizing that the complex velocity is a function of the attenuation normalized by the angular frequency $\frac{\alpha(\omega))}{\omega}$ (see Equation 2.10). Thus, for high frequencies (like the ultrasonic range), this ratio is a small number.

The measured phase angle will also be affected by wave scattering effects. The phase angle measured via the ultrasonic method is higher than the phase angle obtained via mechanical testing. Similarly, the Poisson's ratio is a function of the complex velocities (dilatational and shear); thus, scattering will cause discrepancies for the aforementioned reasons.

2.3.4 Construction of the Master Curve

Previous studies [6–8] have measured the group velocity at different temperatures without considering frequency dependency; thus, the velocity at each temperature was a discrete value. When constructing the master curve, it is necessary to shift the data via time-temperature superposition. Shifting the data, however, requires that the shift factor be known. If velocity measurements are not taken with respect to frequency, then the only way to obtain the shift factor is by comparing it to a known master curve (*e.g.*, a model fitted to data obtained via conventional mechanical testing). Consequently, the need for mechanical testing is not eliminated. To construct the master curve

from solely the ultrasonic data, the measurements must be known over a range of frequencies.

2.3.5 Important Implications of Results and Correlation with Other Tests

The linear acoustic results, shown in Figure 2.13, exhibit an interesting trend with respect to the level of oxidative aging. Although a brief explanation of this trend was offered earlier in this chapter, a more in-depth discussion will now be provided.

Ultrasonic velocity is proportional to the stiffness $\left(c = \sqrt{\frac{E}{\rho}}\right)$. It is well known that the binder stiffness increases with the level of oxidative aging (see Appendix A), and as a result, it might be expected that the ultrasonic velocities should follow a similar trend. While upon first glance it may appear that the ultrasonic results are inconsistent with the expected oxidative aging trend, in fact they are not. This can be realized by noting that the ultrasonic velocity measurements reflect the overall global composite (*i.e.*, mastic + aggregate) stiffness and not just that of the binder. During the oxidative aging process of asphalt concrete, two major mechanisms occur: 1. the binder stiffness increases with an increase in aging level and 2. the cohesive strength in the mastic decreases with an increase in aging level. At low aging levels, the first mechanism dominates, resulting in an increase in the overall composite stiffness. After a certain aging level, however, the second mechanism (cohesive strength loss) begins to dominate. The loss in cohesive strength in the mastic results in an increase in the diffuse micro-flaw population, *i.e.*, cracks. The presence of these flaws has the effect of lowering the overall composite stiffness. Thus, during oxidative aging, there are two competing effects on the composite stiffness, where the "critical point" (for this mix-design 24 hours) is the point where the material properties experience a transition from regime to the other (*i.e.*, from the regime where the first mechanism dominates the global stiffness to the second).

This behavior, which exhibits a trend containing a critical aging time, is in agreement with data from other studies using different methods; however, the amount of aging at which these peaks (or troughs) occur varies slightly between tests. See Figure 2.21, which contains results from other experiments on the oxidative aging effects on AC. Notice that all exhibit similar trends, where a critical aging time exists, much like the ultrasonic results from Figure 2.13. For the mixture used in

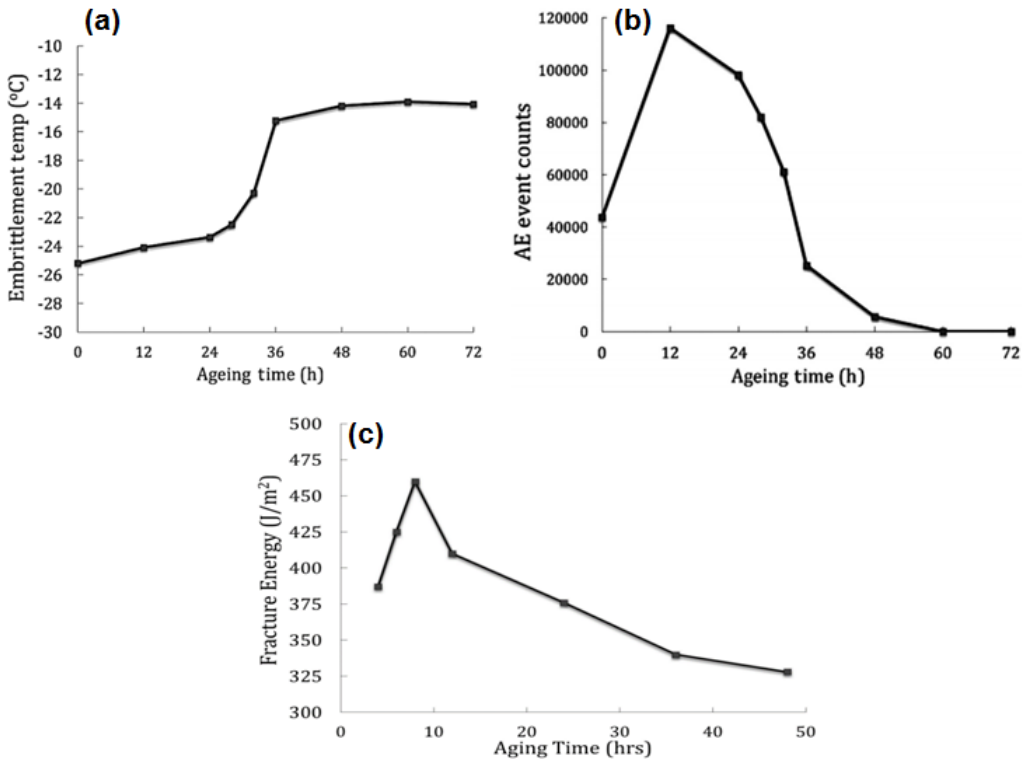

Figure 2.21: Experimental results on oxidized asphalt concrete from other studies. Notice that all tests exhibit a "critical aging time" similar to results shown in Figure 2.13. Acoustic emission results are shown in (a) and (b), and fracture toughness results are shown in Figure (c). Figures (a) and (b) were extracted from McGovern et al. [13], and Figure (c) was extracted from Braham et al. [20].

this study, this critical time appears to be around 24 hours of oven-aging for this mixture. Figures 2.21 (a) and (b) contain results from an acoustic emission study [13]. In these tests, the rate of change of the embrittlement temperatures, with respect to aging time, increases relatively slowly until 24 hours of aging, after which it rapidly increases. The results are also supported by reported disc shaped compact tension (DC(T)) fracture energy test results shown in Figure 2.21 (c), where the fracture energy increases up to a critical aging time (≈10 hours of oven-aging), after which it decreases [20].

Thus, oxiditation in AC follows a damage trajectory, where there exists a critical aging time. Before this critical time, the pavement has the ability to self-heal. After the critical aging time, pavement deterioration rapidly accelerates. The ability to keep the pavement in a state below the critical time is crucial for pavement preservation.

Chapter 3

Assessment using Nonlinear Acoustics

The results in Chapter 2 demonstrated that linear acoustic measurements, such as ultrasonic velocity, can detect high levels of oxidative aging; however, the dependence on the level of aging is not unique. For oven-aged AC, the ultrasonic velocity increases from 0 hours to 24 hours aging, after which it decreases with increasing aging. Therefore, more than one aging level will yield the same velocity measurement. In this chapter, non-collinear wave mixing, a nonlinear acoustic technique, will be used to assess the amount of oxidative aging present in asphalt concrete. Two parameters will be used as metrics to quantify the oxidation level. One of the parameters is inherently related to the velocity, and the other parameter helps to circumvent the problem of non-uniqueness. For a complete in-depth discussion on the theory and derivations of nonlinear acoustic wave-mixing, please refer to Appendix C. Here, only the important aspects to the theory, essential to understanding the subsequent investigations will be presented for facilitation of the reading.

3.1 Nonlinearities in Asphalt Concrete

Distributed damage, such as damage induced by fatigue, typically consists initially of phenomena affecting the material at many locations in the form of local variations in the material microstructure. In metals, such as aluminum, these local variations in microstructure consist of fatigue induced entanglement of dislocation substructures such as the side bands. These side bands, which accumulate at the grain boundaries, produce strain localization, which eventually leads to microcracking initiation with increasing number of fatigue cycles. While these local changes in microstructure do not change macroscopic elastic moduli or acoustic linear parameters, such as acoustic velocity and attenuation, the stress field in the dislocation(s) creates a local nonlinear stress-strain response in the localized volume of the dislocation(s). Before the initiation of a visible terminal crack, these local variations in the microstructure at the scale of single grains develop. This more or less even degradation of the material significantly reduces the material's resistance against crack growth later when microcracking coalescence occurs.

The ultimate strength of most structural materials is limited by the presence of these microscopic microstructural variations, *i.e.*, defects, which can be produced by mechanical or thermal loading, and subsequently serve as nuclei of the fracture process. Because these nuclei (local variations) are significantly shorter that the acoustic wavelength at the frequencies normally used in ultrasonic nondestructive evaluation, linear acoustic parameters (*i.e.*, attenuation, velocities, etc.) are usually not sensitive enough to this kind of microscopic degradation of the material structural integrity. However, the presence of an increasing number of entangled forests of dislocations with an increase of fatigue damage causes a nonlinear distortion in a propagating wave.

Nonlinearities in asphalt concrete may arise from multiple sources. Asphalt concrete is a composite material comprised of two phases: an asphalt cement matrix and an aggregate reinforcement. The asphalt cement (*i.e.*, binder) of the asphalt concrete is inherently nonlinear as it is governed by nonlinear constitutive stress-strain relations. The aggregate structure of asphalt concrete is typically composed of crystalline stone, such as limestone aggregate. The microstructure of limestone is a brick and mortar type and consequently exhibits nonlinear mesoscopic elastic behavior [21, 22]. The bricks (*i.e.*, grains, crystals, and impurities) interface with one another across a distinctive, elastic different system, which behaves as the mortar. In limestone, the mortar is a system of asperities that provides the connectivity among the bricks, *i.e.*, at the grain/crystal boundaries. Given that most of deformation occurs in this mortar, the system of asperities that provide the connectivity among grains is the source of inherent nonlinear response in limestone. Experimentally, limestone has already been shown to exhibit nonlinear behavior using an ultrasonic resonance technique [23] and non-collinear wave mixing [24].

The overall composite material, asphalt concrete, *itself* is also a nonlinear mescoscopic structure, where the limestone aggregate behave as the bricks and the mastic behaves as the mortar. Again, most of the deformation occurs in the mastic, where for a given load, the strains in the mastic can be ten times the strains experienced by the aggregates. In asphalt concrete, the void content (4% for the mix design used in this study) is another potential source of nonlinearity. Air voids can behave similar to cracks and can cause nonlinear distortions in a propagating acoustic wave. So, asphalt concrete, even in its undamaged, unaged state, is nonlinear on many scales, as it is

composed of inherently nonlinear phases in an inherently nonlinear manner. Oxidation, which results in an increase in the diffuse micro-flaw population, only serves to increase this nonlinear behavior.

3.2 Fundamentals of Non-Collinear Wave Mixing

Consider the case of two monochromatic, sinusoidal waves propagating through a linear, elastic medium so that they cross paths. In the region where they cross paths, the resultant wave is the linear superposition of the two waves. In other words, the waves do not interact with each other, and superposition holds. In a nonlinear, elastic medium, this is not necessarily true. Under the right conditions, two waves which cross paths may interact to produce a third wave. Refer to Appendix C for a complete discussion on non-collinear wave mixing. References [25–30] also contain detailed discussions on nonlinear interaction between elastic waves.

The presence of higher-order terms in the nonlinear equations of motion gives rise to the possibility of generating a third nonlinear scattered wave when the two primary waves cross paths. Here, to maintain consistency with the literature, "primary wave" will be used to refer to the two waves which interact and should not be confused with the alternative designation for dilatational waves. Primary waves in this context can either be shear or dilatational waves. The shear waves may be polarized either in or out of the interaction plane. The two primary waves are denoted by their wave vectors, $\boldsymbol{k}_1$ and $\boldsymbol{k}_2$, and have frequencies f_1 and f_2, respectively. Without any loss of generality, f_2 is defined to be less than f_1. The type and polarization of the scattered nonlinear wave, $\boldsymbol{k}_3$, depends on the type and polarization of the two primary waves. The scattered nonlinear wave has different frequency, propagation direction, and mode than the two primary waves. Thus, the advantages of non-collinear wave-mixing, when compared to its collinear counterpart and other nonlinear acoustic techniques like harmonic generation, are the frequency, modal, and spatial separation between the primary and scattered waves.

For interaction to be possible, both resonance *and* polarization conditions must be met. Consequently, out of fifty-four potential interaction cases, there are only eight interaction cases which satisfy both the resonance and polarization conditions for non-collinear mixing (summarized in

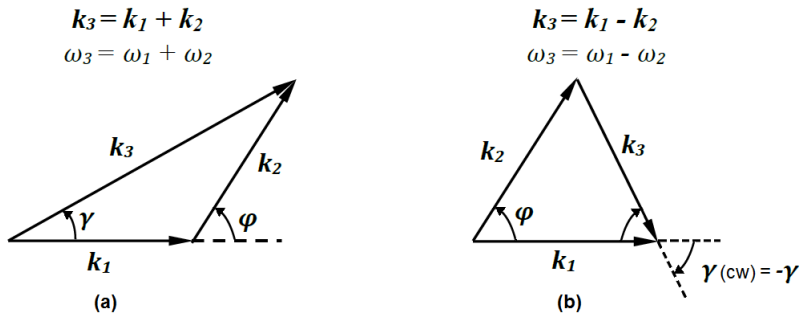

Figure 3.1: Two intersecting waves $\boldsymbol{k}_1$ and $\boldsymbol{k}_2$ which interact to produce a scattered wave with **(*a*)** a sum frequency $\omega_3 = \omega_1 + \omega_2$ or **(*b*)** a difference frequency $\omega_3 = \omega_1 - \omega_2$. for the difference frequency case, the angle γ between $\boldsymbol{k}_1$ and $\boldsymbol{k}_3$ is negative to denote a clockwise rotation of γ.

Table C.4 in Appendix C). The conditions for the existence of resonant interactions will be described shortly. The polarization condition is met when the resulting scattered wave has a non-zero amplitude. The interaction cases that satisfy resonance conditions and generate a strong scattered wave for non-collinear wave-mixing were first presented by Jones and Kobett [27]. In the current investigation, the case where two dilatational waves interact to produce a nonlinear scattered shear wave with a difference frequency was used. This case was chosen since dilatational waves suffer much less attenuation than shear waves when propagating through asphalt concrete.

For interaction to occur between two primary waves, the following must be satisfied,

$$\omega_3 = \omega_1 \pm \omega_2 \tag{3.1}$$

$$\boldsymbol{k}_3 = \boldsymbol{k}_1 \pm \boldsymbol{k}_2 \tag{3.2}$$

where $\boldsymbol{k}$ is the wave vector for a wave propagating in the $\boldsymbol{k}$ direction with a frequency ω. The magnitude of the wave vector is the wave number,

$$|\boldsymbol{k}| = k = \frac{\omega}{c} \tag{3.3}$$

where c is the propagation speed. From the criteria in Equations 3.1 and 3.2, $\boldsymbol{k}_3$ is the scattered nonlinear wave with a sum ($\omega_3 = \omega_1 + \omega_2$) or difference ($\omega_3 = \omega_1 - \omega_2$) frequency generated by the interaction between the primary waves $\boldsymbol{k}_1$ and $\boldsymbol{k}_2$. The angle at which the primary waves interact is denoted as φ. See Figure 3.1.

For non-collinear waves,

$$-1 < \cos(\varphi) < 1 \tag{3.4}$$

The direction of propagation of the scattered wave $\boldsymbol{k}_3$ is described by the angle γ with respect to $\boldsymbol{k}_1$. To maintain a consistent sign convention, $\boldsymbol{k}_2$ and $\boldsymbol{k}_3$ propagate in directions which are described by angles measured with respect to $\boldsymbol{k}_1$. For the difference frequency case, $\boldsymbol{k}_3 = \boldsymbol{k}_1 - \boldsymbol{k}_2$, the scattered wave propagates in the direction corresponding to a clockwise rotation of γ, *i.e.*, $-\gamma$. See Figure 3.1 (b). For the case where two dilatational waves interact to produce a shear wave (with a difference frequency), the resonance and polarization conditions are met when the following two equations are satisfied,

$$\cos\varphi = \left(\frac{c_L}{c_S}\right)^2 \left[1 - \frac{1}{2}\left(1 - \frac{c_S^2}{c_L^2}\right)\left(\frac{f_2^2}{f_1^2} + 1\right)\right] \tag{3.5}$$

$$\tan\gamma = \frac{-f_2 \sin\varphi}{f_1 - f_2 \cos\varphi} \tag{3.6}$$

where c_L and c_S are the dilatational and shear wave ultrasonic velocities of the medium, respectively. The three parameters of Equations 3.5 and 3.6 are interrelated; when one is chosen (*e.g.*, φ), the other two are fixed (*e.g.*, $\frac{f_2}{f_1}$ and γ). Appendix C contains the derivation of Equations 3.5 and 3.6.

3.3 Characterizing Oxidative Aging of AC using Non-Collinear Wave-Mixing of Bulk Waves

This section will discuss how the non-collinear wave-mixing technique can be used to characterize the oxidative aging in AC. This method takes advantage of the fact that AC exhibits increasingly nonlinear behavior as it undergoes oxidative aging. This increasing nonlinear behavior can be attributed to the increase of the diffuse micro-flaw population with age.

3.3.1 Choosing the Experimental Set-Up

The ultrasonic velocities and attenuations of the asphalt concrete specimens were already determined for the entire sample set of aged specimens (0 to 36 hours) in Chapter 2. Prior to cutting the asphalt concrete specimens, the appropriate angles must be chosen such that wave interaction occurs and the resulting scattered wave is received based on Equations 3.5 and 3.6. Recall that the

three parameters of Equations 3.5 and 3.6 (φ, $\frac{f_2}{f_1}$ and γ) are interrelated. For relatively uncomplicated materials (*e.g.*, isotropic, homogeneous, non-dispersive) the task of determining a testing set-up is typically relatively straightforward: for a known set of ultrasonic material properties (*i.e.* dilatational and shear velocities/attenuations), one parameter can be chosen, which sets the other two. Then, the specimen dimensions can be selected and appropriate angles can be cut into the specimen.

In this study, the goal is to use the non-collinear wave mixing method to assess aging level of asphalt concrete. It follows that the testing set-up remain consistent for all of the specimens, since presumably nothing is known about the aging level of the AC prior to testing.[1] The ultrasonic velocities vary with the level of aging, which complicates the matter of choosing the appropriate testing set-up (*i.e.*, specimen dimensions, interaction/scattered angles, sensor placement, and frequencies) that is suitable for the entire set of aged specimens. The determination of the final testing set-up is thus an iterative process, where the goal is to find one testing set-up that meets all the conditions which will now be outlined.

Interaction Angle, φ

To maintain a consistent testing set-up, the interaction angle should not change between experimental set-ups. The interaction angle will remain the same over the entire desired age range (*e.g*, 0 to 36 hours of oven-aging) of AC samples. Since the AC material properties change with oxidation level, this will result in different $\frac{f_2}{f_1}$ and γ for the different ages. The interaction angle will be chosen solely based on its effects on the scattered wave angle and frequency ratio.

Primary and Scattered Wave Frequencies

In a non-dispersive material, the frequencies of the primary and scattered waves (ω_1, ω_2, and ω_3) only need to be considered with regards to attenuation (to ensure a measurable signal) and separability (*i.e*, ω_3 much different than ω_1 and ω_2 to facilitate isolating the scattered signal from the primary signals). In the case of AC, a highly dispersive material, choosing the appropriate

[1] It would make no sense to have the testing configuration vary with the level of aging, as this would require some knowledge of the level of aging *a priori*, and hence become circular problem.

frequencies at which to perform non-collinear wave mixing is not quite so simple. Since the velocities, attenuations, and wave-distortion effects are all dependent on frequency, a poor choice of wave frequencies has the potential to result in unnecessarily complex results. Thus, the overarching goal in choosing the frequencies, is to avoid unnecessary complexities and ensure that the resulting test set-up fits the theoretical assumptions (a non-dispersive material) as close as possible. The details behind determining a suitable frequency range and some of the potential complexities that may arise from a poor choice will now be discussed.

The primary wave frequencies should be chosen to be low enough to minimize the distortion of the wave (from scattering and attenuation). To achieve this, the wavelength of the propagating wave should be larger than the aggregate size (NMAS = 9.5mm). With these considerations, the upper frequency bound for shear waves is 110 kHz, which corresponds to a shear wave wavelength ($\approx$ 9.5 mm) through the 36 hours aged specimen. The dilatational waves have wavelengths greater than 9.5 mm for all ages for the measured frequency range ($\leq$ 350 kHz). Thus, the upper frequency bound for dilatational waves corresponds to the highest measurable (before attenuation effects become too great) frequency.

The two primary wave frequencies should be chosen such that their resulting velocities are similar to agree with the theory presented in Equations 3.5 and 3.6. Above 100 kHz, the dilatational wave velocities all plateau (Figure 2.11). Thus, the frequencies of the primary waves should be chosen to be greater than 100 kHz, because Equations 3.5 and 3.6 were derived with the assumption that $\boldsymbol{k}_1$ (f_1) and $\boldsymbol{k}_2$ (f_2) have the same velocity. Above 200 kHz, the attenuation increases dramatically. In fact, for the specimen aged 36 hours, no signal was able to be received through the smallest sample dimension (30 mm) above 250/200 kHz for dilatational/shear waves. Therefore, the primary wave frequency should be restricted to 200 kHz or below. It is difficult to detect shear waves below 50 kHz with the transducers employed in the set-up; therefore, the scattered shear wave should have a frequency above 50 kHz.

With these considerations, the primary waves should be chosen within a frequency range of 100 to 200 kHz, and the resulting scattered shear wave should be within a frequency range of 50 to 110 kHz. Also, the scattered wave frequency (f_3) should have a sufficient separation from the primary

wave frequencies (f_1 and f_2), so that they can be easily separated in the frequency domain. Of course, in choosing the frequencies, one should also consider the effects on the interaction and scattered wave angles.

Scattered Wave Angle, γ

As previously noted, one testing set-up will be chosen and used across a sample set of AC specimens subjected to various levels of oven-aging. This means that for a chosen interaction angle ϕ (Equation 3.5), the direction of the scattered wave γ (Equation 3.6) will vary, since the material properties vary with oxidation.

In this investigation, the testing set-up will be chosen based on the virgin, unaged AC specimen properties. Consequently, for a virgin AC specimen, if the primary waves are interacted at ϕ, the resulting scattered nonlinear wave will incidentally strike the receiving transducer. For oxidatively aged AC specimens (with properties that deviate from virgin conditions), if the primary waves are interacted at ϕ, the resulting scattered wave will propagate in a direction that deviates from that of the virgin γ, *e.g.*, $\gamma + \Delta\gamma$. Since the testing configuration is to remain unchanged, it is important to minimize this $\Delta\gamma$ to ensure that the scattered wave is received, even if the receiving transducer is not positioned in the ideal location.

Specimen Dimensions

Asphalt concrete is highly attenuative (see Figure 2.11), which will greatly diminish the amplitudes of the primary and scattered waves as they propagate through the specimen. This attenuation loss should be minimized by minimizing the distance through which the wave propagates to ensure that the scattered nonlinear wave can be detected by the receiver. The propagation distances should be at least one wavelength long such that the waves are stabilized by the time they interact. For simplicity, $\boldsymbol{k}_1$ and $\boldsymbol{k}_2$ can be chosen to have the same propagation distances.

3.3.2 Nonlinear Characterization Parameters

Two important metrics in the assessment of the nonlinearities of AC via the non-collinear wave mixing technique are: 1. the normalized nonlinear wave generation parameter, $\frac{\beta}{\beta_0}$, and 2. the

frequency ratio, $\frac{f_2}{f_1}$, of the two primary waves at which the nonlinear scattered wave is generated. The $\frac{\beta}{\beta_0}$ parameter represents the conversion efficiency of the energy transferred, via interaction, from the primary waves to the scattered nonlinear wave. Thus, the $\frac{\beta}{\beta_0}$ parameter is a good indicator of the material's inherent nonlinear behavior. Neither of these two metrics alone is sufficient to uniquely assess the level of oxidative aging due to a lack of separation at particular aging levels; however, when combined, they provide a unique characterization of the oxidative aging level.

It is useful to note that the frequency ratio is directly related to the linear acoustic measurements, *i.e.*, the shear to dilatational velocity ratio, via Equation 3.5. Thus, for a known testing set-up (interaction angle ϕ) and experimentally measured frequency ratio, the velocity ratio can be back-calculated. For this reason, the nonlinear acoustic technique is a more robust method than traditional linear acoustic measurements, as it inherently contains more than one metric for damage assessment: $\frac{f_2}{f_1}$ and $\frac{\beta}{\beta_0}$. Also, the nonlinear acoustic technique is more suitable for damage detection than traditional linear acoustic approaches, because it is more sensitive to the presence of micro-flaws.

Nonlinear Wave Generation Parameter, $\frac{\beta}{\beta_0}$

The scattered wave has an amplitude proportional to the product of the primary wave amplitudes at the interaction [28]. The primary waves suffer attenuation as they propagate through the specimen before they interact, and the scattered wave is further attenuated as it travels to the receiver. Accounting for the attenuation, the received amplitude of the scattered wave can be described by the following expression (assuming perfect couplant conditions),

$$A_{age}^{(k_3)} = \beta_{age} A_{sent}^{(k_1)} A_{sent}^{(k_2)} \exp\left(-\alpha^{(k_1)} D_{k_1} - \alpha^{(k_2)} D_{k_2} - \alpha^{(k_3)} D_{k_3}\right) \tag{3.7}$$

where,

$\beta \equiv$ Conversion Efficiency

$A_{sent}^{(k_n)} \equiv$ Transmitted amplitude of $\boldsymbol{k}_n$ (Volts)

$\alpha^{(k_n)} \equiv$ Attenuation coefficient of $\boldsymbol{k}_n$ (Np/m)

$D_{k_n} \equiv$ Propagation distance of $\boldsymbol{k}_n$ (m)

The conversion efficiency β is a dimensionless parameter which accounts for the fraction of the interacting waves that is converted to the scattered wave. The propagation distances assume straight ray paths. The attenuation coefficients were measured (Chapter 2). Normalizing the amplitude by the attenuation,

$$A_{age}^{*(k_3)} = \frac{A_{age}^{k_3}}{\exp\left(-\alpha^{(k_1)}D_{k_1} - \alpha^{(k_2)}D_{k_2} - \alpha^{(k_3)}D_{k_3}\right)} = \beta_{age}A_{sent}^{(k_1)}A_{sent}^{(k_2)} \tag{3.8}$$

If changes in the couplant conditions between testing set-ups are small enough to be neglected, then the transmitted amplitudes of the primary waves ($A_{sent}^{(k_1)}$ and $A_{sent}^{(k_2)}$) will be the same for all tests performed. Thus, β_{age} can be normalized by the virgin β_0 to characterize the level of aging,

$$\frac{\beta_{age}}{\beta_0} = \frac{A_{age}^{*(k_3)}}{A_0^{*(k_3)}} \tag{3.9}$$

By way of the formulation, the attenuation is thus accounted for, and the nonlinear wave generation parameter represents the conversion efficiency of the energy transferred from the primary wave interaction to produce the scattered nonlinear wave. Thus, this parameter is a good indicator of the material's inherent nonlinear behavior.

3.3.3 Specimen Preparation

Six gyratory compacted asphalt concrete specimens were prepared in the same manner (using the same mix design and aging method) as was done in the linear acoustic characterization (see Section 2.2) to obtain specimens at aging levels of 0, 12, 24, 28, 32, and 36 hours. The cylindrical specimens (150 mm height and 150 mm diameter) were created by compacting the aged mixtures with a servo-controlled gyratory compactor (IPC Servopac) at a temperature of 155°C. Each of the cylinders was cut to obtain a 5 cm thick cylinder.

Appropriate angles were then cut into the cylinders so that the transducers could be mounted directly on the flat faces of the specimen. Figure 3.2 shows the geometry and dimensions of the extracted test samples from each of the cylindrical compacted gyratory specimens. The specimens were cut so that transducers could be mounted incidentally on the faces and transmit two primary waves ($\boldsymbol{k}_1$ and $\boldsymbol{k}_2$) to interact at 31° to produce a nonlinear scattered shear wave, which is received

at -42° with respect to $\boldsymbol{k}_1$. These angles were chosen based on virgin specimen properties (with the considerations in Section 2.2.2) and used for all six specimens. Table 3.1 contains the measured and computed values for all aged specimens.

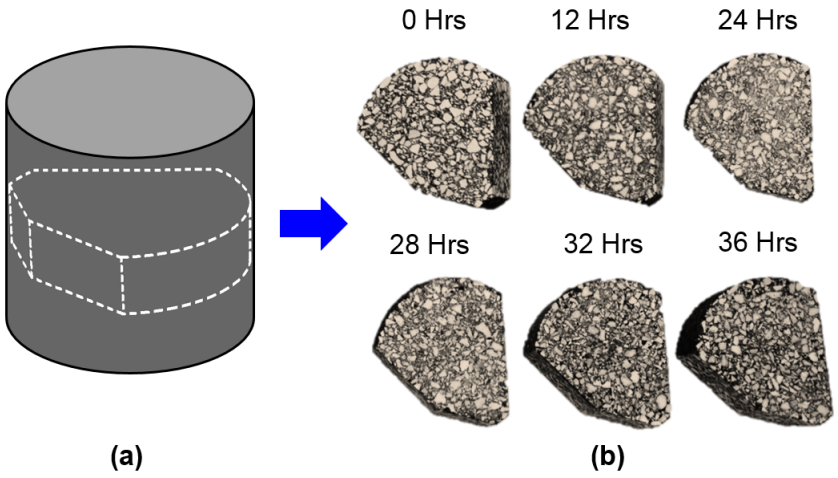

Figure 3.2: Test specimens (a) gyratory compacted and (b) test specimens with different levels of oven aging. The angles at which these specimens were cut was such that the sending and receiving transducers could be incidentally mounted and positioned at the appropriate angles as in Figure 3.3. Extracted from McGovern et al. [31]

3.3.4 Experimental Set-Up and Procedure

The velocities used to calculate the velocity ratio were computed using the mean velocities across 140 - 200 kHz. The specimen dimensions were cut so that $\boldsymbol{k}_1$ and $\boldsymbol{k}_2$ propagated a distance of 5

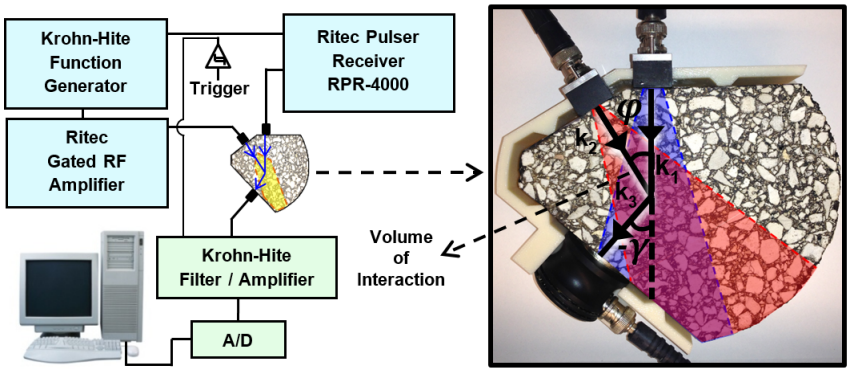

Figure 3.3: Schematic diagram of the ultrasonic data collection system illustrating the angle of interaction of the two longitudinal waves and the location of the shear transducer to receive the generated scattered shear wave. The blue and red regions denote the areas of signals $\boldsymbol{k}_1$ and $\boldsymbol{k}_2$, respectively, due to beam spread. The region where they overlap is the volume of interaction. Extracted from McGovern et al. [31]

cm, and $\boldsymbol{k}_3$ propagated a distance of 4 cm. A plastic template was created using a 3-D printer to ensure reproducibility of transducer placement between tests. The asphalt concrete specimen was mounted on screws threaded through the plastic template to minimize the contact surface between the specimen and the template. All specimens were tested at room temperature (≈23°C).

A pulser-reciever (Ritec RPR 4000) was used to generate and amplify a 15-cycle sinusoidal signal at $f_1 = 200$ kHz. This signal ($\boldsymbol{k}_1$) was sent to a transmitting dilatational wave transducer (Panametrics V413, center frequency 500 kHz). A function generator (Krohn-Hite Model 5920) was used to generate an 8-cycle sinusoidal wave which swept from $f_2 = 110$ kHz to 180 kHz in 1 kHz increments. This signal ($\boldsymbol{k}_2$) was amplified using a gated amplifier (Ritec GA-2500A) and sent to another transmitting dilatational wave transducer (Panametrics V413, center frequency 500 kHz). The number of cycles in each toneburst was chosen to ensure the intersection of the primary dilatational waves in the specimen. See Figure 3.3 (b) for the orientation of the transducers. The scattered shear wave ($\boldsymbol{k}_3$) was received by a shear transducer (Panametrics V1548, center frequency 100 kHz), filtered/amplified by a 4-pole Butterworth filter (Krohn-Hite model 3945), and sent to the computer for data acquisition.

Table 3.1: Dilatational and shear mean velocities (between 140 - 200 kHz) and corresponding frequency ratio $\frac{f_2}{f_1}$ and scattered wave angle γ for an interaction angle φ of 31°. For time-of-flight calculations, the shear velocity at the scattered wave frequency f_3 is also presented. Extracted from McGovern et al. [31]

Amount Aged (Hours)	Dilatational Velocity Mean (140 - 200 kHz) c_L (m/s)	Shear Velocity Mean (140 - 200 kHz) c_S (m/s)	Velocity Ratio c_S/c_L	Interaction Angle φ (°)	Frequency Ratio f_2/f_1	Angle of Scattered Wave γ (°)	Scattered Wave Frequency $f_3 = f_1 - f_2$ (kHz)	Shear Velocity at f_3 c_S (m/s)
0	3559	1992	0.560	**31***	0.700	**-42***	60	1384
12	3785	2066	0.546		0.710	-43	58	1334
24	4005	2088	0.521		0.724	-44	55.2	1343
28	3285	1629	0.496		0.738	-46	52.4	1013
32	2780	1313	0.472		0.751	-47	49.8	904
36	2868	1273	0.444		0.764	-49	47.2	648

*** Note:** The specimens (for all ages) were all cut to the angles determined for the virgin specimen. Care was taken to find a case where the difference in the scattered wave angle was minimal (i.e. $\gamma_{36Hrs} - \gamma_{Virgin} = 7°$) so that the receiving transducer could detect the scattered wave for all specimens. Keeping the angles constant causes the frequency ratio at which the nonlinear wave interaction occurs to shift.

Data aquisition consisted of three steps: (1) operating the two sending transducers simultaneously, (2) individually operating only the first sending transducer, and (3) individually operating only the second sending transducer. To obtain the nonlinear scattered wave, the signals obtained from steps (2) and (3) subtracted from the signal obtained from the signal obtained in step (1). The remaining signal will now be referred as the difference signal. The difference signal (containing the scattered shear wave), resulting from the nonlinear interaction of the two intercepting waves, is very low in amplitude due to: (1) low conversion efficiency of the interaction between the two primary dilatational waves, (2) inherent dispersion in the asphalt concrete (especially at high frequencies), and (3) the presence of the dominating (large amplitude) primary waves in the imperfect subtraction. To expand on (3), a portion of the signal energy is lost in the conversion to the nonlinear scattered wave; this leads to the signal resulting from the addition of the signals obtained when the dilatational transducers are operated individually being larger than the signal obtained from the two longitudinal transducers are operated simultaneously. To circumvent the low amplitude and maximize the ability to detect the scattered wave, a high sample rate (50 MHz) was used in order to avoid trigger jitter as suggested by Johnson and Shankland [32, 33], and an average of 500 waveforms was taken to mitigate the scattering affects. For each aging level, 10 independent measurements were taken, which required removal of the three sensors, removal of the used couplant, and subsequent application of new couplant, and reposition of the three sensors.

3.3.5 Experimental Results

To ensure that the received wave is a nonlinear wave resulting from interaction between the primary waves in the specimen, selection criteria (proposed by Johnson and Shankland [32, 33]) are used. Once it is verified that the nonlinear wave results from the primary wave interaction within the bulk of the sample, the data from the specimens at different aging levels can be compared.

Amplitude Criterion

To satisfy the amplitude criterion, the amplitude of the nonlinear signal must be proportional to the product of the amplitude of the primary dilatational waves. An experiment was conducted where it was observed that as the voltage of the primary waves was increased, the amplitude of the nonlinear signal also increased in a manner proportional to the amplitudes of the primary waves.

Directionality Criterion

To satisfy the directionality criterion, the propagating direction of the scattered wave must match the propagating direction predicted by theory. The geometry of the samples were selected using the virgin parameters shown in Table 3.1, which were calculated using Equations 3.5 and 3.6. As a result, since the scattered nonlinear wave was received, the directionality criterion was satisfied. Care was taken to ensure that even though the scattered wave angle γ deviated from the virgin scattered wave angle, it still struck the transducer face, by choosing the testing parameters (frequencies) to minimize this deviation.

Frequency Criterion

To satisfy the frequency criterion, the frequency of the nonlinear scattered wave must match the frequency predicted by theory (*i.e.* $f_3 = f_1 - f_2$ at the appropriate $\frac{f_2}{f_1}$). The experimental set-up is based on virgin specimen properties; therefore, for each aged specimen, the frequency ratio at which interaction takes place will vary. To verify that the nonlinear interaction takes place at the predicted frequency ratio, the amplitude of the nonlinear scattered wave can be monitored as f_2 is swept and f_1 is held constant. The maximum amplitude of the nonlinear scattered wave should occur when f_2 reaches the frequency where $\frac{f_2}{f_1}$ matches the ratio predicted by the theory.

The amplitude of the scattered wave can be measured by taking the fast Fourier transform (FFT) of the difference signal and recording the amplitude at the appropriate frequency (f_3) as f_2 was swept. Since the nonlinear scattered wave frequency f_3 changes with the amount of aging of the specimen, instead of monitoring the f_3 amplitude via taking the FFT, a 4th-order Butterworth bandpass (30 - 90 kHz) filter was used. These filter limits ensured that the primary waves were filtered out as well as any very low frequencies. Recording the difference wave amplitude over a relatively wide band of frequencies (instead of a discrete point as is done with the FFT method) ensured that even when f_3 changed (with aging), the $\boldsymbol{k}_3$ amplitude could still be monitored. It was verified that filtering with such a broadband filter and taking the FFT yielded nearly the same results for the amplitudes.

For the different specimens, the nonlinear frequencies were theoretically predicted to be: $(f_3)_0 = 60$ kHz, $(f_3)_{12} = 58$ kHz, $(f_3)_{24} = 55$ kHz, $(f_3)_{28} = 55.4$ kHz, $(f_3)_{32} = 49.8$ kHz, and $(f_3)_{36} = 47.2$ kHz. Accordingly, for the chosen angle of interaction, the nonlinear scattered wave should reach a maximum amplitude in the different specimens when: $\left(\frac{f_2}{f_1}\right)_0 = 0.700$, $\left(\frac{f_2}{f_1}\right)_{12} = 0.710$, $\left(\frac{f_2}{f_1}\right)_{24} = 0.724$, $\left(\frac{f_2}{f_1}\right)_{28} = 0.738$, $\left(\frac{f_2}{f_1}\right)_{32} = 0.751$, and $\left(\frac{f_2}{f_1}\right)_{36} = 0.764$.

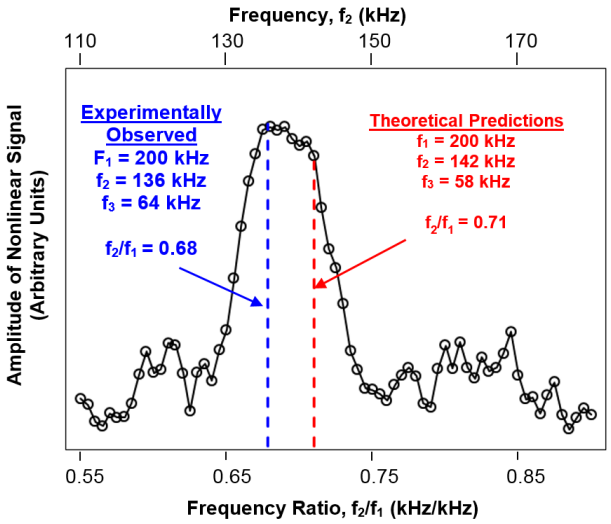

Figure 3.4: Experimentally obtained amplitude of scattered shear wave, *i.e.*, difference signal, $(f_3 = f_1 - f_2)$ as f_2 is swept from 110 kHz to 180 kHz ($\frac{f_2}{f_1} = 0.55$ to 0.90) and f_1 is held constant at 200 kHz. This analysis was performed for all specimens to obtain the data shown in Figure 3.5. The plot shown above is from the specimen aged 12 hours and shown as a representative case. The blue dashed line represents the experimentally observed maximum and the red dashed line represents the predicted maximum. Extracted from McGovern et al. [31]

Data collected from the specimen aged 12 hours is shown in Figure 3.4 as a representative example of the measured amplitude of the filtered difference signal (*i.e.*, the nonlinear scattered wave amplitude). As f_2 is swept, the nonlinear wave amplitude reaches a maximum at $\frac{f_2}{f_1} = 0.68$ ($f_2 = 136$ kHz). This is close ($\approx 4\%$ difference) to the predicted value of $\frac{f_2}{f_1} = 0.71$ ($f_2 = 142$ kHz).

Theoretically, the amplitude of the received shear wave should vanish when f_2 deviates from 136 kHz, because the theory assumes the test sample material to be isotropic and homogeneous and the two interacting longitudinal waves to be monochromatic. The width of the amplitude curve shown in Figure 3.4 is likely due to wave scattering induced by the presence of the random aggregate structure, which leads to different propagation paths of the wave energy, beam spread of

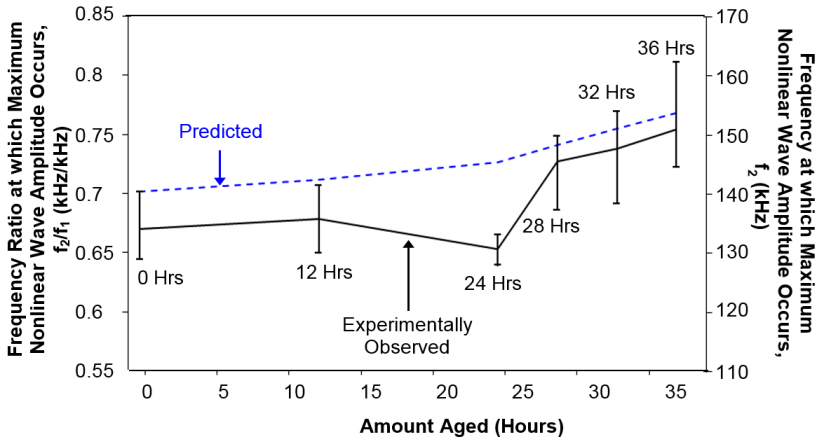

Figure 3.5: Experimentally observed frequency ratio at which maximum nonlinear wave amplitude occurs. The location of the amplitude was predicted via the theory (see Equations 3.5 and 3.6) using the experimentally recorded dilatational and shear velocities. Extracted from McGovern et al. [31]

the primary waves, and to the large interaction volume. The primary wave beam spread will cause the waves to interact at angles at and about the intended interaction angle, resulting in a band of interactions in lieu of the theoretically predicted discrete interaction angle. The relatively large interaction volume and the asphalt concrete structure, *i.e.*, aggregate - binder matrix, may also have the effect of smearing the theoretical frequency ratio over a range of values centered about the theoretically predicted value [34].

The frequency ratios at which the maximum nonlinear wave amplitudes occurred were recorded from all the measured data and plotted as a function of amount aged in Figure 3.5. The theoretical prediction was calculated using the mean of the measured velocities across 140 to 200 kHz and is denoted by the dashed line. The measured amplitudes of the scattered waves for the different

Table 3.2: Frequency ratio at which the maximum nonlinear wave amplitude occurs obtained by experiment and theoretically predicted. Extracted from McGovern et al. [31]

Amount Aged (Hours)	Experimentally Recorded Mean f_2/f_1	Standard Deviation of Experimental Results (kHz)	Theoretical f_2/f_1	% Difference
0	0.67	0.0200	0.70	4.61
12	0.68	0.0199	0.71	4.25
24	0.66	0.0080	0.724	8.65
28	0.73	0.0209	0.738	1.81
32	0.74	0.0275	0.751	1.01
36	0.75	0.0282	0.764	1.18

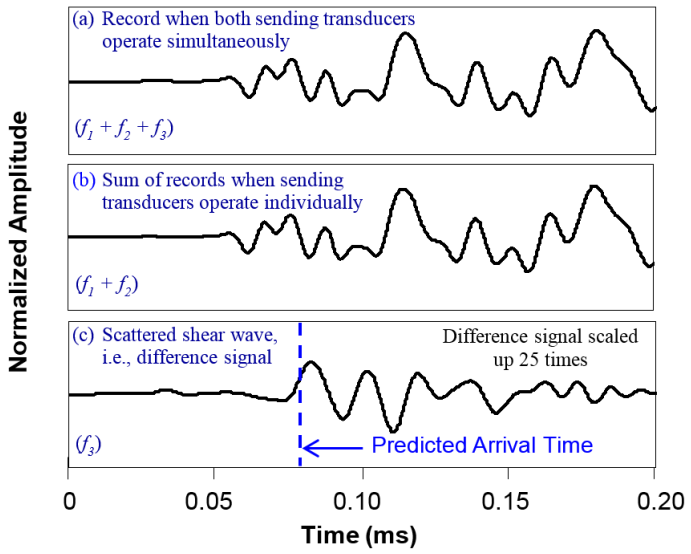

Figure 3.6: Time domain records required to obtain the nonlinear scattered shear wave. (a) record obtained when both sending transducers were operated simultaneously, (b) record obtained when sending transducers were operated one at a time and the received waveforms added, and (c) nonlinear scattered wave, *i.e.*, the difference signal, obtained from subtracting the signals obtained from operating the sending transducers individually from the signal obtained when operating the two sending transducers simultaneously. The records are all normalized by the maximum amplitude of the record in (b). The difference signal was scaled up 25 times. Extracted from McGovern et al. [31]

aged specimens do each reach a maximum close to the theoretical predictions. Please see Table 3.2. for a summary of these results. The largest deviation from the theoretical prediction is for 24 hours (8.65% difference). Even though the 36 hours had a low percent difference (1.18%), it had the highest standard deviation amongst the measurements. There is a statistically significant observable trend for the experimentally observed frequency ratio as a function of aging, similar to that which was observed in the linear characterization (see Chapter 2). This makes sense, considering that the frequency ratio is an indicator of the linear acoustic properties, *i.e.*, the velocity ratio $\frac{c_S}{c_L}$.

Time-of-Arrival

The signals were also viewed in the time domain to see if a time separation existed. If the nonlinear signal originated from the equipment, *e.g.* the function generator, amplifiers, transducers, etc., a separation in time between the primary waves and the difference signal should not exist. In other words, the nonlinear signal inherent to instrumentation should arrive at the same time as the primary waves. However, when the difference signal is due to nonlinear response in the asphalt concrete, a time separation should exist. The theoretical time of arrival of the difference signal, *i.e.*,

scattered wave, can be calculated assuming mean velocities, see Table 3.1, and a straight ray-path analysis.

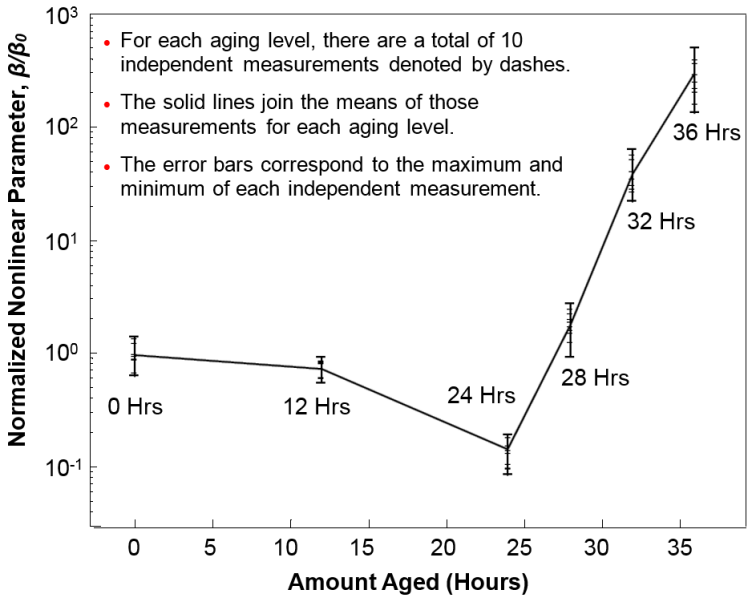

Figure 3.7: Nonlinear wave generation parameter, β, normalized with parameter, β_0, corresponding to the virgin, *i.e.*, unaged, mixture. For each aging level, each independent measurement required removal of the three sensors, removal of the used couplant, and subsequent application of new couplant, and reposition of the three sensors. Extracted from McGovern et al. [31]

As a representative example, Figure 3.6 shows a set of time domain records obtained from the asphalt concrete specimen aged 36 hours (a) when both sending transducers are operating simultaneously, (b) when the sending transducers are operated individually one at a time, and (c) the resulting scattered wave, *i.e.*, the difference signal. The theoretical arrival time for the difference signal is found to be 81.5 μs, which matches closely ($\approx$8.8% difference) with the observed arrival time of 74.9 μs. Note, the stochastic nature of the asphalt concrete causes some disparities in the independent measurements, as even a slight variation in the placement of the transducers can alter the travel paths of the waves.

Volume of Interaction

The volume of interaction is a function of the specimen dimensions and transducer beam divergence (see Figure 3.3) for an illustration of the interaction region). Considering the beam divergence, as the angle between the transducer centerline and the point where the signal is half its strength,

a characteristic length of the volume of interaction can be estimated at the point where the two primary beams intersect. The most limiting case corresponds to the specimen aged 24 hours, which corresponds to the longest wavelengths. Comparing this characteristic length with the number of possible signal wavelengths within the region of interaction, the characteristic length of the volume of interaction is always greater than 3.5 times the largest signal wavelength, *i.e.*, $\boldsymbol{k}_2$, for the entire test sample set.

The Nonlinear Wave Generation Parameter, β

Recall, the nonlinear wave generation parameter, β, is an indicator of the conversion efficiency of the energy transferred from the primary waves interacting to produce the scattered nonlinear wave (Equation 3.9). Figure 3.7 shows β normalized by β_0 (corresponding to the virgin mixture). The normalized parameter decreases with increased amount of aging until 24 hours, where after it exponentially increases with increasing aging. Again, a similar trend was observed in the linear characterization (see Section 2.3.5).

Due to the nature of the experimental set-up (based on virgin parameters), the scattered wave will not always hit the received transducer in the optimal manner (*i.e.* incidentally and in the center); thus, the experimentally measured beta parameter will be affected by this. Specifically, it may increasingly be an underestimate as aging increases, since the scattered wave hits the transducer increasingly off-center and at an angle as aging increases.

The attenuation increases drastically with aging (see Figure 2.11). If attenuation is not accounted for, it can dominate the observable trend of the nonlinear wave amplitude with respect to aging. Accounting for attenuation (see Section 2.2.2) reveals that the asphalt concrete exhibits increasingly strong nonlinear behavior with aging. This is further evidenced by the fact that the nonlinear scattered wave can still be detected even with such a strong counteracting effect of attenuation.

The above results show that the increasing nonlinear behavior of AC with oxidative aging level can be exploited via nonlinear acoustics, specifically non-collinear wave mixing, as a means to assess the pavement. While these results demonstrate the feasibility of using such a technique,

in its current form, it is not very practical for field use. The next chapter will address this by modifying the technique to be practical for in-situ field use.

Chapter 4
One-Sided Approach for Field Assessment

In the previous chapter, it was demonstrated that the non-collinear wave mixing technique can be used successfully to estimate the amount of oxidative aging by means of two metrics: the nonlinear wave generation parameter $\frac{\beta}{\beta_0}$ and the frequency ratio $\frac{f_2}{f_1}$ at which interaction occurs. However, the technique requires that the test be performed on specimens cut to a geometry dictated by the ideal sensor placement for through-transmission wave propagation. For use in the field, this would require removal (coring) of a portion of the pavement and subsequent cutting for testing. To be truly non-destructive, the method should be extended such that it can be performed on the pavement in-situ with only access to one side (*i.e.* the surface). Since most of the damage is located at the top, a non-destructive technique to evaluate the surface and subsurface (*i.e.* directly below the surface in the bulk of the medium) of the pavement would prove useful in assessing the level of damage and aid in the decision making process of maintenance and rehabilitation of the pavement.

In this chapter, the non-collinear wave mixing method from Chapter 3 is modified to be one-sided so that it can be employed readily in the field. This is done by mixing critically refracted longitudinal subsurface waves (waves which propagate close and parallel to the surface), which are generated via transducers mounted on angle wedges are used in lieu of incidentally mounted transducers. A brief introduction to subsurface waves will be presented, including some basic background theory. The nonlinear damage characterization curve is also introduced. This curve is damage trajectory, where the two nonlinear parameters $\left(\frac{\beta}{\beta_0}, \frac{f_2}{f_1}\right)$ are plotted against each other for various levels of oxidation. This curve only needs to be generated once for a particular mixture, and can then be used as a reference plot. Practitioners can take field measurements $\left(\frac{\beta}{\beta_0}, \frac{f_2}{f_1}\right)$ of the pavement, and plot it against the nonlinear damage characterization curve to determine the level of oxidation. This chapter will conclude with a discussion on two proposed approaches for field use and some blind studies which were performed to validate the methods.

4.1 Critically Refracted Longitudinal Subsurface Waves

Critically refracted longitudinal (or subsurface longitudinal) waves are longitudinal bulk waves that travel nearly parallel to the free surface of a bulk medium [18]. Subsurface waves have the advantage that they propagate in the bulk of the medium (*i.e.* right below the surface) and can still be detected at the surface. These waves can be generated by employing angle wedge transducers set to an angle close to or equal to the critically refracted angle governed by Snell's law [11]. Prior to 1979, others [35–37] had observed what at times was termed the "fast surface wave" which traveled at the speed of a bulk wave and arose when the incident angle was set above the critical angle; however, not much was done in the way of theoretical analysis. The first theoretical studies on the beam pattern of longitudinal subsurface waves were performed by Basatskaya and Ermolov [38] in 1979. They also studied the resulting beam pattern when the incident angle was set slightly above and below the first critical angle and made recommendations on how to utilize these waves to best inspect defects in materials. In 1988, Pilarski and Rose [39] demonstrated the feasibility of using subsurface longitudinal waves to characterize materials. Langenberg et al. [40] were the first to perform a numerical study of the wave field of subsurface longitudinal waves in 1990. In 1991, Junghans and Bray [41] experimentally characterized the subsurface longitudinal wave beam profile generated by high-angle longitudinal wave probes. From 1996 to 2001, a number of studies utilizing subsurface waves to measure residual stresses in various mechanical components and materials were performed by Bray and others [42–44] using acoustoelastic theory. Most recently (2013), Chaki and Demouveau [45] experimentally and numerically characterized the beam profile of the longitudinal subsurface wave. The results from their study revealed that the displacement amplitude of the critically refracted longitudinal wave reaches a maximum at an incident angle slightly larger ($\approx 1^\circ$) than the critical angle.

The two names, "critically refracted longitudinal waves" and "subsurface longitudinal waves," will be used interchangeably. Longitudinal subsurface waves have the properties of a bulk longitudinal wave while still able to be detected at the surface. In contrast to surface waves, subsurface waves have the advantage that they are insensitive to surface defects and exist well into the bulk of the material [18]. Thus, subsurface waves can be employed to measure the bulk of material right below

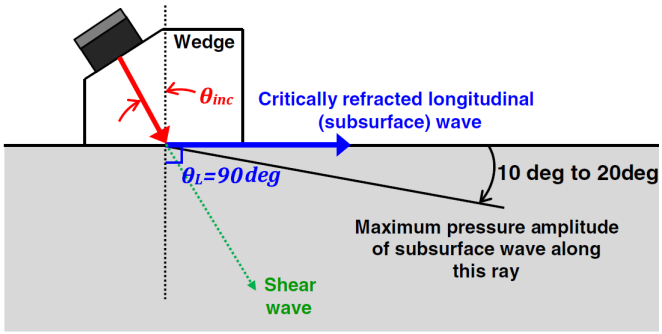

Figure 4.1: A subsurface longitudinal wave is generated when θ_{inc} is set close to the first critically refracted angle. Extracted from McGovern et al. [46]

the surface where the most aging in the asphalt concrete pavement is present. Critically refracted longitudinal waves are generated at the first critical angle governed by Snells law [11],

$$[\theta_{inc}]_{Critical} = \left[\sin^{-1}\left(\frac{c_{wedge}\sin\theta_R}{c_L}\right)\right]_{\theta_R=90^\circ} \tag{4.1}$$

where c_{wedge} and c_L are the dilatational velocities in the wedge and medium, respectively, and θ_R is angle of the dilatational wave with respect to the vertical ($\theta_R = 90^\circ$ for critically refracted waves). Please refer to Figure 4.1, which shows a schematic of the set-up which can be employed to generate subsurface dilatational waves via transducers mounted on angle wedges.

Basatskaya and Ermolov [38] found that the beam pattern of the subsurface wave is comprised of many lobes. At the critically refracted angle, most of the energy in the main lobe is contained at the surface, but the maximum displacement occurs at an angle below the surface (*e.g.*, $\approx 18^\circ$ below the surface for steel). See Figure 4.1. Note, the portion of the wave on the free surface is not purely longitudinal due to the boundary conditions (*i.e.*, stress-free surface). When the incident angle is slightly larger than the critical angle, the main lobe becomes narrower, and the maximum displacement moves closer to the surface. As the angle is further increased beyond the critical angle, the side lobes start to dominate in amplitude over the main lobe. For incident angles slightly smaller than the critical angle, the main lobe moves away from the surface. Chaki et al. [45] verified these results via a numerical study and found that the energy of the subsurface wave is maximum at the surface for an incident angle of 1° greater than the first critical angle.

4.2 Effect of Incident Angle on Beam Profile

Theoretical and experimental studies [18, 38–40, 45] have discussed the dependence of the beam profile upon deviations of the incident angle from the critical angle. This change in beam profile are now explained with regards to the aged AC sample set (same sample set as in Chapters 2 and 3, *i.e.*, 0, 12, 24, 28, 32, and 36 hours) by way of two examples. Table 4.1 contains the critical angles for the AC sample set.

Consider the case where a plastic wedge with an incident angle of $\theta_{cr,virgin}$ is used, where $\theta_{cr,virgin}$ corresponds to the first critical angle for the unaged virgin asphalt concrete sample. Let this same angle be used over the entire aged sample set. Recall that the velocities increase with increased aging from 0 to 24 hours, after which the velocities decrease with increased aging (Figure 2.13). This corresponds to a similar trend in the first critical angles, where the first critical angle decreases from 0 to 24 hours, after which it increases with increased aging. Therefore, if an incident angle of $\theta_{cr,virgin}$ is used over the entire sample set, the following observations can be made. For the samples aged 12 and 24 hours, the maximum displacement ray of subsurface wave will move closer to the surface, since their first critical angles are lower than that of the virgin sample. However, there is a counteracting effect: the main lobe of the ultrasonic beam becomes smaller in amplitude,

Table 4.1: Theoretically predicted critical angle + 1° based on Snell's law, and the experimentally determined critical angle + 1°.

Levels of oven-aging (Hours)	**Theoretically Predicted Critical Angle + 1° * (°)**
0	51
12	47
24	44
28	57
32	79**
36	73
* Based on literature, the angle at which the subsurface wave is able to be best detected, i.e., maximum displacement at the surface, corresponds to around 1° above the first critical angle. ** Due to constraints with the angle wedges, the incident angle could not be greater than 75°.	

narrower, and the side lobes become more dominant. For the specimens aged beyond 24 hours (*e.g.*, 28, 32, and 36 hours), the first critical angles are higher than the virgin sample. This means that for an incident angle of $\theta_{cr,virgin}$, the main lobe will increasingly move farther from the surface with increased aging. However, the main lobe also becomes wider, which combined with the already high beam spread means that a portion of the wave may still propagate parallel to the surface, in effect being a highly attenuated subsurface wave.

Now consider the case where the critical angle corresponding to the 36 hours aged specimen, $\theta_{cr,36}$, is used across the entire asphalt concrete sample set. For the specimens aged 32 hours and 36 hours, a subsurface wave propagating nearly parallel to the surface will be generated, since the two have very similar dilatational velocities (<100 m/s difference for the 100 to 250 kHz range). The rest of the specimens (aged 0 to 28 hours) have critical angles much lower than $\theta_{cr,36}$, with the farthest deviation being for the 24 hours aged specimen, where $\theta_{cr,36}$ - $\theta_{cr,24} \approx 29°$. As previously mentioned, the farther the incident angle is moved above the first critical angle, the more the side lobes begin to dominate. This means that any subsurface waves received at the surface of the specimens aged 0 to 28 hours are probably due to the side lobes.

4.3 Non-Collinear Wave-Mixing of Subsurface Waves

Two subsurface waves can be transmitted such that they interact and generate a third scattered shear wave, which propagates in the same plane as the two subsurface waves, *i.e.*, close to the surface. Just as in Chapter 3, two dilatational waves will be interacted to produce a scattered shear wave with a difference frequency. Implementing the non-collinear wave mixing technique in this way allows for the nonlinear scattered wave to be received by a transducer mounted on the same side of the medium as the sending transducers. Thus, this technique is especially advantageous when there is only access to one side of the medium being assessed, such as the top surface of an AC pavement. In the case of aged AC, the appropriate incident angle (*i.e.*, critical angle + 1°) varies with aging level since the velocities depend on the level of aging. The determination of the incident angle will be addressed in subsequent sections.

4.4 Nonlinear Damage Characterization Curve

The "nonlinear damage characterization curve" is a reference plot where $\frac{\beta}{\beta_0}$ is plotted versus $\frac{f_2}{f_1}$ for AC specimens with various levels of oxidative aging. Thus, it represents a trajectory of aging for a particular mixture in a two-dimensional space defined by the $\frac{f_2}{f_1}$ and $\frac{\beta}{\beta_0}$ parameters. The following scenario is envisioned: a practitioner can take some field measurements on the pavement and determine the level of oxidative aging of the pavement based on where the measurement(s) lie with respect to the reference curve. The pavement mixture-type must be identified in order to select the appropriate curve; however, if this information is not known, measurements could be taken at the bottom of an extracted core, presuming that the bottom of the core is protected and thus shares characteristics similar to the virgin mix.

To minimize experimental error, the nonlinear damage characterization curve should be generated in laboratory conditions by characterizing the AC specimens via the non-collinear wave mixing technique across a sufficient sample size of oxidatively aged AC specimens. Also, to minimize experimental error, the dilatational and shear velocities and corresponding attenuations should be obtained in the laboratory for the entire sample as was done in Chapter 2. The dilatational velocities are used to obtain the appropriate incident angles of the wedges (1° above the first critical angle). The attenuations are used in conjunction with the received nonlinear scattered wave amplitude to determine the value of $\frac{\beta}{\beta_0}$; the details of which were described in Section 3.3.2.

As noted above, the manner in which the non-collinear wave mixing is carried out is the same as in Chapter 3; however, now angle wedges are employed. The major assumption here is that the $\frac{\beta}{\beta_0}$ is not affected by such a change in the testing set-up. Hence, as will be discussed later, one crucial and primary goal of this portion of the study should be to verify that the $\frac{\beta}{\beta_0}$ can be determined using this one-sided set-up.

Each nonlinear damage characterization curve only needs to be generated once for a particular mixture type in the laboratory. A library of nonlinear damage characterization curves can be generated for different mixture designs, *e.g.*, different binders, aggregate gradations, aggregate types, etc.. Thus, for use in the field, all that needs to be known *a priori* is the type of mixture. It is

important that the laboratory testing set-up used to generate the nonlinear damage characterization curve is kept consistent with that used in the field (the same testing apparatus, filtering, signal gains, etc.) for comparison purposes, since all the data obtained is normalized by the data received from the virgin specimen. Any inconsistencies in the testing apparatus, procedure, or data post-processing will render subsequent comparisons with the virgin data invalid.

4.5 Implementation of Wave-Mixing Technique when the Linear Acoustic Properties are Unknown

If the linear acoustic properties are known, Snell's law can be used to determine the appropriate incident wedge angle. This can be readily done in laboratory-type conditions. Presumably, however, in the field there is no prior knowledge of the oxidative aging level of the asphalt concrete, rendering the appropriate incident angle unknown. Here, two systematic approaches are proposed to address the issue of the unknown incident critical angle, and evidence supporting the validity of the two methods is presented. These two methods will allow the technique to be employed by practitioners in the field for pavement inspection, where the only preexisting knowledge of the pavement is its mixture-type. Once the incident angle is known, the velocities and attenuations can be determined, as will be shown.

4.5.1 Method 1: Iterative Incident Angle Technique

For this method, the critical refracted angle is found iteratively. From this point forward, this method will be referred to as the "Iterative Angle" technique. The Iterative Angle technique contains a way to find the appropriate incident angle to generate subsurface dilatational waves, as well as a way to estimate the necessary linear parameters (*i.e.*, velocities and attenuations). Once the critical refracted angle and linear parameters are found via this technique, then the subsurface non-collinear wave-mixing technique can be employed as usual.

Determination of the Critical Angle

The determination of the first critical angle (the incident angle at which the subsurface wave travels parallel to the surface) can then be found experimentally via an iterative process. Two transducers

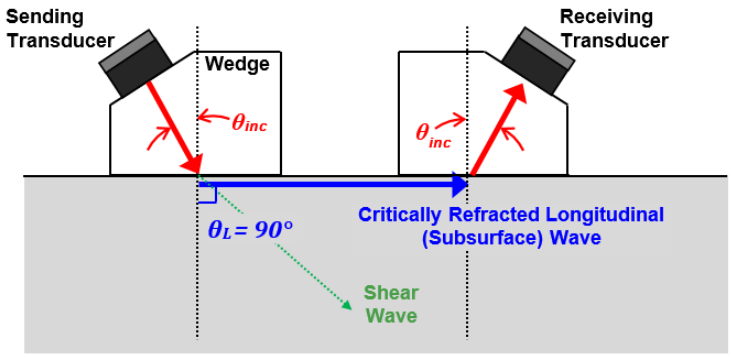

Figure 4.2: Schematic of the pitch-catch set-up used to obtain experimental measurements of dilatational velocity and attenuation. A sending and receiving transducer are both mounted on wedges set to the same incident angle to generate and receive a critically refracted longitudinal subsurface wave, respectively. Extracted from McGovern et al. [46]

mounted on variable angle wedges are set-up in a pitch-catch configuration so that one sends a square-wave at the appropriate frequency (*i.e.*, in the range of f_2 to f_1) and the other receives the signal.[1] Both wedges are set to the same incident angle. Please see Figure 4.2. The distance between the wedges should be chosen sufficiently small to try to avoid any interference with bulk waves which may be generated via mode conversion from the wedges and reflected back from discontinuities or large inhomogeneities in the bulk of the medium.

The wedge angle is varied and the amplitude is recorded at each angle. When changing the angle, care should be taken to not disturb the couplant conditions, which will affect the amplitude measurement. The wedges used in the study were limited to an incident angle of 75°. To avoid any interference with waves other than the subsurface wave, the amplitude should be taken from the beginning portion of the signal, as most of the energy in the first arriving signal should correspond to the fastest (*i.e.*, dilatational) wave which travels the shortest path (*i.e.*, closest to the surface). A parabola can then be fitted to the amplitude measurements, which are plotted with respect to the incident angle. The maximum of the parabola corresponds to the ideal incident angle to use in the testing set-up. This angle subtracted by 1° corresponds to the first critical angle.

[1] A square-wave is a convenient choice, because it is comprised of many frequencies, thus generating a wide-band signal. Alternatively, frequency-dependent measurements could be taken by performing a frequency sweep with sinusoidal waves.

Velocities and Attenuations

Once the ideal incident angle is known, the velocity and attenuation of the mixture can be found. The dilatational velocity can be found either using Snell's law (assuming critical refraction), or by measuring the time-of-flight of the subsurface waves via the pitch-catch set-up with the angle wedges set to the ideal incident angle. The dilatational attenuation can also be found by utilizing the pitch-catch configuration to measure subsurface wave amplitudes over a range of frequencies. See Figure 4.2. Similar to the testing set-up described in the previous section, the distance between the wedges should be chosen sufficiently small, and the beginning portion of the signal should be windowed to ensure that the velocity and attenuation measurements correspond to the first-arriving subsurface dilatational wave.

Shear Attenuation Estimation using Empirical Relationship

For the shear wave attenuation, subsurface shear waves are not used due to uncertainty in how the stress-free surface boundary condition affects the propagation and detection of the shear wave. Recall the relationship between the aging level and global stiffness: the stiffness increases with age until a critical point, after which it decreases with increasing age. In Chapter 2, Section 2.3.5, this relationship was discussed in some detail. It was observed that the global stiffness, which is directly proportional to the velocity, can be directly related to the micro-flaw population. As the micro-flaw population increases, the velocity decreases. The attenuation is also directly related to the micro-flaw population; the attenuation increases with the micro-flaw population. Thus, the shear wave attenuation is directly related to the micro-flaw population. Based on this reasoning, a relationship between the shear wave attenuation and the longitudinal wave velocity was empirically found using the attenuations and velocities from the measurements in Chapter 2. See Figure 4.3. This relationship was found to be,

$$\alpha_S(60kHz \leq f \leq 90kHz) \approx -0.031c_L + 152.991 \tag{4.2}$$

The longitudinal velocity is denoted by c_L and is the mean longitudinal velocity from 120 to 200 kHz. Above 120 kHz, the longitudinal velocity is non-dispersive. This empirical relationship is

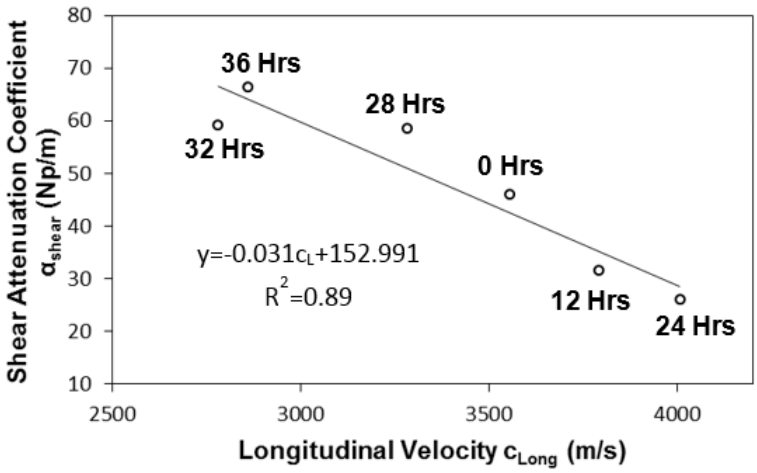

Figure 4.3: Empirically derived relationship between the longitudinal velocity and the shear attenuation coefficient. This relationship is only valid for the specific asphalt concrete mixture and aggregate gradation used in this study. Extracted from McGovern et al. [47]

only valid for the AC mixture-type of the sample set used in this study, for α_S in a frequency range of 60 to 90 kHz (which corresponds to the range of the nonlinear wave frequencies in this study), and for the longitudinal velocity above the frequency at which it becomes non-dispersive (*i.e.*, frequency independent). There is very little variation between 60 and 90 kHz for α_S. The longitudinal velocity was related to the shear attenuation instead of the longitudinal attenuation, because although α_L is proportional to α_S, the proportionality constant is not the same across the entire sample set of aged specimens.

Shear Attenuation Estimation using Rayleigh Wave Measurements

An alternate method to finding the shear wave attenuation is through the use of surface waves, otherwise known as Rayleigh waves. A Rayleigh wave is a combination of dilatational and shear waves. Consequently, the attenuation coefficient of a Rayleigh wave can be written in terms of the dilatational and shear wave attenuation coefficients [48].

$$\alpha_R \lambda_R = C\alpha_L \lambda_L + (1 - C)\alpha_S \lambda_S \tag{4.3}$$

where,

$$C = \frac{16\zeta^2(1-\eta^2)}{\eta^2(3\eta^4 - 16\eta^2 - 16\zeta^2 + 24)}$$
$$\eta = \frac{k_S}{k_R} \approx \frac{0.87 + 1.12\nu}{1+\nu} \tag{4.4}$$
$$\zeta = \frac{k_L}{k_S}$$

Where the subscripts R, L, and S, denote Rayleigh, longitudinal, and shear waves respectively, k denotes the wavenumber, λ denotes the wavelength, ν is the Poissons ratio, and α is the attenuation coefficient, which has units of Nepers per unit length. Recall, the dilatational attenuation coefficient is already estimated via the use of subsurface waves. For the frequency range used in this study ($f_3 < 100$ kHz), the Poissons ratio varies from 0.4 to 0.5 as a function of aging [13, 19]. At this range, the $(1-C)$ term in Equation 4.3 dominates over the C term and the following approximation can be made,

$$\alpha_R \lambda_R \approx (1-C)\alpha_S \lambda_S \tag{4.5}$$

Thus,

$$\alpha_S \approx \frac{\alpha_R \lambda_R}{(1-C)\lambda_S} \tag{4.6}$$

The Rayleigh wavelength can be found by recording the velocity and dividing it by the frequency of the transmitted wave. The shear wavelength can be estimated via the velocity ($\lambda = c/f$) by considering that for a Poissons ratio between 0.4 to 0.5 the Rayleigh velocity varies from 0.94 c_S to 0.95 c_S; thus, an estimate can be made for the shear wavelength by considering the shear velocity to be $c_R/0.945$, so that Equation 4.6 simplifies to,

$$\alpha_S \approx \frac{0.945\alpha_R}{(1-C)} \tag{4.7}$$

Please refer to Viktorov [48] for a detailed discussion on Rayleigh waves and the above equations.

Rayleigh waves can be generated most efficiently by employing angle wedges set to an incident angle at the third critically refracted angle. This angle can be found in a manner similar to the Iterative Angle method as described in a previous subsection. Note, in order to generate the Rayleigh wave via wedges in AC, the ultrasonic velocity in the wedge must be slower than the velocity in AC. The ultrasonic velocity of the more aged specimens is very low, so wedges should

be made of a material with a sufficiently low velocity. This may be a difficult material to find: typically, very low-velocity materials also have high ultrasonic attenuation coefficients. Rayleigh waves can also be generated by other means, which have the advantage that there is no ambiguity in choosing an incident angle; however, the efficiency is much lower [48, 49].

Non-Collinear Wave Mixing

Once the incident angle and attenuations have been estimated, the non-collinear wave mixing technique can be performed as usual (see Chapter 3). Prior to taking field measurements, the virgin nonlinear wave generation parameter β_0 should be known, whether it be by laboratory measurements on a mixture of the same type or via measurements taken using the bottom protected layer of an extracted field core. Then, the β measured in the pavement can be normalized by β_0, and the point $\left(\frac{\beta}{\beta_0}, \frac{f_2}{f_1}\right)$ can be plotted on the reference nonlinear damage characterization curve to see where it lies to determine the amount of aging.

For every measurement, it is crucial to verify that the selection criteria [32, 33] are satisfied to ensure that the nonlinear interaction has taken place within the bulk of the material. As per the frequency criterion, the interaction should only take place at a particular set of primary wave frequencies (f_1 and f_2) for a set interaction angle ϕ. This frequency ratio $\frac{f_2}{f_1}$ will change with respect the amount of aging of the material, and can be found by identifying the point at which the nonlinear wave amplitude reaches a maximum as f_2 is swept. The $\frac{\beta}{\beta_0}$ parameter is found via Equation 3.9.

4.5.2 Method 2: Fixed Incident Angle Technique

The determination of the suitable incident angle via an iterative technique can be time-consuming and tedious. To address this difficulty, a second method, termed the "Fixed Angle" technique is introduced. In this method, the wedges are set to a predetermined fixed incident angle based on the AC mixture type for practical and quick implementation in the field. The considerations in choosing this appropriate fixed angle will be discussed in detail. Once a suitable angle is found for a particular AC mixture type, it need not be found again. Linear parameters (*i.e.*, velocities and corresponding attenuations) can also be estimated in the Fixed Angle approach, as will be discussed

in subsequent text. Once the linear parameters are estimated, then the subsurface non-collinear wave mixing technique can be employed as usual using the predetermined fixed angle.

Incident Angle

The variable angle wedges should be set to an incident angle such that non-collinear wave mixing of subsurface dilatational waves can take place, produce a nonlinear scattered shear wave, and that scattered wave can then be detected at the surface by a receiving transducer for the entire sample set of aged specimens (0 to 36 hours aged). Since the critical angle is dependent on the dilatational velocity from Snell's law, and the velocity varies depending on the aging level, then there are six distinct critical angles corresponding to each of the six aged specimens, respectively. See Table 4.1 on page 56.

To determine a suitable incident angle to use across the entire set of aged specimens, non-collinear wave mixing measurements should be performed for various incident angles. For each measurement, it should be determined if a nonlinear interaction took place by using the selection criteria developed by Johnson and Shankland [32, 33]. These measurements should be taken with the goal of determining which angle(s) could be used when there is no prior knowledge of the level of oxidative aging. Since the material properties over the sample set of aged specimens (from 0 to 36 hours) vary so significantly, it is possible that one incident angle alone may not be sufficient to take usable measurements across the entire sample set; rather, measurements would need to be taken using more than one incident angle. Therefore, a goal in the selection of the incident angle should be to minimize the number of incident angles necessary to characterize the amount of oxidative aging in asphalt concrete aged in the desired range (*e.g.*, from 0 to 36 hours) for a particular mixture. This can be a time-consuming and tedious process; however, once performed, this angle will be a known suitable angle for that particular mixture type over a particular aged range. This angle will be referred to as θ_{inc} from this point forward.

Effect of Incident Angle on Beam Profile

If one incident angle is to be used across the entire sample set, then it stands to reason that at least a couple of the specimens will be tested at angles that differ (possibly greatly) from their first

critical angle. Please refer to Section 4.2 for more a detailed discussion on the effect of the incident angle on the beam profile.

Velocities and Attenuations

In Chapter 3, the experimentally measured attenuations were used to normalize the scattered nonlinear wave amplitude in order to estimate the inherent nonlinearities. For the Fixed Angle method, only one incident angle θ_{inc} is being used in the generation of the subsurface waves across the entire aged sample set. From the discussion in Section 4.2 regarding the longitudinal subsurface beam profile as the incident angle is increased beyond the critical refracted angle, it is apparent that normalizing the amplitudes by the actual attenuations is an ambiguous task, unless there is absolute knowledge about the wave path (deviation from traveling parallel to the surface), wave field (the beam pattern changes with respect to aging), and amount of oxidative aging in the specimen. Therefore, to assess the amount of oxidative aging in asphalt concrete using the non-collinear wave mixing method, the "perceived" attenuation (*i.e.*, energy loss at the surface) of the dilatational waves are measured experimentally, and the loss of the shear wave at the surface is estimated using Equation 4.2. This process of estimating the energy loss will now be described.

Consider the through-transmission set-up from Figure 4.2 (page 60), where a sinusoidal toneburst (swept from 120 kHz to 200 kHz) is transmitted through the asphalt concrete specimen via a dilatational transducer mounted on an angle wedge. The signal propagates through the asphalt concrete, and it is received by another dilatational transducer mounted on the same side of the specimen. Both the sending and receiving dilatational transducers are mounted on variable angle wedges set to the predetermined incident angle θ_{inc} and spaced a prescribed distance apart that corresponds to the distance from the center of the wedge to the center of the region of interaction in the non-collinear wave mixing set-up. As the wave propagates through the material, it suffers attenuation due to beam spread and inherent material attenuation (absorption and scattering). Since the case is being considered where there is only one incident angle across the entire sample set of aged specimens, the beam profile changes with respect to the amount of aging in the specimen. Accordingly, since the receiving transducer is placed on the same side of the specimen as the sending transducer, the perceived attenuation changes with aging as well. This energy loss at the surface

is a function of the material's properties (at its aging level), the distance the wave travels, the incident angle, and the frequency.

$$\mu = \mu(f, d, \theta_{inc}, age) \tag{4.8}$$

Thus, the received amplitude for a subsurface dilatational wave sent by transducer mounted on an angle wedge with an incident angle of θ_{inc}, received by a transducer mounted on an angle wedge with the same angle, propagated at a distance D with frequency f can be expressed as,

$$[A_{age}(f, D, \theta_{inc})]_{PC} = A_{Sent} e^{-\mu_L(f, D, \theta_{inc}, age)D} \tag{4.9}$$

where the subscript "L" denotes a longitudinal wave and the subscript "PC" denotes the pitch-catch configuration. Normalizing above equation by the received amplitude through the virgin specimen,

$$\left[\frac{A_{age}(f, D, \theta_{inc})}{A_0(f, D, \theta_{inc})}\right]_{PC} = \frac{e^{-\mu_L(f, D, \theta_{inc}, age)D}}{e^{-\mu_L(f, D, \theta_{inc}, 0)D}} \tag{4.10}$$

So, Equation 4.10 describes the normalized energy loss at the surface in a pitch-catch set-up for dilatational waves.

The "perceived" energy loss of shear waves through the material must also be estimated. Shear subsurface waves should not be used to measure the shear wave attenuation due to inaccuracies arising from interaction with the free surface (*e.g.*, mode conversion into dilatational waves). Furthermore, conventional wedges (*e.g.*, plastic) cannot be used, as very low wedge ultrasonic velocities would be required to generate subsurface shear waves that would propagate parallel to the surface. The shear attenuation can be estimated via an empirical relation between the longitudinal velocity and shear attenuation coefficient, which was presented in Equation 4.2 (page 61). Since this method only uses one incident angle θ_{inc} across the entire sample set, there may be large errors in the dilatational wave velocity estimate due to a change in the beam profile. The validity of this technique is based on the principle that the fastest arriving portion of the wave should be the dilatational component of the wave that travels the most parallel to the surface.

Non-Collinear Wave Mixing

Once the mixture-type of the pavement is identified, then θ_{inc} is known for that mixture, and the non-collinear wave mixing technique can be employed as usual. Recalling that the energy loss at the surface μ is a function of the distance and frequency, the amplitude of the nonlinear scattered wave can be written (in a similar fashion as Equation 3.7) as,

$$\left[A_{age}^{(k_3)}\right]_{\theta_{inc}} = \beta_{age} A_{sent}^{(k_1)} A_{sent}^{(k_2)} \exp\left[-\mu_L(f_1, D, \theta_{inc}, age)D_{k_1} - \mu_L(f_2, D, \theta_{inc}, age)D_{k_2} - \mu_S(f_3, D_{k_3}, \theta_{inc}, age)D_{k_3}\right] \tag{4.11}$$

The subscripts "L" and "S" denote dilatational and shear waves, respectively. The expression above can be similarly written for the unaged sample. Normalizing by the amplitude of received nonlinear scattered wave with the corresponding scattered wave amplitude obtained in the unaged specimen yields,

$$\left[\frac{A_{age}^{(k_3)}}{A_0^{(k_3)}}\right]_{\theta_{inc}} = \frac{\beta_{age}}{\beta_0} \frac{e^{-\mu_L(f_1, D_{k_1}, \theta_{inc}, age)D_{k_1}}}{e^{-\mu_L(f_1, D_{k_1}, \theta_{inc}, 0)D_{k_1}}} \frac{e^{-\mu_L(f_2, D_{k_2}, \theta_{inc}, age)D_{k_2}}}{e^{-\mu_L(f_2, D_{k_2}, \theta_{inc}, 0)D_{k_2}}} \frac{e^{-\mu_S(f_3, D_{k_3}, \theta_{inc}, age)D_{k_3}}}{e^{-\mu_S(f_3, D_{k_3}, \theta_{inc}, 0)D_{k_3}}} \tag{4.12}$$

Using the empirical relation from Equation 4.2 as an approximation to estimate the shear wave attenuation gives,

$$\frac{e^{-\mu_S(f_3, D_{k_3}, \theta_{inc}, age)D_{k_3}}}{e^{-\mu_S(f_3, D_{k_3}, \theta_{inc}, 0)D_{k_3}}} \approx \frac{e^{-\alpha_S(c_L(age))D_{k_3}}}{e^{-\alpha_S(c_L(0))D_{k_3}}} \tag{4.13}$$

This approximation will be an underestimate, of the perceived attenuation (energy loss at surface), because the empirical relationship does not account for the beam pattern or the fact that the shear wave does not necessarily propagate parallel to the surface. Substituting the relationships from Equations 4.10 and 4.13 into Equation 4.12, and solving for $\frac{\beta_{age}}{\beta_0}$ yields,

$$\frac{\beta_{age}}{\beta_0} \approx \left[\frac{A_{age}^{(k_3)}}{A_0^{(k_3)}}\right]_{\theta_{inc}} \left[\frac{A_0(f_1, D, \theta_{inc})}{A_{age}(f_1, D, \theta_{inc})} \frac{A_0(f_2, D, \theta_{inc})}{A_{age}(f_2, D, \theta_{inc})}\right]_{PC} \left(\frac{e^{-\alpha_S(c_L(0))D_{k_3}}}{e^{-\alpha_S(c_L(age))D_{k_3}}}\right) \tag{4.14}$$

Due to the approximations, $\frac{\beta_{age}}{\beta_0}$ is only an estimate of the actual normalized nonlinear wave generation parameter. Note that f_1 and f_2 are known, as the $\frac{f_2}{f_1}$ peak is found experimentally. Therefore, the primary wave attenuation estimates should be used at the appropriate frequencies.

Similar to the Iterative Angle technique, it is assumed that the parameters for unaged AC in the above equations are known prior to taking field measurements, whether by laboratory measurements performed on specimens of the same mix-type, or measurements performed on test samples made of the protected bottom layer from extracted field cores. These values should be found using the same testing set-up as used in the field so as to be consistent with the equations above. Then, the measured point $\left(\frac{\beta}{\beta_0}, \frac{f_2}{f_1}\right)$ can be plotted on the reference curve, where its relative location allows the estimation of the pavement top layer oxidative aging level.

4.6 Specimen Preparation

Six gyratory compacted asphalt concrete specimens were prepared in the same manner (using the same mix design and aging method) as done for both linear and nonlinear damage characterization as discussed in Chapters 2 and 3, respectively. The only difference in specimen preparation for this portion of the study was in the cylindrical specimen height, which was increased to 180 mm. The increase in height was done to maximize the surface area of the specimen to accommodate the positioning of the relatively large, finite dimensions of the angle wedges. Of course, the aggregate and binder proportions were modified accordingly to maintain a consistent mix design, (*e.g.*, void content, gradation, etc.) After compaction, each cylinder was cut to obtain a rectangular prism with dimensions 155 × 175 × 50 mm. See Figure 4.4. For "blind study" measurements (to be

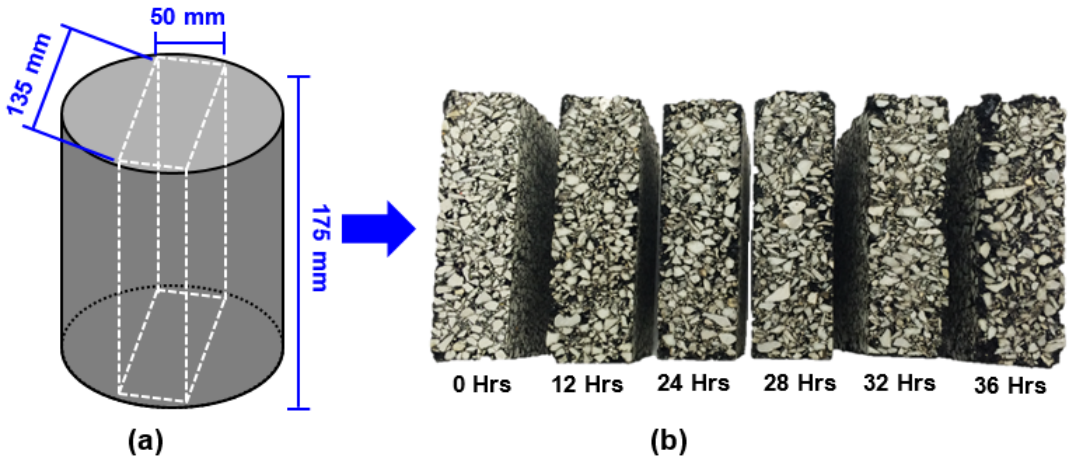

Figure 4.4: Asphalt concrete with different levels of oven aging (a) gyratory compacted and (b) then cut into prismatic test specimens. Extracted from McGovern et al. [46]

discussed in later), an additional three specimens were made with oven-aging levels of 18 hours, 26 hours, and 30 hours.

4.7 Experimental Set-Up and Procedures

The experimental set-up was chosen so that it was kept the same for all AC specimens in the sample set. Therefore, the interaction angle was kept constant across the set. Since the material properties vary with aging, the scattered wave angle γ was not consistent across the set. Therefore, determination of the final testing set-up was done following the conditions outlined in Section 3.3.

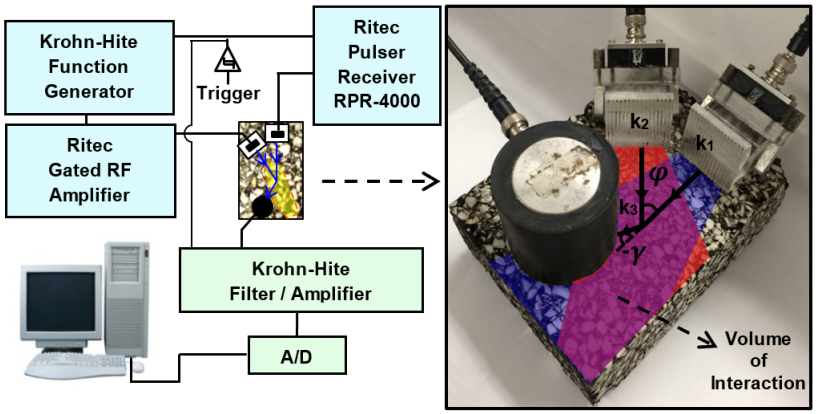

Figure 4.5: Schematic diagram of the ultrasonic data collection system illustrating the angle of interaction of the two longitudinal waves and the location of the shear transducer to receive the generated scattered shear wave. The blue and red regions denote the areas of signals $\boldsymbol{k}_1$ and $\boldsymbol{k}_2$, respectively, due to beam spread. The region where they overlap is the volume of interaction. Extracted from McGovern et al. [46]

Figure 4.5 shows a schematic of the experimental set-up. Two longitudinal transducers (Panametrics V413, center frequency 500 kHz) were mounted on plastic variable angle wedges. The wedge angle was set by using a digital protractor with an accuracy of 1°. The wedges were positioned such that the interaction angle between the two primary waves was $\varphi = 47°$, and both $\boldsymbol{k}_1$ and $\boldsymbol{k}_2$ propagated a distance of 8.2 cm (from the center of the angle wedge to the center of the volume of interaction) before interacting.[2] The scattered nonlinear wave propagated a distance of 4 cm (from the center of the volume of interaction to the center of the receiving transducer face) and was received by a third longitudinal transducer (Panametrics V1011, center frequency 100 kHz),

[2]It was necessary to use a different interaction angle from that used in Chapter 3 (42°) to accommodate the positioning of the wedges on the limited surface area of the specimen. This change in interaction angle necessitated other minor changes in the testing conditions, the considerations of which were discussed in Section 3.3.1.

which was mounted incidentally on the surface in the path of $\boldsymbol{k}_3$ (γ = -37° to with respect to $\boldsymbol{k}_1$). The placement of the sending/receiving transducers were based on the angles (φ and γ) calculated for the virgin specimen properties. The same transducer placement was used for all 6 specimens. Table 4.2 contains the theoretical values for all aged specimens. The velocities used to calculate the velocity ratio were computed using the mean velocities across 120 - 200 kHz. A plastic template was created using a 3-D printer to ensure reproducibility of transducer placement between tests. All specimens were tested at room temperature (≈23°C).

A 15-cycle sinusoidal signal with a frequency f_1 = 200 kHz was generated and amplified with a pulser-receiver (Ritec RPR 4000) and sent to one of the angle wedge mounted longitudinal transducers. An 8-cycle sinusoidal wave was generated by a function generator (Krohn-Hite Model 5920) and amplified by a gated amplifier (Ritec GA-2500A). This signal was swept from f_2 = 100 kHz to 180 kHz in 1 kHz increments and sent to the other angle wedge mounted longitudinal transducer. The number of cycles in the tonebursts was chosen to ensure the intersection of the primary longitudinal waves in the specimen. The received scattered shear wave was filtered by a

Table 4.2: Average dilatational and shear velocities (between 120 - 200 kHz), corresponding frequency ratio $\frac{f_2}{f_1}$ and scattered wave angle γ for an interaction angle φ of 47°. For time-of-flight calculations, the shear velocity at the scattered wave frequency f_3 is also presented. Extracted from McGovern et al. [46]

Amount Aged (Hours)	Dilatational Velocity Mean (120 - 200 kHz) c_L (m/s)	Shear Velocity Mean (120 - 200 kHz) c_S (m/s)	First Critical Incident Angle* $\theta_{cr} = \theta_{inc} - 1°$ (°)	Velocity Ratio c_S/c_L	Interaction Angle φ (°)	Frequency Ratio f_2/f_1	Angle of Scattered Wave γ (°)	Scattered Wave Frequency $f_3 = f_1 - f_2$ (kHz)	Shear Velocity at f_3 c_S (m/s)
0	3554	1943	50	0.547	47***	0.600	-37***	80.0	1510
12	3792	2007	46	0.529		0.613	-38	77.4	1467
24	4007	2030	43	0.507		0.630	-39	74.0	1482
28	3284	1576	56	0.480		0.650	-40	70.0	1108
32	2780	1282	78**	0.461		0.664	-42	67.2	969
36	2861	1240	72	0.433		0.685	-43	63.0	786

* The wedges were set to have an incident angle 1° greater than the critically refracted angle.
** An incident angle of 79° was too large of an angle to be achieved with the angle wedges, so an incident angle of 76° was used instead. Note, this angle is within error of the angle predicted by velocity measurements.
*** For all aged specimens, the sensors were all positioned to the angles determined for the virgin specimen. Care was taken to find a case where the difference in the scattered wave angle was minimal (i.e. $\gamma_{36Hrs} - \gamma_{Virgin} = 6°$) so that the receiving transducer could detect the scattered wave for all specimens. Keeping the angles constant causes the frequency ratio at which the nonlinear wave interaction occurs to shift.

4-pole Butterworth filter (Krohn-Hite model 3945), amplified, and sent to the computer for data acquisition. As in Section 3.3, the data aquistion consisted of three steps: (1) data was collected while the two transducers were operated simultaneously, (2) data was collected while one transducer was individually operated, and (3) data was collected while the other transducer was individually operated. The nonlinear signal was obtained by subtracting the signals from steps (2) and (3) from the signal obtained in step (1).

The data collection and test set-up remained the same for all of the tests. Only the incident wedge angle varied by method. To generate the reference nonlinear damage characterization curve, the incident angles were set to the critical angle using Snell's law and the known velocities. For the iterative angle technique, the incident wedge angle was found experimentally (see Section 4.5.1). For the fixed angle technique, the incident wedge angle was held constant at 73° for the entire sample set of AC specimens (see Section 4.5.2). The determination of this angle will be described in the following section.

It is worth calling attention to the fact that a longitudinal transducer was used in the reception of the scattered wave, which is theoretically predicted to be a shear wave polarized in the $\boldsymbol{k}_1 - \boldsymbol{k}_2$ plane (hence, parallel to the transducer face). Furthermore, the boundary conditions for a plane, isotropic, homogeneous media at the surface theoretically prohibit the propagation of surface shear-horizontal waves. For these reasons, for an isotropic, homogeneous material, *e.g.*, steel, the reception of the scattered wave would be impossible with such a set-up. Asphalt concrete consists of crushed stone of different sizes and shapes, randomly distributed and held together by thin films of bituminous binder. As a result of traveling through a highly heterogeneous media, the resulting shear wave goes through a significant level of mode conversion and scattering. Therefore, while the wave may begin its trajectory as a shear wave polarized in the $\boldsymbol{k}_1 - \boldsymbol{k}_2$ plane, it does not end as such. This scattering and mode conversion leads to a spatially-incoherent normal particle displacement at the surface. When this random normal displacement distribution is averaged over the large aperture of the receiving transducer ($> 1''$), it leads to a temporally-coherent but spatially-incoherent output signal. The peak amplitude or total power of this signal can be measured to assess the strength of the resulting shear wave. This allows for the reception of the wave via the longitudinal transducer

in the aforementioned configuration. For more discussion on shear-horizontal surface waves, please refer to Appendix E. Maradudin [50, 51] and Maugin [52, 53] are also excellent references for review/discussions on shear horizontal surface acoustic waves in solids.

4.8 Experimental Results

For all of the following tests, the selection criteria proposed by Johnson and Shankland [32,33] were used to verify that the nonlinear wave was generated as a result from the interaction between the two primary waves in the specimen bulk and not the testing apparatus. The details behind this were discussed in Chapter 3 and will not be repeated here. The collected data was only used after it satisfied the criteria.

As was done in Chapter 3, the amplitude of the nonlinear scattered wave was monitored as f_2 was swept and f_1 was held constant. This was done to determine $\frac{f_2}{f_1}$, since the maximum amplitude of the nonlinear scattered wave should occur when $\frac{f_2}{f_1}$ matches the ratio predicted by the theory. The amplitude was measured by passing the difference signal through a bandpass (30 - 90 kHz) filter as f_2 was swept. The selected bandpass frequency range ensured that the primary waves were filtered out as well as any very low frequencies.

Generation of the Nonlinear Characterization Curve

Non-collinear wave-mixing measurements were taken on the sample set of specimens, where the incident wedge angle was set to the 1° above the first critical angle (found using Snell's law), and the velocities and attenuations were known (from Chapter 2). See Table 4.2. There were two primary purposes of this set of measurements: 1. to demonstrate the feasibility of the technique for surface waves by validation against previous results (Chapter 3), and 2. to generate the so-called nonlinear damage characterization curve (see Section 4.4) to be used for reference in performing "blind study" measurements.

For the experimental set-up, the nonlinear scattered wave was predicted to reach a maximum amplitude for each specimen when: $\left(\frac{f_2}{f_1}\right)_0 = 0.600$, $\left(\frac{f_2}{f_1}\right)_{12} = 0.613$, $\left(\frac{f_2}{f_1}\right)_{24} = 0.630$, $\left(\frac{f_2}{f_1}\right)_{28} = 0.650$, $\left(\frac{f_2}{f_1}\right)_{32} = 0.664$, and $\left(\frac{f_2}{f_1}\right)_{36} = 0.685$.

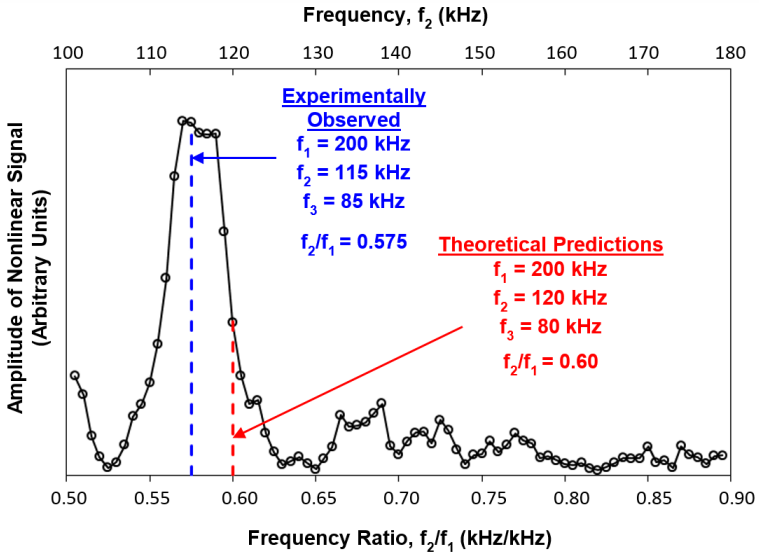

Figure 4.6: Experimentally obtained amplitude of scattered shear wave, *i.e.*, difference signal, ($f_3 = f_1 - f_2$) as f_2 is swept from 100 kHz to 180 kHz ($\frac{f_2}{f_1} = 0.50$ to 0.90) while f_1 is held constant at 200 kHz. This analysis was performed for all specimens to obtain the data shown in Figures 4.7 and 4.9. The plot shown above is from the specimen oven-aged for 12 hours and shown as a representative case. The dashed blue-line represents the experimentally observed maximum and the dashed red-line represents the theoretically predicted maximum (using the experimentally determined velocity data). Extracted from McGovern et al. [46]

Figure 4.6 shows a representative example of the recorded nonlinear scattered wave amplitude as f_2 was swept. The example shown is from the virgin specimen. The amplitude was predicted to reach a maximum when $\frac{f_2}{f_1} = 0.6$ ($f_2 = 120$ kHz). The experimental data shows that the amplitude actually reached a peak at $\frac{f_2}{f_1} = 0.575$ ($f_2 = 115$ kHz). The theoretical and experimental values are quite close with only a 4.1% difference (*i.e.*, 5 kHz). The frequency ratios at which maximum amplitude of the nonlinear signal occurred are plotted as a function of aging in Figure 4.7. The predicted values were calculated using the mean velocities (over 120 kHz - 200 kHz) and are denoted by the dashed line. The experimentally observed frequency ratios matched closely with the theoretical predictions as shown in Table 4.3. The largest deviation from the theoretical prediction is for 24 hours (≈12% error). This deviation is due to uncertainty in measuring the shear wave velocity, which was difficult due to scattering and mode-conversion as the shear wave propagated through the specimen.

To further validate that the nonlinear scattered wave was a result of nonlinear wave-mixing inside the sample and not the testing apparatus, the time-domain records were examined. Nonlinearities

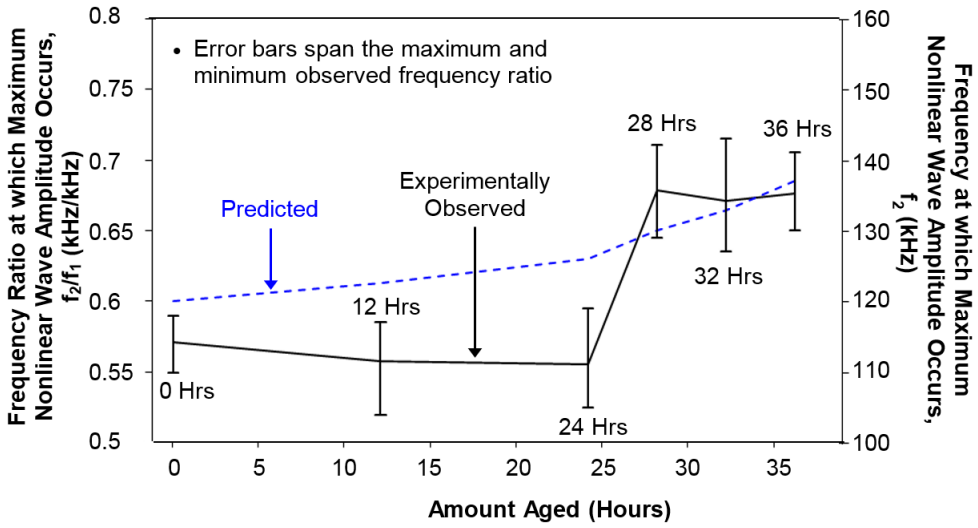

Figure 4.7: Experimentally observed frequency ratio at which the maximum nonlinear scattered wave amplitude occurs. The theoretically amplitude was predicted (see Equations 3.5 and 3.6) using the experimentally obtained dilatational and shear velocities. Extracted from McGovern et al. [46]

generated by the testing equipment will have the same arrival time as the primary waves, whereas nonlinearities arriving from wave-mixing in the specimen will have an arrival time corresponding to the paths dictated by the transducer placement and scattered wave angle γ (Equation 3.6). Thus, a time separation between the primary waves and the nonlinear scattered wave should exist, and experimental time-of-arrival should match with the theoretical time-of-arrival. The theoretical time of arrival of the difference signal, *i.e.*, scattered wave, can be calculated assuming mean velocities, see Table 4.2, and a straight ray-path analysis.

Table 4.3: Experimentally obtained and theoretically predicted frequency ratios corresponding to the maximum amplitude of the scattered wave. Extracted from McGovern et al. [46]

Amount Aged (Hours)	Experimentally Recorded Mean f_2/f_1	Standard Deviation of Experimental Results (kHz)	Theoretical f_2/f_1	% Difference
0	0.572	0.0125	0.600	4.75
12	0.558	0.0212	0.613	8.97
24	0.556	0.0223	0.630	11.82
28	0.679	0.0274	0.650	5.38
32	0.671	0.0288	0.664	0.99
36	0.676	0.0190	0.685	1.17

Figure 4.8 shows the time-domain records for the specimen aged 36 hours as a representative example. The time-domain records shown are for the cases when: (a) the transducers were operated simultaneously, (b) the transducers were operated individually and their time-domain records were summed, and (c) the difference between the records obtained in (a) and (b). The theoretical time of flight of the nonlinear scattered wave was calculated assuming straight ray paths. The primary velocities were calculated using the mean longitudinal velocity between 120 kHz 200 kHz. The shear wave velocity (at the appropriate frequency) was used for the nonlinear scattered wave velocity. The predicted arrival time (0.0982 ms) of the nonlinear scattered wave matched closely ($\approx$ 4.7% difference) with the experimentally observed arrival time (0.1028 ms).

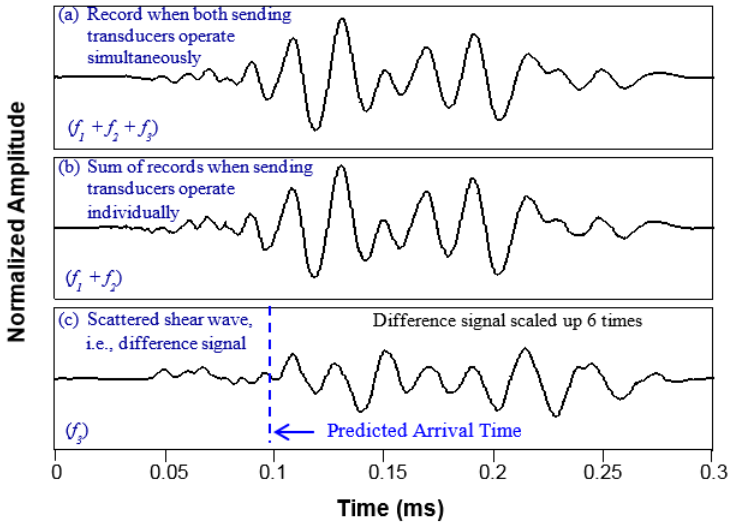

Figure 4.8: Time domain records required to obtain the nonlinear scattered shear wave; (a) time record obtained when both sending transducers were operated simultaneously, (b) time record obtained when sending transducers were operated one at a time and the received waveforms added, and (c) nonlinear scattered wave, i.e., the difference signal, obtained from subtracting the signals obtained from operating the sending transducers individually from the signal obtained when operating the two sending transducers simultaneously. The theoretically predicted time of arrival (0.0982 ms) for the difference signal matches closely ($\approx$ 4.7% difference) with the experimentally observed time of arrival (0.1028 ms). The records are all normalized by the maximum amplitude of the record in (b). The difference signal was scaled up 6 times. Extracted from McGovern et al. [46]

Once it was determined that the difference signal satisfied the selection criteria, the nonlinear wave generation parameter β was computed. Figure 4.9 shows β for all aged specimens normalized by the average of β_0, corresponding to the virgin mixture. The results from this one-sided technique (denoted by the solid black line) are superimposed on the results from the set-up involving the incidentally mounted transducers from Chapter 3 (denoted by the dashed blue line). It is observed

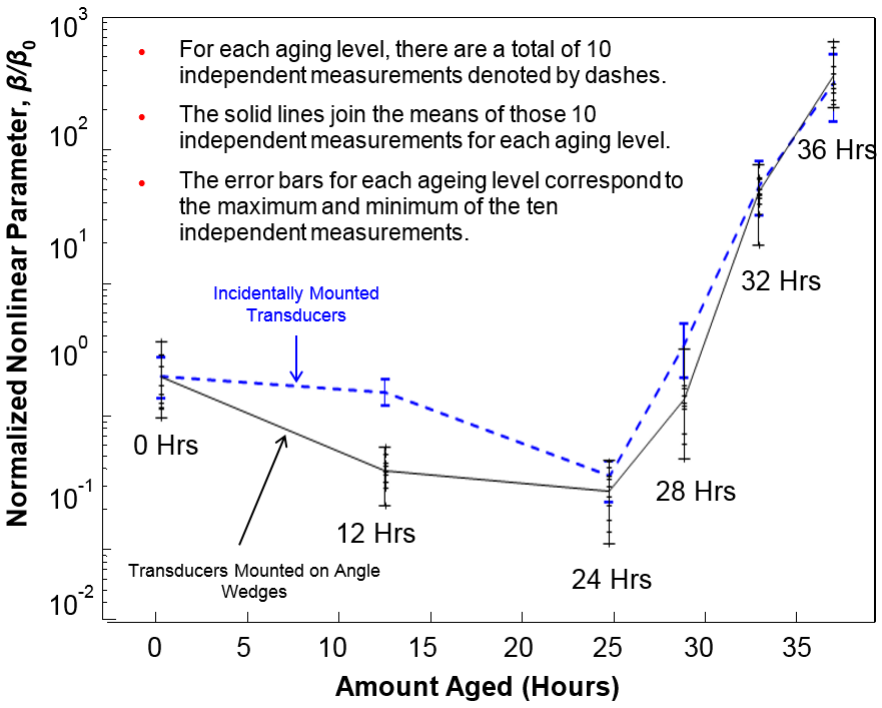

Figure 4.9: Normalized nonlinear parameter, β, versus different levels of oven-ageing via the incidentally mounted transducer configuration (Chapter 3, dashed blue line) and subsurface waves (solid black line). The parameter β is normalized with the parameter, β_0, which corresponds to the virgin, *i.e.*, unaged, mixture. Extracted from McGovern et al. [46]

that $\frac{\beta}{\beta_0}$ decreases from 0 to 24 hours aging, and increases exponentially from 24 to 36 hours of aging. The results between the two testing configurations agree quite well, with the exception of the sample aged for 12 hours. This disparity can be attributed to a non-uniform aging process. Recall that in the construction of the samples, the loose mixtures were hand-stirred every 12 hours during the oxidative aging process to promote uniform exposure to the oxygen. Thus, the 12 hour samples did not benefit from this hand-stirring.

The agreement between the two sets of data in 4.9 demonstrate the validity of using subsurface waves in the non-collinear wave mixing technique. The interaction angle between this study and the previous study was changed slightly to accommodate positioning of the angle wedge transducers on the finite width of the test specimen. In doing so, it is noted that the frequency ratios changed according to theory (shifted up/down). The nonlinear wave generation parameter remained nearly the same. This latter observation lends credence to the claim that the nonlinear wave generation parameter is an inherent material property, and not a function of the testing set-up. This agrees

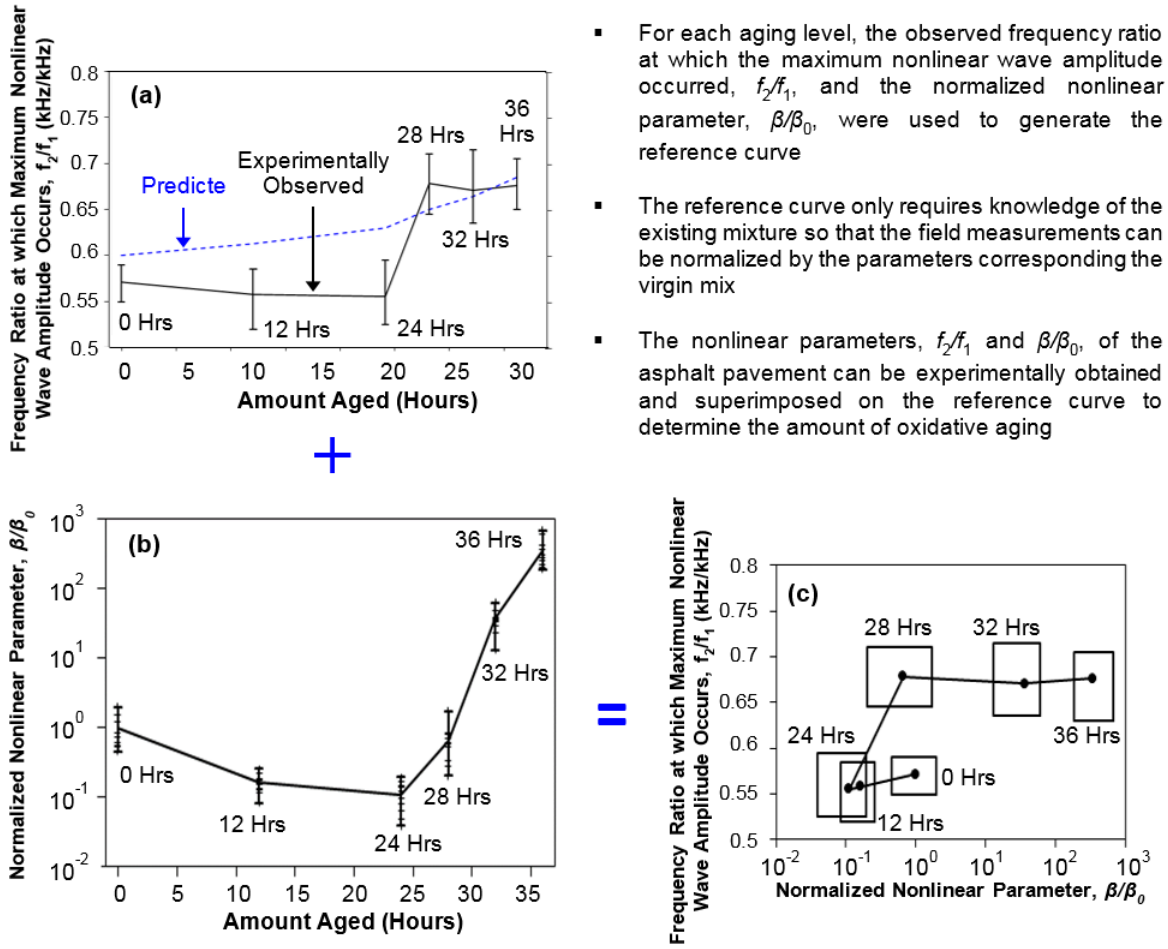

Figure 4.10: Generation of the reference curve, *i.e.*, the normalized nonlinear parameter $\frac{\beta}{\beta_0}$ versus the frequency ratio $\frac{f_2}{f_1}$. The frequency ratio and normalized nonlinear parameter data, shown in (a) and (b), respectively, is used to create the nonlinear damage characterization curve in (c).

with expectations, because β is defined as the "efficiency" at which the nonlinear scattered wave is generated. Of course, normalization is necessary, because relative values of β (not absolute) are utilized to assess the level of aging. Relative measurements will account for any changes in the beam profile. The agreement of the results from these two studies indicates that subsurface waves can be used successfully to characterize oxidative aging in asphalt concrete using the non-collinear wave mixing technique.

The measurements from Figures 4.7 and 4.9 were used to construct the reference nonlinear damage characterization curve. Please refer to Figure 4.10. This reference curve was used in the subsequent studies, which will now be discussed.

Blind Study using Method 1: Iteratively Determined Incident Angle

For this portion of the study, it was assumed that there was no prior knowledge of the AC sample other than the mix design. The incident angle was found iteratively for each aged sample. Please refer to Figure 4.11, which shows amplitude measurements as a function of the incident angle for the virgin specimen. The maximum of this data corresponds to the incident angle. From a previous study, it is known that the critical incident angles will be between 43° and 79° for the range of oxidative aging (0 to 36 hours) of sample set of AC specimens used in this study. The measurements were begun by recording the signal for incident angles every 10°, starting at 40°. The amplitude measurement was taken at the beginning portion of the signal, which corresponds to the first arriving subsurface dilatational wave. Later portions of the signal may include other modes such as surface waves, or in this case due to the finite dimensions of the sample, shear waves reflected from the bottom surface.

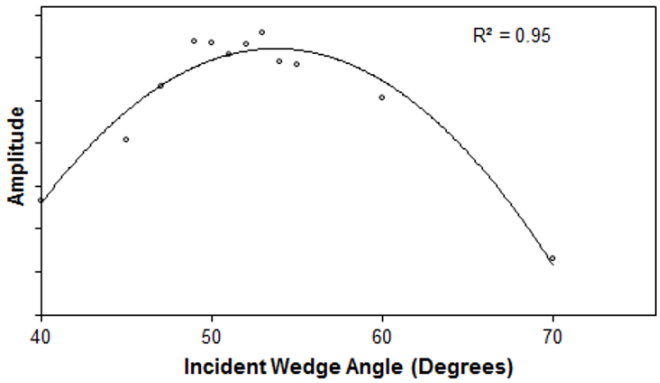

Figure 4.11: Amplitude of received wave as the incident angle $\theta_{incident}$ of the variable angle wedges are set to different angles using the set-up in Figure 4.2. This technique is used to find the first critically refracted angle when there is no prior knowledge of the material properties. A parabola is fitted to the data to find the maximum. The R^2 of the parabola is 0.95. Extracted from McGovern et al. [47]

This process will now be described by way of an example. Consider the case where measurements were taken on the virgin specimen (Figure 4.11). After taking the first four measurements (at 40°, 50°, 60°, and 70°), the amplitudes of the signal were examined at each measurement. From the first four amplitude measurements, a parabolic trend was observed that peaked at 50°. The next two amplitude measurements were taken at 45° and 55°. After these two measurements, the peak was still observed at 50°. The next measurements were taken at 47° and 53°, where the observed

peak was then 53°. The peak at 53° did not shift when subsequent measurements were taken for the incident angles of 51°, 52°, and 54°. Thus, the optimal incident angle was concluded to be 53°, which corresponds to a critically refracted angle of 52°.

The above procedure was repeated for all specimens until amplitudes were recorded for a sufficient number of angles. A parabola was then fit to the measurements, and the location (incident angle) of the maximum amplitude was found to the nearest degree. However, for the specimens aged 32 hours and 36 hours, the first critical angles are near the limitations of the variable angle wedges, making fitting a parabola to the data unfeasible. Thus, in these cases, the maximum value of the data was reported. Table 4.4 contains the critical angles found via this technique along with the theoretically predicted values (via previous velocity measurements).

Table 4.4: Theoretically predicted critical angle + 1° based on Snell's law, and the experimentally determined critical angle + 1°. Extracted from McGovern et al. [47]

	Amount Aged (Hours)					
	0	12	24	28	32	36
Theoretically Predicted Critical Angle + 1° *	51°	47°	44°	57°	79°	73°
Experimentally Measured Critical Angle + 1°	53°	50°	45°	55°	75° **	73°
Percent Error	3.9	6.4	2.3	3.5	5.1	0.0

* Based on literature, the angle at which the subsurface wave is able to be best detected, i.e., maximum displacement at the surface, corresponds to around 1° above the first critical angle.
** Due to constraints with the angle wedges, the incident angle could not be greater than 75°.

Once the appropriate incident angle was found, the velocities and attenuations were determined as described in Section 4.5.1. Tables 4.5 and 4.6 show the dilatational velocity and attenuation estimates, respectively, using the iterative angle technique, along with the percent errors when compared against measurements from the more accurate technique (see McGovern et al. [13]). It is observed that the velocity estimate using Snell's law yielded smaller errors than the estimate using the pitch-catch configuration of subsurface waves. Table 4.7 contains the estimated shear attenuations using the empirical relationship (Equation 4.2) with the velocities obtained via longitudinal subsurface waves. Also included in Table 4.7 are measurements obtained from the more accurate technique (see McGovern et al. [13]). These errors are higher than desirable; however, they are the best available estimate given the testing set-up constraints (*e.g.*, access to only one

side of the specimen). One major source of error in the linear acoustic measurements arises from the fact that the beam pattern of subsurface waves is different than that generated by incidentally mounted transducers. Couplant conditions can also add to errors in the attenuation measurement; however, multiple independent attenuation measurements were taken to minimize this error. Also, recall that the attenuation coefficients found in the previous study were done so on a different set of samples of the same mixture type. Although care was taken to make the samples in a consistent manner, variations can exist in the random aggregate structure, oxidative aging uniformity of the mixture, amount of time spent in the oven while mixing the samples, etc.

Table 4.5: Dilatational velocities using a normal incidence through-transmission technique and the procedure outlined in Section 4.5.1. Extracted from McGovern et al. [47]

		Theoretically Predicted from Snell's Law (m/s)	Percent Error (%)	Experimentally Measured from Longitudinal Subsurface Waves in a Through-Transmission Set-up (m/s)	Percent Error (%)
0	3554	3452	2.9	3586	0.9
12	3792	3604	5.0	3674	3.1
24	4007	3916	2.3	4389	9.5
28	3284	3362	2.4	3346	1.9
32	2780	2830	1.8	2874	3.4
36	2861	2844	0.6	2667	6.8

Once the non-collinear wave-mixing was performed and the nonlinear scattered wave signal (*i.e.*, the difference signal) was obtained, Johnson and Shanklands' [32,33] selection criteria was used to verify that the nonlinear wave arose from the primary wave interaction. It was verified that all of the difference signals met the frequency, amplitude, and directionality criterion.

For each sample, the frequency ratio $\frac{f_2}{f_1}$ at which the maximum nonlinear scattered wave amplitude occurred was recorded. The normalized wave generation parameter $\frac{\beta}{\beta_0}$ was found for each specimen using the recorded amplitudes and estimated attenuations as described in Section 4.5.1. The average of five independent measurements for each specimen is superimposed as red x's on the laboratory determined nonlinear characterization curve in Figure 4.12.

Table 4.6: Dilatational attenuations at different frequencies using a normal incidence through-transmission technique and the procedure outlined in Section 4.5.1. Extracted from McGovern et al. [47]

Amount Aged (Hours)	Dilatational Attenuations								
	Experimentally Measured using Normal Incidence Through-Transmission Set-up[13] (Np/m)			Experimentally Measured using Critically Refracted Longitudinal Subsurface Waves in a Through-Transmission Set-up (Np/m)					
	120 kHz	160 kHz	200 kHz	120 kHz	Percent Error (%)	160 kHz	Percent Error (%)	200 kHz	Percent Error (%)
0	35.8	35.4	42.2	36.8	2.8	41.7	17.9	48.7	15.4
12	33.0	32.5	39.3	36.1	9.3	38.6	18.8	48.4	23.1
24	32.9	31.6	37.3	33.5	1.7	33.2	5.1	38.4	3.0
28	30.2	33.4	45.4	35.1	16.3	40.9	22.3	50.2	10.5
32	47.1	58.9	77.5	41.8	11.2	59.0	0.2	74.4	3.9
36	59.6	68.0	95.9	70.1	17.6	81.0	19.0	108.2	13.3

Table 4.7: Shear attenuations for different aged amounts at the corresponding f3 frequency using a normal incidence through-transmission technique and the procedure outlined in Section 4.5.1. Extracted from McGovern et al. [47]

Amount Aged (Hours)	Shear Attenuations		
	Experimentally Measured using Normal Incidence Through-Transmission Set-up (At Corresponding f_3)[13] (Np/m)	Estimated using Critically Refracted Longitudinal Subsurface Waves in a Through-Transmission Set-up (Np/m)	Percent Error (%)
0	48.1	37.8	21.5
12	33.2	34.9	5.3
24	27.0	33.9	25.7
28	54.6	36.4	33.5
32	54.5	61.1	12.1
36	65.9	74.4	12.8

It is observed that the "blind study" measurements are consistent with expectations as they are superimposed on the nonlinear damage characterization curve. All of the measurements (0, 12, 24, 28, 32, and 36 hours) fall within the error boxes. The measurement with largest deviation from the expected trend was for the $\frac{f_2}{f_1}$ of the sample aged 18 hours; however, the $\frac{\beta}{\beta_0}$ fell within the expected range. Although care was taken to prepare the samples in a consistent manner, differences in the sample can arise during the aging process (non-uniformity of the oxidation) and the random nature of the aggregate structure. The greatest source of error is from the attenuation estimate, as it was

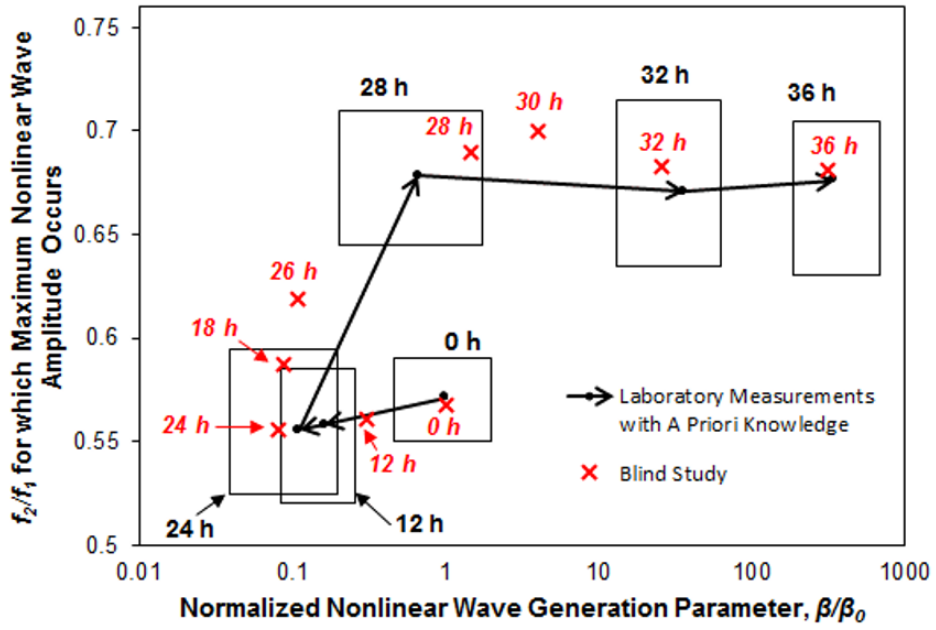

Figure 4.12: The frequency ratio $\frac{f_2}{f_1}$ at which maximum amplitude of the nonlinear wave occurs vs. the nonlinear wave generation parameter β, normalized by the virgin β_0 for asphalt concrete specimens subjected to oven-aging. The figure represents the evolution of the nonlinearities associated with oven-aging. The trajectory of damage accumulation for an increasing number of hours of oven-aging is mixture dependent. The solid dots represent an average of 10 independent measurements. The intervals of confidence represent the maximum and minimum of these 10 independent measurements. These values were obtained via using the subsurface waves at the respective critical angles for each specimen (Table 4.2) Normalization by attenuation was done using Equation 3.8, and assuming straight ray path propagation and that the waves propagated nearly parallel to the surface of the specimen. The red xs represent the average of five measurements taken from the top surface without any prior knowledge of the specimen aging (only the type of mixture was known) using the procedure outlined in Section 4.5.1. Extracted from McGovern et al. [47].

done using subsurface waves which is not as accurate as using a through-transmission set-up with incidentally mounted transducers.

Blind Study using Method 2: Fixed Incident Angle

Again, it was assumed that there was no prior knowledge of the AC sample other than the mix design. This time, the Fixed Incident angle technique from 4.5.2 was utilized to perform a "blind study" in the same manner as it would be performed in the field. First, a study was performed to determine which single incident angle(s), if any, could be used to implement subsurface non-collinear wave mixing across the entire age range (0 to 36 hours of oven-aging) of the samples in the set. For each aged specimen, non-collinear wave mixing measurements were taken using all six incident angles listed in Table 4.2. Five independent measurements were taken for each test.

Amplitudes of the nonlinear scattered wave signal $\boldsymbol{k}_3$ were recorded by passing the difference signal (*i.e.*, scattered wave) through a band-pass filter centered about the range of expected f_3's (for 0 to 36 hours) as f_2 was swept and f_1 was held constant. The amplitude-versus-frequency ratio plots were then "stacked" to create a surface plot. Figure 4.13 shows surface plots created by using (a) incident angles set to each respective samples' critical angle for a baseline comparison, and incident angles set to the critical angle corresponding to (b) 0 hours aging level (51°), (c) 24 hours aging level (44°), and (d) 36 hours aging level (73°). The grayscale denotes the normalized amplitude, where each specimens' amplitude was normalized by its own maximum (in the range over which f_2 swept).

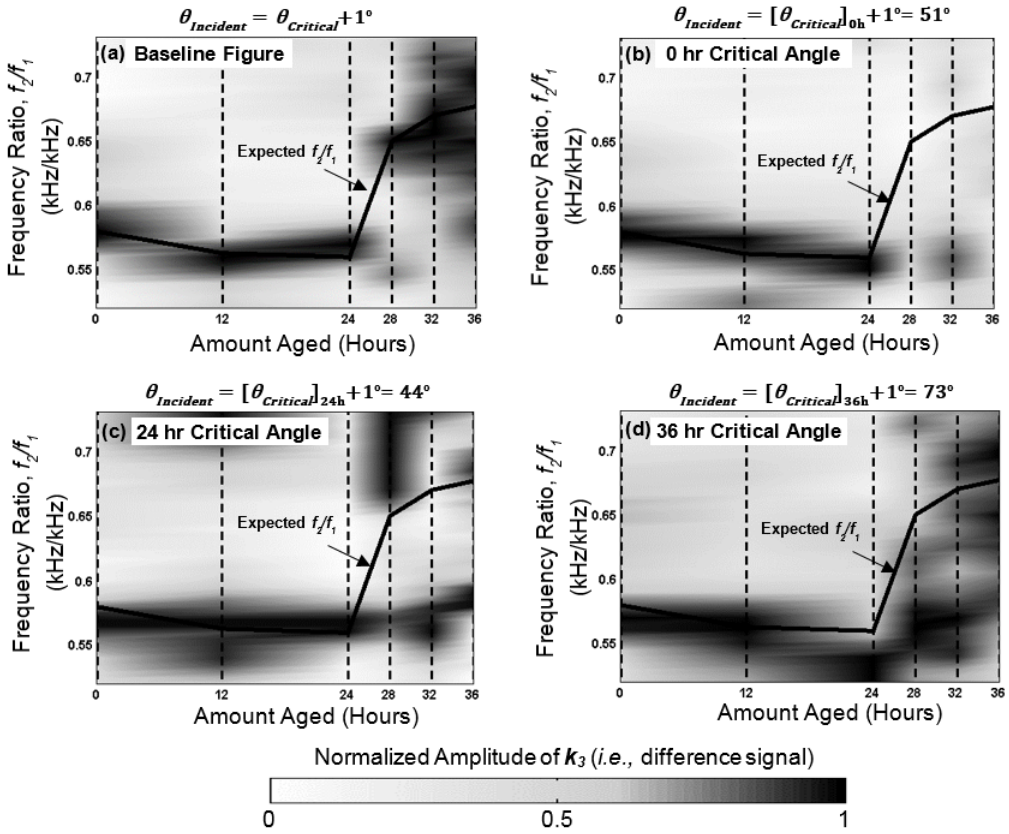

Figure 4.13: Frequency ratio vs. aging level (hours) showing the expected $\frac{f_2}{f_1}$ ratio based on experimentally obtained critical angles. The color coded amplitude of the scattered wave is in the axis perpendicular to the plane. For each aging level sample, these amplitudes are normalized using the maximum value for that sample (see color bar). This was done to enhance visualization of the results, but prevents comparison of the difference signal amplitudes among the test specimens. The color code representation in the graph is a linear interpolation of the values obtained for the discrete levels of aging. At each aging level, along the dashed vertical lines, the color code is normalized from 0 to 1. Figure (a) was obtained using the correct critical angle for each aging level for each specimen. Figures (b), (c), and (d) represent the amplitude of the difference signal when the critical angle for the virgin, 24, and 36 hours of aging, respectively, are used for all of the specimens. Extracted from McGovern et al. [54] (currently under review).

Thus, the surfaces reflect the shape of the $\boldsymbol{k}_3$ amplitude and not the absolute magnitude. If this normalization were instead done using the maximum value of all of the specimens, the normalized amplitude of the difference signal for the higher aging level specimens would be relatively small (due to higher attenuations), which would impair the visualization. The expected frequency ratios are superimposed on the figures and denoted by a solid black line. These expected frequency ratios correspond to the observed frequency ratios in the baseline figure, Figure 4.13 (a). For the baseline measurements, it was observed that for the higher aged specimens, there is more of a "spread" in the frequencies observed. This may be due to nonuniform aging in the mixture of the test sample, which would have the effect of causing iteractions at various frequencies for the same interaction angle.

The measurements taken using the incident angles corresponding to 0, 24, and 36 hours are shown in Figures 4.13 (b), (c), and (d), respectively, as these samples bound the entire sample set. The samples aged 0 and 36 hours characterize the extremes of the sample set in terms of aging, and the samples aged 24 and 36 hours characterize the bounds in terms of their respective critical angles. For the incident angle corresponding both the 0 and 24 hours aged specimen (Figures 4.13 (b) and (c), respectively), it was observed that these incident angles work well for specimens aged 0 to 24; however, they do not work well for specimens aged beyond 24 hours.

For the mixture type and angle wedges used in this study, it was found that an incident angle of 73° was the best suited angle to show the nonlinearities across the entire sample set (Figure 4.13 (d)). It is hypothesized that the reason the 73° angle works across the entire sample set is due to interaction of the side-lobes present in the subsurface beam. As the incident angle is moved beyond the first critical refracted angle, the side lobes begin to dominate [40, 45] as discussed in Section 4.2. The presence of side lobes, along with the large beam spread in the sample, may cause the scattered wave to be generated and received at the surface for incident angles much larger than the critical refracted angle. The nonlinearities in the sample aged for 24 hours were most difficult to observe at this angle due to a relatively low amplitude. However, this was not unexpected, as this sample's critical angle has the largest deviation from the incident angle (*i.e.*, 73° - 44° = 29°), as shown in Table 4.2. The nonlinear response in the sample aged 28 hours was slightly more difficult

to investigate, as multiple pronounced peaks in the frequency spectra of the resultant scattered wave were observed. This is most likely due to non-uniformities in the aging of the mixture in that particular test sample.

For the measurements taken using an incident angle of 73°, the two nonlinear parameters, $\frac{f_2}{f_1}$ and $\frac{\beta}{\beta_0}$, were found for the entire sample set. The $\frac{\beta}{\beta_0}$ was found by normalizing the scattered wave amplitude by the experimentally determined energy loss as discussed in Section 4.5.2. Table 4.8 shows the experimentally recorded amplitude ratios. The dilatational velocities were estimated using a pitch-catch set-up, and the values are shown in Table 4.9. Note the relatively high errors. Since only one incident angle was used across the entire set (*i.e.*, an angle equal to 73°, which corresponds to the critical angle for the 36 hours aged sample), the subsurface wave did not necessarily travel parallel to the surface for the samples that were aged less than 36 hours; consequently, the measured velocity was an underestimate of the actual velocity. Also, for the specimens with the lowest amounts of aging (0 to 24 hours), the incident angle is so far beyond the first critical angle that the side lobes dominate and effectively become the new main lobe. This drastic change in the beam pattern introduced errors in the velocity measurements (6 - 12%). The shear wave attenuations were estimated using the empirical relationship with the experimentally estimated subsurface dilatational velocities. The energy loss at the surface was measured directly using the technique described in Section 4.5.2.

Table 4.8: Dilatational energy loss and shear attenuation for different aging levels at the corresponding f_3 frequency. Extracted from McGovern et al. [54]

		Theoretically Predicted from Snell's Law (m/s)	**Percent Error (%)**	**Experimentally Measured from Longitudinal Subsurface Waves in a Through-Transmission Set-up (m/s)**	**Percent Error (%)**
0	3554	3452	2.9	3586	0.9
12	3792	3604	5.0	3674	3.1
24	4007	3916	2.3	4389	9.5
28	3284	3362	2.4	3346	1.9
32	2780	2830	1.8	2874	3.4
36	2861	2844	0.6	2667	6.8

Table 4.9: Dilatational velocities using a normal incidence through-transmission technique. Extracted from McGovern et al. [54]

Amount Aged (Hours)	Dilatational Attenuations								
	Experimentally Measured using Normal Incidence Through-Transmission Set-up[13] (Np/m)			Experimentally Measured using Critically Refracted Longitudinal Subsurface Waves in a Through-Transmission Set-up (Np/m)					
	120 kHz	160 kHz	200 kHz	120 kHz	Percent Error (%)	160 kHz	Percent Error (%)	200 kHz	Percent Error (%)
0	35.8	35.4	42.2	36.8	2.8	41.7	17.9	48.7	15.4
12	33.0	32.5	39.3	36.1	9.3	38.6	18.8	48.4	23.1
24	32.9	31.6	37.3	33.5	1.7	33.2	5.1	38.4	3.0
28	30.2	33.4	45.4	35.1	16.3	40.9	22.3	50.2	10.5
32	47.1	58.9	77.5	41.8	11.2	59.0	0.2	74.4	3.9
36	59.6	68.0	95.9	70.1	17.6	81.0	19.0	108.2	13.3

The average of five independent measurements for each specimen is superimposed as red x's on the laboratory determined nonlinear-characterization curve in Figure 4.14. As expected, the specimens with the lowest amounts of aging (0 to 24 hours) deviate the most from the laboratory determined reference curve due to the large deviations in the first critical angle with respect to the incident angle.

4.9 Comparison of the Two Methods: Iterative Incident Angle versus Fixed Angle

A comparison between the two methods presented in the previous section will now be made. Both methods introduce a means to characterize the AC pavement via the one-sided non-collinear wave mixing approach when the linear acoustic properties are unknown.

The biggest advantage to determining the incident angle via the Iterative Angle technique is that the normalized nonlinear wave generation parameter $\frac{\beta}{\beta_0}$ can be found with some accuracy. Since the best possible angle (1° above the first critical refracted angle) is used to generate the subsurface wave, normalizing the amplitude to obtain $\frac{\beta}{\beta_0}$ can be readily done by using the estimated attenuations. The disadvantages to Iterative Angle method are that it is time-consuming and more

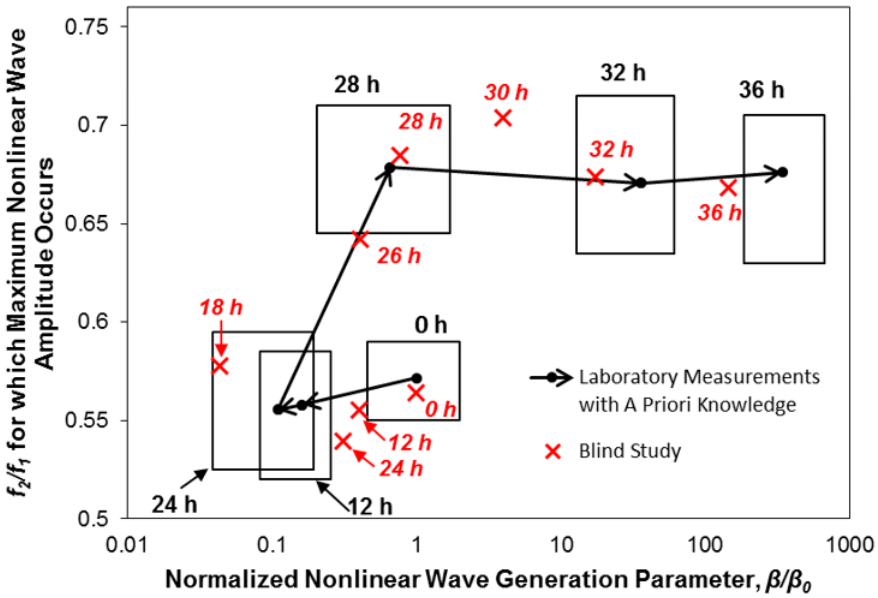

Figure 4.14: The frequency ratio $\frac{f_2}{f_1}$ at which maximum amplitude of the scattered nonlinear wave occurs vs. the nonlinear wave generation parameter β, normalized by the value corresponding to the un-aged mixture β_0 for asphalt concrete specimens subjected to oven-aging. The figure represents the evolution of the nonlinearities, *i.e.*, damage, associated with oven-aging. The trajectory of damage accumulation for an increasing number of hours of oven-aging is mixture dependent. The solid dots represent an average of 10 independent measurements. The intervals of confidence represent the maximum and minimum of these 10 independent measurements. These values were obtained using the subsurface longitudinal waves at the respective critical angles for each specimen. Normalization by attenuation was done using Equation 4.14, assuming a straight ray path propagation, and assuming that the waves propagated nearly parallel to the surface of the specimen. The red xs represent the average of the 10 independent measurements taken from the top surface without any prior knowledge of the specimen aging (only the type of mixture was known). Extracted from McGovern et al. [54].

difficult to implement in the field, since determining the incident angle is an iterative process. Of course, the potential for this procedure to be automated exists with the use of a automated variable wedges and a simple automated algorithm for choosing the incident angle based on experimental data. Another potential approach would be the utilization of phase-array transducers to steer the beam; however, it is difficult to say whether or not phase array transducers would function properly in a heterogeneous material such as asphalt, since phase array transducers rely on constructive and destructive interference in the beam patterns to create a steered beam profile. Also, although $\frac{\beta}{\beta_0}$ can be calculated using the estimated attenuations, these attenuation estimates are not exact due to beam spread, the fact that the wave is not ever perfectly parallel to the surface, and variation in the couplant conditions.

The biggest advantage of using one Fixed Incident Angle technique, is the ease at which it can be implemented, rendering it ideal for field use. However, there are drawbacks in terms of its accuracy. Although the $\frac{f_2}{f_1}$ ratio metric does not suffer using this method, the estimation of the $\frac{\beta}{\beta_0}$ parameter suffers due to relative larger errors in the attenuation estimates. Another drawback to fixed angle technique is that although the chosen incident angle may be ideal for a small range of aged specimens, it is not the best possible angle for generating subsurface longitudinal waves for the entire aged sample set. This may have the effect of making it more difficult to detect the nonlinear wave for specimens with critical angles far from the chosen incident angle. Furthermore, for other AC mixture-types, more than one incident angle may be necessary to achieve a wide range of aging-assessment. Finally, since the most suitable incident angle is not necessarily being used, multiple peaks in the frequency ratio versus amplitude curve may be detected which may complicate the analysis.

Chapter 5

Corrective Action: Rejuvenator Efficacy

In Chapters 3 and 4, the non-collinear wave-mixing technique was demonstrated to be a practical, non-destructive tool for the assessment of the level of oxidative aging in asphalt pavements. Upon determination of the level of oxidative aging in the pavement, engineers may decide to take preventative or corrective measures. The ability to monitor the aging level of the pavement subsequent to taking corrective action is necessary to assess the effectiveness of the action(s) as well as make future decisions toward preserving the pavement. Thus, the natural extension to the work presented in Chapters 3 and 4 is to investigate the feasibility of using the non-collinear wave-mixing technique to assess the effectiveness of the corrective action. Here, the effectiveness of rejuvenators to restore the material properties of the aged asphalt back to their original state was studied. This chapter will begin with a brief discussion on asphalt rejuvenators, followed by the experimental investigation and a discussion of the results.

5.1 Rejuvenators

The oxidation process increases the asphaltene-to-maltene ratio of the binder, resulting in a stiffer and more brittle binder. Please refer to Appendix A, which contains the fundamentals of oxidative aging of asphalt. Rejuvenators, and their efficacy in restoring the properties of aged bitumen to their original state, tend to be a controversial topic. Past overselling of some rejuvenating products has caused rejuvenators to gain the not necessarily accurate reputation of being a "snake oil" type product. [55, 56] However, it is important to remember that the term "rejuvenator" is an all-encompassing, hence very broad term, which refers to any product that aims to restore the physical and chemical properties of aged binder. Rejuvenators, therefore, can refer to number of different products such as refined tallow, waste vegetable or frying oils, waste motor oils, lube extracts, extender oils, emulsions, soft virgin binders, and "bio-binders" [57–59]. In this study, the commercial product, *Reclamite Asphalt Rejuvenation*, manufactured by Pavement Technology, Inc and donated by the Heritage Group was used. This product claims to reverse the aging effects of AC pavements by replacing the volatile components (lost during the aging process) [60].

Rejuvenators are generally applied to the surface of existing pavements; therefore, it is essential for the rejuvenator to have the ability to penetrate the surface and diffuse through the aged asphalt. If the rejuvenator lacks this ability, not only will the aged asphalt be unaffected, but the unabsorbed rejuvenator will reduce skid resistance [61, 62]. To avoid creating slick, over-coated surfaces, it is often good practice to apply rejuvenators in several coats at a lower application rate [56]. During the diffusion process, the rejuvenator first forms a low-viscosity layer around the layer of aged binder which coats the aggregate. Then, the rejuvenator starts to diffuse into the aged binder, thus softening it. Eventually, all the rejuvenator penetrates into the aged binder and the inner layer becomes less viscous and the outer layer becomes relatively more viscous as the mixture approaches a state of equilibrium [61,62]. Oliver [63] found that the rate of diffusion can be increased by adding diluents or by increasing temperature. Thus, the environment in which the rejuvenator is applied is a critical consideration, especially in terms of application rate. After a sufficient dwell time, the performance of the rejuvenator should be evaluated.

Currently, researchers are still pursuing a thorough and quantitative understanding of the effect of rejuvenators. There exists a need for a more reliable method for determining the effectiveness of rejuvenating agent(s). The non-collinear wave-mixing technique has been shown [31, 46, 47, 54] to be a reliable method for assessing the level of oxidation in AC pavements. In this portion of the investigation, the effectiveness of rejuvenators, *i.e.*, the effective amount of aging of the AC after rejuvenator application, was assessed via the non-collinear wave mixing technique as a function of the dwell time. The data collected from the rejuvenator-coated specimens was compared to the known nonlinear damage characterization curve from Chapter 4 to determine the degree of restoration the rejuvenator had on the AC as a function of the dwell time. This study will now be detailed in the following sections.

5.2 Sample Preparation

A set of gyratory compacted asphalt specimens was created with the same mix-design as in Chapters 2 through 4 of 5.9% (by weight of total mixture) PG 64-22 binder with a 4% air void content. Prior to compaction, *all* of the loose mixtures were oven-aged for a total of 36 hours at 135°C. To

Figure 5.1: Asphalt concrete specimen immediately upon application of rejuvenator (10% by weight of the binder in the mixture)

encourage uniform aging throughout the specimen, the loose mixture was hand stirred every 12 hours. A gyratory compactor was used to compact the loose mixture into cylinders with a nominal height of 170 mm and radius of 150 mm. Rectangular specimens were then cut from the gyratory specimens with dimensions 150 × 175 × 50 mm.

Rejuvenator was applied to one face of each specimen, the amount of which corresponded to 10% of the binder (by weight of the mixture). Care was taken to apply the rejuvenator in a thin, even layer across the entire face of the specimen. See Figure 5.1, which shows a specimen immediately upon being coated with rejuvenator. Each coated specimen was left to soak in the rejuvenator for a specific amount of time: 3 to 6 days in 1 day increments and, 1 to 8 weeks in 1 week increments, and 12 weeks for a total of 13 test specimens with different dwell time periods. Once the dwell time reached the desired amount, the specimen was wiped of any excess rejuvenator, to improve couplant conditions, and immediately ultrasonically tested. The specimens were weighed before and after wiping the rejuvenator to determine how much rejuvenator was removed during the wiping process. Figure 5.2 shows a specimen at a dwell time of 2 weeks.

5.3 Experimental Set-Up

The set-up described in Chapter 4 was utilized in this investigation, as it is representative of field testing application. Both the Iterative Incident Angle technique (see Section 4.5.1) and the Fixed Incident Angle technique (see Section 4.5.2) were employed in this study. For the Fixed Incident

Figure 5.2: Asphalt concrete specimen coated with rejuvenator for a dwell time of 2 weeks.

Angle technique, an incident angle of 73° was used as before. Non-collinear wave mixing data acquisition was performed as usual (see Section 4.7).

5.4 Results

The variability in the surface porosity in localized regions due to the random aggregate structure caused the rejuvenator to penetrate and act on the specimen in a non-uniform fashion. This non-uniform penetration is evident in Figure 5.2, which shows a rejuvenator-coated specimen after a dwell time of 2 weeks. All specimens were coated with rejuvenator at the same time; thus, for each passing time period, the specimen with the least visible amount of rejuvenator remaining on the surface was chosen for testing for that time period. The specimen was weighed, wiped of excess rejuvenator, and weighed again before testing. The amount of rejuvenator lost, *i.e.*, unabsorbed rejuvenator wiped from the surface, is shown in Table 5.1. The samples with low dwell times (*i.e.*, < 5 days) had the greatest rejuvenator loss, because the rejuvenator did not have time to penetrate fully into the sample. It was observed that the rejuvenator penetrated some samples quicker than others and not always in a uniform manner. The rejuvenator penetrates the specimen via gravity and capillary action; thus, variability can be attributed to the porosity of the structure. Globally, the specimens were all compacted to have the same porosity; however, the random aggregate structure will cause local variations in the porosity, which attributed to the variation in the penetration of the rejuvenator.

Conventional through-transmission linear acoustic measurements, where the sending and receiving transducers are mounted on opposite sides of the specimen, were not taken on the rejuvenated samples due to the non-uniformity of the rejuvenator penetration. Through-transmission measurements through the samples would yield *average* velocity and attenuation values, and not be representative of the "rejuvenated" portion of the specimen (*e.g.*, near the surface for early dwell times).

5.4.1 Rejuvenator Efficacy - Iterative Incident Angle Technique

The rejuvenator efficacy was first studied using the Iterative Incident Angle technique from Section 4.5.1. These results will now be discussed.

Determination of Incident Angle

Prior to implementing the non-collinear wave mixing technique, the optimal incident angle was found experimentally. Please refer to Figure 5.3 and Table 5.1. The experimentally observed

Table 5.1: Rejuvenator lost from wiping excess off the surface for samples of various dwell times, and linear characterization of the rejuvenator coated samples with different dwell times. Extracted from McGovern et al. [64]

Dwell Time (Weeks)	Unabsorbed Rejuvenator (%)	Experimentally Determined Critical Angle (°)	Dilatational Velocity* (m/s)	Dilatational Attenuation** (Np/m)		Shear Attenuation*** (Np/m)
				k_1	k_2	k_3
0.50 (≈ 3 Days)	34.1	72	3287	35.4	42.2	64.82
0.70 (≈ 4 Days)	19.5	62	3445	64.14	61.28	57.49
0.78 (≈ 5 Days)	7.5	55	3316	40.30	37.71	50.06
0.93 (≈ 6 Days)	7.5	55	3468	53.00	57.00	50.06
1	2.0	50	3276	60.08	60.89	42.92
2	2.0	50	3687	31.29	31.64	42.92
3	5.7	54	3234	17.94	11.74	53.33
4	12.5	45	3215	52.18	47.23	38.05
5	9.3	56	3621	54.70	52.47	40.73
6	14.7	44	3708	47.11	46.68	33.74
7	7.5	55	3465	35.78	26.29	33.74
8	9.3	56	3754	55.98	41.01	51.28
12	1.8	52	3385	57.94	56.61	45.99

* The dilatational velocity was measured using the experimentally measured critical angle with Snell's Law
** The dilatational attenuation was measured experimentally via subsurface waves in a through-transmission configuration
*** The shear attenuation was estimated using an empirical relationship between the shear attenuation and dilatational velocity

optimal angles were found to vary with the dwell time.

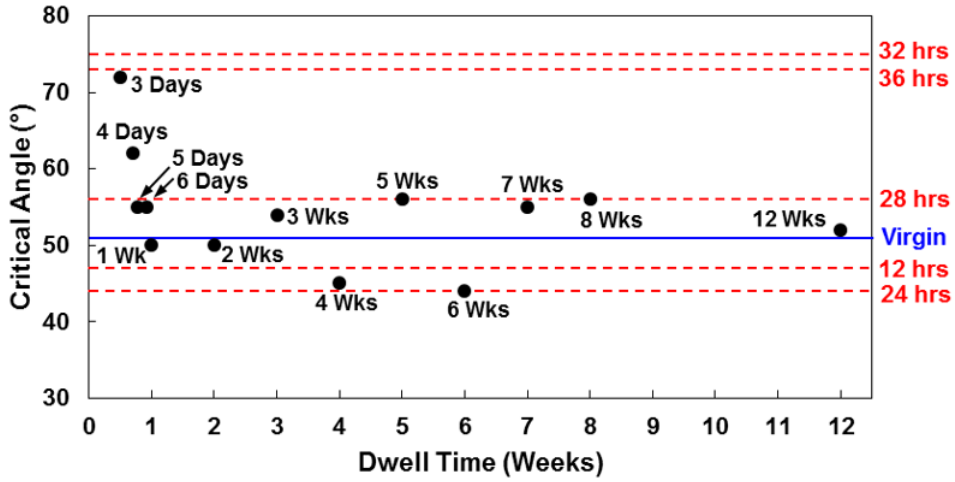

Figure 5.3: Experimentally measured critical angles for samples with different dwell times. The blue line indicates the critical angle for a reference virgin specimen (no rejuvenator). The dashed red lines indicate the critical angles for specimens subjected to various amounts of aging with no rejuvenator for comparison purposes. Extracted from McGovern et al. [64]

In Chapter 4, the optimal angle for a virgin specimen (*i.e.*, no rejuvenator or oxidative aging) was found as 51°, and the optimal angle for a specimen aged 36 hours (with no rejuvenator) was found as 73°. For specimens with a dwell time of 3 to 5 days, the optimal angle approached the virgin optimal angle with each successive day. For the specimens with a dwell time greater than 5 days, the optimal angles varied about the virgin optimal angle within a ±7° range. These angles were all observed to be closer to the angle corresponding to the virgin sample than that of the 36 hours, indicating that the rejuvenator may be having a restorative effect on the aged specimens. For the specimens with a dwell time greater than 5 days, largest difference (14.7% difference with respect to the virgin angle of 51°) corresponded to the sample with a dwell time of 6 weeks, which had an experimentally determined optimal angle of 44°. It is interesting to note that the samples with 5, 7, and 8 weeks dwell time had incident angles of 56° (55° for the 7 week sample), which was larger than the virgin incident angle. This might suggest that the oxidative damage was not fully reversed. It is possible that the rejuvenator did not penetrate as thoroughly as in the other samples, leaving areas of unaffected binder.

Velocities and Attenuations

Once the incident angle was determined, the dilatational velocity and corresponding attenuation were found using subsurface waves in the pitch-catch configuration as described in Section 4.5.1 (Figure 4.2, page 60). Alternatively, Snell's law could have been used to calculate the dilatational velocity. The shear attenuation coefficient was calculated using the empirical relation from Equation 4.2. Recall, this empirical relation was determined in Chapter 4 via data obtained using bulk waves in a traditional through-transmission set-up, where sending and receiving sensors were placed on opposite sides of the specimen (Chapter 2). Subsurface dilatational waves have a different beam profile than traditional bulk waves, which accounts for discrepancies between the shear attenuation estimate and the actual shear attenuation. Please refer to Table 5.1 for a summary of the experimentally determined linear acoustic parameters.

At this point, it should be mentioned that the experimentally determined linear acoustic parameters (*i.e.*, critical angles, velocities, and attenuations) do not necessarily entirely reflect the state of the material, because they are largely influenced by the aggregate structure and aging of the binder. The random aggregate structure and non-uniformity in the binders oxidative aging may result in measurements which vary with the location of the transducer placement. Also, by nature of the test, the measurements are indicative only of the state of the material located very close to the surface, since only the first arriving portion of the signal is used in the calculation. Thus, while the linear acoustic parameters can be used as an indicator of the amount of aging, they should be used in conjunction with nonlinear measurements for a more accurate and robust representation of the material behavior.

Non-Collinear Wave Mixing

Non-collinear wave mixing with subsurface dilatational waves was carried out for each specimen using the experimentally determined optimal incident angle. The difference signal was checked against the selection criteria [32, 33] to verify that it was a result of the primary wave interaction and not the testing equipment.

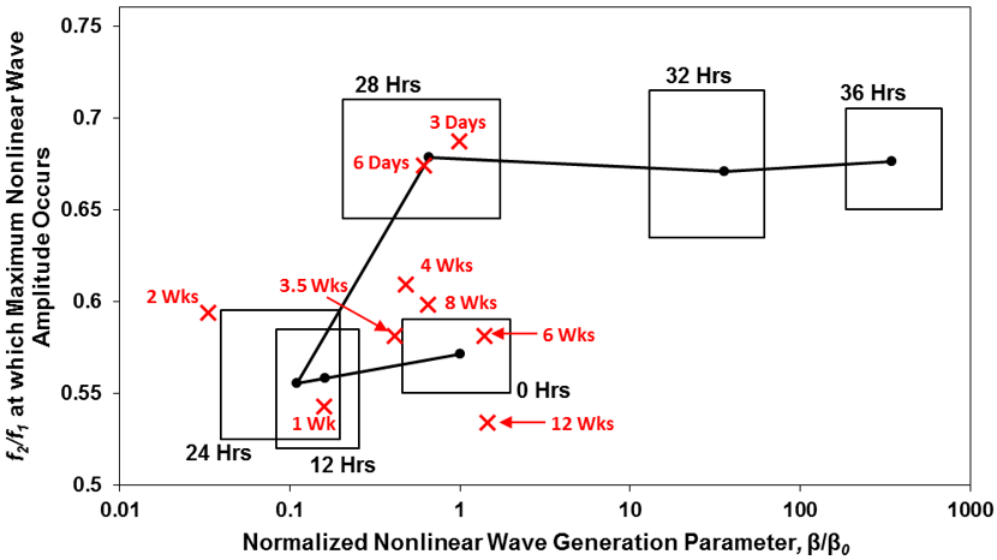

Figure 5.4: The Iterative Incident Angle method was used to find the frequency ratio $\frac{f_2}{f_1}$ at which maximum amplitude of the nonlinear wave occurs vs. the nonlinear wave generation parameter β, normalized by the virgin β_0. The average of 5 nonlinear measurements of the rejuvenator-coated specimens, denoted by the red x's, are superimposed on the reference curve, denoted in black. The reference curve was found in Chapter 4, and it represents the evolution of the nonlinearities associated with oven-aging. The trajectory of damage accumulation for an increasing number of hours of oven-aging is mixture dependent. Extracted from McGovern et al. [64]

The frequency ratio $\frac{f_2}{f_1}$ and normalized nonlinear wave generation parameter $\frac{\beta}{\beta_0}$ were determined for each specimen and plotted on the reference nonlinear damage characterization curve. The reference curve was found in Chapter 4, by measuring the $\frac{f_2}{f_1}$ and $\frac{\beta}{\beta_0}$ values for AC specimens at various levels of oxidative aging. Please refer to Figure 5.4, which shows selected data from some of the rejuvenator coated specimens' $\left(\frac{f_2}{f_1}, \frac{\beta}{\beta_0}\right)$ values superimposed (and denoted by red "x's") on the reference curve. Not all of the data was plotted to facilitate viewing. Table 5.2 contains the nonlinear parameters $\left(\frac{f_2}{f_1}, \frac{\beta}{\beta_0}\right)$ measured for the entire sample set.

It is observed that beyond 4 weeks of dwell time, the samples have $\left(\frac{f_2}{f_1}, \frac{\beta}{\beta_0}\right)$ values which fall within error of the nonlinear parameters for the virgin specimen. For the specimen with a dwell time of 8 weeks, there was a large amount of excess rejuvenator which was wiped off. This may explain why the nonlinear parameters deviated from the virgin nonlinear parameters further than the specimens with a lower dwell time of 5 and 6 weeks. For the specimens with a dwell time of 4 weeks and under, the nonlinear parameters deviated further from the virgin parameters in a

Table 5.2: Nonlinear characterization of the rejuvenator coated samples with different dwell times. Extracted from McGovern et al. [64]

Dwell Time (Weeks)	Normalized Nonlinear Wave Generation Parameter, β/β_0	Frequency Ratio at which Maximum Nonlinear Wave Amplitude Occurs, f_2/f_1
0.50 (≈ 3 Days)	0.99	0.687
0.70 (≈ 4 Days)	0.64	0.706
0.78 (≈ 5 Days)	0.63	0.697
0.93 (≈ 6 Days)	0.61	0.674
1	0.16	0.543
2	0.03	0.594
3	0.91	0.520
4	0.41	0.581
5	0.48	0.609
6	1.07	0.587
7	1.39	0.581
8	0.24	0.555
12	1.45	0.534

manner that may be correlated with the dwell time. From $\frac{1}{2}$ to 4 weeks, the nonlinear parameters become closer to the virgin parameters with each successive week. This may be an indication that the rejuvenator takes time to chemically act on the aged binder. It is difficult to know whether the observed changes in the specimens are due to a composite effect of the rejuvenator (a fairly large amount of rejuvenator was used) and asphalt concrete, or a result from the rejuvenator chemically acting on the aged binder.

Figure 5.5 shows some representative selected data that was used to find the frequency ratios $\frac{f_2}{f_1}$. Recall, $\frac{f_2}{f_1}$ is found by holding f_1 constant, monitoring the amplitude of $\boldsymbol{k}_3$ (f_3=f_1-f_2) as f_2 is swept, and determining the point at which $\boldsymbol{k}_3$ reaches maximum. Figure 5.5 (a) shows the amplitude of $\boldsymbol{k}_3$ as f_2 was swept for a few selected samples. For some samples (*e.g.*, the samples with dwell times of 4 days, 1 week, and 2 weeks), the process was relatively straightforward: the peak amplitude was located with respect to the $\frac{f_2}{f_1}$ ratio. However, the presence of multiple peaks in some samples served to complicate the analysis (*e.g.*, the samples with dwell times of 6 days, 4 weeks, 6 weeks, and 8 weeks).

Multiple peaks can arise due to non-uniformity of the rejuvenator penetration. The nonlinear interaction occurs over a finite volume (see Figure 4.5), the size of which is dependent on the beam spread (hence: frequency, wavelength, and transducer element size) and relative positioning of the transmitting transducers. Within this interaction volume, the rejuvenator does not necessarily penetrate and act on the binder in a uniform matter, which may result in pockets of unaffected,

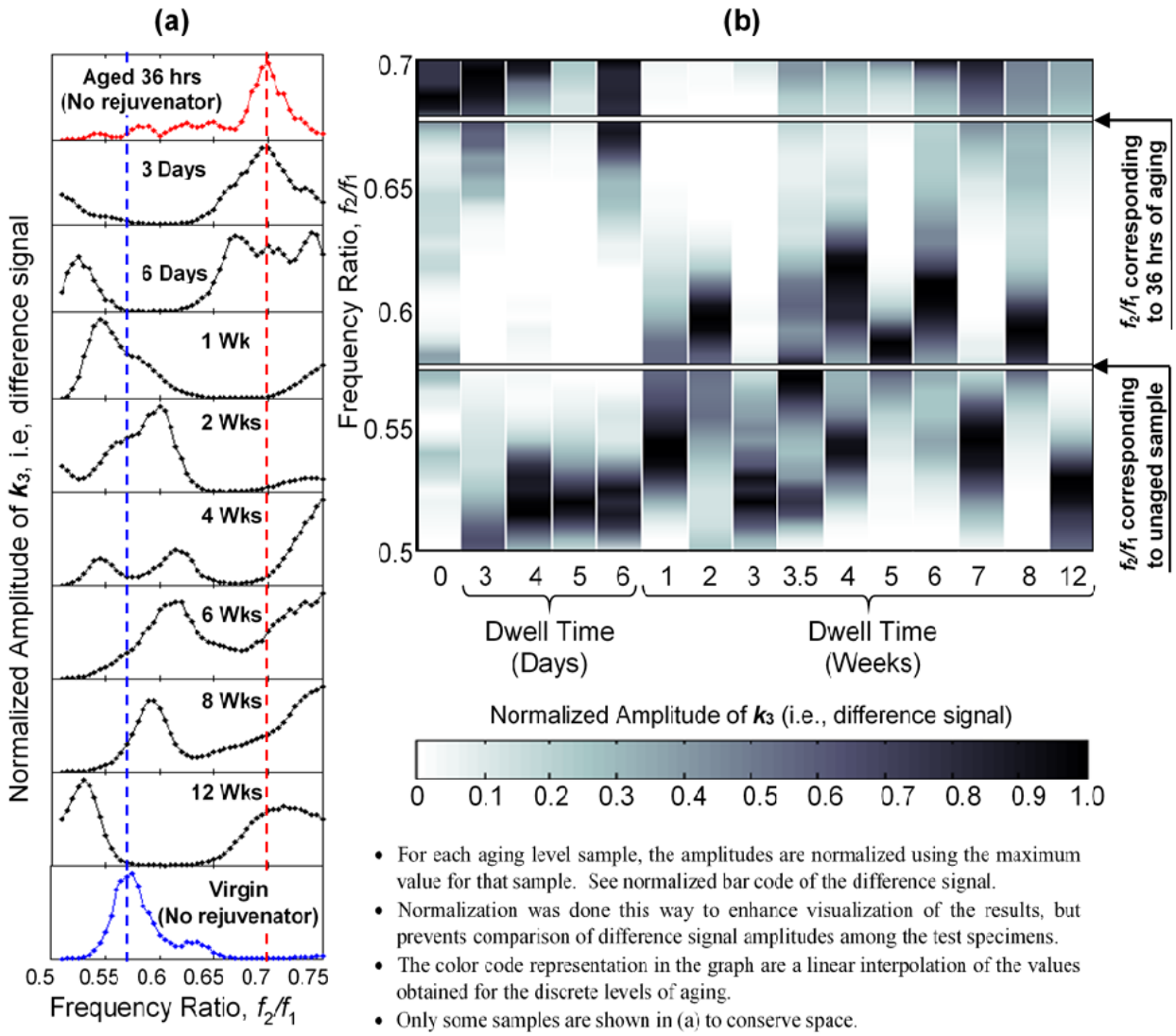

Figure 5.5: Figures (a) and (b) shows the normalized amplitude (A) of the scattered wave with respect to the dwell time and frequency ratio $\frac{f_2}{f_1}$, where (b) depicts A as a color code in the axis perpendicular to the plane. For each sample, these amplitudes are normalized using the maximum value for that sample, see normalized bar code of the difference signal. This was done to enhance visualization of the results, but prevents comparison of the difference signal amplitudes among the test specimens. The color code representation in the graph are a linear interpolation of the values obtained for the different samples. Please note that at each dwell time, the color code is normalized from 0 to 1. Extracted from McGovern et al. [64]

aged binder and pockets of rejuvenated binder. Thus, interactions will occur at different $\frac{f_2}{f_1}$ ratios, since the binder properties vary with location within the interaction region. Recall that the ability of the rejuvenator to penetrate the specimen and act on the binder in a uniform manner depends on the porosity of the specimen and the aggregate structure; therefore, the uniformity of the rejuvenation effects is random and specimen dependent. Furthermore, the non-uniformity of the degree of restoration of the binder will have the effect of lowering the experimentally measured velocity and increasing the experimentally measured attenuation, because the primary waves and resulting scattered wave may travel through both areas of unaffected binder and rejuvenated binder before being received by the receiving transducer.

Figure 5.5 (b) shows the normalized amplitude of the scattered wave $\boldsymbol{k}_3$ with respect to the dwell time and frequency ratio $\frac{f_2}{f_1}$, where the amplitude is depicted as a color code in the axis perpendicular to the plane. For each sample, these amplitudes are normalized using the maximum value for that sample (see normalized bar code of the difference signal). This was done to enhance visualization of the results, but prevents direct comparison of the difference signal amplitudes among the test specimens. The color code representation in the graph are a linear interpolation of the values obtained for the different samples. Please note that at each dwell time, the color code is normalized from 0 to 1. Black lines are superimposed on the plot showing the expected location of the peaks for unrejuvated virgin and 36 hour aged samples for reference.

A few observations can be made about this plot. For a very short dwell time of $\frac{1}{2}$ week ($\approx$ 4 days), the peak falls at 0.7, close to that of the 36 hour aged specimen. This indicates that the rejuvenator has not yet discernibly acted on the binder, and the AC specimen still very much behaves that of a 36 hour aged specimen. For the following days, multiple peaks begin to appear, one around $\frac{f_2}{f_1} =$ 0.67 to 0.7 and the other around $\frac{f_2}{f_1} = 0.52$, which correspond to 36 hours and 12 - 24 hours aged, respectively. At 1 week, most of the energy is concentrated around $\frac{f_2}{f_1} = 0.55$, which corresponds to 12 - 24 hours aged. From 1 to 4 weeks, there are very broad, and sometimes multiple sets of peaks around $\frac{f_2}{f_1} = 0.53$ to 0.61. From 5 to 8 weeks, most of the energy seems to converge about one peak centered at $\frac{f_2}{f_1} = 0.59$, which corresponds to 0 hours aged (virgin). Note, there is still some energy at $\frac{f_2}{f_1} = 0.7$, which indicates that portions of the binder remain unaffected by the rejuvenator.

For this reason, measurements were also taken after 12 weeks of dwell time to determine if these portions of unaffected binder were completely isolated from the rejuvenator, or if the rejuvenator was still acting on the binder. It was observed that the 12 week sample exhibited two peaks at $\frac{f_2}{f_1}$ = 0.53 and $\frac{f_2}{f_1}$ = 0.7; the peak at $\frac{f_2}{f_1}$ = 0.53 was more dominant. The presence of the peak at $\frac{f_2}{f_1}$ = 0.7 may indicate that portions of the binder do remain unaffected by the rejuvenator. The peak at $\frac{f_2}{f_1}$ = 0.53 corresponds to a sample aged 12 - 24 hours. This may indicate that the rejuvenator did not fully restore the binder to its original properties. These findings may be specific to the sample. Whether or not the rejuvenator will fully act on the binder in a uniform manner will depend on the rejuvenator's ability to reach all portions of the binder.

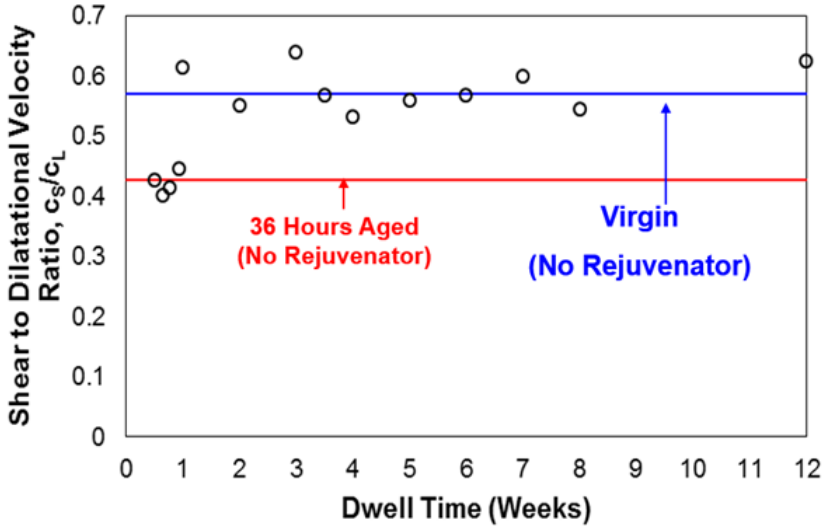

Figure 5.6: Velocity ratio, $\frac{c_T}{c_L}$, for each dwell time as determined by the experimentally measured frequency ratios, $\frac{f_2}{f_1}$. The solid lines denote the values for specimens with no rejuvenator aged 0 hours, *i.e.*, virgin, and 36 hours, respectively.

Using experimentally observed frequency ratios, the velocity ratios can be calculated via Equation 3.5. See Figure 5.6, which shows the velocity ratio, $\frac{c_T}{c_L}$, as a function of the dwell time. The velocity ratios were computed by plugging the experimentally obtained frequency ratios into Equation 3.5 and solving for the positive root. Please note that the softening of the binder has a stronger effect on the dilatational velocity, because the stiffness associated with the shear velocity also depends upon the aggregates interlocking.

5.4.2 Fixed Incident Angle Method

The variable angle wedges were set to an incident angle of $\theta_{inc} = 73°$, which was determined most suitable for the particular AC mixture used in this study (as discussed in Section 4.5.2).

Velocities and Attenuations

As in the previous method, linear acoustic measurements were taken on each specimen to obtain dilatational velocity and amplitude measurements prior to carrying out nonlinear measurements, see Table 5.3. While the linear acoustic parameters, *i.e.*, the velocities and corresponding attenuations, will be affected by the aging level of the AC specimen [13], these properties are also affected by the lack of parallelism in the propagation path when the subsurface wave is generated away from the first critical refracted angle. Thus, for the fixed angle method, these linear acoustic measurements are not very accurate and are only used as an estimate for the parameters in Equation 4.14.

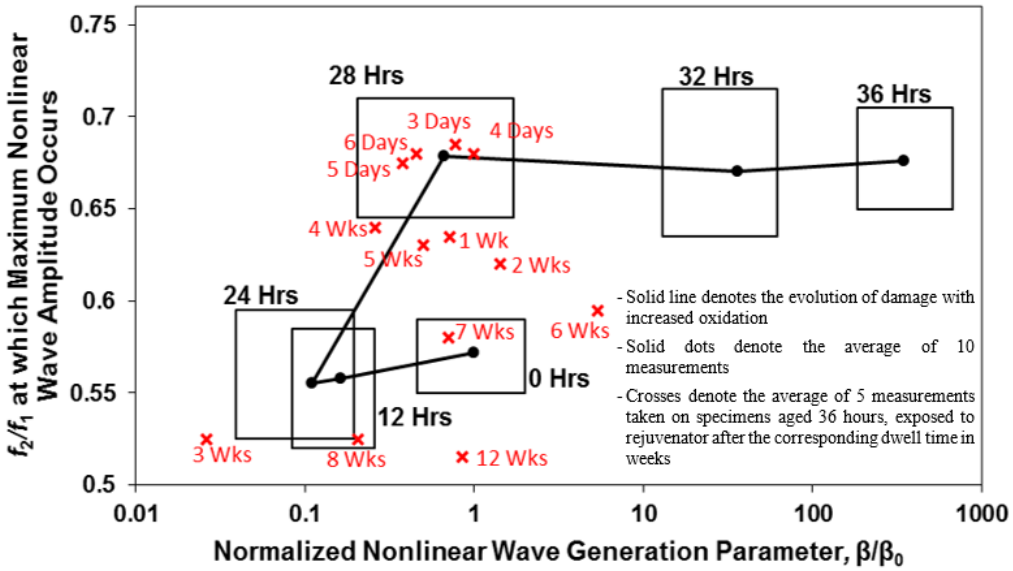

Figure 5.7: The Fixed Incident Angle method was used to find the frequency ratio $\frac{f_2}{f_1}$ at which maximum amplitude of the nonlinear wave occurs vs. the nonlinear wave generation parameter β, normalized by the virgin β_0. The average of 5 nonlinear measurements of the rejuvenator-coated specimens, denoted by the red x's, are superimposed on the reference curve, denoted in black. The reference curve was found in Chapter 4, and it represents the evolution of the nonlinearities associated with oven-aging. The trajectory of damage accumulation for an increasing number of hours of oven-aging is mixture dependent. Extracted from McGovern et al. [65]

Non-Collinear Wave Mixing

Non-collinear wave-mixing measurements were carried out to determine $\left(\frac{f_2}{f_1}, \frac{\beta}{\beta_0}\right)$ for each specimen exposed to rejuvenator for a prescribed amount of dwell time. Refer to Figure 5.7 and Table 5.3. The data (denoted by the red "x's") consisted of the average of 5 independent measurements and are superimposed on the corresponding reference nonlinear damage characterization curve for the mixture used in this study, which is denoted by the solid black lines.

Again, the presence of multiple $\frac{f_2}{f_1}$ peaks posed difficulties when recording the frequency ratios. To circumvent this, the lowest $\frac{f_2}{f_1}$ peak was recorded, as it corresponded to the binder most affected by the rejuvenator.

Table 5.3: Nonlinear characterization of the rejuvenator coated samples with different dwell times. Extracted from McGovern et al. [65]

Dwell Time (Weeks)	Rejuvenator Lost	Dilatational Velocity*	Normalized Dilatational Energy Loss at Surface**		Shear Attenuation*** (Np/m)	Frequency Ratio at which Maximum Nonlinear Wave Amplitude Occurs	Normalized Nonlinear Wave Generation Parameter
			k_1	k_2			
	(%)	(m/s)	(Np/m)	(Np/m)	k_3	f_2/f_1	β/β_0
0.50 (≈ 3 Days)	< 1	3298	0.57	0.64	50.8	0.685	0.77
0.64 (≈ 4 Days)		3372	0.68	0.78	48.5	0.680	0.99
0.78 (≈ 5 Days)		3370	1.15	1.06	48.5	0.675	0.38
0.93 (≈ 6 Days)		3222	0.95	1.11	53.1	0.680	0.45
1		3372	0.53	0.58	48.5	0.635	0.71
2		3371	0.26	0.34	48.5	0.620	1.43
3		3531	1.79	2.02	43.5	0.525	0.03
4		3323	0.87	0.92	50.0	0.640	0.26
5		3726	0.47	0.57	37.5	0.630	0.50
6		3517	0.42	0.45	44.0	0.595	5.39
7		3644	0.65	0.94	40.0	0.580	0.71
8		3649	0.50	1.07	39.9	0.525	0.21
12		3675	0.57	0.62	39.1	0.515	0.85

* The dilatational velocity was measured using the experimentally measured via subsurface waves in a through-transmission configuration

** The dilatational energy loss was measured experimentally via subsurface waves in a through-transmission configuration and normalized by measurements through the virgin specimen, see Equation 7.

*** The shear attenuation was estimated using an empirical relationship between the shear attenuation and dilatational velocity, see Equation 8.

For specimens with a dwell time of 0 to 7 weeks, it was generally observed that the specimen exhibited nonlinear properties $\left(\frac{f_2}{f_1}, \frac{\beta}{\beta_0}\right)$ increasingly closer to that of virgin specimens with an increase in the dwell time. Beyond 7 weeks, the specimen properties also exhibited properties which corresponded to a binder with a lower stiffness than the virgin binder. This can be seen in Figure 5.8, which shows the velocity ratio, $\frac{c_T}{c_L}$, as a function of the dwell time. As before, the velocity ratios were computed by plugging the experimentally obtained frequency ratios into Equation 3.5 and solving for the positive root.

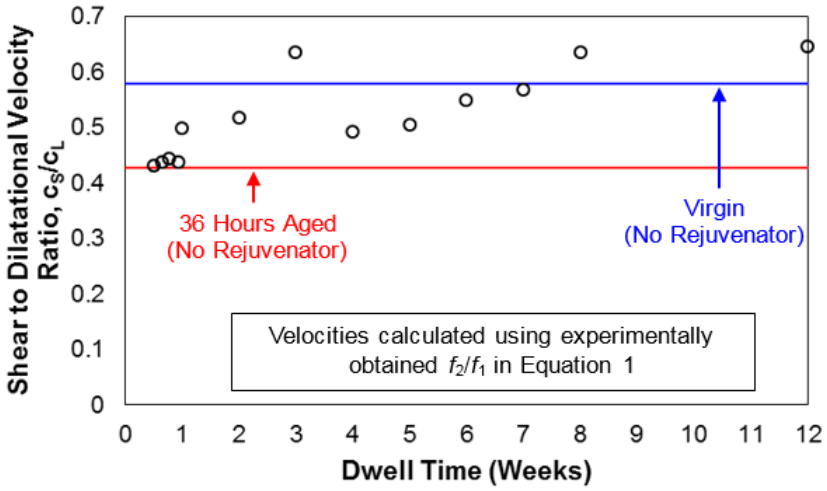

Figure 5.8: Velocity ratio, $\frac{c_T}{c_L}$, for each dwell time as determined by the experimentally measured frequency ratios, $\frac{f_2}{f_1}$. The solid lines denote the values for specimens with no rejuvenator aged 0 hours, *i.e.*, virgin, and 36 hours, respectively. Extracted from McGovern et al. [65]

5.5 Efficacy of Rejuvenators

As discussed in Section 5.1, asphalt rejuvenators can refer to a vast array of products. Only the commercial rejuvenator, *Reclamite Asphalt Rejuvenation* (manufactured by Pavement Technology, Inc. [60]) efficacy was studied here. The non-collinear wave mixing results from both the Iterative and Fixed Incident Angle techniques indicated that this rejuvenator does indeed act on the binder to restore its original virgin properties. These results are consistent with findings in past studies, summarized by Boyer [56]. *Reclamite* was found to improve the viscosity of aged binder, improve the resistance to loss of aggregates via the pellet abrasion test, and ultimately prolong the life of the pavement.

The restorative effects are evidenced in Figures 5.4 and 5.7, which demonstrate that the rejuvenator has the effect of reversing the damage trajectory. In other words, for a sample with an oven-aging level of 36 hours, the application of rejuvenator will cause it to traverse the nonlinear damage characterization curve in reverse, back to that of the 0 hours aged specimen (and possibly beyond). These results are interesting, in that they indicate that the rejuvenator restores the cohesive properties (perhaps allowing the binder to self-heal) as well as softens (lower the stiffness of) the binder.

The amount of rejuvenator used in this study (10% of the binder by weight of the mixture) was selected in order to obtain a thin, even coat. It was observed that rejuvenator restored the binder to its virgin acoustic properties, then continued to act passed the point of virgin acoustic properties. Likely, too much rejuvenator was utilized. In practice, this would cause problems with rutting, excessive deformation; thus, it would be necessary to quantify the appropriate amount of rejuvenator to apply.

As mentioned in the previous sections, uneven rejuvenator penetration caused pockets of the aged binder to remain unaffected. This, of course, will lower the efficacy of the rejuvenator when considering the properties of the pavement as a whole. Thus, it will be necessary to adopt standards in order to ensure the most efficient application of rejuvenators for the strongest efficacy.

Chapter 6
Conclusions

This research has addressed the need for a non-destructive method capable of quantifiably assessing the oxidation level of AC pavements. The results from this study have the potential to lead to a tool for pavement engineers to use to aid in cost-conscious decision making so that they may take proactive measures for the extension of pavement life.

The work presented in this report has followed a natural trajectory, starting with an investigation of the effects of oxidation on the linear acoustic properties (velocities and attenuations) of AC. It was recognized that oxidation results in the development of a diffuse microflaw population. Since nonlinear acoustic techniques are inherently more sensitive to damage, non-collinear wave mixing, a nonlinear acoustic technique, was thus employed. First, a feasibility study was performed, where samples were cut to the appropriate geometry to allow for incident mounting of the transducers for bulk wave mixing. The nonlinear acoustic technique was then extended to be applicable for field use by modifying the set-up to be one-sided, so that all measurements could be taken from the pavement surface. This was done by mounting the transducers on variable angle wedges and generating and mixing subsurface waves. Two methods were introduced to determine the appropriate the incident angle, when no linear acoustic properties are known *a priori*. Finally, this field approach was employed on aged AC specimens, treated with a rejuvenation product, to test both the feasibility of the method and the efficacy of the rejuvenator. The major results and conclusions from these investigations, which were presented in Chapters 2 through 5 of this report, will now be outlined. This chapter will conclude with some recommendations for future work.

6.1 Conclusions of Linear Characterization of AC

In Chapter 2, ultrasonic dilatational and shear velocities and corresponding attenuations were determined for a sample set of AC specimens subjected to various amounts of oxidative aging (0, 12, 24, 28, 32, and 36 hours). Shear wave propagation through such an inhomogeneous and attenuative medium as asphalt concrete poses difficulties in the measurements. During shear wave propagation, it suffers distortion, mode conversion, and attenuation due to scattering. These difficulties were

addressed by utilizing the phase-comparison method to measure the velocities, as it is less sensitive than other techniques to the effects of distortion. This work is the first to measure and report the ultrasonic shear velocities and attenuations of asphalt concrete.

With respect to aging level, the average (across frequencies) velocity increased with an increase in aging, until it reached a critical point of 24 hours, beyond which the velocity decreased with an increase in aging. The attenuations exhibited a similar trend. From 0 to 24 hours, the average attenuation coefficient was observed to decrease; beyond 24 hours, the attenuation coefficient increased with an increase in aging level. Thus, for the mix design used in this study, 24 hours of laboratory oxidative aging appears to be a critical point which divides the oxidative aging behavior of AC into two regimes. Based on these results, some observations were made. It is important to realize that the velocity is directly proportional to the stiffness. During oxidative aging, two major physical changes occur: the binder stiffness increases with aging, and the cohesive strength of the mastic decreases with an increase in aging. In the first regime, *i.e.*, below 24 hours of aging, the binder stiffness increase is the dominating mechanism on the global stiffness. In the second regime, *i.e.*, above 24 hours, the decrease in cohesive strength, which results in the development of microflaws and consequently decreases the overall stiffness, is the dominating mechanism.

It is concluded that for the mix-design used in this study, that 24 hours is the critical aging level, beyond which deterioration of the pavement rapidly accelerates. The field-aging time equivalent to 24 hours of intense laboratory oven aging seems to be a proper time to apply preventive pavement maintenance for this mixture-type. The results from the linear characterization were also necessary for the implementation of the nonlinear characterization techniques in the succeeding chapter.

Chapter 2 also contains dynamic moduli measurements, which were determined using the velocity and attenuation measurements. It was observed that the complex moduli calculated via ultrasonics do not overlap with complex moduli measured from conventional mechanical testing; however, a correlation does exist. The discrepancies between the two methods are due to the scattering effects which exist in the ultrasonic testing that are not present in mechanical testing. The shear wave measurements from the first part of the study eliminated the need for "guessing" Poisson's ratio, as is commonly done. Also, in order to eliminate the need for conventional E^* mechanical testing,

frequency dependent ultrasonic measurements must be made to calculate frequency dependent complex moduli. Similar to the velocity and attenuations, it was observed that across all frequencies, the dynamic modulus increases from 0 hours to 24 hours and decreases from 24 hours to 36 hours.

The results from the linear acoustic characteriztion correlated well with other, unrelated tests performed on specimens of the same mix/aging conditions in that they all exhibited a "critical aging time." These tests include acoustic emission and DC[T] tests.

6.2 Conclusions of Nonlinear Acoustic Characterization of AC

The asphalt concrete specimens, subjected to various amounts of laboratory-induced oven aging (0, 12, 24, 28, 32, and 36 hours), were assessed using a nonlinear ultrasonic approach involving the mixing of two dilatational waves. A nonlinear scattered shear wave was observed as a result of the interaction of two intersecting waves. The nonlinear scattered wave was able to be detected, even though the material is highly attenuative and dispersive. Criteria were used to confirm that the detected scattered waves originated via wave interaction in the asphalt concrete and not from nonlinearities in the testing instrumentation. These criteria, proposed by Johnson and Shankland [32, 33] include: 1. the frequency criterion: the frequencies must match that predicted by the theory, 2. the directionality criterion: the wave must propagate in the direction as dictated by the theory, and 3. the amplitude criterion: the scattered nonlinear wave must be proportional to the product of the amplitudes of the two primary waves.

Two metrics were used to assess the level of oxidative aging: the frequency ratio $\frac{f_2}{f_1}$ at which interaction occurred, and the nonlinear wave generation parameter $\frac{\beta}{\beta_0}$. The nonlinear wave generation parameter $\frac{\beta}{\beta_0}$ was defined to describe the conversion efficiency of energy from the primary waves into the generation of the nonlinear scattered wave. It was observed that the nonlinearities exhibited by the asphalt concrete increased exponentially with aging via the use of this nonlinear wave generation parameter. The observed nonlinear response has the potential of also being used for assessment of the aging of asphalt concrete, including durability and damage accumulation due to loading and environmental conditions.

6.3 Conclusions on One-Sided Approach

The natural extension to the results presented in Chapter 3 is to adapt the testing configuration for use in the field. This was done by altering the testing set-up to be one-sided by mounting the sending transducers on variable angle wedges for the generation of longitudinal subsurface waves. Longitudinal subsurface waves are dilatational waves which propagate close to and parallel to the surface.

The feasibility of using the non-collinear wave mixing of subsurface dilatational waves as a way to assess the amount of oxidative aging of asphalt concrete was first demonstrated. Two subsurface dilatational waves were mixed, and the resulting nonlinear scattered wave was received by a transducer placed on the same side. Thus, this technique is truly non-destructive, in that it only requires access to one side (*i.e.*, the top) of the pavement. The angle wedges must be set to an angle close to ($+1^\circ$) the first critical angle for dilatational waves to be generated, which requires knowledge of the dilatational velocity of the AC pavement. In this chapter, two methods were presented, which allow for the non-collinear wave mixing technique to be employed when the only prior knowledge of the AC pavement is the mixture type. The first method, the Iterative Incident Angle technique, involves the use of an iterative technique to find the appropriate incident angle. The second technique, the Fixed Incident Angle technique, involves the use of one fixed incident angle. For the mix-design and testing set-up used in this study, an incident angle of 73° was found to be suitable for the entire sample set. Although the second technique is less accurate than the first, it is faster and more practical for field use.

The nonlinear damage characterization curve was also introduced. This curve is generated under laboratory conditions for a particular mixture type by plotting the two nonlinear parameters $\frac{\beta}{\beta_0}$ and $\frac{f_2}{f_1}$ against each other ($\frac{\beta}{\beta_0}$ vs. $\frac{f_2}{f_1}$) to create a damage trajectory (in the range from 0 to 36 hours of oven-aging). Once this curve is generated for a particular mix-design, it need not be generated again. The idea is that a pavement engineer could take a ($\frac{\beta}{\beta_0}, \frac{f_2}{f_1}$) and plot it against the appropriate nonlinear damage characterization curve to determine the level of aging. A "blind study" was performed on specimens using both the Iterative and Fixed Incident Angle Methods to

validate the use of this curve.

6.4 Conclusions on Rejuvenator Efficacy

An application of the one-sided non-collinear wave mixing method from Chapter 4 would involve the use of nonlinear ultrasonics to assess and treat asphalt pavement surfaces (such as using penetrating rejuvenators), to retain material behavior safely in the right-hand side of the lower plateau (healing region), *i.e.*, in the 0 - 24 hour equivalent oven-aging regime. This would prevent allowing the pavement surface to age to a condition where permanent damage and the vulnerability towards large, discrete cracks (such as thermal and block cracks) occur. In Chapter 5, the one-sided non-collinear wave mixing technique was used to study the efficacy of Reclamite, an asphalt rejuvenation product.

Asphalt concrete specimens were subjected to 36 hours of laboratory-induced oxidative oven aging. The aged specimens were then coated with rejuvenator (10% by weight of the binder) and left to soak in the rejuvenator for a specific amount of time: 3 to 6 days in 1 day increments, and 1 to 8 weeks in 1 week increments. Once the dwell time reached the desired amount, the specimen was wiped of any excess rejuvenator, to improve couplant conditions, and immediately ultrasonically tested using non-collinear wave mixing of subsurface waves. The frequency ratio, $\frac{f_2}{f_1}$, at which the interaction took place and the normalized nonlinear wave generation parameter, $\frac{\beta}{\beta_0}$, were recorded and compared against a reference plot. The reference plot was created using asphalt concrete samples (with no rejuvenator) subjected to various amounts of oxidative oven aging. It was observed that the samples with a dwell time of greater than 4 weeks exhibited nonlinear characteristics similar to the reference virgin specimen. From 0.5 to 4 weeks, the nonlinear parameters become closer to the virgin parameters, indicating that the rejuvenator takes time to chemically act on the aged binder. It is difficult to know whether the observed changes in the specimens are due to a composite effect of the rejuvenator and asphalt concrete, or a result from the rejuvenator chemically acting on the aged binder. Also, the rejuvenator penetrated the specimens in a non-uniform manner, which had the effect of acting on the binder non-uniformly. The non-collinear wave mixing technique was able to capture this behavior.

6.5 Recommendations for Future Work

Based on the major results presented in this report, there are many potential avenues for beneficial future work to be performed. Some possibilities are now briefly discussed.

Studies on the shape of the damage trajectory could prove useful. As mentioned, the nonlinear damage characterization curve must be generated for each mix-design type. It is uncertain which particulars of the mix design most strongly control the shape of the nonlinear damage characterization curve, whether it be gradation, binder grade, air void content, etc. On a similar note, the nonlinear acoustic characterization of damage mechanisms other than oxidation, such as moisture damage, would prove beneficial. Additionally, the determination of the relationship between the nonlinear acoustic measurements and mechanical and thermal response of the AC mixture would be a useful study.

A more immediate study would be the design and implementation of a sensor unit for the employment of the one-sided non-collinear wave mixing technique. It is envisioned that a number of the experimental and analysis steps presented herein could be fully automated or further simplified with additional testing, validation, and development of practitioner-friendly equipment and software. A relatively low-cost, portable test system appears to be feasible, which would provide practitioners with a new and powerful tool for in-situ evaluation of asphalt pavement surfaces and strategic timing of preventive maintenance treatments.

To bring such a unit to the field, it would be necessary to take certain steps, which will now be discussed. Blind studies should be performed with the sensor unit to validate the technique. These blind studies could be performed in a similar manner as was done in Chapters 4 and 5. Field validation tests would also be necessary to verify that laboratory results translate well to the field. It would be necessary to draft and put in place a standard for testing. In order to specify such a standard, a ruggedness study [66] and repeatability study should be performed. The ruggedness study provides insight into the various testing factors that have the potential to the influence results and how much fluctuation of those factors is allowable. A standard would ensure proper calibration and testing procedures are followed for accurate and repeatable testing. The

effect of various testing conditions on the nonlinear damage characterization curve should also be quantified, such as moisture content in the pavement. Finally, as mentioned before, studies on various mixes and rejuvenation products should be carried out to understand the relationship with the nonlinear damage characterization curve.

References

[1] Y.R. Kim, *Modeling of Asphalt Concrete*. Chicago: McGraw-Hill, American Society of Civil Engineers, (2009).

[2] J. Petersen, "A Review of the Fundamentals of Asphalt Oxidation," Transportation Research Circular Number E-C140, Washington, DC: Transportation Research Board, (2009).

[3] Adi, *"The Drive Towards Self-Repairing Cities"*. Retrieved from *http://adigaskell.org/2015/10/20/the-drive-towards-self-repairing-cities/*, Accessed: April 20, 2016.

[4] M. Mirza and M. Witczak, "Development of a Global Aging System for Short and Long Term Aging of Asphalt Cements," *Journal of Association of Asphalt Paving Technologists*, vol. 64, pp. 363–430, (1995).

[5] E.R. Brown, P.S. Kandhal, F.L. Roberts, Y.R. Kim, D-Y. Lee, and T.W. Kennedy, *Hot Mix Asphalt Materials, Mixture Design, and Construction, Third Edition*. Maryland: NAPA Research and Education Foundation, (2009).

[6] J. Norambuena-Contreras, D. Castro-Fresno, A. Vega-Zamanillo, M. Celaya, and I. Lombillo-Vozmediano, "Dynamic Modulus of Asphalt Mixture by Ultrasonic Direct Test," *NDT and E International*, vol. 43, pp. 629–634, (2010).

[7] J.K. Van Velsor, L. Premkumar, G. Chehab, and J.L. Rose, "Measuring the Complex Modulus of Asphalt Concrete Using Ultrasonic Testing," *Journal of Engineering Science and Technology Review*, vol. 4, no. 2, pp. 160–168, (2011).

[8] D. Mounier, H.D. Benedetto, and C. Sauzeat, "Determination of Bituminous Mixtures Linear Properties Using Ultrasonic Wave Propagation," *Construction and Building Materials*, vol. 36, pp. 638–647, (2012).

[9] I.A. Beresnev, "Interaction of Two Spherical Elastic Waves in a Nonlinear Five-Constant Medium," *Journal of Acoustical Society of America*, vol. 94, no. 6, pp. 3400–3404, (1993).

[10] "Standard Method of Test for Determining the Dynamic Modulus of Hot Mix Asphalt (HMA)," *American Association of State Highway and Transportation Officials*, vol. AASHTO T342-11, (2011).

[11] L.E. Kinsler, A.R. Frey, A.B. Coppens, and J.V. Sanders, *Fundamentals of Acoustics*. Hoboken: John Wiley and Sons, Inc., (2000).

[12] "Standard Test Methods for Measuring Ultrasonic Velocity in Materials," *Annual Book of ASTM Standards*, vol. ASTM E494-10, (2010).

[13] M.E. McGovern, B. Behnia, W.G. Buttlar, and H. Reis, "Characterization of Oxidative Aging in Asphalt Concrete - Part 1: Ultrasonic Velocity and Attenuation Measurements and Acoustic Emission Response under Thermal Cooling," *Insight Non-Destructive Testing and Condition Monitoring Journal*, vol. 55, no. 11, pp. 596–604, (2013).

[14] L. Kleeman, *"Ultrasonic Sensors" in The Industrial Electronics Handbook*. Boca Raton: CRC Press, IEEE Press, (1996).

[15] D.R. Hull, H.E. Kautz, and A. Vary, "Ultrasonic Velocity Measurement using Phase-Slope and Cross-Correlation Methods," Denver: Spring Conference of the American Society for Nondestructive Testing, NASA Technical Memorandum, (1984).

[16] E.P. Papadakis, "Absolute Accuracy of the Pulse-Echo Overlap Method and the Pulse-Superposition Method for Ultrasonic Velocity," *Journal of Acoustical Society of America*, vol. 52, no. 3, pp. 843–846, (1972).

[17] W. Sachse, and Y-H. Pao, "On the Determination of Phase and Group Velocities of Dispersive Waves in Solids," *Journal of Applied Physics*, vol. 49, no. 1, pp. 4320–4327, (1978).

[18] D.E. Bray and R.K. Stanley, *Nondestructive Evaluation, Revised Edition*. Boca Raton: CRC Press, Inc., (1997).

[19] M.E. McGovern, B. Behnia, W.G. Buttlar, and H. Reis, "Characterization of Oxidative Aging in Asphalt Concrete - Part 2: Estimation of Complex Moduli," *Insight Non-Destructive Testing and Condition Monitoring Journal*, vol. 55, no. 11, pp. 605–609, (2013).

[20] A.F. Braham, W.G. Buttlar, T.R. Clyne, M.O. Marasteanu, and M.I. Turos, "The Effect of Long-Term Laboratory Aging on Asphalt Concrete Fracture Energy," *Journal of the Association of Asphalt Paving Technologists*, vol. 78, pp. 417–454, (2009).

[21] R.A. Guyer and P.A. Johnson, "Nonlinear Mesoscopic Elasticity: Evidence for a New Class of Materials," *Physics Today*, vol. 52, no. 4, (1999).

[22] R.A. Guyer and P.A. Johnson, *Nonlinear Mesoscopic Elasticity: The Complex Behavior of Granular Media Including Rocks and Soil*. Weinheim: Wiley-VCH, (2009).

[23] P.A. Johnson, B. Zinszner, and P.N.J. Rasolofosaon, "Resonance and Elastic Nonlinear Phenomena in Rock," *Journal of Geophysical Research*, vol. 101, no. B5, pp. 11553–11564, (1996).

[24] M.E. McGovern and H. Reis, "Damage Characterization of Dimension Stone Using Non-Collinear Ultrasonic Wave Mixing," *Optical Engineering*, vol. 55, no. 1, pp. 011012–1 – 011012–12, (2015).

[25] F.D. Murnaghan, *Finite Deformation of an Elastic Solid*. New York: John Wiley and Sons, Inc., (1951).

[26] L.D. Landau and E. M. Lifshitz, *Theory of Elasticity*. Massachusetts: Addison-Wesley Publishing Company, Inc., (1959).

[27] G.L. Jones and D.R. Kobett, "Interaction of Elastic Waves in an Isotropic Solid," *Journal of Acoustical Society of America*, vol. 35, no. 1, pp. 5–10, (1962).

[28] L.H. Taylor and F.R. Rollins, "Ultrasonic Study of Three-Phonon Interactions. I. Theory," *Physical Review*, vol. 136, no. 3A, pp. A591–A596, (1964).

[29] F.R. Rollins and L.H. Taylor, "Ultrasonic Study of Three-Phonon Interactions. II. Experimental Results," *Physical Review*, vol. 136, no. 3A, pp. A597–A601, (1964).

[30] V.A. Korneev and A. Demcenko, "Possible Second-Order Nonlinear Interactions of Plane Waves in an Elastic Solid," *Journal of Acoustical Society of America*, vol. 135, no. 2, pp. 591–598, (2013).

[31] M.E. McGovern, W.G. Buttlar, and H. Reis, "Characterization of Oxidative Aging in Asphalt Concrete using a Non-Collinear Ultrasonic Wave Mixing Approach," *Insight Non-Destructive Testing and Condition Monitoring Journal*, vol. 56, no. 7, pp. 367–374, (2014).

[32] P.A. Johnson, T.J. Shankland, R.J. O'Connell, and J.N. Albright, "Nonlinear Generation of Elastic Waves in Crystalline Rock," *Journal of Geophysical Research*, vol. 92, no. B5, pp. 3597–3602, (1987).

[33] P.A. Johnson and T.J. Shankland, "Nonlinear Generation of Elastic Waves in Granite and Sandstone: Continuous Wave and Travel Time Observations," *Journal of Geophysical Research*, vol. 94, no. B12, pp. 17729–17733, (1989).

[34] P.B. Nagy, "Fatigue Damage Assessment by Nonlinear Ultrasonic Materials Characterization," *Ultrasonics*, vol. 36, pp. 375–381, (1998).

[35] J. Couchman, B. Yee, and F. Chang, "Energy Partitioning of Ultrasonic Waves Beyond the Critical Angle Flat Boundaries," *Ultrasonics*, vol. 16, no. 6, pp. 272–274, (1974).

[36] M.A. Breazeale and L. Bjorno, "Forward and Backward Displacement of Ultrasonic Waves Relected from a Water-Sediment Interface," Proceedings Ultrasonics Intern 77, IPC Science and Technology Press, (1977).

[37] J. Couchman and J. Bell, "Prediction, Detection, and Characterization of a Fast Surface Wave Produced Near the First Critical Angle," *Ultrasonics*, vol. 12, no. 2, pp. 69–71, (1978).

[38] L. Basatskaya and I. Ermolov, "Theoretical Study of Ultrasonic Longitudinal Subsurface Waves in Solid Media," *Soviet Journal of Nondestructive Testing*, vol. 16, pp. 524–530, (1981).

[39] A. Pilarski and J. Rose, "Utility of Subsurface Longitudinal Waves in Composite Material Characterization," *Ultrasonics*, vol. 27, pp. 226–233, (1989).

[40] K. Langenberg, P. Fellinger, and R. Marklein, "On the Nature of the So-called Subsurface Longitudinal Wave and/or the Subsurface Longitudinal Creeping Wave," *Research Nondestructive Evaluation*, vol. 2, pp. 59–81, (1990).

[41] P. Junghans and D. Bray, "Beam Characteristics of High-Angle Longitudinal Wave Probes," pp. 39–44, NDE: Applications, Advanced Methods, and Codes and Standards, R N Pangborn (Ed), Proceedings of the Pressure Vessels and Piping Conference, Vol 216 of PVP, Vol 9 of NDE, ASME, (1991).

[42] T. Leon-Salamana and D. Bray, "Residual Stress Measurement in Steel Plates and Welds using Critically-Refracted Longitudinal (LCR) Waves," *Research in Non-Destructive Evaluation*, vol. 7, pp. 169–184, (1996).

[43] D. Bray and M. Dietrich, "Stress Evaluation in High-Speed Rotating Machinery with the LCR Ultrasonic Technique," pp. 143–149, Proceedings of the 26th Turbo Machinery Symposium, (1997).

[44] D. Bray and W. Tang, "Subsurface Stress Evaluation in Steel Plates and Bars using the LCR Ultrasonic Wave," *Nuclear Engineering and Design*, vol. 207, pp. 231–240, (2001).

[45] S. Chaki, W. Ke, and H. Demouveau, "Numerical and Experimental Analysis of the Critically Refracted Longitudinal Beam," *Ultrasonics*, vol. 53, pp. 65–69, (2013).

[46] M.E. McGovern, W.G. Buttlar, and H. Reis, "Estimation of Oxidative Aging in Asphalt Concrete Pavements using Non-Collinear Wave Mixing of Critically Refracted Longitudinal Waves," *Insight Non-Destructive Testing and Condition Monitoring Journal*, vol. 57, no. 1, pp. 25–34, (2014).

[47] M.E. McGovern, W.G. Buttlar, and H. Reis, "Field Estimation of Oxidative Aging in Asphalt concrete Pavements using Non-Collinear Wave Mixing," *Insight Non-Destructive Testing and Condition Monitoring Journal*, vol. 57, no. 11, pp. 1–10, (2014).

[48] I.A. Viktorov, *Rayleigh and Lamb Waves*. New York: Plenum Press, (1967).

[49] J.L. Rose, *Ultrasonic Waves in Solid Media*. New York: Cambridge University Press, (1999).

[50] A.A. Maradudin, *Surface Acoustic Waves*, pp. 395–599. New York: Plenum Press, (1985).

[51] A.A. Maradudin, *Surface Acoustic Waves on Real Surfaces*, pp. 1–66. University of California, Irvine, (1985).

[52] G.A. Maugin, *Elastic Surface Waves with Transverse Horizontal Polarization*, pp. 373–434. University of California, Irvine: Academic Press, Inc., (1983).

[53] G.A. Maugin, *Shear Horizontal Surface Acoustic Waves on Solids*, pp. 158–172. New York: Springer-Verlag, (1987.

[54] M.E. McGovern, W.G. Buttlar, and H. Reis, "Field Assessment of Oxidative Aging in Asphalt Concrete Pavements with Unknown Acoustic Properties," *Journal of Construction and Building Materials (Under Review)*.

[55] M. Mueller, "A View From the Buereau of Materials and Physical Research," Springfield: IAPA March 2015, Illinois Dept of Transportation, (2015).

[56] R.E. Boyer, "Asphalt Rejuvenators: Fact or Fable," *Asphalt Institute, Panama City, FL*, (2000).

[57] E. Buenrostro-Gonzalez, H. Groenzin, C. Lira-Galeana and O. C. Mullins, "The Overriding Chemical Principles that Define Asphaltenes," *Energy and Fuels*, vol. 15, pp. 972–978, (2001).

[58] S. N. Nahar, J. Qiu, A. Schmets, E. Schlangen, M. Shirazi, M. van de Ven, G. Schitter and A. Scarpas, "Turning Back Time: Rheological and Microstructural Assessment of Rejuvenated Bitumen," Washington, DC: Transportation Research Board 93rd Annual Meeting: Compendium of Papers, (2014).

[59] D. Oldham, E. H. Fini and T. Abu-Lebdeh, "Investigating the Rejuvenating Effect of Bio-Binder on Recycled Asphalt Shingles," Washington, DC: Transportation Research Board 93rd Annual Meeting: Compendium of Papers, (2014).

[60] *Reclamite Asphalt Rejuvenation.* Pavement Technology, Inc., Retrieved from *http://pavetechinc.com/reclamite-asphalt-rejuvenation.asp*, Accessed: January 20, 2016.

[61] A. Garcia, E. Schlangen and M. Van de Ven, "Properties of Capsules Containing Rejuvenators for Their Use in Asphalt Concrete," *Fuel*, vol. 90, pp. 583–591, (2010).

[62] E.R. Brown, "Preventative Maintenance of Asphalt Concrete Pavements," Auburn, AL: National Center for Asphalt Technology, (1988).

[63] J.W.H. Oliver, "Diffusion of Oils in Asphalts," *Industrial and Engineering Chemistry Research*, vol. 13, no. 1, pp. 65–70, (1974).

[64] M.E. McGovern, N. Farace, W.G. Buttlar, and H. Reis, "Effectiveness of Rejuvenators on Aged Asphalt Concrete using Ultrasonic Non-Collinear Subsurface Wave Mixing," *Materials Evaluation*, vol. 73, no. 10, pp. 1365–1376, (2014).

[65] M.E. McGovern, W.G. Buttlar, and H. Reis, "Nondestructive Field Evaluation of Aging Levels of Rejuvenated Asphalt Concrete Pavements," *Transportation Research Board (Under Review)*.

[66] "Standard Practice for Conducting Ruggedness Tests," *Annual Book of ASTM Standards*, vol. ASTM E1169-14, (2014).

[67] E.V. Dave, *Asphalt Pavement Aging and Temperature Dependent Properties using Functionally Graded Viscoelastic Model*. Doctoral Dissertation, University of Illinois at Urbana-Champaign, Urbana, Illinois, (2009).

[68] J. Petersen, *"Chemical Composition of Asphalt as Related to Asphalt Durability"*, pp. 363–399. In Asphaltenes and Asphalts, Developments in Petroleum Science, T.F. Yen and G.V. Chilingarian Eds., (2000).

[69] T. Fan, J. Wang, and J.S. Buckley, "Evaluating Crude Oils by SARA Analysis," Tulsa, Oklahoma: SPE/DOE Improved Oil Recovery Symposium, Society of Petroleum Engineers, Inc., (2002).

[70] L. Corbett, "Composition of Asphalt Based on Generic Fractionation, Using Solvent Deasphaltening, Elution-Adsorption Chromatography, and Densimetric Characterization," *Analytical Chemistry*, vol. 41, pp. 576–579, 1969.

[71] F. S. Rostler and R. M. White, "Rejuvenation of Asphalt Pavements," Oakland, California: Materials Research and Development, Inc., (1970).

[72] R.L. Hubbard and K.E. Stanfield, "Determination of Asphaltenes, Oils, and Resins in Asphalt," *Analytical Chemistry*, vol. 20, pp. 460–465, (1948).

[73] G. O'Donnell, "Separating Asphalt into its Chemical Constituents," *Analytical Chemistry*, vol. 23, pp. 11–20, (1951).

[74] A.J. Hoiberg and W.E. Garris, Jr., "Analytical Fractionation of Asphalts," *Analytical Edition, Industrial and Engineering Chemistry*, vol. 16, pp. 294–302, (1944).

[75] L.R. Kleinshmidt, "Chromotographic Method for the Fractionation of Asphalt into Distinctive Groups of Components," *Journal of Research of the National Bureau of Standards*, vol. 54, no. 3, pp. 163–166, (1955).

[76] K.J. Leontaritis, "Asphaltene Deposition: A Comprehensive Description of Problem Manifestations and Modeling Approaches," pp. 599–613, Society of Petroleum Engineers, SPE Production Operations Symposium, Oklahoma City, Oklahoma, (1989).

[77] D.A. Netzel, T.F. Turner, F.P. Miknis, J. Soule, and A.E. Taylor, "Molecular Dynamics and the Structure of Asphalts and Modified Asphalts at Low Temperatures," *Preprints of Papers-American Chemical Society Division Fuel Chemistry*, vol. 41, pp. 1260–1266, 1996.

[78] J. Shen, S. Amirkhanian and J. A. Miller, "Effects of Rejuvenating Agents on Superpave Mixtures Containing Reclaimed Asphalt Pavement," *Journal of Materials in Civil Engineering*, vol. 19, no. 5, pp. 376–384, (2007).

[79] H.F. Pollard, *Sound Waves in Solids*. London: Pion Limited, (1977).

[80] H. Kolsky, *Stress Waves in Solids*. New York: Dover Publications, Inc., (1963).

[81] R.S.C. Cobbold, *Foundations of Biomedical Ultrasound*. New York: Oxford University Press, Inc., (2007).

[82] I.M. Daniel and O. Ishai, *Engineering Mechanics of Composite Materials, 2nd Edition*. New York: Oxford University Press, (2006).

[83] L. Rayleigh, "On Waves Propagated Along the Plane Surface of an Elastic Solid," *Proceedings of the London Mathematical Society*, vol. s1-17, no. 1, pp. 4–11, (1885).

[84] K.F. Graff, *Wave Motion in Elastic Solids*. New York: Dover Publications, Inc., (1975).

[85] L.K. Zarembo and V.A. Krasil'nikov, "Nonlinear Phenomena in the Propagation of Elastic Waves in Solids," *Soviet Physics*, vol. 35, no. 1, pp. 778–797, (1970).

[86] S.N. Gurbatov, O.V. Rudenko, and A.I. Saichev, *Waves and Structures in Nonlinear Nondispersive Media*. New York: Higher Education Press, (2012).

[87] K.E. Van Den Abeele, J. Carmeliet, J.A. Ten Cate, and P.A. Johnson, "Nonlinear Elastic Wave Spectroscopy (NEWS) Techniques to Discern Material Damage, Part II: Single-Mode Nonlinear Resonance Acoustic Spectroscopy," *Research in Nondestructive Evaluation*, vol. 12, no. 1, pp. 31–42, (2000).

[88] F. Windels, and K. Van Den Abeele, "The Influence of Localized Damage in a Sample on its Resonance Spectrum," *Ultrasonics*, vol. 42, pp. 1025–1029, (2004).

[89] C. Payan, V. Garnier, J. Moysan, and P.A. Johnson, "Applying Nonlinear Resonant Ultrasound Spectroscopy to Improving Thermal Damage Assessment in Concrete," *The Journal of the Acoustical Society of America*, vol. 121, no. 4, pp. EL125–EL130, (2007).

[90] K.C. Kim, H. Yamawaki, J.W. Park, H.S. Jang, H.J. Kim, W.H. Hwang, and K.Y. Jhang, "Research on the Nondestructive Measurement of Nonlinear Elastic Modulus by using Ultrasonic Waves," *JSME International Journal*, vol. 44, no. 3, pp. 383–389, (2001).

[91] O. Buck, "Harmonic Generation for Measurement of Internal Stresses as Produced by Dislocations," *IEEE Transactions on Sonics and Ultrasonics*, vol. SU-23, no. 5, pp. 346–350, (1976).

[92] W.L. Morris, O. Buck, and R.V. Inman, "Acoustic Harmonic Generation Due to Fatigue Damage in High-Strength Aluminum," *Journal of Applied Physics*, vol. 50, no. 11, pp. 6737–6742, (1979).

[93] A. Hikata, F.A. Sewell, and C. Elbaum, "Generation of Ultrasonic Second and Third Harmonics due to Dislocations. II," *Physical Review*, vol. 151, no. 2, pp. 442–449, (1966).

[94] J.H. Cantrell and W.T. Yost, "Determination of Precipitate Nucleation and Growth Rates from Ultrasonic Harmonic Generation," *Applied Physics Letters*, vol. 77, no. 13, pp. 1952–1954, (2000).

[95] Z.A. Gol'dberg, "Interaction of Plane Longitudinal and Transverse Elastic Waves," *Soviet Physical Acoustics*, vol. 6, no. 3, pp. 306–310, (1960).

[96] K.R. McCall, "Theoretical Study of Nonlinear Elastic Wave Propagation," *Journal of Geophysical Research*, vol. 99, no. B2, pp. 2591–2600, (1994).

[97] V.E. Nazarov, L.A. Ostrovsky, I.A. Soustova, and A.M. Sultin, "Nonlinear Acoustics of Micro-Inhomogeneous Media," *Physics of the Earth and Planetary Interiors*, vol. 50, pp. 65–73, (1987).

[98] I.A. Beresnev, "Interaction of Two Spherical Elastic Waves in a Nonlinear Five-Constant Medium," *Journal of Acoustical Society of America*, vol. 94, no. 6, pp. 3400–3404, (1993).

[99] V. Gusev, "Theory of Non-Collinear Interactions of Acoustic Waves in an Isotropic Material with Hysteretic Quadratic Nonlinearity," *Journal of Acoustical Society of America*, vol. 111, no. 1, pp. 80–94, (2001).

[100] V. Gusev, "Quasi-Synchronous Excitation of Acoustic Waves in Materials with Hysteretic Quadratic Nonlinearity," *Wave Motion*, vol. 38, pp. 241–250, (2003).

[101] D.S. Hughes and J.L. Kelly, "Second-Order Elastic Deformation of Solids," *Physical Review*, vol. 92, no. 5, pp. 1145–1149, (1953).

[102] N.S. Shiren, "Nonlinear Acoustic Interaction in MgO at 9Gc/sec," *Physical Review Letters*, vol. 11, no. 1, pp. 3–6, (1963).

[103] F.R. Rollins Jr., "Interaction of Ultrasonic Waves in Solid Media," *Applied Physics Letters*, vol. 2, no. 8, pp. 147–148, (1965).

[104] J.D. Childress and C.G. Hambrick, "Interactions Between Elastic Waves in an Isotropic Solid," *Physical Review*, vol. 136, no. 2A, pp. A411–A418, (1964).

[105] F.R. Rollins, "Phonon Interactions at Ultrasonic Frequencies," *Proceedings of the IEEE*, vol. 53, no. 10, pp. 1534–1539, (1965).

[106] V.A. Krasilnikov and L.K. Zarembo, "Nonlinear Interaction of Elastic Waves in Solids," *IEEE Transactions on Sonics and Ultrasonics*, vol. SU-14, no. 1, pp. 12–17, (1967).

[107] R.W. Dunham, and H.B. Huntington, "Ultrasonic Beam Mixing as a Measure of the Nonlinear Parameters of Fused Silica and Single-Crystal NaCl," *Physical Review*, vol. 2, no. 4, pp. 1098–1107, (1970).

[108] Y. Hiki and K. Mukai, "Ultrasonic Three-Phonon Process in Copper Crystal," *Journal of the Physical Society of Japan*, vol. 34, no. 2, pp. 454–461, (1973).

[109] L.A. Ostrovsky, "Wave Processes in Media with Strong Acoustic Nonlinearity," *Journal of Acoustical Society of America*, vol. 90, no. 6, pp. 3332–3337, (1991).

[110] X. Liu, "Nonlinear Elasticity, Seismic Anisotropy, and Petrophysical Properties of Reservoir Rocks." PhD Dissertation, Stanford University, (1994).

[111] V.A. Korneev, *"Time Domain Solutions for Nonlinear Elastic 1-D Plane Wave Propagation"*. Report: LBL-37411, Ernest Orlando Lawrence Berkeley National Laboratory, (1998).

[112] V.A. Korneev, K.T. Nihei, and L.R. Myer, *"Nonlinear Interaction of Plane Elastic Waves"*. Report: LBNL-41914, Ernest Orlando Lawrence Berkeley National Laboratory, (1998).

[113] A.J. Croxford, P.D. Wilcox, B.W. Drinkwater, and P.B. Nagy, "The Use of Non-Collinear Mixing for Nonlinear Ultrasonic Detection of Plasticity and Fatigue," *The Journal of Acoustical Society of America*, vol. 126, no. 5, pp. EL117–EL122, (2009).

[114] J. Lin, P. Guo, L. Wan and S. Wu, "Laboratory investigation of rejuvenator seal materials on performances of asphalt mixtures," *Construction and Building Materials*, vol. 37, pp. 25–41, (2012).

[115] G. Tang, M. Liu, L.J. Jacobs, and J. Qu, "Detecting Localized Plastic Strain by a Scanning Collinear Wave Mixing Method," *Journal of Nondestructive Evaluation*, vol. 32, no. 4, pp. 1–9, (2013).

[116] V. Koissin, A. Demcenko, and V.A. Korneev, "Isothermal Epoxy-Cure Monitoring using Nonlinear Ultrasonics," *International Journal of Adhesion and Adhesives*, vol. 52, pp. 11–18, (2014).

[117] A. Demcenko, R. Akkerman, P.B. Nagy, and R. Loendersloot, "Non-Collinear Wave Mixing for Nonlinear Ultrasonic Detection of Physical Aging in PVC," *NDT and E International*, vol. 49, pp. 34–39, (2013).

[118] A. Demcenko, L. Mainini, and V.A. Korneev, "A Study of the Nonlinear Ultrasonic Wave-Mixing Technique Under Imperfect Resonance Conditions," *Ultrasonics*, vol. 57, pp. 179–189, (2015).

[119] P. Blanloeuil, A. Meziane, and C. Bacon, "2D Finite Element Modeling of the Non-Collinear Mixing Method for Detection and Characterization of Closed Cracks," *NDT and E International*, vol. 76, pp. 43–51, (2015).

[120] M.A. Breazeale, "Whither Nonlinear Acoustics," *Review of Progress in Quantitative Nondestructive Evaluation*, vol. 9, pp. 1653–1660, (1990).

[121] I.A. Viktorov, "Types of Acoustic Surface Waves in Solids (Review)," *Soviet Physical Acoustics*, vol. 25, no. 1, pp. 1–9, (1979).

[122] A.E.H. Love, *Some Problems of Geodynamics.* Cambridge: Cambridge University Press, (1911).

[123] S.N. Bhattacharya, "Exact Solutions of SH Wave Equation for Inhomogeneous Media," *Bulletin of the Seismological Society of America*, vol. 60, no. 6, pp. 1847–1859, (1970).

[124] R.E. Camley, B. Djafari-Rouhani, L. Dobrzynski, and A.A. Maradudin, "Transverse Elastic Waves in Periodically Layered Infinite and Semi-Infinite Media," *Physical Review B*, vol. 27, no. 12, pp. 7318–7329, (1983).

[125] J.E. Gubernatis and A.A. Maradudin, "A Laguerre Series Approach to the Calculation of Wave Properties for Surfaces of Inhomogenous Elastic Materials," *Wave Motion*, vol. 9, pp. 111–121, (1987).

[126] P. Kielczynski and W. Pajewski, "Determination of the Depth of a Non-Homogenous Surface Layer in Elastic Materials Using Shear Surface Acoustic Waves," *NDT International*, vol. 18, no. 1, pp. 25–29, (1985).

[127] I.A. Viktorov, "Surface Waves on Cylindrical Crystal Surfaces," *Soviet Physical Acoustics*, vol. 20, no. 2, pp. 123–127, (1974).

[128] B.A. Auld and B-H Yeh, "Theory of Surface Skimming SH Wave Guidance by a Corrugated Surface," in *Ultrasonics Symposium*, pp. 786–790, (1979).

[129] O. Hardouin Duparc and A.A. Maradudin, "Roughness-Trapped Shear Horizontal Surface Acoustic Waves," *Journal of Electron Spectroscopy and Related Phenomena*, vol. 30, pp. 145–150, (1983).

[130] D.E. Chimenti and O.I. Lobkis, "Effect of Rough Surfaces on Guided Waves in Plates," *Review of Progess in Quantitative Nondestructive Evaluation*, vol. 17, pp. 129–136, (1998).

[131] D. H. Simpson, C. T. Chin, and P. N. Burns, "Pulse Inversion Doppler: A New Method for Detecting Nonlinear Echoes from Microbubble Contrast Agents," *IEEE Transactions on Ultrasonics, Ferroelectrics, and Frequency Control*, vol. 46, no. 2, pp. 372–382, (1999).

[132] G. Tang, M. Liu, L. J. Jacobs, J. Qu, "Detecting Localized Plastic Strain by a Scanning Collinear Wave Mixing Method," *Journal of Nondestructive Evaluation*, vol. 32, no. 4, pp. 1–9, (2014).

Appendix A
Oxidative Aging of Asphalt

Figure A.1: Freshly laid pavement section (left) and after 19 months (right) of environmental exposure at the University of Illinois' Advanced Testing and Research Engineering Laboratory (ATREL). Figure extracted from [67].

During the oxidative aging process, AC pavements undergo complex chemical and physical alterations, resulting in a change in material properties. This is apparent in Figure A.1, which shows a pavement at the University of Illinois' Advanced Testing and Research Engineering Laboratory (ATREL) after it was freshly laid (left) and after 19 months (right). The resulting color change is very aparent. Perhaps not quite as apparent from the photo is the change in surface texture. The aim of this chapter is to provide a fundamental background on this phenomena as it pertains to the primary investigation (nondestructive assessment of oxidative aging level.)

Much of the following discussion was obtained from Petersen [2, 68], who describes the chemical composition and structure of asphalt and the oxidation process in great detail. The reader is strongly encouraged to review these reports for a complete discussion on the topic. Here, only the aspects important to the current investigation will be discussed. Since oxidation affects the binder portion of the composite AC, a fundamental understanding of the structure of asphalt is thus required. This chapter will begin with a description on the basic structure of asphalt, followed by a review of the oxidative aging process, where the chemical and physical changes of asphalt during oxidatation will be presented. Finally, a brief discussion on laboratory long-term aging will be provided.

A.1 Basic Structure of Asphalt

Asphalt, at ambient temperatures, is a sticky, viscoelastic substance. At cooler temperatures, it is more solid and elastic. At warmer temperatures, it liquefies. It may be naturally occurring or produced via refining crude petroleum during the distillation process. The latter is the most common source of asphalt in the modern day, owing to the prevalence of oil refineries since the rise in popularity of automobiles [5].

Asphalt molecules are primarily composed of carbon and hydrogen, with one or more heteroatom (nitrogen, sulfer, oxygen) and trace amounts of metals (vanadium and nickel). Heteroatoms are responsible for the polarity and functionality of the molecules, and they contribute largely to the differences in chemical and physical properties among asphalts from different sources. This elemental composition of asphalt, however, does not shed much light on its behavioral properties. Rather, the molecular types and structures govern the physical properties and chemical reactivity of the asphalt material.

A.1.1 Asphalt Fractions

It is widely accepted that asphalt is a complex colloidal system, and not a solution, consisting of a varied array of molecular types. Owing to this extremely complex and diverse nature, asphalts are typically characterized via fractionation schemes, in lieu of separating and identifying the complete set of molecules. In fractionation schemes, asphalt constituents are grouped based on their chemical functionalities. Petersen [2, 68] provides more detail on some of these fractionation procedures.

The SARA analysis is one common fractionation scheme [69] used in the petroleum industry, which separates asphalt into saturates, aromatics, resins, and asphaltenes. Another widely used fractionation scheme, introduced by Corbett [70], divides asphalt into four functional groups, which, in order of increasing polarity, are: saturates, napthene aromatics, polar aromatics, and asphaltenes. Of course, many other fractionation schemes exist [68, 71–75], and the two aforementioned contain overlapping/equivalent functional groups. The fractionation scheme by Rostler and White [71] is not commonly used in industry; however, fractions from this scheme are commonly referred to in

the literature when discussing the microstructural makeup of asphalt. The five Rostler and White fractions are: asphaltenes, nitrogen bases, first acidaffins, second acidaffins, and paraffins.

It is important to note that functional groups are named so to describe the predominant function of that group; however, each of these groups are highly complex mixtures. Corbett [70] recognized that all fractions of the binder play an important role in the overall properties. The behavior of binder is thus the combined total of the individual contributions of the various fractions as well as their relative interactions. The relative proportions of the various fractions play a key role in the overall binder material properties. Corbett's generic asphalt fractions are now briefly outlined.

Saturates The Corbett saturates fraction, sometimes termed the paraffins fraction [71], is a colorless oil comprised of unpolarized functional groups. It is primarily composed of saturated hydrocarbons and has a low chemical reactivity.

Napthene Aromatics The Corbett napthene aromatic fraction is a yellow to red liquid, which contains condensed nonaromatic and aromatic ring systems. This fraction overlaps with Rostler's first and second acidaffins fractions.

Polar Aromatics The Corbett polar aromatics fraction is a black solid, which contains highly condensed aromatic ring systems and heteroatom functional groups. This fraction overlaps with the resins fraction from the SARA fractionation and Rostler's [71] Nitrogen bases and first acidaffins fractions.

Asphaltenes The asphaltene fraction is a brown to black solid. It is insoluble in nonpolar paraffinic solvents such as n-Butanol, n-Heptane, and n-Pentane; thus, it is insoluble in much of the remaining fractions of asphalt. This fraction is the most polar of Corbett's fractions. Many fractionation schemes of asphalt begin by first partitioning off the asphaltenes fraction.

A.1.2 Molecular Structure of Asphalt

Asphaltenes form molecular agglomerates via molecular association (hydrogen bonding and dipole interactions) between the polar components of the asphalt. These agglomerates are stabilized and

dispersed by highly polarized resins (the Corbett polar aromatics fraction), which act as stabilizing peptizers on the surface of the asphaltenes (see Figure A.2). Thus, asphalt is a colloidal suspension of molecular agglomerates in oil. These agglomerates are similar in size to polymer molecules at ambient temperatures. Owing to this structure, asphalts exhibit "polymeric" type properties. Of course, asphalt differs greatly from polymers in that it contains many molecules of differing types (polymers are formed of chains of repeating units held together by chemical bonds.) The bonding forces in the agglomerates are temperature susceptible. At high temperatures, the bonds are broken, effectively reducing the agglomerate size. At lower temperatures, the bonds again form. The temperature susceptibility of these bonding forces imputes a temperature dependence on the asphalt as a whole [77].

Corbett described the function of the asphaltene fraction as the thickener. The saturate and napthene aromatics fractions serve as the gelling agent to the peptized asphaltenes, and as such, impart fluidity to the binder.

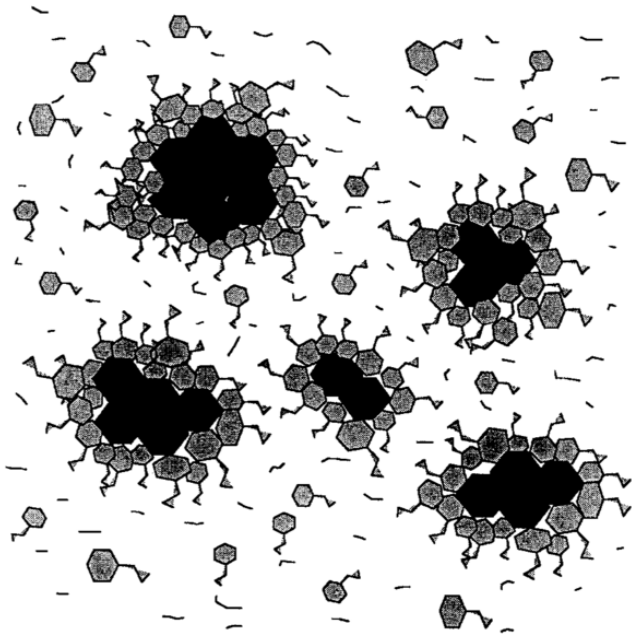

Figure A.2: Asphalt is a colloidal suspension of asphaltenes (denoted by the black) susepended in oil. Highly polarized resins (denoted by the gray) act as the stabilizing peptizers on the surface of the asphaltenes. Extracted from [76].

If asphaltenes are separated from the asphalt mixture, what remains is a petrolene fraction, commonly referred to as "maltenes." The relative proportions of the asphaltenes and maltenes fractions directly influences the rheological properties of asphalt. A higher asphaltene-to-maltene ratio results in a stiffer binder.

The rheological properties of asphalt are very important to its structural performance. A durable asphalt binder is one where the asphaltenes are properly dispersed for compatibility. Compatibility requires appropriate proportions of each fraction.

Asphalts rheological properties are directly based on the molecular dynamics of the system. Molecular interactions (or association) restrict motion, resulting in a harder and stiffer binder. Stronger molecular interactions will result in a higher viscosity. Since the saturate fraction exhibits only weak interaction forces, it is a relatively low viscosity fluid. Resins, on the other hand, which contain polarizable aromatic systems and heteroatom functionality, exhibit strong association forces and hence have a much higher viscosity.

A.2 Oxidative Aging Process

Asphalt experiences its first significant oxidative aging during construction, when it is exposed to high temperatures (135 to 165°C) during the mixing process. This is short term aging. In service conditions, the pavement is exposed to air at much more ambient temperatures. While the process is slower, over time, it can have significant affects. This is the long term aging process. To prepare AC samples that reflect the properties of pavements with long term oxidative aging, the standard procedure is to subject the loose mixture to high-temperature oxygen via a force draft oven. A study by Braham et al. [20] showed that 24-hours of oven-aging represented approximately 7 years of field aging (for a similar mixture to the one used in this study).

Balance, *i.e.*, compatibility, in structure of asphalt (well dispersed, appropriate proportions of fractions) is very important to the performance properties of asphalt, as outlined in the previous section. A well balanced asphalt is more durable and resistant to the effects of oxidative aging. Oxidative aging perturbs this balance, and as a result, the asphalt becomes increasingly less resis-

tant to further oxidation effects: a compounding effect. The rheological properties of the oxidized binder are altered from their original design state.

A.2.1 Oxidative Hardening

Oxidative hardening is the chief deleterious effect of binder oxidation, which causes an increased binder stiffness and ultimately leads to pavement embrittlement (reduced cracking resistance, and reduced self-healing capacity.) It is mainly caused by the introduction of polar chemical functionalities on asphalt molecules, which enhance molecular interactions. The primary physical changes that contribute to oxidative hardening during oxidation are: 1. the loss of oily components, 2. chemical reactions with the oxygen (resulting in chemical compositional changes of the asphalt molecules), and 3. thixotropic effects via molecular structuring. The latter is a reversible phenomenon caused via molecular structuring of the binder molecules. Asphalt is a thixotropic material and forms a structure over periods of time, which results in thixotropic, or steric, hardening. Mechanical loading, such as traffic, breaks these bonds, essentially reversing the phenomenon. For this reason, steric hardening is typically only observed in rarely traveled and abandoned pavements, and is not considered to strongly contribute to long term aging effects on well-traveled roadways.

Oxidative hardening during oxidation can chiefly be attributed to the first two listed physical changes, as these two contribute the most to rheological changes on in-service roads. The first, the loss of oily components (e.g. the saturates fraction), may be due to volatility or absorption by porous aggregates. Volatilization, *i.e.*, evaporation of lighter constituents, is a mostly a function of temperature. Since the oily components impart fluidity to the asphalt, a loss in these components will serve to increase the viscosity. The resulting effect is a stiffer binder with a lessened capacity for self-healing.

The second, owing changes in chemical composition of asphalt molecules from reaction with atmospheric oxygen, affects the molecular dynamics of the binder. Recall that the temperature dependent properties of asphalt can be attributed to molecular dynamics, where at cold temperatures, molecular association (due to intermolecular bonds) restricts molecular motions. Chemical reactions between the oxygen and binder also enhances molecular association by forming polar

functional groups. Ketones and sulfoxides are the major oxidation products (as identified by functional group analysis in Petersen [2]). Carboxylic acids and anhydrides are also formed, but in much smaller amounts. The types of oxidation products formed do not depend on the source of the asphalt; however, the concentrations do. An increase in the concentration of these polar functional groups results in enhanced molecular associations, which restricts the relative flow of the asphalt molecules and molecular agglomerates under thermal or mechanical stresses. This restricted motion is the principle characteristic of an embrittled pavement, and causes the asphalt to be susceptible to fracture and resistant to self-healing.

A.2.2 Asphaltenes-to-Maltenes Ratio

The various fractions have differing degrees of reactivity with oxygen. The saturates fraction is resistive to oxidation at ambient temperatures, due to low chemical reactivity. The remaining fractions, however, do react with oxygen (albeit differently). Naphthene aromatics are slightly reactive; whereas, polar aromatics and asphaltenes are highly reactive with oxygen. The net result, is that oxidation causes a loss in naphthene aromatics and polar aromatics, while increasing the asphaltenes fraction. In industry, it is common to quantify this net change in terms of the asphaltenes-to-maltenes ratio, where maltenes refer to the non-asphaltenes fractions of the asphalt.

It has been recognized that a higher asphaltenes-to-maltenes ratio directly influences the rheology of the binder and corresponds to a stiffer and more brittle binder. In fact, effective rejuvenators address the issue of oxidative hardening by softening the aged asphalt via the restoration of the original asphaltenes-to-maltenes ratio [57, 61, 78].

While the asphaltene-to-maltene ratio is commonly referred to in the literature as a durability predictor of asphalt, Petersen stressed an important idea. Experimental results indicate that the asphalt's component balance, which controls the sensitivity to the oxidation products, may be more important than the actual amount of the oxidation product. As a result, not all binders age in the same manner upon exposure to oxygen. This makes intuitive sense when realizing how chemically varied asphalt is from source to source. For this reason, Petersen notes that the generic fraction ratios are not necessarily an accurate predictor of the durability of asphalt with respect to oxditive

aging.

Regardless, a proper balance of different asphalt constituents is necessary to resist oxidation. Asphaltenes must be properly dispersed by the resinous components for proper compatibility and hense durability.

Appendix B
Fundamentals of Linear Acoustics in Solid Media

In order to understand nonlinear acoustics, the fundamentals of linear acoustics must be understood. The aim of this chapter is to provide the necessary background for the nonlinear theory subsequently presented in this document; however, it is by no means comprehensive. Several great texts exist, which provide strong, detailed fundamentals on the subject of acoustics [11, 26, 49, 79–81]. Here, the linear acoustic wave equation will be derived. Then, some basic fundamental relationships will be provided.

B.1 The Strain Tensor

The following discussion on the strain tensor will follow closely the discussion presented by Landau and Lifshitz [26]. Consider a point P in an undeformed body, where its position is defined by the radius vector $\boldsymbol{r}$. If the body is then deformed, the position of P is defined by a new radius vector $\boldsymbol{r'}$. The radius vectors in the undeformed and deformed cases have components x_i and x'_i, respectively. The displacement vector can thus be written as,

$$\boldsymbol{u} = \boldsymbol{r'} - \boldsymbol{r} \tag{B.1}$$

or in index notation,

$$u_i = x'_i - x_i \tag{B.2}$$

Refer to Figure B.1. Now, consider a point Q close to point P in the undeformed body. The radius vector joining these two points has components $\mathrm{d}x_i$. Similarly, these same two points after deformation of the body will have a vector between them with components $\mathrm{d}x'_i$, where,

$$\mathrm{d}x'_i = \mathrm{d}x_i + \mathrm{d}u_i \tag{B.3}$$

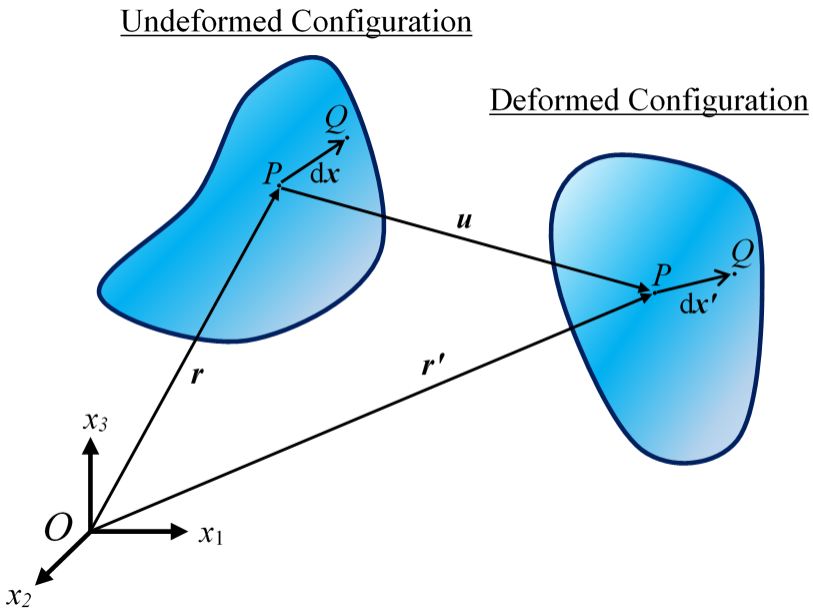

Figure B.1: Geometry of an arbitrary body in the deformed and undeformed states.

The distance between the two points in the undeformed body is denoted as $\mathrm{d}l$,

$$\begin{aligned} \mathrm{d}l &= \sqrt{\sum_{i=1}^{3} \mathrm{d}x_i^2} \\ \Rightarrow \mathrm{d}l^2 &= \sum_{i=1}^{3} \mathrm{d}x_i^2 \end{aligned} \tag{B.4}$$

Similarly, for the deformed body, the distance between the two points is denoted by $\mathrm{d}l'$. Along with Equation B.3,

$$\mathrm{d}l' = \sum_{i=1}^{3} \mathrm{d}x_i'^2 = \sum_{i=1}^{3} (\mathrm{d}x_i + \mathrm{d}u_i)^2 \tag{B.5}$$

From this point forward, the Einstein summation convention will be used, where a repeated index indicates summation. Since the displacement is only a function of the coordinates x_i, the following relationship holds,

$$\begin{aligned} \frac{\mathrm{d}u_i}{\mathrm{d}x_k} &= \frac{\partial u_i}{\partial x_k} \\ \Rightarrow \mathrm{d}u_i &= \frac{\partial u_i}{\partial x_k} \mathrm{d}x_k \end{aligned} \tag{B.6}$$

Plugging Equations B.4 and B.6 into B.5, and noting that,

$$\frac{\partial u_i}{\partial x_k}\frac{\partial u_i}{\partial x_l}\mathrm{d}x_k\mathrm{d}x_l = \frac{\partial u_l}{\partial x_k}\frac{\partial u_l}{\partial x_i}\mathrm{d}x_k\mathrm{d}x_i \tag{B.7}$$

yields,

$$\mathrm{d}l'^2 = \mathrm{d}l^2 + 2\left[\frac{\partial u_i}{\partial x_k} + \frac{\partial u_k}{\partial x_i} + \frac{\partial u_l}{\partial x_k}\frac{\partial u_l}{\partial x_i}\right]\mathrm{d}x_k\mathrm{d}x_i \tag{B.8}$$

The quantity contained in the square brackets is the generalized strain tensor and is denoted by ε_{ik}.

$$\varepsilon_{ik} = \frac{1}{2}\left(\frac{\partial u_i}{\partial x_k} + \frac{\partial u_k}{\partial x_i} + \frac{\partial u_l}{\partial x_k}\frac{\partial u_l}{\partial x_i}\right) \tag{B.9}$$

In linear elasticity, the third term is assumed to be small and thus dropped to obtain,

$$\varepsilon_{ik} = \frac{1}{2}\left(\frac{\partial u_i}{\partial x_k} + \frac{\partial u_k}{\partial x_i}\right) \tag{B.10}$$

The above expression is the linear strain tensor, and it is symmetric so that $\varepsilon_{ij} = \varepsilon_{ji}$.

B.2 The Stress Tensor

Please refer to Landau and Lifshitz [26] for a good discussion on the fundamentals of the theory of elasticity. When an undeformed body is in equilibrium, the net resultant of the forces on that body are zero. If deformation occurs, the body is no longer in the original state of equilibrium, and internal forces arise to keep the body in an equilibrium state. These internal forces are termed internal stresses. The total force on a portion of the body is equal to the summation of all of the forces on the volume elements $\mathrm{d}V$ in that portion of the body. Thus, the total force can be written as,

$$\boldsymbol{F}_{Total} = \int_V \boldsymbol{F}\mathrm{d}V \tag{B.11}$$

where $\boldsymbol{F}$ is the force per unit volume, and $\boldsymbol{F}\mathrm{d}V$ is the force on the volume element $\mathrm{d}V$. Using the divergence theorem, the volume integral from above can be transformed to a surface integral as

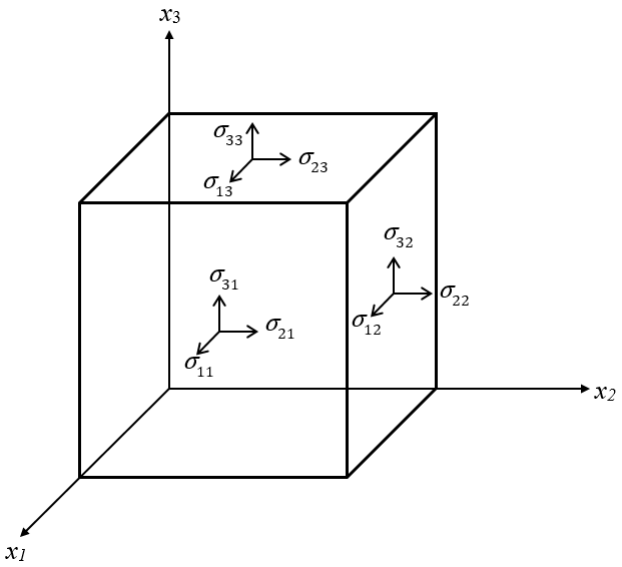

Figure B.2: Components of the stress tensor σ_{ik} acting on a small rectangular volume element.

long as the vector is the divergence of a second-order tensor. So, F_i must be of the following form,

$$F_i = \frac{\partial \sigma_{ik}}{\partial x_k} \tag{B.12}$$

Then, using the divergence theorem,

$$\int F_i \mathrm{d}V = \int \frac{\partial \sigma_{ik}}{\partial x_k} = \oint \sigma_{ik} \mathrm{d}f_k \tag{B.13}$$

where $\mathrm{d}\boldsymbol{f}$ is pointed in the direction of the outward normal, and σ_{ik} is the stress tensor. Please refer to Figure B.2, which shows the components of the stress tensor acting on a small rectangular volume element. To obtain a useful (for the purposes of deriving the nonlinear equations of motion) expression for the stress tensor, consider the work done on a deformed body by the internal stresses. The deformation is such that u_i changes by a small amount δu_i. The work done by internal stresses per unit volume is thus,

$$\delta R = F_i \delta u_i \tag{B.14}$$

Using Equations B.12 and B.13 and integrating over the volume of the body yields,

$$\int \delta R \mathrm{d}V = \oint \sigma_{ik} \delta u_i \mathrm{d}V - \int \sigma_{ik} \frac{\partial \delta u_i}{\partial x_k} \mathrm{d}V \tag{B.15}$$

For an infinite medium, where there is no deformation at infinity, the surface integral in the above equation goes to zero. Thus,

$$\begin{aligned} \int \delta R \mathrm{d}V &= -\int \sigma_{ik} \left(\frac{\partial \delta u_i}{\partial \delta x_k} \right) \mathrm{d}V \\ &= -\int \sigma_{ik} \delta \left(\frac{\partial u_i}{\partial x_k} \right) \mathrm{d}V \\ \Rightarrow \delta R &= -\sigma_{ik} \delta \left(\frac{\partial u_i}{\partial x_k} \right) \end{aligned} \tag{B.16}$$

From thermodynamics,

$$\mathrm{d}U = T\mathrm{d}S - \mathrm{d}R \tag{B.17}$$

where, U is the internal energy, T is temperature, and S is entropy. Using the expression for the work from Equation B.16,

$$\mathrm{d}U = T\mathrm{d}S + \sigma_{ik}\mathrm{d}\left(\frac{\partial u_i}{\partial x_k} \right) \tag{B.18}$$

For constant entropy, a useful relation for the stress tensor is then,

$$\sigma_{ik} = \frac{\mathrm{d}U}{\mathrm{d}\left(\frac{\partial u_i}{\partial x_k} \right)} \tag{B.19}$$

When the material is linear elastic, this is equivalent to,

$$\sigma_{ik} = \frac{\mathrm{d}U}{\mathrm{d}\varepsilon_{ik}} \tag{B.20}$$

B.3 Generalized Hooke's Law

For a linearly elastic material, the expression in Equation B.20 is linear in ε_{ik}. The most general form of Hooke's law is therefore a linear relationship between the stress and strain tensors,

$$\sigma_{ik} = c_{iklm}\varepsilon_{lm} \tag{B.21}$$

where c_{iklm} is the elastic constant (or stiffness) tensor. The elastic constant tensor is a fourth rank tensor, and for the most general case, has 81 independent components. The number of independent constants can be reduced by exploiting symmetry. Since the stress tensor σ_{ik} and strain tensor ε_{lm}

are symmetric, then,

$$\begin{aligned} c_{iklm} &= c_{kilm} \\ c_{iklm} &= c_{ikml} \end{aligned} \tag{B.22}$$

Furthermore, using energy considerations [26, 79] yields,

$$c_{iklm} = c_{lmik} \tag{B.23}$$

With these conditions, the number of independent elastic constants is reduced to 21 for a general anisotropic body. The number of elastic constants can be further reduced by considering the crystal system of the medium. Here, the simplest case of an isotropic material is considered, which has two independent constants [82]. The components of the elastic constant tensor are shown in matrix form for an isotropic material below,

$$[\boldsymbol{c}] = \begin{pmatrix} c_{11} & c_{12} & c_{12} & 0 & 0 & 0 \\ c_{12} & c_{11} & c_{12} & 0 & 0 & 0 \\ c_{12} & c_{12} & c_{11} & 0 & 0 & 0 \\ 0 & 0 & 0 & \frac{1}{2}(c_{11} - c_{12}) & 0 & 0 \\ 0 & 0 & 0 & 0 & \frac{1}{2}(c_{11} - c_{12}) & 0 \\ 0 & 0 & 0 & 0 & 0 & \frac{1}{2}(c_{11} - c_{12}) \end{pmatrix} \tag{B.24}$$

where,

$$\begin{aligned} c_{11} &= \lambda + 2\mu \\ c_{12} &= \lambda \end{aligned} \tag{B.25}$$

and λ and μ are the Lamé constants. Hooke's law (from Equation B.21) for a linear, elastic, isotropic material can then be written in terms of the elastic constants as,

$$\sigma_{ik} = 2\mu\varepsilon_{ik} + \lambda\varepsilon_{jj}\delta_{ik} \tag{B.26}$$

B.4 Wave Propagation in Linear Elastic Solid Media

The equations of motion are determined by equating the resultant forces acting on a small volume to the product of the acceleration with the mass per unit volume. Using the expression for the resultant forces from Equation B.12 and neglecting the body forces yields the equations of motion,

$$\rho \frac{\partial^2 u_i}{\partial t^2} = \frac{\partial \sigma_{ik}}{\partial x_k} \tag{B.27}$$

Then, Hooke's law from Equation B.26 can be plugged into Equation B.27,

$$\rho \frac{\partial^2 u_i}{\partial t^2} = \mu \frac{\partial^2 u_i}{\partial x_k^2} + (\lambda + \mu) \frac{\partial^2 u_k}{\partial x_i \partial x_k} \tag{B.28}$$

Equation B.28 is the three-dimensional linear elastic wave equation for wave propagation in solid media. It can be written in vector notation as,

$$\rho \ddot{\boldsymbol{u}} = (\lambda + \mu) \boldsymbol{\nabla} \boldsymbol{\nabla} \cdot \boldsymbol{u} + \mu \boldsymbol{\nabla}^2 \boldsymbol{u} \tag{B.29}$$

B.4.1 Dilatational and Shear Waves

In this manuscript, waves with polarizations in the direction of propagation, *i.e.*, compressional waves, will be referred to as dilatational or longitudinal waves. Waves with polarizations orthogonal to the direction of propagation will be referred to as shear or transverse waves.

The following vector identity,

$$\boldsymbol{\nabla}^2 \boldsymbol{u} = \boldsymbol{\nabla} \boldsymbol{\nabla} \cdot \boldsymbol{u} - \boldsymbol{\nabla} \times \boldsymbol{\nabla} \times \boldsymbol{u} \tag{B.30}$$

can be substituted into Equation B.29 to obtain another form of the linear wave equation as,

$$\rho \ddot{\boldsymbol{u}} = (\lambda + 2\mu) \boldsymbol{\nabla} (\boldsymbol{\nabla} \cdot \boldsymbol{u}) - 2\mu \boldsymbol{\nabla} \times \left(\frac{1}{2} \boldsymbol{\nabla} \times \boldsymbol{u} \right) \tag{B.31}$$

The advantage to this form of the equation is that the dilatational and rotational portions of the wave are separated. This is realized by noting that the dilatation of the material is defined by $\boldsymbol{\nabla} \cdot \boldsymbol{u}$

and the rotation is defined by $\frac{1}{2}\boldsymbol{\nabla} \times \boldsymbol{u}$. Using the following,

$$\begin{aligned} \boldsymbol{\nabla} \cdot \boldsymbol{\nabla} &\approx \boldsymbol{\nabla}^2 \\ \boldsymbol{\nabla} \cdot (\boldsymbol{\nabla}^2 \boldsymbol{u}) &= \boldsymbol{\nabla}^2 (\boldsymbol{\nabla} \cdot \boldsymbol{u}) \end{aligned} \tag{B.32}$$

the divergence vector operation can be performed on Equation B.31, which yields,

$$\rho \boldsymbol{\nabla} \ddot{\boldsymbol{u}} = (\lambda + 2\mu) \boldsymbol{\nabla}^2 (\boldsymbol{\nabla} \cdot \boldsymbol{u}) \tag{B.33}$$

Thus, only the dilatational component $(\boldsymbol{\nabla} \cdot \boldsymbol{u})$ remains. The above equation is recognized to be of the form of the equation of motion in Equation B.27. Therefore, the dilatational velocity given by,

$$c_L = \sqrt{\frac{\lambda + 2\mu}{\rho}} \tag{B.34}$$

A similar procedure can be done to obtain the shear wave velocity. Now, the curl operation can be performed on Equation B.31 to yield,

$$\mu \boldsymbol{\nabla}^2 \left(\frac{1}{2} \boldsymbol{\nabla} \times \boldsymbol{u} \right) = \rho \frac{\partial^2 \left(\frac{1}{2} \boldsymbol{\nabla} \times \boldsymbol{u} \right)}{\partial t^2} \tag{B.35}$$

So that the shear velocity is given by,

$$c_S = \sqrt{\frac{\mu}{\rho}} \tag{B.36}$$

In an infinite, bulk, isotropic, homogeneous medium, only these two types of waves (dilatational and shear) can exist.

B.4.2 Plane Waves in Infinite Media

A solution to the wave equation from Equation B.28 is a simple harmonic plane wave. The displacement profile of a plane wave propagating through an isotropic medium is given by,

$$u(\boldsymbol{r}, t) = B_0 e^{i(\boldsymbol{k} \cdot \boldsymbol{r} - \omega t + \psi)} \tag{B.37}$$

where ψ is the phase shift of the wave, $\boldsymbol{r}$ is the position vector, ω is the angular frequency, t is time, B_0 is the amplitude, and $\boldsymbol{k}$ is the wave vector. The above equation can be written in a more compact form by defining a complex amplitude $A_0 = e^{i\psi}$ so that,

$$u(\boldsymbol{r}, t) = A_0 e^{i(\boldsymbol{k}\cdot\boldsymbol{r} - \omega t)} \tag{B.38}$$

The wave vector points in the direction of the wave propagation. The magnitude of this vector is the wave number and is related to the medium's ultrasonic velocity as follows,

$$k = \frac{\omega}{c} \tag{B.39}$$

where, c is the velocity.

B.5 Rayleigh Surface Waves

So far, only bulk waves propagating in an infinite medium have been considered. In that case, it was shown that only two types of waves can exist: dilatational and shear. Now, the case of a semi-infinite medium, bounded by a traction free surface is considered. The surface is smooth and flat, and the medium is still isotropic, elastic, and homogeneous. The traction free surface has the effect of adding a boundary condition to the equations of motion (Equation B.28) considered in the previous section. The resulting surface waves have been named Rayleigh waves, after Lord Rayleigh, who in 1885 wrote about the possibility of two-dimensional wave propagation along a surface [83]. Here, there derivation behind Rayleigh surface waves will be shown, and some important features of this type of wave will be discussed. This discussion will be primarily drawn from Landau and Lifshitz [26]; however, there are a number of great references [48,49,80,84] which contain a thorough discussion on Rayleigh waves.

Consider a monochromatic, plane wave propagating in the x_1 direction along a surface $x_3 = 0$ of a semi-infinite medium with a half space $x_3 > 0$. In order to correspond to a surface wave, solutions

to Equation B.28 of the following form are sought,

$$u_R = f(x_3)e^{i(kx_1-\omega t)} \tag{B.40}$$

where $f(x_3)$ is some function that depends on the depth x_3. For the solution to correspond to a surface wave, $f(x_3)$ should be such that u decays with depth x_3. Substituting u_R into Equation B.28 yields,

$$\frac{\partial^2 f(x_3)}{\partial x_3^2} = \left(k^2 - \frac{\omega^2}{c^2}\right) f(x_3) \tag{B.41}$$

The bracketed quantity, $k^2 - \frac{\omega^2}{c}$, should be greater than zero so that the wave is damped in the depth of the medium. Then, the solution to the above equation is,

$$f(x_3) = Ae^{\sqrt{k^2-\frac{\omega^2}{c^2}}z} \tag{B.42}$$

where A is a constant. Then, substituting this into Equation B.40 yields a solution of,

$$u_R = Be^{i(kx_1-\omega t)}e^{\kappa z} \tag{B.43}$$

where,

$$\kappa = \sqrt{k^2 - \frac{\omega^2}{c^2}} \tag{B.44}$$

At the surface $x_3 = 0$, the traction free boundary condition is given by,

$$\sigma_{ik}\hat{n}_k|_{x_3=0} = 0 \tag{B.45}$$

where $\hat{n}_k$ is the unit normal vector of the surface. Since the surface lies in the $x_1 - x_2$ plane, $\hat{\boldsymbol{n}}$ is parallel to the x_3 axis, and the boundary condition yields,

$$\sigma_{13} = \sigma_{23} = \sigma_{33} = 0 \tag{B.46}$$

Then, using Hooke's law from Equation B.26 yields,

$$\begin{aligned} \varepsilon_{13} = \varepsilon_{23} = 0 \\ (2\mu + \lambda)\varepsilon_{33} + \lambda(\varepsilon_{11} + \varepsilon_{22}) = 0 \end{aligned} \tag{B.47}$$

Furthermore, recognizing that the displacement expression in B.43 is independent of x_2 yields,

$$\begin{aligned} \varepsilon_{23} = \frac{1}{2}\left(\frac{\partial u_2}{\partial x_3} + \frac{\partial u_3}{\partial x_2}\right) \\ \Rightarrow u_2 = 0 \end{aligned} \tag{B.48}$$

This indicates that there is no horizontal motion. Rather, in a Rayleigh wave, all of the particle motion is confined to the $x_1 - x_3$ plane. This can have important consequences, which will be discussed in Appendix E. For now, the motion of a Rayleigh wave and its characteristics will be discussed further. Since there is motion in both the x_1 and x_3 directions, the displacement vector can be written as a combination of the dilatational $\boldsymbol{u_L}$ and transverse $\boldsymbol{u_T}$ displacement vectors. Each of these vectors individually satisfy the wave equation from Equation B.28 with the appropriate velocities, that is, c_L and c_S for the dilatational and shear waves respectively. In an infinite bulk medium, these two waves will propagate independently of each other at their respective speeds; however, now the boundary conditions at the surface make it such that these two waves cannot propagate independently. Rather, on the surface, the dilatational and shear components comprise the Rayleigh wave and propagate as one. Thus, the Rayleigh wave displacement vector $\boldsymbol{u}_R$ must be a linear combination of $\boldsymbol{u_L}$ and $\boldsymbol{u_S}$. From Equation B.43, these vectors must be of the form,

$$\begin{aligned} u_L = q_1 e^{i(kx_1 - \omega t)} e^{\kappa_L x_3} \\ u_T = q_2 e^{i(kx_1 - \omega t)} e^{\kappa_T x_3} \end{aligned} \tag{B.49}$$

where κ_L and κ_T are defined by substituting c_L and c_T, respectively, into Equation B.44.

For dilatational motion, the curl of the vector must be zero. For transverse motion, the divergence of the vector must be zero. This will be used to determine the dilatational and shear displacement

vectors so that $\boldsymbol{u}_R$ can be determined. For the transverse portion,

$$\begin{aligned} \boldsymbol{\nabla} \cdot \boldsymbol{u}_T &= 0 \\ \Rightarrow \frac{\partial (u_1)_T}{\partial x_1} + \frac{\partial (u_3)_T}{\partial x_3} &= 0 \end{aligned} \tag{B.50}$$

Using the form of u_T from Equation B.49 yields,

$$\frac{(u_1)_T}{(u_3)_T} = -\frac{\kappa_T}{ik} \tag{B.51}$$

So that the components of the shear wave displacement vector can be written as,

$$\begin{aligned} (u_1)_T &= \kappa_T a e^{i(kx_1 - \omega t)} e^{\kappa_T x_3} \\ (u_1)_T &= -ika e^{i(kx_1 - \omega t)} e^{\kappa_T x_3} \end{aligned} \tag{B.52}$$

For the dilatational portion,

$$\begin{aligned} \boldsymbol{\nabla} \times \boldsymbol{u}_L &= 0 \\ \Rightarrow \frac{\partial (u_1)_L}{\partial x_3} - \frac{\partial (u_3)_L}{\partial x_1} &= 0 \end{aligned} \tag{B.53}$$

Using the form of u_L from Equation B.49 yields,

$$\frac{(u_1)_L}{(u_3)_L} = \frac{ik}{\kappa_L} \tag{B.54}$$

So that the components of the dilatational wave vector can be written as,

$$\begin{aligned} (u_1)_L &= kbe^{i(kx_1 - \omega t)} e^{\kappa_L x_3} \\ (u_1)_L &= -i\kappa_L b e^{i(kx_1 - \omega t)} e^{\kappa_L x_3} \end{aligned} \tag{B.55}$$

where b is a constant. Recall, the Rayleigh wave displacement vector is the linear combination of the dilatational and shear displacement vectors. Therefore, from Equations B.48, B.55, and B.52,

the components of the Rayleigh wave vector are known in all three directions.

$$\begin{aligned}(u_1)_R &= \left(kbe^{\kappa_L x_3} + \kappa_T a e^{\kappa_T x_3}\right) e^{i(kx_1 - \omega t)} \\ (u_2)_R &= 0 \\ (u_1 = 3)_R &= \left(-i\kappa_L b e^{\kappa_L x_3} - ika e^{\kappa_T x_3}\right) e^{i(kx_1 - \omega t)}\end{aligned} \tag{B.56}$$

A few comments will now be made on the nature of this type of wave. The particle motion is elliptical with the vertical component being larger than the horizontal component. The motion is also retrograde. For example, the motion is counterclockwise for a wave traveling to the right. Of course, most of the energy is concentrated as the surface and decays with depth. In an isotropic, elastic, homogeneous material, Rayleigh waves are non-dispersive. The velocity of a Rayleigh wave is only slightly smaller than that of the shear wave velocity.

B.6 Elastic Relationships

For an isotropic homogeneous material, only two independent elastic constants are required to fully characterize the material. Some useful relationships between these elastic constants are presented below. The bulk modulus K can be written in terms of the Lamé constants as follows,

$$K = \lambda + \frac{2}{3}\mu \tag{B.57}$$

The Young's modulus E in terms of the Lamé constants and Poisson's ratio ν is,

$$\begin{aligned}E &= 2\mu(1+\nu) \\ &= \frac{\lambda(1+\nu)(1-2\nu)}{\nu}\end{aligned} \tag{B.58}$$

The shear modulus in terms of the λ and ν,

$$\mu = \frac{\lambda(1-2\nu)}{2\nu} \tag{B.59}$$

Obviously, there are many more relationships; since, any of the elastic constants can be determined as long as two other elastic constants are known.

Appendix C

Nonlinear Interaction of Elastic Waves: Collinear and Non-Collinear Wave-Mixing

In linear elastic wave propagation, superposition holds: two or more waves can cross paths and their resultant (in the region which they crossed paths) is the addition of the two. In nonlinear wave propagation, two waves which cross paths may result in a third wave (see Figure C.1). In essence, when waves governed by nonlinear equations of motion cross paths, they may interact and superposition does not hold. Acoustic nonlinearities in materials can manifest in a variety of ways, including harmonic generation, wave interaction, changes in velocity with stress, and nonlinear acoustic resonance to name a few. The theory of elastic wave propagation is simply an approximation to nonlinear wave propagation. In many cases, this approximation is accurate; however, in highly nonlinear cases, linearization may not be adequate. Material irregularities such as micro-cracks, dislocations, regions of plasticity, etc. can lead to large acoustic nonlinearities which violate conventional linear elastic theory. Thus, one natural application to nonlinear acoustics is as a means to nondestructively monitor material damage. Of course, the presence of acoustic nonlinearities in materials is not limited to those with damage; nonlinearities may be inherent to the material. Nonlinear elastic theory defines two types of nonlinearities: geometrical and material (or physical) [85, 86]. Geometrical nonlinearities occur from the strain-displacement relationships and can arise due to large deformations. Material nonlinearities occur from nonlinear stress-strain relationships.

Many ultrasonic methods have been employed to characterize material nonlinearities. These methods include: resonance techniques [23, 87–89], acousto-elastic techniques [34, 90], harmonic generation [91–94], and wave-mixing techniques. The focus here is on the latter. In wave-mixing techniques, two (or more) waves are transmitted such that they cross paths and interact to produce a third, scattered wave. The two interacting waves may be collinear or non-collinear. The non-collinear wave mixing technique has an advantage over other ultrasonic nonlinear techniques (including collinear wave-mixing) for a variety of reasons: 1. system nonlinearities can be separated from material nonlinearities in time, 2. nonlinear scattered wave can be isolated from the primary waves, because

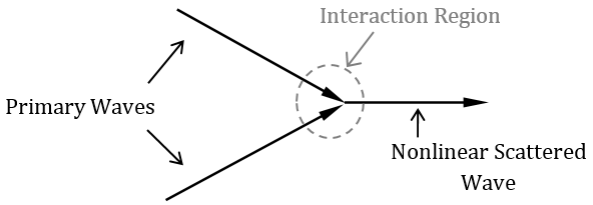

Figure C.1: Simple schematic depicting two primary waves interacting to produce a nonlinear scattered wave.

it must follow a set of selection rules (to be described later), and 3. the nonlinear scattered wave will be of a certain, predictable mode (transverse or dilatational) based on the testing parameters.

Much of the theoretical work and interest in wave mixing of elastic waves in solid materials took place in the 1950s and throughout the 1960s. Beyond 1960 up to the present, there have been a handful of authors who have applied the theory experimentally and have extended the theory to account for more complex material behavior; however, interest in wave mixing of ultrasonic waves has remained relatively low and has only recently picked up again. The relatively low interest may have been due to limitations in technology and computational power. The general field of nonlinear acoustics, however, has remained a topic of great interest due to its numerous applications in fields ranging from seismic [32, 33] to medical [81]. The focus of this chapter will be confined mainly to non-collinear wave mixing of ultrasonic waves in solid media. It will begin with a brief literature review on the subject of non-collinear wave mixing of ultrasonic waves in solid materials. Then, the derivation for the nonlinear equations of motion following the methods described by Landau and Lifshitz, [26] Gol'dberg [95], and Zarembo and Krasil'nikov [85] will be presented. Solutions to the nonlinear equation equations of motion and interaction cases will then be provided. Finally, different interaction cases will be presented and discussed. Note, this theory will be presented for plane ultrasonic waves propagating in homogeneous, elastic, isotropic materials. Extension of the theory to include various wave-propagation characteristics (e.g. spherical waves, attenuation, inhomogeneous materials, etc.) has been treated by various authors [96–100]. Both the classical and quantum mechanics approach have been used in literature to arrive at the nonlinear elastic theory. Here, the focus will be on the classical approach.

C.1 Non-Collinear Wave-Mixing: A Literature Review

The third-order nonlinear equations of motion were first developed in 1951 by Murnaghan [25] by using equilibrium equations and virtual work. He proposed a set of third-order elastic constants (TOECs) l, m, and n. Hughes and Kelly (1953) [101] used Murnaghan's theory to derive expressions for elastic wave velocities in stressed solids. They experimentally measured the TOECs in polystyrene, iron, and Pyrex glass by measuring the ultrasonic dilatation and shear wave velocities as a function of applied stress. In 1954, Landau and Lifshitz [26] suggested using the relationship between the stress tensor and elastic energy function as a way of deriving third-order nonlinear equations of motion and proposed a different set of TOECs A, B, and C. The two sets of TOECs are linear combinations of each other. Gol'dberg (1960) [95] derived the nonlinear equations of motion by using the method described by Landau and Lifshitz. Gol'dberg considered 1-D propagation of monochromatic waves and the effects of self-interaction.

In 1963, Shiren [102] experimentally observed nonlinear interaction of collinear bulk dilatational waves in magnesium oxide at microwave frequencies. Shiren confirmed that the results were indeed from nonlinear interaction, and not from the equipment or at the bonding material or interfaces, by checking that the frequencies and the wave polarizations matched that predicted by theory. The presence of the nonlinear wave was not directly detected; however, Shiren verified its existence by using a phase velocity mismatching technique to check that the nonlinear interaction was suppressed when expected. In 1963, Jones and Kobett [27] solved the third-order nonlinear elastic equations of motion and developed criteria for the occurrence of a strong scattered wave. They also demonstrated, by way of example, that the polarization condition must be met for the scattered wave to have a non-zero amplitude. From these resonance and polarization conditions, they identified the possible bulk wave interaction cases. Rollins (1963) [103] experimentally validated the work of Jones and Kobett by successfully directly detecting a scattered wave resulting from interaction of pulsed ultrasonic waves. Rollins observed nonlinear scattered waves in fused silica, polycrystalline aluminum, and polycrystalline magnesium for the five interaction cases introduced by Jones and Kobett. Childress and Hambrick (1964) [104] used a quantum-mechanical approach to derive interaction cases, which verified the results of Jones and Kobett. They suggested that the

non-collinear wave mixing technique could be useful for measuring the third-order elastic constants. Taylor and Rollins (1964) [28,29] used a quantum-mechanical approach to derive the scattered wave displacement amplitudes arising from the different interaction cases and experimentally validated their results. They also considered the case where three waves were mixed to generate a fourth wave; however, the intensity of the scattered wave in this case was very low as to be undetectable. In 1965, Rollins [105] considered the effect of anharmonic properties of materials on the experimental results of non-collinear wave mixing. He also discussed the possibility of extending the theory to include single crystals; however, he noted the difficulties involved. Notably, these difficulties include the fact that in non-collinear wave mixing of single crystals, momentum and energy conservation conditions are rarely satisfied because the waves do not necessarily propagate as pure modes. He suggested that a next step to studying non-collinear wave mixing in single crystals would be to study non-collinear interactions in the basal plane of hexagonal single crystals, because pure mode waves can propagate in any direction perpendicular to the unique axis. In 1967, Krasil'nikov and Zarembo [106] presented experimental results on elastic wave interactions in solids. They studied both harmonic generation and interaction between bulk waves. For the harmonic generation experiments, they observed a second harmonic generation in shear waves, which does not follow the nonlinear elastic theory. They attributed the discrepancy to the fact that nonlinear elastic theory does not consider the presence of dislocations that exist in real, imperfect solid materials. For the wave interaction experiment, they considered non-collinear wave mixing in an aluminum block, where they observed a nonlinear scattered wave resulting from the primary wave interaction in the time-domain. To verify that the observed nonlinear scattered wave was a result of the wave interaction and not from the testing equipment, they studied time-domain records when both transducers were operated simultaneously and individually. It was observed that the nonlinear scattered wave disappeared when the transducers were operated individually. They also confirmed that the nonlinear scattered wave propagated in the direction predicted by theory, by observing the scattered wave oscilloscope record as the receiving transducer location was varied.

The 1970's saw a decline in the interest in of non-collinear ultrasonic wave mixing in solids; however, there are a few notable works from this time period. Zarembo and Krasil'nikov (1970) [85] provided an excellent review of the nonlinear theory of elastic waves in solids. In their paper, they described

Gol'dberg's [95] derivation in greater detail, discussed the possibility of extending the theory to single crystals, and provided an overview on collinear and non-collinear wave mixing in solids including experimental results of past studies. Dunham and Huntington (1970) [107] extended the traditional five-constant nonlinear elastic theory for the case of single cubic crystals. They then determined third-order elastic constants experimentally for fused silica and NaCl. To obtain accurate results, they measured the conversion efficiency of the wave interaction. In 1973, Hiki and Mukai [108] experimentally studied non-collinear wave interactions in a copper single crystal. They considered two interaction cases: 1. the case where two shear waves interact to produce a dilatational wave, and 2. the case where a shear and dilatational wave interact to produce a dilatational wave. In both cases, they verified the existence of the third scattered wave by changing the interaction volume and observing the change in amplitude of the received signal. The interaction volume was changed by introducing a delay to one of the primary waves. As the interaction volume was increased, it was observed that the amplitude increased, as predicted by theory. They also verified the existence of the scattered wave by checking that the amplitude was proportional to the product of the amplitudes of the primary waves. Finally, they checked that the resulting wave matched predicted polarization conditions. The authors noted that measuring the third-order elastic constants via this method is difficult due to difficulty in accurately obtaining absolute amplitudes of the waves.

In the late 1980's and early 1990's, a few authors were interested in extending the theory to include materials of a more complex nature. Nazarov et. al (1987) [97] considered nonlinear acoustics in micro-inhomogeneous media by conducting a theoretical analysis and providing experimental evidence of acoustic nonlinearities in micro-inhomogeneous materials from other studies. Micro-inhomogeneous media is defined as media containing inhomogeneities (e.g., different phase, cracks, dislocations, etc.) which are small compared to the wavelength of the propagating wave. They concluded that the presence of inhomogeneities in a medium may enhance the medium's nonlinear acoustic response. Ostrovsky (1991) [109] expanded on his theoretical study of 1987 [97], by considering models of micro-inhomogeneous material from an acoustical standpoint. In two studies (1987 and 1989), Johnson and Shankland [32,33] demonstrated the feasibility of non-collinear wave mixing in rock, which is an inherently nonlinear material due to the presence of microcracks and

its mesoscopic structure. They introduced a set of selection criteria to verify that the generated scattered wave originated from the bulk wave interaction and not the testing apparatus. In addition to the three selection criteria, they demonstrated that the nonlinear scattered wave could be detected in the time-domain and matched the expected time-of-arrival as predicted by a straight ray-path analysis. Beresnev (1993) [98] studied interaction of spherical waves, which can be more realistic in some cases than plane waves. For simplicity, he considered the case where two dilatational spherical waves interact to generate a shear wave with a difference frequency. He obtained the displacement field (in a single propagation direction) of the scattered wave resulting from the interaction of two dilatational spherical waves by solving the nonlinear equation of motion via the same method as Jones and Kobett [27]. For the general case, the resulting solution can only be analyzed numerically; thus, Beresnev provided a numerical example, where he calculated the directivity patterns of the scattered wave for varying sizes of an interaction volume. The results showed that the interaction volume size (as compared to the wavelength) greatly influences the directivity and shape of the wave pattern, unlike the plane-wave case. McCall (1994) [96] performed a theoretical study on nonlinear interactions of large-amplitude waves with a focus on rocks, which exhibit highly nonlinear characteristics. He derived the nonlinear equation of motion and solved for the displacement field with the inclusion of attenuation. In his 1994 dissertation, Liu [110] provided experimental results from a brief study on non-collinear wave mixing in Berea sandstone. He found that the recorded frequency ratio of the two primary waves matched closely to that predicted by the theory. He attributed any discrepancies to the velocity dispersion inherent to stone.

In 1998, Korneev [111] prepared a manuscript in which he presented time-domain solutions for 1-D nonlinear elastic wave propagation and obtained numerical estimates of the nonlinearities in rocks. That same year, Korneev et al. [112] prepared an in depth report on nonlinear ultrasonic wave-mixing, which detailed the derivation of the nonlinear equations of motion and the displacement field solution as found by Jones and Kobett [27]. They also derived analytical expressions for the amplitude of the generated nonlinear scattered wave for all of the possible interaction cases. This work was tedious, and the mathematical expressions were lengthy. As a result, some mathematical errors were published in the manuscript; however, Korneev and Demcenko recently corrected these errors and simplified some of the lengthy analytical expressions in a 2013 journal publication [30].

The study was motivated with seismic applications; therefore, they used sandstone rock for experimental and theoretical calculations. In the newer manuscript, they verified the accuracy of the corrected analytic expressions by comparing them with numerical solutions of the equations of motion. In 2001, Gusev [99] identified the wave interaction cases possible in isotropic materials with hysteretic quadratic nonlinearities. Materials of this type have constitutive relationships in which the strain lags the stress; equivalently, materials in which the elastic modulus exhibits a "bow-tie" behavior. This theory differed from the conventional 5-constant theory of Landau and Lifshitz [26] (for nonlinear elastic materials) in that he used a different form of the energy function to derive the nonlinear equations of motion. He then solved for the displacement field of the nonlinear scattered wave and found that the theory predicts more possible interaction cases for materials with hysteresis of quadratic nonlinearity than nonlinear elastic materials. Notably, collinear interactions between shear waves are allowed, a forbidden interaction in traditional nonlinear elastic materials. In 2009, Croxford et al. [113] proposed the use of non-collinear wave mixing for the detection of material degradation. They applied the method to aluminum samples subjected to varying amounts of either laboratory induced fatigue damage or plastic deformation. The method consisted of measuring the amplitude of the generated scattered wave and normalizing it by the amplitudes of the two primary waves. This normalized parameter was termed the "normalized nonlinearity" by the authors. Experimental results showed the method to be successful in characterizing the changes in the material in both cases. In general, as the level of damage due to fatigue/plasticity increased, so did the normalized nonlinear parameter. The authors also showed time domain records obtained when the transducers were operated simultaneously and operated separately and summed. Comparison of the two time domain records clearly showed the presence of the nonlinear scattered wave when the two transducers were operated simultaneously. The arrival of the scattered wave matched that predicted by theory.

In recent years, literature focus has been on applications of wave mixing. In 2012 and 2013, Liu and Tang et al. [114, 115] showed that the acoustic wave parameters, which are linearly related to Murnaghan's [25] and Landau and Lifshitz's [26] higher order constants, can be experimentally measured using wave mixing. In their report, they used a collision interaction between dilatational and shear wave to monitor local plastic deformation and fatigued zones in metals. The method

was shown capable of detecting such zones. In 2014, Koissin et al. [116] used non-collinear wave mixing to monitor isothermal epoxy curing in an aluminum-adhesive-aluminum laminate. Their set-up consisted of an immersion tank, where the primary waves propagated through water upon penetrating the specimen. Such a set-up eliminated the use of angle wedges for generating refracted waves at the appropriate angles for interaction in the bulk of the specimen. They found that the wave mixing was sensitive to the material transformations during curing, whereas conventional linear acoustic techniques were not. They were able to detect several important characteristic points of the cure process, such as maximal viscosity, gel time, and vitrification time. Also very recently, Demenko and others [117,118] successfully applied the non-collinear wave mixing method to estimate the physical aging state of PVC and thermoplastics and to monitor epoxy curing. They again used the immersion set-up, which enabled them to construct c-scan images. In [118], the authors noted that the reality of material testing deviates from the assumptions of nonlinear elasticity, namely the homogeeity condition. They observed that deviation from theory can result in extra scattered wave beams and potentially a decrease in the signal amplitude. Blanloeuil et al. [119], via the use of finite elements, found that the non-collinear wave mixing technique could be applied for the detection of closed cracks.

C.2 The Five-Constant Nonlinear Theory of Elasticity

When a mechanical wave propagates through a material that exhibits nonlinear behavior, it can undergo nonlinear distortion. There are multiple ways to model this nonlinear distortion, and which model should be used depends on the origin of the nonlinearity. Generally, most methods involve the Taylor expansion of a parameter, where some of the higher ordered terms are kept. This of course differs from traditional linear theory, where the higher order terms are truncated such that the parameter of interest is linearized. One common derivation technique involves the expansion of the pressure in a Taylor series about the density to obtain a nonlinear equation of state, *i.e.*, the relationship between pressure and density. Of course, a nonlinear equation of state will yield nonlinearities in the strain through Euler's equation of force [81]; therefore, one would expect that a derivation starting with a nonlinear equation of state might result in the same equations of motion as that in which the derivation starts by using a nonlinear (via Taylor series expansion) constitutive

relationship. The consideration of a nonlinear equation of state for the derivation of the nonlinear equations of motion is widely used in the field of acoustics and is particularly useful when the change in velocity of the wave and/or the generation of higher harmonics which arise as an acoustic wave propagates through a nonlinear medium is of interest. For completeness, this derivation is presented in Appendix D. For the research presented in this manuscript, the nonlinear equations of motion are derived by considering the origin of nonlinearities as a result of the nonlinear strain tensor. The derivation follows the method outlined by Landau and Liftshitz [26] (later presented by Korneev and Demcenko [30].)

An expression for the internal energy is found by Taylor expansion about the strain tensor invariants. Then, an expression for the wave equation can be obtained by using the internal energy expression with the relation to the stress tensor. Please refer to Appendix B for a discussion on the stress and strain tensors. The strain tensor for a nonlinear elastic material was provided in Equation B.9, and repeated here for readability,

$$\varepsilon_{ik} = \frac{1}{2}\left(\frac{\partial u_i}{\partial x_k} + \frac{\partial u_k}{\partial x_i} + \frac{\partial u_l}{\partial x_k}\frac{\partial u_l}{\partial x_i}\right) \tag{C.1}$$

For the linear elastic case, the third term was assumed small and dropped. To derive the nonlinear equations of motion, however, the term will be retained. Thus, the origin of nonlinearities in the resulting equations of motion will arise from nonlinearities in the constitutive relationship. Note, the strain tensor, even in its nonlinear form, is symmetric. Thus, $\varepsilon_{ij} = \varepsilon_{ji}$. For constant entropy, a useful relation for the stress tensor was shown in Equation B.19 and repeated here,

$$\sigma_{ik} = \frac{\mathrm{d}U}{\mathrm{d}\left(\frac{\partial u_i}{\partial x_k}\right)} \tag{C.2}$$

These two expressions will be used in the derivation of the nonlinear wave equation in the following sections.

C.2.1 Internal Energy

The relationship between the internal energy U and the stress tensor σ_{ik} was presented in Equation C.2. Therefore, it is necessary to find an expression for the internal energy. Landau and Lifshitz [26] noted that the adiabatic internal elastic energy is invariant under coordinate transformation and is only dependent on the deformation of the elastic body. Thus, the internal energy is only a function of the invariants of the strain tensor.

$$U = U(I_1, I_2, I_3) \tag{C.3}$$

where,

$$\begin{aligned} I_1 &= trace(\boldsymbol{\varepsilon}) = \varepsilon_{ii} \\ I_2 &= \frac{1}{2}\left(trace(\boldsymbol{\varepsilon})^2 - \boldsymbol{\varepsilon}\cdot\boldsymbol{\varepsilon}\right) = \frac{1}{2}(\varepsilon_{ii}\varepsilon_{jj} - \varepsilon_{ij}\varepsilon_{ji}) \\ I_3 &= det(\boldsymbol{\varepsilon}) = \frac{1}{6}e_{ijk}e_{lmn}\varepsilon_{il}\varepsilon_{jm}\varepsilon_{kn} \end{aligned} \tag{C.4}$$

where e is the permutation symbol. The permutation symbol has a value of 1 for positive permutations, a value of -1 for backward permutations, and a value of 0 for non-permutations.

$$e_{ijk} = \begin{cases} 0, & \text{for } i = j, j = k, \text{ or } k = i \\ +1, & \text{for } (i,j,k) \in \{(1,2,3),(2,3,1),(3,1,2)\} \\ -1, & \text{for } (i,j,k) \in \{(3,2,1),(1,3,2),(2,1,3)\} \end{cases} \tag{C.5}$$

An expression for the internal energy can be obtained by Taylor expanding U about $(I_1, I_2, I_3) = (0,0,0)$ and omitting terms higher than the 3^{rd} degree in ε_{ik}.

$$\begin{aligned} U \approx U(0,0,0) + \frac{\partial U}{\partial I_1}|_{(0,0,0)} I_1 + \frac{\partial U}{\partial I_2}|_{(0,0,0)} I_2 + \frac{\partial U}{\partial I_3}|_{(0,0,0)} I_3 + \frac{\partial^2 U}{\partial I_1 \partial I_2}|_{(0,0,0)} \frac{I_1 I_2}{2} \\ + \frac{\partial^2 U}{\partial I_1^2}|_{(0,0,0)} \frac{I_1^2}{2} + \frac{\partial^2 U}{\partial I_1^3}|_{(0,0,0)} \frac{I_1^3}{6} \end{aligned} \tag{C.6}$$

The expressions for the invariants from Equation C.4 can be plugged into Equation C.6. Thus, U in terms of the components of the strain tensor is,

$$\begin{aligned} U \approx U(0,0,0) + \left(\frac{\partial U}{\partial I_1}|_{(0,0,0)}\right)\varepsilon_{ii} + \left(\frac{\partial U}{\partial I_2}|_{(0,0,0)}\right)\left[\frac{1}{2}\left(\varepsilon_{ii}^2 - \varepsilon_{ij}^2\right)\right] + \left(\frac{\partial U}{\partial I_3}|_{(0,0,0)}\right)\epsilon_{ijk}\varepsilon_{1i}\varepsilon_{2j}\varepsilon_{3k} \\ + \left(\frac{\partial^2 U}{\partial I_1 \partial I_2}|_{(0,0,0)}\right)\left[\frac{1}{4}\varepsilon_{ll}\left[\varepsilon_{ii}^2 - \varepsilon_{ij}^2\right]\right] + \left(\frac{\partial^2 U}{\partial I_1^2}|_{(0,0,0)}\right)\varepsilon_{ii}^2 + \left(\frac{\partial^2 U}{\partial I_1^3}|_{(0,0,0)}\right)\varepsilon_{ii}^3 \end{aligned} \tag{C.7}$$

Equilibrium for the undeformed body implies that $U(0,0,0) = 0$ and $\frac{\partial U}{\partial I_1} = 0$. The coefficients preceding the 2^{nd} degree terms (in ε_{ik}) are in terms of the linear elastic moduli, and the coefficients preceding the 3^{rd} degree terms are in terms of the 3^{rd} order moduli. The 2^{nd} order terms from Equation C.6 are,

$$\begin{aligned} \frac{\partial U}{\partial I_2} &= -2\mu \\ \frac{\partial^2 U}{\partial I_2^2} &= \lambda + 2\mu \end{aligned} \tag{C.8}$$

The μ and λ in the above coefficients are the familiar Lamé coefficients, where μ is the shear modulus. The third-order nonlinear constants A, B and C were introduced by Landau and Lifshitz [26]. The coefficients in front of the 3^{rd} order terms in Equation C.6 can be written in terms of these constants.

$$\begin{aligned} \frac{\partial^2 U}{\partial I_2 \partial I_1} &= -2A - 4B \\ \frac{\partial^3 U}{\partial I_1^3} &= 2A + 6B + 2C \\ \frac{\partial U}{\partial I_3} &= A \end{aligned} \tag{C.9}$$

These relationships are so that a simple resulting expression for U can be obtained. After some algebraic manipulation, this expression for U is,

$$U = \mu\varepsilon_{ik}^2 + \left(\frac{1}{2}K - \frac{1}{3}\mu\right)\varepsilon_{ll}^2 + \frac{A}{3}\varepsilon_{ik}\varepsilon_{il}\varepsilon_{kl} + B\varepsilon_{ik}^2\varepsilon_{ll} + \frac{C}{3}\varepsilon_{ll}^3 \tag{C.10}$$

Murnaghan [25] also introduced nonlinear elastic constants, which he termed l, m, and n. They are linearly related to the constants of Landau and Lifshitz.

$$\begin{aligned} l &= B + C \\ m &= \frac{A}{2} + B \\ n &= A \end{aligned} \tag{C.11}$$

The expression for the strain tensor from Equation C.1 can be used in C.10 to obtain U in terms of $\frac{\partial u_i}{\partial x_k}$. The internal energy U in terms of $\frac{\partial u_i}{\partial x_k}$ is then,

$$\begin{aligned} U \approx \frac{\mu}{4}\left(\frac{\partial u_i}{\partial x_k} + \frac{\partial u_k}{\partial x_i}\right)^2 + \left(\frac{K}{2} - \frac{\mu}{3}\right)\left(\frac{\partial u_l}{\partial x_l}\right)^2 + \left(\mu + \frac{A}{4}\right)\frac{\partial u_i}{\partial x_k}\frac{\partial u_l}{\partial x_i}\frac{\partial u_l}{\partial x_k} \\ + \left(\frac{B}{2} + \frac{K}{2} - \frac{\mu}{3}\right)\frac{\partial u_l}{\partial x_l}\left(\frac{\partial u_i}{\partial x_k}\right)^2 + \frac{A}{12}\frac{\partial u_i}{\partial x_k}\frac{\partial u_k}{\partial x_l}\frac{\partial u_l}{\partial x_i} + \frac{B}{2}\frac{\partial u_i}{\partial x_k}\frac{\partial u_k}{\partial x_i}\frac{\partial u_l}{\partial x_l} \\ + \frac{C}{3}\left(\frac{\partial u_l}{\partial x_l}\right)^3 \end{aligned} \tag{C.12}$$

C.2.2 Generalized Hooke's Law

Recall that stress tensor is related to the internal energy as shown in Equation C.2. Using the internal energy from Equation C.12, an expression for the stress tensor in terms of $\frac{\partial u_i}{\partial x_k}$ is found as follows,

$$\begin{aligned} \sigma_{ik} = \mu\left(\frac{\partial u_i}{\partial x_k} + \frac{\partial u_k}{\partial x_i}\right) + \lambda\frac{\partial u_l}{\partial x_l}\delta_{ik} + \left(\mu + \frac{A}{4}\right)\left[\frac{\partial u_l}{\partial x_i}\frac{\partial u_l}{\partial x_k} + \frac{\partial u_i}{\partial x_l}\frac{\partial u_k}{\partial x_l} + \frac{\partial u_l}{\partial x_k}\frac{\partial u_i}{\partial x_l}\right] \\ + \left(\frac{B+\lambda}{2}\right)\left[\left(\frac{\partial u_l}{\partial x_j}\right)^2\delta_{ik} + 2\frac{\partial u_l}{\partial x_l}\frac{\partial u_i}{\partial x_k}\right] + \frac{A}{4}\frac{\partial u_k}{\partial x_l}\frac{\partial u_l}{\partial x_i} \\ + \frac{B}{2}\left[2\frac{\partial u_k}{\partial x_i}\frac{\partial u_l}{\partial x_l} + \frac{\partial u_j}{\partial x_l}\frac{\partial u_l}{\partial x_j}\delta_{ik}\right] + C\left(\frac{\partial u_l}{\partial x_l}\right)^2\delta_{ik} \end{aligned} \tag{C.13}$$

The above equation is the generalized three-dimensional Hooke's law for an isotropic, homogeneous, nonlinear elastic material. The nonlinearities in this equation are apparent, as it contains the three higher-order constants that were discussed in the previous section.

C.2.3 The Nonlinear Equations of Motion

The three-dimensional wave equation for a homogeneous, elastic solid presented in Appendix B and repeated here,

$$\rho \frac{\partial^2 u_i}{\partial t^2} = \frac{\partial \sigma_{ik}}{\partial x_k} \tag{C.14}$$

The expression for the stress tensor from Equation C.13 can be plugged into the wave equation to obtain the equations of motion for nonlinear elastic materials.

$$\begin{aligned} \rho \frac{\partial^2 u_i}{\partial t^2} - \mu \frac{\partial^2 u_i}{\partial x_k^2} - (\lambda + \mu) \frac{\partial^2 u_k}{\partial x_i \partial x_k} = & \left(\mu + \frac{A}{4}\right) \left(\frac{\partial^2 u_l}{\partial x_k^2} \frac{\partial u_l}{\partial x_i} + \frac{\partial^2 u_l}{\partial x_k^2} \frac{\partial u_i}{\partial x_l} + 2 \frac{\partial^2 u_i}{\partial x_l \partial x_k} \frac{\partial u_l}{\partial x_k} \right) \\ & + \left(\mu + \frac{A}{4} + B + \lambda\right) \left(\frac{\partial^2 u_l}{\partial x_i \partial x_k} \frac{\partial u_l}{\partial x_k} + \frac{\partial^2 u_k}{\partial x_l \partial x_k} \frac{\partial u_i}{\partial x_l} \right) \\ & + (B + \lambda) \left(\frac{\partial^2 u_k}{\partial x_l \partial x_k} \frac{\partial u_l}{\partial x_i} + \frac{\partial^2 u_l}{\partial x_i \partial x_k} \frac{\partial u_k}{\partial x_l} \right) \\ & + \left(\frac{A}{4} + B\right) \left(\frac{\partial^2 u_k}{\partial x_i \partial x_k} \frac{\partial u_l}{\partial x_l} \right) \\ & + (B + 2C) \left(\frac{\partial^2 u_i}{\partial x_k^2} \frac{\partial u_l}{\partial x_l} \right) \end{aligned} \tag{C.15}$$

This version of the nonlinear equations of motion has been termed the five-constant nonlinear wave equation. The right-hand side can be thought of as a source term. The conventional linear acoustic wave equation can be recovered by setting the right-hand side to zero. The implications of this equation on elastic wave propagation will be treated in the following sections.

C.3 Interaction of Two Non-Collinear Intersecting Elastic Waves

Recall that due to the presence of nonlinear terms in the equations of motion, when two monochromatic waves interact, a third scattered wave may arise. The scattered wave has a different frequency and propagation direction than the primary waves. Thus, one of the advantages of non-collinear wave-mixing, when compared to its collinear counterpart, is the existence of frequency and spatial separation. In order for a scattered wave to occur, resonance and polarization conditions must be met. The interaction cases that satisfy resonance conditions and generate a strong scattered wave for non-collinear wave-mixing were first found by Jones and Kobett [27] in 1963. The following discussion will primarily follow the work done by Jones and Kobett. Zarembo and Krasil'nikov [85],

Taylor and Rollins [28, 29], Childress and Hambrick [104], and Korneev et. al [30] also provide excellent reviews of these conditions. In this section, the basic theory will be reviewed, followed by a detailed discussion on the resonance and polarization conditions for each interaction case. Due to the tedious nature of some of the algebra, typos in the literature are not uncommon. It is the goal of this chapter to correct some of these typos and provide sufficiently detailed calculations so that anyone who wishes to derive the interaction cases themselves can readily do so.

For interactions to occur, the following must be satisfied,

$$\omega_3 = \omega_1 \pm \omega_2 \tag{C.16}$$

$$\boldsymbol{k}_3 = \boldsymbol{k}_1 \pm \boldsymbol{k}_2 \tag{C.17}$$

where, $\boldsymbol{k}_i$ is the wave vector for a wave propagating in the $\boldsymbol{k}_i$ direction with a frequency ω_i. From the above equations, $\boldsymbol{k}_3$ is the scattered wave with a sum ($\omega_3 = \omega_1 + \omega_2$) or difference ($\omega_3 = \omega_1 - \omega_2$) frequency generated by interaction between $\boldsymbol{k}_1$ and $\boldsymbol{k}_2$, which are denoted as the primary waves. Note, to maintain consistency with the literature, the term "primary" will be used to refer to the waves which interact and should not be confused with the alternative name for dilatational waves. In other words, primary waves in this context can be either shear or dilatational waves.

Refer back to Equation C.15. The right-hand side (RHS) can be thought of as a source. The method of successive approximations can be used to write an approximation to the differential equation in Equation C.15 [27], where the solution depends on the right-hand side. The displacement is written as follows,

$$\boldsymbol{u} = \boldsymbol{u}^0 + \boldsymbol{u}^{(1)} + \boldsymbol{u}^{(2)} + ... \tag{C.18}$$

where $\mathbf{u}^0$ is the solution to the homogeneous equation, *i.e.*, $RHS = 0$, $\boldsymbol{u}^0 + \boldsymbol{u}^{(1)}$ is the second approximation, $\boldsymbol{u}^0 + \boldsymbol{u}^{(1)} + \boldsymbol{u}^{(2)}$ is the third approximation, and so on. The above summation is adequate provided that the strain components on the right-hand side of Equation C.15 are small compared to the strain components on the left-hand side. To solve Equation C.15, the second approximation will be used. Since $\boldsymbol{u}^{(1)}$ arises due to the system nonlinearity, it represents the displacement of the scattered wave, and thus from this point forward will be denoted as $\boldsymbol{u}^s$. If $\boldsymbol{u}^s$

is small compared to $\boldsymbol{u}^0$, then Equation C.15 can be approximated by plugging in $\boldsymbol{u}^0 + \boldsymbol{u}^s$ on the left-hand side and $\boldsymbol{u}^0$ on the right-hand side. Since $\boldsymbol{u}^0$ is the solution to the homogeneous equation, it disappears from the left-hand side and Equation C.15 reduces to,

$$\begin{aligned}
\rho\frac{\partial^2 u_i^s}{\partial t^2} - \mu\frac{\partial^2 u_i^s}{\partial x_k^2} - (\lambda+\mu)\frac{\partial^2 u_k^s}{\partial x_i \partial x_k} = &\left(\mu + \frac{A}{4}\right)\left(\frac{\partial^2 u_l^0}{\partial x_k^2}\frac{\partial u_l^0}{\partial x_i} + \frac{\partial^2 u_l^0}{\partial x_k^2}\frac{\partial u_i^0}{\partial x_l} + 2\frac{\partial^2 u_i^0}{\partial x_l \partial x_k}\frac{\partial u_l^0}{\partial x_k}\right) \\
&+ \left(\mu + \frac{A}{4} + B + \lambda\right)\left(\frac{\partial^2 u_l^0}{\partial x_i \partial x_k}\frac{\partial u_l^0}{\partial x_k} + \frac{\partial^2 u_k^0}{\partial x_l \partial x_k}\frac{\partial u_i^0}{\partial x_l}\right) \\
&+ (B+\lambda)\left(\frac{\partial^2 u_k}{\partial x_l \partial x_k}\frac{\partial u_l^0}{\partial x_i} + \frac{\partial^2 u_l^0}{\partial x_i \partial x_k}\frac{\partial u_k^0}{\partial x_l}\right) \\
&+ \left(\frac{A}{4} + B\right)\left(\frac{\partial^2 u_k^0}{\partial x_i \partial x_k}\frac{\partial u_l}{\partial x_l}\right) \\
&+ (B+2C)\left(\frac{\partial^2 u_i^0}{\partial x_k^2}\frac{\partial u_l^0}{\partial x_l}\right)
\end{aligned} \tag{C.19}$$

From this point forward, $L(\omega)$ and $S(\omega)$ will denote dilatational and shear waves, respectively, with an angular frequency of ω. The polarizations of the shear wave will be denoted by the subscripts $\parallel$ and $\perp$. Thus, $S_\parallel$ denotes a shear wave polarized in the $\boldsymbol{k}_1 - \boldsymbol{k}_2$ plane, *i.e.*, a shear-horizontal wave, and $S_\perp$ denotes a shear wave polarized out of the $\boldsymbol{k}_1 - \boldsymbol{k}_2$ plane, *i.e.*, a shear-vertical wave. Jones and Kobett considered the scattered wave which results from the interaction of two non-collinear, monochromatic, plane waves. The homogeneous solution to Equation C.19 is then,

$$\boldsymbol{u}^0 = \boldsymbol{A}_0 \cos(\omega_1 t - \boldsymbol{k}_1 \cdot \boldsymbol{r}) + \boldsymbol{B}_0 \cos(\omega_2 t - \boldsymbol{k}_2 \cdot \boldsymbol{r}) \tag{C.20}$$

where $\boldsymbol{A}_0$ and $\boldsymbol{B}_0$ are the amplitude vectors in the direction of the polarization of the wave. The vector $\boldsymbol{r}$ is the radius vector from the center of the point of interaction to the point of observation. Another vector $\boldsymbol{r'}$ is now defined, which is the radius vector of integration inside the interaction region to the point of observation. Please refer to Figure C.2. The expression for $\boldsymbol{u}^0$ can be plugged into the right-hand side of Equation C.19. Note, the following trigonometric identity is useful,

$$\sin(u)\cos(v) = \frac{1}{2}\left[\sin(u+v) + sin(u-v)\right] \tag{C.21}$$

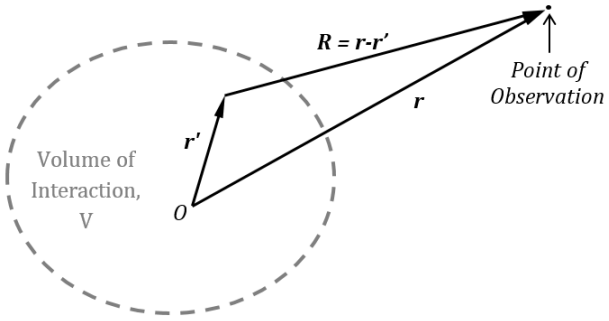

Figure C.2: Definition of position vectors, where $\boldsymbol{r}$ is the radius vector from the center of the interaction to the point of observation, $\boldsymbol{r'}$ is the radius vector from the center of interaction to the integration limit (within the volume of interaction), and $\boldsymbol{R} = \boldsymbol{r} - \boldsymbol{r'}$

After some algebraic manipulation, the right-hand side (RHS) of Equation C.19 becomes,

$$\begin{aligned} RHS = \boldsymbol{I}^{+} \sin\left[(\omega_1+\omega_2)t - (\boldsymbol{k}_1+\boldsymbol{k}_2)\cdot\boldsymbol{r}\right] + \boldsymbol{I}^{-} \sin\left[(\omega_1-\omega_2)t - (\boldsymbol{k}_1-\boldsymbol{k}_2)\cdot\boldsymbol{r}\right] \\ + \boldsymbol{I}^{(\omega_1)} \sin\left[(2\omega_1)t - 2\boldsymbol{k}_1\cdot\boldsymbol{r}\right] + \boldsymbol{I}^{(\omega_2)} \sin\left[(2\omega_2)t - 2\boldsymbol{k}_2\cdot\boldsymbol{r}\right] \end{aligned} \tag{C.22}$$

where,

$$\begin{aligned} \boldsymbol{I}^{\pm} = &-\frac{1}{2}\left(\mu + \frac{A}{4}\right)\left[(\boldsymbol{B}_0\cdot\boldsymbol{k}_1)(\boldsymbol{k}_2\cdot\boldsymbol{k}_2)\boldsymbol{A}_0 \pm (\boldsymbol{A}_0\cdot\boldsymbol{k}_2)(\boldsymbol{k}_1\cdot\boldsymbol{k}_1)\boldsymbol{B}_0 \pm (\boldsymbol{A}_0\cdot\boldsymbol{B}_0)(\boldsymbol{k}_1\cdot\boldsymbol{k}_1)\boldsymbol{k}_2\right. \\ &\left. + (\boldsymbol{A}_0\cdot\boldsymbol{B}_0)(\boldsymbol{k}_2\cdot\boldsymbol{k}_2)\boldsymbol{k}_1 \pm 2(\boldsymbol{k}_1\cdot\boldsymbol{k}_2)(\boldsymbol{B}_0\cdot\boldsymbol{k}_1)\boldsymbol{A}_0 + 2(\boldsymbol{k}_1\cdot\boldsymbol{k}_2)(\boldsymbol{A}_0\cdot\boldsymbol{k}_2)\boldsymbol{B}_0\right] \\ &-\frac{1}{2}\left(K + \frac{\mu}{3} + \frac{A}{4} + B\right)\left[\pm(\boldsymbol{A}_0\cdot\boldsymbol{k}_1)(\boldsymbol{k}_1\cdot\boldsymbol{k}_2)\boldsymbol{B}_0\right] + (\boldsymbol{B}_0\cdot\boldsymbol{k}_2)(\boldsymbol{k}_1\cdot\boldsymbol{k}_2)\boldsymbol{A}_0 \\ &+ (\boldsymbol{A}_0\cdot\boldsymbol{B}_0)(\boldsymbol{k}_1\cdot\boldsymbol{k}_2)\boldsymbol{k}_2 \pm (\boldsymbol{A}_0\cdot\boldsymbol{B}_0)(\boldsymbol{k}_1\cdot\boldsymbol{k}_2)\boldsymbol{k}_1 \\ &-\frac{1}{2}\left(K - \frac{2}{3}\mu + B\right)\left[\pm(\boldsymbol{k}_1\cdot\boldsymbol{k}_1)(\boldsymbol{B}_0\cdot\boldsymbol{k}_2)\boldsymbol{A}_0 + (\boldsymbol{k}_2\cdot\boldsymbol{k}_2)(\boldsymbol{A}_0\cdot\boldsymbol{k}_1)\boldsymbol{B}_0\right] \\ &-\frac{1}{2}\left(\frac{A}{4} + B\right)\left[(\boldsymbol{A}_0\cdot\boldsymbol{k}_2)(\boldsymbol{B}_0\cdot\boldsymbol{k}_2)\boldsymbol{k}_1 \pm (\boldsymbol{A}_0\cdot\boldsymbol{k}_1)(\boldsymbol{B}_0\cdot\boldsymbol{k}_1)\boldsymbol{k}_2\right. \\ &\left. + (\boldsymbol{A}_0\cdot\boldsymbol{k}_2)(\boldsymbol{B}_0\cdot\boldsymbol{k}_1)\boldsymbol{k}_2 \pm (\boldsymbol{A}_0\cdot\boldsymbol{k}_2)(\boldsymbol{B}_0\cdot\boldsymbol{k}_1)\boldsymbol{k}_1\right] \\ &-\frac{1}{2}(B+2C)\left[(\boldsymbol{B}_0\cdot\boldsymbol{k}_2)(\boldsymbol{A}_0\cdot\boldsymbol{k}_1)\boldsymbol{k}_2 \pm (\boldsymbol{A}_0\cdot\boldsymbol{k}_1)(\boldsymbol{B}_0\cdot\boldsymbol{k}_2)\boldsymbol{k}_1\right] \end{aligned} \tag{C.23}$$

$$\begin{aligned} \boldsymbol{I}^{\omega_1} = &-\frac{1}{2}\left(K + \frac{7}{3}\mu + B + \frac{3}{4}A\right)(\boldsymbol{A}_0\cdot\boldsymbol{k}_1)(\boldsymbol{k}_1\cdot\boldsymbol{k}_1)\boldsymbol{A}_0 - \frac{1}{2}(B+2C)(\boldsymbol{A}_0\cdot\boldsymbol{k}_1)(\boldsymbol{A}_0\cdot\boldsymbol{k}_1)\boldsymbol{k}_1 \\ &-\frac{1}{2}\left(K + \frac{4}{3}\mu + B + \frac{A}{2}\right)(\boldsymbol{A}_0\cdot\boldsymbol{A}_0)(\boldsymbol{k}_1\cdot\boldsymbol{k}_1)\boldsymbol{k}_1 \end{aligned} \tag{C.24}$$

$$\boldsymbol{I}^{\omega_2} = -\frac{1}{2}\left(K + \frac{7}{3}\mu + B + \frac{3}{4}A\right)(\boldsymbol{B}_0 \cdot \boldsymbol{k}_2)(\boldsymbol{k}_2 \cdot \boldsymbol{k}_2)\boldsymbol{B}_0 - \frac{1}{2}(B + 2C)(\boldsymbol{B}_0 \cdot \boldsymbol{k}_2)(\boldsymbol{B}_0 \cdot \boldsymbol{k}_2)\boldsymbol{k}_2 - \frac{1}{2}\left(K + \frac{4}{3}\mu + B + \frac{A}{2}\right)(\boldsymbol{B}_0 \cdot \boldsymbol{B}_0)(\boldsymbol{k}_2 \cdot \boldsymbol{k}_2)\boldsymbol{k}_2 \quad \text{(C.25)}$$

The terms containing $\boldsymbol{k}_1 \pm \boldsymbol{k}_2$ are the scattered wave with a sum/difference frequency of $\omega_1 \pm \omega_2$. The term containing $2\boldsymbol{k}_1(2\boldsymbol{k}_2)$ is the harmonic which arises from $\boldsymbol{k}_1(\boldsymbol{k}_2)$ interacting with itself. The self-interaction cases were treated by Gol'dberg [95], and is detailed in Chapter D. Since self-interaction was already treated, Jones and Kobett [27] chose only to consider the terms which represent interactions between two waves. Thus, Equation C.22 reduces to,

$$RHS = \boldsymbol{I}^{+}\sin\left[(\omega_1 + \omega_2)t - (\boldsymbol{k}_1 + \boldsymbol{k}_2)\cdot\boldsymbol{r}\right] + \boldsymbol{I}^{-}\sin\left[(\omega_1 - \omega_2)t - (\boldsymbol{k}_1 - \boldsymbol{k}_2)\cdot\boldsymbol{r}\right] \quad \text{(C.26)}$$

In their paper, Jones and Kobett inadvertently omitted the final term in Equation C.23, *i.e.*, the term succeeding the coefficient $(K + \frac{2}{3}\mu + B)$. This error was pointed out by Childress and Hambrick [104]; however, they too made a slight error (in the dot products involving $\boldsymbol{k}_1$ and $\boldsymbol{k}_2$ in the last term). This error has been corrected in Equation C.23.

Neglecting the terms in which the primary waves interact with themselves, Equation C.19 can be rewritten as the standard form for the inhomogeneous vector equation as follows,

$$\frac{\partial^2 \boldsymbol{u}^2(\boldsymbol{r},t)}{\partial t^2} - c_L^2\boldsymbol{\nabla}(\boldsymbol{\nabla}\cdot\boldsymbol{u}^s(\boldsymbol{r},t)) + c_S^2\boldsymbol{\nabla}\times\boldsymbol{\nabla}\times\boldsymbol{u}^s(\boldsymbol{r},t) = 4\pi\boldsymbol{q}(\boldsymbol{r},t) \quad \text{(C.27)}$$

where,

$$4\pi\boldsymbol{q}(\boldsymbol{r},t)\rho_0 = \boldsymbol{I}^{+}\sin\left[(\omega_1 + \omega_2)t - (\boldsymbol{k}_1 + \boldsymbol{k}_2)\cdot\boldsymbol{r}\right] + \boldsymbol{I}^{-}\sin\left[(\omega_1 - \omega_2)t - (\boldsymbol{k}_1 - \boldsymbol{k}_2)\cdot\boldsymbol{r}\right] \quad \text{(C.28)}$$

Using the Fourier transform pair,

$$\begin{aligned}\boldsymbol{f}(\boldsymbol{r},\omega) &= \int_{-\infty}^{\infty} e^{i\omega t}\boldsymbol{f}(\boldsymbol{r},t)dt \\ \boldsymbol{f}(\boldsymbol{r},t) &= \frac{1}{2\pi}\int_{-\infty}^{\infty} e^{-i\omega t}\boldsymbol{f}(\boldsymbol{r},\omega)d\omega\end{aligned} \quad \text{(C.29)}$$

Equations C.27 and C.28 can be written in the frequency domain. The calculation for the transformation of the left-hand side of Equation C.27 is fairly straight forward. To calculate $\boldsymbol{q}(\boldsymbol{r},\omega)$ on the right-hand side, use is made of Euler's formula,

$$\sin(x) = \frac{e^{ix} - e^{-ix}}{2i} \tag{C.30}$$

and Dirac's delta function,

$$\int_{-\infty}^{\infty} \delta(x)dx = 1 \tag{C.31}$$

$$\delta(x) = \begin{cases} 0, & \text{for } x \neq 0 \\ \infty, & \text{for } x = 0 \end{cases} \tag{C.32}$$

where a useful expression for Dirac's delta function is,

$$\delta(x-\alpha) = \frac{1}{2\pi}\int_{-\infty}^{\infty} e^{ip(x-\alpha)}dp \tag{C.33}$$

So that the Equations C.27 and C.28 can be written in the frequency domain as follows,

$$-\omega^2\boldsymbol{u}^s(\boldsymbol{r},\omega) - c_L^2\boldsymbol{\nabla}(\boldsymbol{\nabla}\cdot\boldsymbol{u}^s(\boldsymbol{r},\omega)) + c_S^2\boldsymbol{\nabla}\times\boldsymbol{\nabla}\times\boldsymbol{u}^s(\boldsymbol{r},\omega) = 4\pi\boldsymbol{q}(\boldsymbol{r},\omega) \tag{C.34}$$

where,

$$\begin{aligned}\boldsymbol{q}(\boldsymbol{r},\omega) = &\frac{\boldsymbol{I}^+}{4i\rho_0}\left[e^{-i(\boldsymbol{k}_1+\boldsymbol{k}_2)\cdot\boldsymbol{r}}\delta(\omega+\omega_1+\omega_2) - e^{i(\boldsymbol{k}_1+\boldsymbol{k}_2)\cdot\boldsymbol{r}}\delta(\omega-\omega_1-\omega_2)\right] \\ &+\frac{\boldsymbol{I}^-}{4i\rho_0}\left[e^{-i(\boldsymbol{k}_1-\boldsymbol{k}_2)\cdot\boldsymbol{r}}\delta(\omega+\omega_1-\omega_2) - e^{i(\boldsymbol{k}_1-\boldsymbol{k}_2)\cdot\boldsymbol{r}}\delta(\omega-\omega_1+\omega_2)\right]\end{aligned} \tag{C.35}$$

Recall that this interaction term, $\boldsymbol{q}(\boldsymbol{r},\omega)$, is composed of the product of the amplitude vectors, $\boldsymbol{A}_0$ and $\boldsymbol{B}_0$, of the primary waves. Therefore, this term should only be non-zero in the region within which the interaction between the primary waves takes place. Outside of this region, $\boldsymbol{q}(\boldsymbol{r},\omega)$ should be zero. The region where the primary beams intersect will be referred to as the region (or volume) of interaction and denoted by V.

The solution of Equation C.34 can be written in the form,

$$\boldsymbol{u}^s(\boldsymbol{r},\omega) = \int_V \boldsymbol{G}(\boldsymbol{r},\boldsymbol{r'},\omega)\boldsymbol{q}(\boldsymbol{r},\omega)dV \tag{C.36}$$

The term $\boldsymbol{G}(\boldsymbol{r},\boldsymbol{r'},\omega)$ is a second-order tensor. The above equation is a solution to Equation C.34 within the infinite region as long as the assumption is made that $\boldsymbol{u}(\boldsymbol{r},\omega)$ decreases at least as fast as $\frac{1}{r}$ for large r. The tensor $\boldsymbol{G}(\boldsymbol{r},\boldsymbol{r'},\omega)$ is the familiar Green's function, which is defined in the infinite region as,

$$\boldsymbol{G}(\boldsymbol{r},\boldsymbol{r'},\omega) = \frac{1}{c_L^2}\boldsymbol{G}_L\left(\boldsymbol{r},\boldsymbol{r'},\frac{\omega}{c_L}\right) + \frac{1}{c_S^2}\boldsymbol{G}_T\left(\boldsymbol{r},\boldsymbol{r'},\frac{\omega}{c_S}\right) \tag{C.37}$$

where $\boldsymbol{G}_L$ and $\boldsymbol{G}_T$ are the dilatational and shear terms, respectively. These terms are given by,

$$\begin{aligned}
\boldsymbol{G}_L\left(\boldsymbol{r},\boldsymbol{r'},\frac{\omega}{c_L}\right) &= \left(\boldsymbol{I}\left[\frac{1-i\left(\frac{\omega}{c_L}\right)R}{\left(\frac{\omega^2}{c_L^2}\right)R^2}\right] - \frac{\boldsymbol{RR}}{R^2}\left[\frac{3-i\left(\frac{\omega}{c_L}\right)R-\left(\frac{\omega^2}{c_L^2}\right)R^2}{\left(\frac{\omega^2}{c_L^2}\right)R^2}\right]\right) \\
&\quad \times \frac{\exp\left[i\left(\frac{\omega}{c_L}\right)R\right]}{R} \\
\boldsymbol{G}_T\left(\boldsymbol{r},\boldsymbol{r'},\frac{\omega}{c_S}\right) &= \left(-\boldsymbol{I}\left[\frac{1-i\left(\frac{\omega}{c_S}\right)R-\left(\frac{\omega^2}{c_S^2}\right)R^2}{\left(\frac{\omega^2}{c_S^2}\right)R^2}\right] + \frac{\boldsymbol{RR}}{R^2}\left[\frac{3-i\left(\frac{\omega}{c_S}\right)R-\left(\frac{\omega^2}{c_S^2}\right)R^2}{\left(\frac{\omega^2}{c_S^2}\right)R^2}\right]\right) \\
&\quad \times \frac{\exp\left[i\left(\frac{\omega}{c_S}\right)R\right]}{R}
\end{aligned} \tag{C.38}$$

where $\boldsymbol{I}$ is the identity tensor, $\boldsymbol{R} = \boldsymbol{r} - \boldsymbol{r'}$, and $R = |\boldsymbol{R}|$. See Figure C.2. The expressions in C.38 can be simplified by considering the point of observation to be in the far field, *i.e.*, large $\boldsymbol{r}$ so that $\left(\frac{\omega}{c_L}\right)R >> 1$ and $\left(\frac{\omega}{c_S}\right)R >> 1$ for all $\boldsymbol{r'}$ in the interaction region. The expressions can be further simplified by considering $|\boldsymbol{r'}| << |\boldsymbol{r}|$ so that $R \approx r - \hat{\boldsymbol{r}}\cdot\boldsymbol{r'}$, where $\hat{\boldsymbol{r}} = \frac{\boldsymbol{r}}{|\boldsymbol{r}|}$ is the unit vector in the $\boldsymbol{r}$ direction.

$$\begin{aligned}
\boldsymbol{G}_L\left(\boldsymbol{r},\boldsymbol{r'},\frac{\omega}{c_L}\right) &\approx \frac{\hat{\boldsymbol{r}}\cdot\hat{\boldsymbol{r}}}{r}\exp\left[i\left(\frac{\omega}{c_L}\right)r\right]\exp\left[-i\left(\frac{\omega}{c_L}\right)\hat{\boldsymbol{r}}\cdot\boldsymbol{r'}\right] \\
\boldsymbol{G}_T\left(\boldsymbol{r},\boldsymbol{r'},\frac{\omega}{c_S}\right) &\approx \frac{\boldsymbol{I}-\hat{\boldsymbol{r}}\cdot\hat{\boldsymbol{r}}}{r}\exp\left[i\left(\frac{\omega}{c_S}\right)r\right]\exp\left[-i\left(\frac{\omega}{c_S}\right)\hat{\boldsymbol{r}}\cdot\boldsymbol{r'}\right]
\end{aligned} \tag{C.39}$$

Thus, $\boldsymbol{G}(\boldsymbol{r},\boldsymbol{r'},\omega)$ can be found by plugging in Equation C.39 into Equation C.37. The expression obtained for $\boldsymbol{G}(\boldsymbol{r},\boldsymbol{r'},\omega)$ and $\boldsymbol{q}(\boldsymbol{r},\omega)$ (from Equation C.26) can be plugged into C.36 to obtain

$\boldsymbol{u}^s(\boldsymbol{r},\omega)$. The inverse Fourier transform (Equation C.29) can then be taken of $\boldsymbol{u}^s(\boldsymbol{r},\omega)$ to find $\boldsymbol{u}^s(\boldsymbol{r},t)$. Finally, the expression for the displacement of the scattered wave is,

$$\begin{aligned}
\boldsymbol{u}^s(\boldsymbol{r},t) = &\frac{\boldsymbol{I}^+\cdot\hat{\boldsymbol{r}}}{4\pi c_L^2\rho_0}\frac{\hat{\boldsymbol{r}}}{|\boldsymbol{r}|}\int_V \sin\left[\left(\frac{\omega_1+\omega_2}{c_L}\hat{\boldsymbol{r}}-\boldsymbol{k}_1-\boldsymbol{k}_2\right)\cdot\boldsymbol{r'}-(\omega_1+\omega_2)\left(\frac{r}{c_L}-t\right)\right]dV \\
&+\frac{\boldsymbol{I}^-\cdot\hat{\boldsymbol{r}}}{4\pi c_L^2\rho_0}\frac{\hat{\boldsymbol{r}}}{|\boldsymbol{r}|}\int_V \sin\left[\left(\frac{\omega_1-\omega_2}{c_L}\hat{\boldsymbol{r}}-\boldsymbol{k}_1+\boldsymbol{k}_2\right)\cdot\boldsymbol{r'}-(\omega_1-\omega_2)\left(\frac{r}{c_L}-t\right)\right]dV \\
&+\frac{\boldsymbol{I}^+-(\hat{\boldsymbol{r}}\cdot\boldsymbol{I}^+)\hat{\boldsymbol{r}}}{4\pi c_S^2\rho_0|\boldsymbol{r}|}\int_V \sin\left[\left(\frac{\omega_1+\omega_2}{c_S}\hat{\boldsymbol{r}}-\boldsymbol{k}_1-\boldsymbol{k}_2\right)\cdot\boldsymbol{r'}-(\omega_1+\omega_2)\left(\frac{r}{c_S}-t\right)\right]dV \\
&+\frac{\boldsymbol{I}^--(\hat{\boldsymbol{r}}\cdot\boldsymbol{I}^-)\hat{\boldsymbol{r}}}{4\pi c_S^2\rho_0|\boldsymbol{r}|}\int_V \sin\left[\left(\frac{\omega_1-\omega_2}{c_S}\hat{\boldsymbol{r}}-\boldsymbol{k}_1+\boldsymbol{k}_2\right)\cdot\boldsymbol{r'}-(\omega_1-\omega_2)\left(\frac{r}{c_S}-t\right)\right]dV
\end{aligned} \tag{C.40}$$

The four terms in Equation C.40 are termed the volume factors. The first and second terms are dilatational waves with a frequency of $\omega_1+\omega_2$ and $\omega_1-\omega_2$, respectively. The third and fourth terms are shear waves with a frequency of $\omega_1+\omega_2$ and $\omega_1-\omega_2$, respectively.

The argument for the sin term within the integral for each volume factor term is of the form,

$$\left(\frac{\omega_1\pm\omega_2}{c}\cdot\hat{\boldsymbol{r}}-\boldsymbol{k}_1\pm\boldsymbol{k}_2\right)\cdot\boldsymbol{r'}-(\omega_1\pm\omega_2)\left(\frac{r}{c}-t\right)$$

During the integration over $\boldsymbol{r'}$, the second term will remain constant. The first term, however, will oscillate between fixed limits depending on the size of the region and on how the waves fit within that region. This is true, unless there is a direction $\hat{\boldsymbol{r}}=\hat{\boldsymbol{r}}_s$ for which the integrand is constant so that,

$$\frac{\omega_1\pm\omega_2}{c}\cdot\hat{\boldsymbol{r}}_s-\boldsymbol{k}_1\pm\boldsymbol{k}_2=0 \tag{C.41}$$

This is called the resonance condition. Thus, when the resonance condition is satisfied at $\hat{\boldsymbol{r}}=\hat{\boldsymbol{r}}_s$, the amplitude of the scattered wave is directly proportional to the size of the interaction region and does not oscillate. In directions where $\hat{\boldsymbol{r}}\neq\hat{\boldsymbol{r}}_s$, the amplitude of the scattered wave will oscillate and the magnitude will depend on the integration limits. In these directions, the wave has the characteristics of a diffracted wave. Therefore, the resonance conditions for the scattered waves for

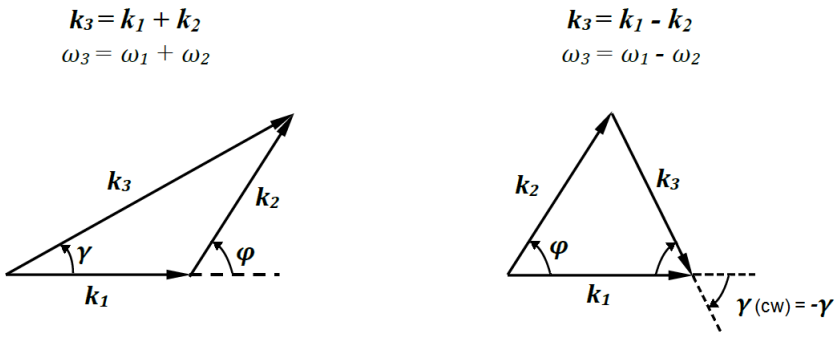

Figure C.3: Two intersecting waves $\boldsymbol{k}_1$ and $\boldsymbol{k}_2$ which interact to produce a scattered wave with **(*a*)** a sum frequency $\omega_3 = \omega_1 + \omega_2$ or **(*b*)** a difference frequency $\omega_3 = \omega_1 - \omega_2$. for the difference frequency case, the angle γ between $\boldsymbol{k}_1$ and $\boldsymbol{k}_3$ is negative to denote a clockwise rotation of γ.

all four volume factors in Equation C.40 are as follows,

$$\begin{aligned}
\frac{\omega_1 + \omega_2}{c_L}\hat{\boldsymbol{r}}_s - (\boldsymbol{k}_1 + \boldsymbol{k}_2) = 0 \\
\frac{\omega_1 - \omega_2}{c_L}\hat{\boldsymbol{r}}_s - (\boldsymbol{k}_1 - \boldsymbol{k}_2) = 0 \\
\frac{\omega_1 + \omega_2}{c_S}\hat{\boldsymbol{r}}_s - (\boldsymbol{k}_1 + \boldsymbol{k}_2) = 0 \\
\frac{\omega_1 - \omega_2}{c_S}\hat{\boldsymbol{r}}_s - (\boldsymbol{k}_1 - \boldsymbol{k}_2) = 0
\end{aligned} \tag{C.42}$$

The angle at which the primary waves interact is denoted as φ. See Figure C.3. For non-collinear waves,

$$-1 < \cos(\varphi) < 1 \tag{C.43}$$

The direction of propagation of the scattered wave $\boldsymbol{k}_3$ is described by the angle γ. For consistency, $\boldsymbol{k}_2$ and $\boldsymbol{k}_3$ propagate in directions which are described by angles measured with respect to $\boldsymbol{k}_1$. The sum frequency case is relatively straightforward, as $\boldsymbol{k}_3 = \boldsymbol{k}_1 + \boldsymbol{k}_2$. See Figure C.3 (a). For the difference frequency case, $\boldsymbol{k}_3 = \boldsymbol{k}_1 - \boldsymbol{k}_2$, the scattered wave propagates in the direction corresponding to a clockwise rotation of γ, *i.e.*, $-\gamma$. See Figure C.3 (b). Thus, when performing the vector algebra, it is important to keep the sign notation consistent throughout the calculation.

A note on the sign of γ...

A few comments should be made on the sign of γ to avoid confusion. Since φ is restricted to angles within the range of $\pm\pi$, sum frequency interactions will always result in a positive γ, whereas difference frequency interactions will always result in a negative γ. This will now be shown.

Since a positive rotation is defined as a counterclockwise rotation from $\boldsymbol{k}_1$, $\boldsymbol{k}_1$ can be chosen to lie along the x-axis so that the vector components are,

$$\begin{aligned} \boldsymbol{k}_1 &= \begin{pmatrix} k_1 \\ 0 \end{pmatrix} \\ \boldsymbol{k}_2 &= \begin{pmatrix} k_2 \cos\varphi \\ k_2 \sin\varphi \end{pmatrix} \\ \boldsymbol{k}_3 &= \begin{pmatrix} k_1 \pm k_2 \cos\varphi \\ \pm k_2 \sin\varphi \end{pmatrix}, \text{ for } \boldsymbol{k}_3 = \boldsymbol{k}_1 \pm \boldsymbol{k}_2 \end{aligned} \tag{C.44}$$

The angle between $\boldsymbol{k}_1$ and $\boldsymbol{k}_3$ is of course denoted by γ, so that,

$$\boldsymbol{k}_1 \cdot \boldsymbol{k}_3 = k_1 k_3 \cos\gamma \tag{C.45}$$

Since cosine is an even function, nothing is known yet of the sign of γ from the above equation. The sign of the cross-product of $\boldsymbol{k}_1$ and $\boldsymbol{k}_3$ will indicate the direction of rotation.

$$\boldsymbol{k}_1 \times \boldsymbol{k}_3 = \det \begin{pmatrix} \hat{\boldsymbol{\imath}} & \hat{\boldsymbol{\jmath}} \\ k_1 & k_1 \pm k_2 \cos\varphi \\ 0 & \pm k_2 \sin\varphi \end{pmatrix} = \pm (k_1 k_2 \sin\varphi)\hat{\boldsymbol{k}} \tag{C.46}$$

where $+/-$ correspond to the sum/difference cases, respectively. Since $0 < \varphi < \pi$, then $\sin\varphi$ is always positive. Thus, for the difference frequency case, the cross product between $\boldsymbol{k}_1$ and $\boldsymbol{k}_3$ yields a vector pointing in the $-(k_1 k_2 \sin\varphi)\hat{\boldsymbol{k}}$ direction, which indicates a clockwise rotation. Conversely, the sum frequency case yields a counterclockwise rotation.

In order for interaction to be possible for a given set of waves, resonance conditions must be satisfied. In addition, polarization conditions must be met for the scattered wave to have a non-

zero amplitude. Polarization conditions will be discussed later. The resonance conditions shown in Equation C.42 be discussed in more detail in the following subsection. From Figure C.3, some useful geometric relations can be summarized. The notation is such that $k = |\boldsymbol{k}|$. For both the sum and difference frequency cases,

$$\boldsymbol{k}_1 \cdot \boldsymbol{k}_2 = k_1 k_2 \cos\varphi \tag{C.47}$$

For the sum frequency case (Figure C.3 (a)),

$$\begin{aligned} \boldsymbol{k}_3 &= \boldsymbol{k}_1 + \boldsymbol{k}_2 \\ k_3^2 &= k_1^2 + k_2^2 + 2k_1 k_2 \cos\varphi \\ k_2^2 &= k_1^2 + k_3^2 - 2k_1 k_3 \cos\gamma \\ \cos\gamma &= \frac{k_1 + k_2 \cos\varphi}{k_3} \\ \sin\gamma &= \frac{k_2}{k_3} \sin\varphi \end{aligned} \tag{C.48}$$

For the difference frequency case (Figure C.3 (b)),

$$\begin{aligned} \boldsymbol{k}_3 &= \boldsymbol{k}_1 - \boldsymbol{k}_2 \\ k_3^2 &= k_1^2 + k_2^2 - 2k_1 k_2 \cos\varphi \\ k_2^2 &= k_1^2 + k_3^2 - 2k_1 k_3 \cos\gamma \\ \cos\gamma &= \frac{k_1 - k_2 \cos\varphi}{k_3} \\ \sin\gamma &= -\frac{k_2}{k_3} \sin\varphi \end{aligned} \tag{C.49}$$

The relationships above will be used repeatedly when checking whether or not the resonance and polarization conditions are satisfied. The results from the next few sections are broadly summarized in Tables C.1, C.2, C.3, and C.4, which are located at the very end of this chapter for referencing convenience.

C.3.1 Satisfying the Resonance Conditions

Neglecting the polarization conditions for the moment (this will be discussed later), there are four sets of interacting primary waves that must be considered:

$$L(\omega_1) + L(\omega_2)$$

$$L(\omega_1) + S(\omega_2)$$

$$S(\omega_1) + L(\omega_2)$$

$$S(\omega_1) + S(\omega_2)$$

where $L(\omega)$ and $S(\omega)$ denote dilatational (longitudinal) and shear (transverse) waves, respectively with a frequency of ω. Note that the 2^{nd} and 3^{rd} cases are reciprocals, but they will still be considered separately. Without any loss of generality, the frequencies are defined such that $\omega_1 > \omega_2$. Each case must be individually checked to determine which, if any, of the four resonance conditions (Equation C.42) are satisfied. If a particular resonance condition is satisfied, the angles φ and γ (see Figure C.3) and corresponding valid frequency range can be determined. The procedure for determining if the resonance conditions are met will now be discussed in detail for each case. First, the case where two shear waves interact will be considered, as it is the simplest.

Interaction of $S(\omega_1) + S(\omega_2)$

Here, the case is considered where two transverse waves $S(\omega_1)$ and $S(\omega_2)$ cross paths at an angle φ. Thus, from Equation C.47,

$$\begin{aligned} |\boldsymbol{k}_1| = \frac{\omega_1}{c_S}, \quad |\boldsymbol{k}_2| = \frac{\omega_2}{c_S} \\ \boldsymbol{k}_1 \cdot \boldsymbol{k}_2 = \frac{\omega_1 \omega_2}{c_S^2} \cos\varphi \end{aligned} \tag{C.50}$$

All four resonance conditions from Equation C.42 must be checked to determine if they can be satisfied. If a resonance condition is satisfied, it means that the scattered wave $\boldsymbol{k}_3$, with the corresponding type for that resonance condition, has a possibility of being generated via interaction between the two primary waves $\boldsymbol{k}_1$ and $\boldsymbol{k}_2$.

Consider the first resonance condition, which corresponds to a dilatational scattered wave with a sum frequency $\omega_3 = \omega_1 + \omega_2$. Squaring both sides, recalling that $\hat{\boldsymbol{r}}_s$ is a unit vector, and using the relations in Equation C.50,

$$\begin{aligned}
\left[\frac{\omega_1+\omega_2}{c_L}\right]^2 \hat{\boldsymbol{r}}_s^2 &= (\boldsymbol{k}_1+\boldsymbol{k_2})^2 \\
\Rightarrow \left[\frac{\omega_1+\omega_2}{c_L}\right]^2 &= |\boldsymbol{k}_1|^2 + |\boldsymbol{k_2}|^2 + 2|\boldsymbol{k}_1||\boldsymbol{k_2}|\cos\varphi \\
\Rightarrow \left[\frac{\omega_1+\omega_2}{c_L}\right]^2 &= \left(\frac{\omega_1}{c_S}\right)^2 + \left(\frac{\omega_2}{c_S}\right)^2 + 2\left(\frac{\omega_1}{c_S}\right)\left(\frac{\omega_2}{c_S}\right)\cos\varphi
\end{aligned}$$

So that,

$$\cos\varphi = \frac{c_S^2}{c_L^2} + \frac{1}{2}\left(\frac{\omega_1}{\omega_2} + \frac{\omega_2}{\omega_1}\right)\left(\frac{c_S^2}{c_L^2} - 1\right) \tag{C.51}$$

Since $0 < \frac{\omega_2}{\omega_1} < 1$, $0 < \frac{c_S}{c_L} < 1$, and $-1 < \cos\varphi < 1$, Equation C.51 is only true when,

$$\frac{c_L - c_S}{c_S + c_L} < \frac{\omega_2}{\omega_1} < 1 \tag{C.52}$$

This means that the case where two shear waves interact to produce a scattered dilatational wave with a sum frequency is possible, so long as the frequency ratio $\frac{\omega_2}{\omega_1}$ is within the correct bounds (and the polarization condition is met). Now the direction of the scattered wave can be determined. Refer to Figure C.3. The direction of the scattered wave is described by γ, which is the angle between $\boldsymbol{k}_1$ and $\boldsymbol{k}_3$. Remember, it is useful to refer back to Figure C.3 and note the sign convention, particularly in the difference frequency cases. The sin and cos expressions from Equation C.48 yield the following expression for γ,

$$\tan\gamma = \frac{\sin\gamma}{\cos\gamma} = \frac{|\boldsymbol{k}_2|\sin\varphi}{|\boldsymbol{k}_1| + |\boldsymbol{k}_2|\cos\varphi} \tag{C.53}$$

So that,

$$\tan\gamma = \frac{\omega_2 \sin\varphi}{\omega_1 + \omega_2\cos\varphi} \tag{C.54}$$

Now, consider the second resonance condition from Equation C.42, which corresponds to a dilatational scattered wave with a difference frequency $\omega_3 = \omega_1 - \omega_2$. Similar to the first case, both

sides are squared and the relations in Equation C.50 are used to obtain,

$$\left[\frac{\omega_1 - \omega_2}{c_L}\right]^2 \hat{\boldsymbol{r}}_s^2 = (\boldsymbol{k}_1 - \boldsymbol{k_2})^2$$
$$\Rightarrow \left[\frac{\omega_1 - \omega_2}{c_L}\right]^2 = |\boldsymbol{k}_1|^2 + |\boldsymbol{k_2}|^2 - 2|\boldsymbol{k}_1||\boldsymbol{k_2}|\cos\varphi$$
$$\Rightarrow \left[\frac{\omega_1 + \omega_2}{c_L}\right]^2 = \left(\frac{\omega_1}{c_S}\right)^2 + \left(\frac{\omega_2}{c_S}\right)^2 - 2\left(\frac{\omega_1}{c_S}\right)\left(\frac{\omega_2}{c_S}\right)\cos\varphi$$

So that,

$$\cos\varphi = \frac{c_S^2}{c_L^2} + \frac{1}{2}\left(\frac{\omega_1}{\omega_2} + \frac{\omega_2}{\omega_1}\right)\left(1 - \frac{c_S^2}{c_L^2}\right) \tag{C.55}$$

Now, in order for this to be physically realizable, the above must be satisfied for $0 < \frac{\omega_2}{\omega_1} < 1$, $0 < \frac{c_S}{c_L} < 1$, and $-1 < \cos\varphi < 1$. For this reason, the second resonance condition *cannot be satisfied* for the case of two interacting shear waves. The third and fourth resonance conditions yield similar results: neither is satisfied for the case of two interacting transverse waves. So, out of the four possible scenarios considered for the interaction between two shear waves, only the case where they interact to produce a dilatational wave with a sum frequency satisfies the resonance conditions.

The same procedure as was shown in the above example can be used to determine if the resonance conditions are met for all 54 possible interaction cases. For completeness, the rest of the results will now be presented. The complete summary of these results is contained in Table C.1 on page 200.

Interaction of $L(\omega_1) + L(\omega_2)$

Here, the case where two dilatational waves $L(\omega_1)$ and $L(\omega_2)$ cross paths at an angle φ. Thus,

$$|\boldsymbol{k}_1| = \frac{\omega_1}{c_L}, \quad |\boldsymbol{k}_2| = \frac{\omega_2}{c_L} \tag{C.56}$$

Following the same procedure as before, it is found that only the fourth resonance condition (scattered shear wave with a difference frequency) is satisfied. The corresponding parameters are,

$$\begin{aligned} \cos\varphi &= \frac{c_L^2}{c_S^2} + \frac{1}{2}\left(1 - \frac{c_L^2}{c_S^2}\right)\left(\frac{\omega_1}{\omega_2} + \frac{\omega_2}{\omega_1}\right) \\ \tan\gamma &= \frac{-\omega_2 \sin\varphi}{\omega_1 - \omega_2 \cos\varphi} \\ \frac{c_L - c_S}{c_L + c_S} &< \frac{\omega_2}{\omega_1} < 1 \end{aligned} \tag{C.57}$$

Interaction of $L(\omega_1) + S(\omega_2)$

For a dilatational wave with frequency ω_1 interacting with a shear wave with frequency ω_2,

$$|\boldsymbol{k}_1| = \frac{\omega_1}{c_L}, \quad |\boldsymbol{k}_2| = \frac{\omega_2}{c_S} \tag{C.58}$$

This case satisfies all of the resonance conditions except for the third one. For the first resonance condition,

$$\begin{aligned} \cos\varphi &= \frac{c_S}{c_L} + \frac{1}{2}\frac{\omega_2}{\omega_1}\left(\frac{c_S}{c_L} - \frac{c_L}{c_S}\right) \\ \tan\gamma &= \frac{c_L \omega_2 \sin\varphi}{c_S\omega_1 + c_L\omega_2 \cos\varphi} \\ 0 < \frac{\omega_2}{\omega_1} &< \begin{cases} \frac{2c_S}{c_L - c_S} & \text{for } 0 < \frac{c_S}{c_L} \leq \frac{1}{3} \\ 1 & \text{for } \frac{1}{3} < \frac{c_S}{c_L} < 1 \end{cases} \end{aligned} \tag{C.59}$$

For the second resonance condition,

$$\begin{aligned} \cos\varphi &= \frac{c_S}{c_L} - \frac{1}{2}\frac{\omega_2}{\omega_1}\left(\frac{c_S}{c_L} - \frac{c_L}{c_S}\right) \\ \tan\gamma &= \frac{-c_L \omega_2 \sin\varphi}{c_S\omega_1 - c_L\omega_2 \cos\varphi} \\ 0 < \frac{\omega_2}{\omega_1} &< \frac{2c_S}{c_L + c_S} \end{aligned} \tag{C.60}$$

Finally, for the fourth resonance condition,

$$\begin{aligned} \cos\varphi &= \frac{c_L}{c_S} - \frac{1}{2}\frac{\omega_1}{\omega_2}\left(\frac{c_L}{c_S} - \frac{c_S}{c_L}\right) \\ \tan\gamma &= \frac{-c_L\omega_2\sin\varphi}{c_S\omega_1 - c_L\omega_2\cos\varphi} \\ \frac{c_L - c_S}{2c_L} &< \frac{\omega_2}{\omega_1} < \frac{c_L + c_S}{2c_L} \end{aligned} \tag{C.61}$$

Interaction of $S(\omega_1) + L(\omega_2)$

Now the case is considered where a dilatational wave with frequency ω_2 interacts with a shear wave with frequency ω_1. This case is the reciprocal case to the one just considered. The difference comes from geometry and the fact that the frequencies were defined such that $\omega_1 > \omega_2$. For this case,

$$|\boldsymbol{k}_1| = \frac{\omega_1}{c_S}, \quad |\boldsymbol{k}_2| = \frac{\omega_2}{c_L} \tag{C.62}$$

Only the first resonance condition is satisfied,

$$\begin{aligned} \cos\varphi &= \frac{c_S}{c_L} + \frac{1}{2}\frac{\omega_1}{\omega_2}\left(\frac{c_S}{c_L} - \frac{c_L}{c_S}\right) \\ \tan\gamma &= \frac{c_S\omega_2\sin\varphi}{c_L\omega_1 + c_S\omega_2\cos\varphi} \\ \frac{c_L - c_S}{2c_S} < \frac{\omega_2}{\omega_1} &< \begin{cases} 1 \text{ for } \frac{1}{3} < \frac{c_S}{c_L} < 1 \\ \text{otherwise does not satisify resonance condition} \end{cases} \end{aligned} \tag{C.63}$$

Refer to Table C.1 on page 200, which contains a summary of the resonance conditions for all 54 potential interaction cases.

C.3.2 Satisfying the Polarization Condition

Once it is determined that the resonance condition can be satisfied, the amplitude of the scattered wave should be calculated. Under certain conditions, the calculations may yield a zero amplitude; thus, in order for a scattered wave to exist, both resonance *and* polarization conditions must be satisfied. The amplitude calculations are carried out in the same manner for all cases. The procedure for obtaining the amplitude will be presented in detail for all of the cases which have been

shown to satisfy the resonance conditions. See Table C.1. First, the case where $S(\omega_1) + S(\omega_2) \rightarrow L(\omega_1 + \omega_2)$ will be discussed, followed by the case where $L(\omega_1) + S(\omega_2) \rightarrow S(\omega_1 - \omega_2)$, as they are the most computationally comprehensive and representative. Discussions on the rest of the cases will follow. Diligence should be taken when defining $\boldsymbol{k}_1$, $\boldsymbol{k}_2$, $\boldsymbol{A}_0$, $\boldsymbol{B}_0$, and $\boldsymbol{C}_0$, and their respective dot products to avoid potential errors.

Jones and Kobett [27] briefly discussed the polarization conditions; however, they did not check every case, nor did they consider shear-vertical and shear-horizontal polarized waves separately. Korneev et. al [30] considered the polarization conditions in more detail and provided expressions for the amplitudes. This section will closely follow their method. In total, there are 8 non-collinear cases which satisfy both the polarization and resonance conditions. Expressions for the amplitudes were calculated for all 8 cases and are summarized in Table C.2. The cases each have an associated assigned number to facilitate future reference. Table C.4 summarizes the interaction cases which meet both the resonance and polarization conditions. The calculations for each of the amplitude expressions will now be presented in detail. From this point forward, the coefficients of Equation C.15 will be renamed in a more succinct manner as follows,

$$C_1 = \mu + \frac{A}{4}, \qquad C_2 = \mu + \frac{A}{4} + B + \lambda, \qquad C_3 = B + \lambda, \qquad C_4 = \frac{A}{4} + B, \qquad C_5 = B + 2C \quad \text{(C.64)}$$

It was shown in the previous sub-section, that a strong scattered wave is generated when a direction is found such that $\hat{\boldsymbol{r}} = \hat{\boldsymbol{r}}_s$ so that first term in the sin argument goes to zero for the volume factors in Equation C.40. Carrying out the integration, the expressions for the four types of scattered waves, which have met resonance conditions, are listed below:

$$\begin{aligned}
L(\omega_1 + \omega_2): \quad & \boldsymbol{u}_s(\hat{\boldsymbol{r}}_{\boldsymbol{s}}, t) = \frac{\boldsymbol{I}^+ \cdot \hat{\boldsymbol{r}}_s}{4\pi c_L^2 \rho_0} \frac{\hat{\boldsymbol{r}}_{\boldsymbol{s}}}{|\boldsymbol{r}|} V \sin\left[(\omega_1 + \omega_2)\left(t - \frac{|\boldsymbol{r}|}{c_L}\right)\right] \\
L(\omega_1 - \omega_2): \quad & \boldsymbol{u}_s(\hat{\boldsymbol{r}}_{\boldsymbol{s}}, t) = \frac{\boldsymbol{I}^- \cdot \hat{\boldsymbol{r}}_s}{4\pi c_L^2 \rho_0} \frac{\hat{\boldsymbol{r}}_{\boldsymbol{s}}}{|\boldsymbol{r}|} V \sin\left[(\omega_1 - \omega_2)\left(t - \frac{|\boldsymbol{r}|}{c_L}\right)\right] \\
S(\omega_1 + \omega_2): \quad & \boldsymbol{u}_s(\hat{\boldsymbol{r}}_{\boldsymbol{s}}, t) = \frac{\boldsymbol{I}^+ - (\boldsymbol{I}^+ \cdot \hat{\boldsymbol{r}}_s)\hat{\boldsymbol{r}}_{\boldsymbol{s}}}{4\pi c_S^2 \rho_0 |\boldsymbol{r}|} V \sin\left[(\omega_1 + \omega_2)\left(t - \frac{|\boldsymbol{r}|}{c_S}\right)\right] \\
S(\omega_1 - \omega_2): \quad & \boldsymbol{u}_s(\hat{\boldsymbol{r}}_{\boldsymbol{s}}, t) = \frac{\boldsymbol{I}^- - (\boldsymbol{I}^- \cdot \hat{\boldsymbol{r}}_s)\hat{\boldsymbol{r}}_{\boldsymbol{s}}}{4\pi c_S^2 \rho_0 |\boldsymbol{r}|} V \sin\left[(\omega_1 - \omega_2)\left(t - \frac{|\boldsymbol{r}|}{c_S}\right)\right]
\end{aligned} \quad \text{(C.65)}$$

At this point, nothing has been said about the polarization of the shear waves, *i.e.*, whether they are polarized in or out of the $\boldsymbol{k_1} - \boldsymbol{k_2}$ plane. The particles in the wave oscillate in the direction of the polarization. The scattered wave displacements in Equation C.65 can therefore be written as the vector projection onto $\hat{\boldsymbol{C}}_0$, which is the unit vector in the direction of the polarization. The amplitude of the wave is then proportional to the projection onto $\hat{\boldsymbol{C}}_0$. Therefore, the amplitudes for the scattered waves are,

$$\begin{aligned}
L(\omega_1+\omega_2): \quad & Amplitude = \left(\frac{\boldsymbol{I}^+ \cdot \hat{\boldsymbol{r}}_s}{4\pi c_L^2 \rho_0} V\right) \frac{\hat{\boldsymbol{r}}_{\boldsymbol{s}} \cdot \hat{\boldsymbol{C}}_0}{|\boldsymbol{r}|} \\
L(\omega_1-\omega_2): \quad & Amplitude = \left(\frac{\boldsymbol{I}^- \cdot \hat{\boldsymbol{r}}_s}{4\pi c_L^2 \rho_0} V\right) \frac{\hat{\boldsymbol{r}}_{\boldsymbol{s}} \cdot \hat{\boldsymbol{C}}_0}{|\boldsymbol{r}|} \\
S(\omega_1+\omega_2): \quad & Amplitude = \left(\frac{\boldsymbol{I}^+ - (\boldsymbol{I}^+ \cdot \hat{\boldsymbol{r}}_s)\hat{\boldsymbol{r}}_{\boldsymbol{s}}}{4\pi c_S^2 \rho_0 |\boldsymbol{r}|} V\right) \cdot \hat{\boldsymbol{C}}_0 \\
S(\omega_1-\omega_2): \quad & Amplitude = \left(\frac{\boldsymbol{I}^- - (\boldsymbol{I}^- \cdot \hat{\boldsymbol{r}}_s)\hat{\boldsymbol{r}}_{\boldsymbol{s}}}{4\pi c_S^2 \rho_0 |\boldsymbol{r}|} V\right) \cdot \hat{\boldsymbol{C}}_0
\end{aligned} \tag{C.66}$$

The polarization condition is met when the amplitude is non-zero. There are certain interaction cases where, even though the resonance condition is satisfied, the amplitude is zero. If the polarization condition is not satisfied, the interaction will not take place. This section will now examine each of the cases which have already been shown to satisfy resonance conditions in detail and amplitude expressions will be provided. Table C.2 contains a summary of these amplitude expressions.

Interaction of $S(\omega_1) + S(\omega_2) \rightarrow L(\omega_1 + \omega_2)$

First, consider the case where two shear waves interact to produce a scattered dilatational wave. For this case, the expression for the scattered wave is given as the first expression in Equation C.65. From the resonance condition (Equation C.42),

$$\hat{\boldsymbol{r}}_s = (\boldsymbol{k}_1 + \boldsymbol{k}_2)\left[\frac{c_L}{\omega_1 + \omega_2}\right] \tag{C.67}$$

And,

$$\boldsymbol{k}_1 = \frac{\omega_1}{c_S}\hat{\boldsymbol{k}}_1, \quad \boldsymbol{k}_2 = \frac{\omega_2}{c_S}\hat{\boldsymbol{k}}_2, \quad \boldsymbol{k}_3 = \frac{\omega_1 + \omega_2}{c_L}\hat{\boldsymbol{r}}_s, \tag{C.68}$$

where $\hat{\boldsymbol{k}}_1$ and $\hat{\boldsymbol{k}}_2$ are unit vectors pointing in the $\boldsymbol{k}_1$ and $\boldsymbol{k}_2$ directions, respectively. It is useful to refer to Figure C.4, which shows the geometry of the interaction for the cases where the shear

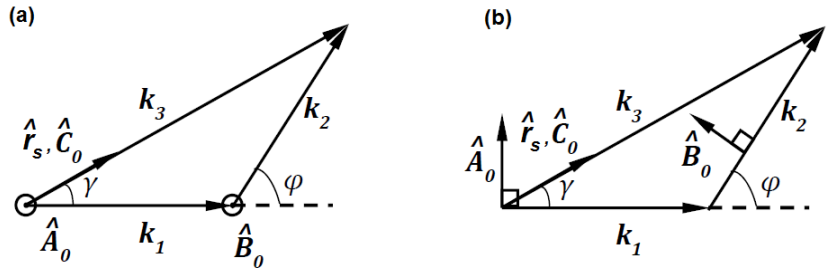

Figure C.4: Geometry of two shear waves $\boldsymbol{k}_1$ and $\boldsymbol{k}_2$ polarized **(*a*)** out of the $\boldsymbol{k}_1 - \boldsymbol{k}_2$ plane and **(*b*)** in the $\boldsymbol{k}_1 - \boldsymbol{k}_2$ plane, which interact to produce a scattered dilatational wave $\boldsymbol{k}_3$. The geometry shown is for the sum frequency ($\omega_3 = \omega_1 + \omega_2$) case. The amplitude vectors $\boldsymbol{A}_0$, $\boldsymbol{B}_0$, and $\boldsymbol{C}_0$, are the unit vectors pointed in the direction of the particle oscillation, *i.e.*, wave polarization.

waves are polarized out of the the $\boldsymbol{k}_1 - \boldsymbol{k}_2$ plane (Figure C.4 (a)) and in the $\boldsymbol{k}_1 - \boldsymbol{k}_2$ plane (Figure C.4 (b)). First, let both shear waves be polarized out of the $\boldsymbol{k}_1 - \boldsymbol{k}_2$ plane,

$$S_\perp(\omega_1) + S_\perp(\omega_2) \rightarrow L(\omega_1 + \omega_2)$$

Along with the dot products defined in Equations C.47 and C.48, the following dot products can be defined based on the geometry in Figure C.4 (a),

$$\begin{gathered}
\boldsymbol{A}_0 \perp \boldsymbol{k}_1 \Rightarrow \boldsymbol{A}_0 \cdot \boldsymbol{k}_1 = 0, \\
\boldsymbol{B}_0 \perp \boldsymbol{k}_2 \Rightarrow \boldsymbol{B}_0 \cdot \boldsymbol{k}_2 = 0 \\
\boldsymbol{C}_0 \cdot \hat{\boldsymbol{r}}_s = C_0 \\
\boldsymbol{A}_0 \cdot \boldsymbol{k}_2 = 0, \quad \boldsymbol{B}_0 \cdot \boldsymbol{k}_1 = 0 \\
\boldsymbol{A}_0 \cdot \boldsymbol{B}_0 = A_0 B_0
\end{gathered} \tag{C.69}$$

Using the expression for $\hat{\boldsymbol{r}}_s$ from Equation C.67, the following useful dot products can be found,

$$\begin{aligned}
\boldsymbol{k}_1 \cdot \hat{\boldsymbol{r}}_s &= (k_1^2 + k_1 k_2 \cos\varphi) \left[\frac{c_L}{\omega_1 + \omega_2}\right] \\
\boldsymbol{k}_2 \cdot \hat{\boldsymbol{r}}_s &= (k_2^2 + k_1 k_2 \cos\varphi) \left[\frac{c_L}{\omega_1 + \omega_2}\right]
\end{aligned} \tag{C.70}$$

By substituting magnitudes from Equation C.68 and the dot products listed in the last two equations into Equation C.23, an expression for $\boldsymbol{I}^+ \cdot \hat{\boldsymbol{r}}_s$ can be found (after some algebraic simplification)

as,

$$\boldsymbol{I}^{+} \cdot \hat{\boldsymbol{r}}_s = -\frac{A_0 B_0}{2}\left(\frac{\omega_1\omega_2}{\omega_1+\omega_2}\right)\frac{c_L}{c_S^4}\left[C_1\left(2\omega_1\omega_2 + (\omega_1^2+\omega_2^2)\cos\varphi\right)\right. \\ \left. + C_2\cos\varphi\left(\omega_1^2+\omega_2+2\omega_1\omega_2\cos\varphi\right)\right] \tag{C.71}$$

which can then be plugged into the corresponding expression, *i.e.*, the first one, for the displacement vector $\boldsymbol{u}_s(\hat{\boldsymbol{r}}_s, t)$ in Equation C.65 to obtain,

$$\boldsymbol{u}_s(\hat{\boldsymbol{r}}_{\boldsymbol{s}}, t) = \frac{-A_0 B_0}{8\pi\rho_0}\left(\frac{\omega_1\omega_2}{\omega_1+\omega_2}\right)\left(\frac{1}{c_L c_S^4}\right)\frac{\hat{\boldsymbol{r}}_s}{|\boldsymbol{r}|}V \\ \times\left[C_1\left(2\omega_1\omega_2 + (\omega_1^2+\omega_2^2)\cos\varphi\right) + C_2\cos\varphi\left(\omega_1^2+\omega_2+2\omega_1\omega_2\cos\varphi\right)\right] \tag{C.72}$$

Since the polarization of the scattered wave is in the same direction as the wave propagation, *i.e.*, a dilatational wave,

$$\hat{\boldsymbol{r}}_s \cdot \hat{\boldsymbol{C}}_0 = 1 \tag{C.73}$$

So that the amplitude of Equation C.66, for the case where the shear waves are polarized out of the $\boldsymbol{k}_1 - \boldsymbol{k}_2$ plane is,

$$\textit{Amplitude} = -\frac{A_0 B_0}{8\pi\rho_0|\boldsymbol{r}|}\left(\frac{\omega_1\omega_2}{\omega_1+\omega_2}\right)\left(\frac{1}{c_L c_S^4}\right)V \\ \times\left[C_1(2\omega_1\omega_2 + (\omega_1^2+\omega_2^2)\cos\varphi) + C_2(\omega_1^2+\omega_2^2+2\omega_1\omega_2\cos\varphi)\cos\varphi\right] \tag{C.74}$$

Now, let the shear waves be polarized in the $\boldsymbol{k}_1 - \boldsymbol{k}_2$ plane,

$$S_{\parallel}(\omega_1) + S_{\parallel}(\omega_2) \rightarrow L(\omega_1+\omega_2)$$

Refer to Figure C.4 (b) for the geometry. The expressions for $\hat{\boldsymbol{r}}_s$, $\boldsymbol{k}_1$, and $\boldsymbol{k}_2$ are the same as for the $S_{\perp}$ case (see Equations C.67 and C.68). Now, in addition to the dot products in Equations

C.47 and C.48, the dot products are,

$$\begin{aligned}
\boldsymbol{A}_0 \cdot \boldsymbol{k}_1 = 0, \quad \boldsymbol{B}_0 \cdot \boldsymbol{k}_2 = 0 \\
\boldsymbol{A}_0 \cdot \boldsymbol{k}_2 = A_0 k_2 \cos\left(\frac{\pi}{2} - \varphi\right) = A_0 k_2 \sin\varphi \\
\boldsymbol{B}_0 \cdot \boldsymbol{k}_1 = B_0 k_1 \cos\left(\frac{\pi}{2} + \varphi\right) = -B_0 k_1 \sin\varphi \\
\boldsymbol{A}_0 \cdot \boldsymbol{B}_0 = A_0 B_0 \cos\varphi \\
\boldsymbol{A}_0 \cdot \hat{\boldsymbol{r}}_s = (A_0 k_2 \sin\varphi)\left(\frac{c_L}{\omega_1 + \omega_2}\right) \\
\boldsymbol{B}_0 \cdot \hat{\boldsymbol{r}}_s = (-B_0 k_1 \sin\varphi)\left(\frac{c_L}{\omega_1 + \omega_2}\right)
\end{aligned} \tag{C.75}$$

Which after some algebra, yields an expression for $\boldsymbol{I}^+ \cdot \hat{\boldsymbol{r}}_s$,

$$\begin{aligned}
\boldsymbol{I}^+ \cdot \hat{\boldsymbol{r}}_s = \frac{-A_0 B_0}{4}\left(\frac{c_L}{c_S^4}\right)\left(\frac{\omega_1\omega_2}{\omega_1 + \omega_2}\right)(\omega_1^2 + \omega_2^2 + 2\omega_1\omega_2\cos\varphi) \\
\times \left[2C_1\cos(2\varphi) + C_2\cos^2\varphi + C_3\sin^2\varphi\right]
\end{aligned} \tag{C.76}$$

As was true in the last case, the polarization of the scattered wave is in the same direction as the wave propagation so that $\hat{\boldsymbol{r}}_s \cdot \hat{\boldsymbol{C}}_0 = 1$. Then from Equation C.66,

$$\begin{aligned}
\textit{Amplitude} = -\frac{A_0 B_0}{8\pi\rho_0|\boldsymbol{r}|}\left(\frac{\omega_1\omega_2}{\omega_1 + \omega_2}\right)\left(\frac{1}{c_L c_S^4}\right)V(\omega_1^2 + \omega_2^2 + 2\omega_1\omega_2\cos\varphi) \\
\times \left[2C_1\cos(2\varphi) + C_2\cos^2\varphi + C_3\sin^2\varphi\right]
\end{aligned} \tag{C.77}$$

At this point, it is worth mentioning that the cases where the primary shear waves have polarizations of different types fail the polarization condition. In other words, the cases where,

$$\begin{aligned}
S_\parallel(\omega_1) + S_\perp(\omega_2) \rightarrow L(\omega_1 + \omega_2) \\
S_\perp(\omega_1) + S_\parallel(\omega_2) \rightarrow L(\omega_1 + \omega_2)
\end{aligned}$$

yield zero amplitude scattered waves. It is noted that the amplitude expressions presented in Equations C.77 and C.74 differ slightly from those presented by Korneev et al. [30]. Particularly, the expressions in Korneev appear to be scaled by a factor of $\frac{c_S^2}{c_L^2}$ when compared to the expressions in Equations C.77 and C.74. It is the author's hope that sufficient detail has been given for the calculations so that the reader may carry out the computations should they wish to check them.

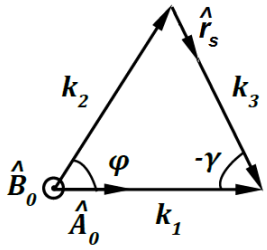

Figure C.5: Geometry of one dilatational and one shear $\boldsymbol{k}_1$ and $\boldsymbol{k}_2$ polarized out of the $\boldsymbol{k}_1 - \boldsymbol{k}_2$ plane, which interact to produce a scattered shear wave $\boldsymbol{k}_3$. The geometry shown is for the difference frequency ($\omega_3 = \omega_1 - \omega_2$) case. The amplitude vectors $\boldsymbol{A}_0$, $\boldsymbol{B}_0$, and $\boldsymbol{C}_0$, are the unit vectors pointed in the direction of the particle oscillation, *i.e.*, wave polarization.

Other differences between Korneev's results and the results presented here will be noted as they occur.

Interaction of $L(\omega_1) + S_\perp(\omega_2) \rightarrow S(\omega_1 - \omega_2)$

Now consider the case where a dilatational wave interacts with a shear wave polarized out of the $\boldsymbol{k}_1 - \boldsymbol{k}_2$ plane. See Figure C.5. The dot products (in addition to those presented in Equations C.47) and C.49 are as follows,

$$\begin{gathered} \boldsymbol{A}_0 \cdot \boldsymbol{k}_1 = A_0 k_1, \quad \boldsymbol{B}_0 \cdot \boldsymbol{k}_2 = 0 \\ \boldsymbol{A}_0 \cdot \boldsymbol{k}_2 = A_0 k_2 \cos\varphi, \quad \boldsymbol{B}_0 \cdot \boldsymbol{k}_1 = 0 \\ \boldsymbol{A}_0 \cdot \boldsymbol{B}_0 = 0 \end{gathered} \tag{C.78}$$

The corresponding expression for $\boldsymbol{u}_s(\hat{\boldsymbol{r}}_s, t)$ is the fourth expression in Equation C.66. Since the direction of propagation of the scattered shear wave is orthogonal to the polarization, $\hat{\boldsymbol{r}}_s \cdot \hat{\boldsymbol{C}}_0 = 0$. Therefore, the second term in the numerator of the amplitude expression (Equation C.66) goes to zero, and the amplitude is proportional to $\boldsymbol{I}^- \cdot \hat{\boldsymbol{C}}_0$. The expression for $\boldsymbol{I}^-$ is found by plugging in the dot products from Equation C.78 into Equation C.23 to obtain,

$$\boldsymbol{I}^- = \frac{-A_0}{2} \left(\frac{\omega_1 \omega_2}{c_L^2 c_S^2} \right) \left[C_1 \left(2 c_L \omega_2 \cos^2\varphi - c_S \omega_1 \cos\varphi \right) - \omega_1 c_S C_2 \cos\varphi + c_L \omega_2 C_5 \right] \boldsymbol{B}_0 \tag{C.79}$$

So that the amplitude is,

$$Amplitude = \frac{-A_0}{8\pi\rho_0|\boldsymbol{r}|}\left(\frac{\omega_1\omega_2}{c_L^2 c_S^4}\right) V\left[C_1\left(2c_L\omega_2\cos^2\varphi - c_S\omega_1\cos\varphi\right) - \omega_1 c_S C_2\cos\varphi + c_L\omega_2 C_5\right](\boldsymbol{B}_0\cdot\hat{\boldsymbol{C}}_0) \tag{C.80}$$

The dot product of $\boldsymbol{B}_0$ and $\hat{\boldsymbol{C}}_0$ depends on the polarization of the scattered shear wave.

$$\boldsymbol{B}_0\cdot\hat{\boldsymbol{C}}_0 = \begin{cases} 0 & \text{for } S_{\parallel}(\omega_1-\omega_2) \\ B_0 & \text{for } S_{\perp}(\omega_1-\omega_2) \end{cases} \tag{C.81}$$

Thus, only the case where the scattered shear wave is polarized in the same plane as the primary shear wave meets the polarization condition.

$$L(\omega_1) + S_{\perp}(\omega_2) \rightarrow S_{\perp}(\omega_1-\omega_2)$$

$$Amplitude = \frac{-A_0 B_0}{8\pi\rho_0|\boldsymbol{r}|}\left(\frac{\omega_1\omega_2}{c_L^2 c_S^4}\right) V\left[C_1\left(2c_L\omega_2\cos^2\varphi - c_S\omega_1\cos\varphi\right) - \omega_1 c_S C_2\cos\varphi + c_L\omega_2 C_5\right] \tag{C.82}$$

At this point it is clear that for all of the cases involving shear waves, every shear wave *i.e.*, primary and scattered, must be polarized in the same direction for the polarization condition to be met.

It is worth pointing out the fact that although the interaction between $L(\omega_1)$ and $S_{\perp}(\omega_2)$ were shown to satisfy the first two resonance conditions, *i.e.*, $L(\omega_1 \pm \omega_2)$, the fact that $\boldsymbol{I}^{-}\cdot\hat{\boldsymbol{r}}_s = 0$ means it fails the polarization condition for these cases as the amplitudes go to zero. This is not true for the case where the primary shear wave is polarized in the $\boldsymbol{k}_1 - \boldsymbol{k}_2$ plane, *i.e.*, $S_{\parallel}(\omega_2)$, which will be shown later.

Interaction of $L(\omega_1) + L_(\omega_2) \rightarrow S(\omega_1 - \omega_2)$

For the case where two dilatational waves interact to produce a shear wave with a difference frequency (see Figure C.6), in addition to Equations C.47 and C.49, the dot products are,

$$\begin{aligned} \boldsymbol{A}_0 \cdot \boldsymbol{k}_1 = A_0 k_1, \quad \boldsymbol{B}_0 \cdot \boldsymbol{k}_2 = B_0 k_2 \\ \boldsymbol{A}_0 \cdot \boldsymbol{k}_2 = A_0 k_2 \cos\varphi, \quad \boldsymbol{B}_0 \cdot \boldsymbol{k}_1 = B_0 k_1 \cos\varphi \\ \boldsymbol{A}_0 \cdot \boldsymbol{B}_0 = A_0 B_0 \cos\varphi \end{aligned} \tag{C.83}$$

The corresponding expressions for $\boldsymbol{u}_s(\hat{\boldsymbol{r}}_s, t)$ and the amplitude are the fourth expressions in Equations C.65 and C.66, respectively. So far, nothing has been said of the polarization of the scattered shear wave. Since the amplitude is proportional to $\boldsymbol{I}^- \cdot \hat{\boldsymbol{C}}_0$ and $\hat{\boldsymbol{r}}_s \cdot \hat{\boldsymbol{C}}_0$, it is apparent that the shear wave perpendicular to the $\boldsymbol{k}_1 - \boldsymbol{k}_2$ plane fails the polarization condition, since both $\boldsymbol{I}^- \cdot \hat{\boldsymbol{C}}_0 = 0$ and $\hat{\boldsymbol{r}}_s \cdot \hat{\boldsymbol{C}}_0 = 0$. Thus, the shear wave must be polarized in the $\boldsymbol{k}_1 - \boldsymbol{k}_2$ plane.

$$L(\omega_1) + L(\omega_2) \rightarrow S_{\|}(\omega_1 - \omega_2)$$

For a shear wave polarized in the $\boldsymbol{k}_1 - \boldsymbol{k}_2$ plane, the amplitude is proportional only to $\boldsymbol{I}^- \cdot \hat{\boldsymbol{C}}_0$ since $\hat{\boldsymbol{r}}_s \cdot \hat{\boldsymbol{C}}_0 = 0$. Then, referring to Figure C.6 (a), the dot products with the polarization vector $\hat{\boldsymbol{C}}_0$

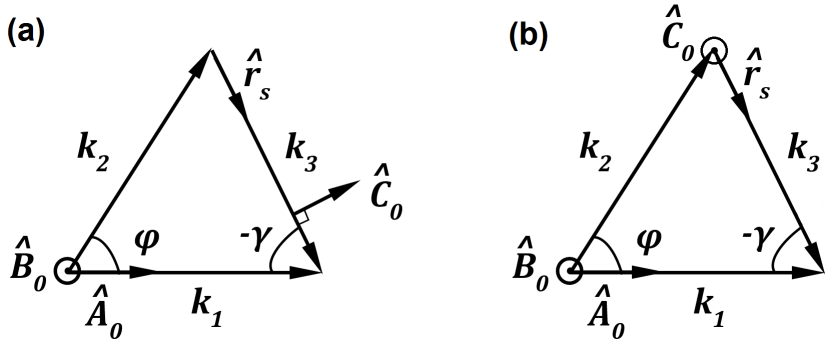

Figure C.6: Geometry of two dilatational waves $\boldsymbol{k}_1$ and $\boldsymbol{k}_2$, which interact to produce a scattered shear wave $\boldsymbol{k}_3$ polarized **(*a*)** in the $\boldsymbol{k}_1 - \boldsymbol{k}_2$ plane and **(*b*)** out of the $\boldsymbol{k}_1 - \boldsymbol{k}_2$ plane. The geometry shown is for the difference frequency ($\omega_3 = \omega_1 - \omega_2$) case. The amplitude vectors $\boldsymbol{A}_0$, $\boldsymbol{B}_0$, and $\boldsymbol{C}_0$, are the unit vectors pointed in the direction of the particle oscillation, *i.e.*, wave polarization.

are,

$$\begin{aligned}
\boldsymbol{A}_0 \cdot \hat{\boldsymbol{C}}_0 &= A_0 \cos(\frac{\pi}{2} + \gamma) = -A_0 \sin\gamma \\
\boldsymbol{k}_1 \cdot \hat{\boldsymbol{C}}_0 &= -k_1 \sin\gamma \\
\boldsymbol{B}_0 \cdot \hat{\boldsymbol{C}}_0 &= B_0 \sin(\varphi - \gamma) \\
\boldsymbol{k}_2 \cdot \hat{\boldsymbol{C}}_0 &= k_2 \sin(\varphi - \gamma)
\end{aligned} \tag{C.84}$$

However, it is more convenient if the arguments of the trigonometric functions are only in terms of the interaction angle φ. The following trigonometric identity is useful,

$$\sin(\gamma + \varphi) = \sin\gamma\cos\varphi + \cos\gamma\sin\varphi \tag{C.85}$$

The above trigonometric identity can be used along with the geometric relationships in Equation C.49 so that the dot products from Equation C.84 can be written in terms of the interaction angle as,

$$\begin{aligned}
\boldsymbol{A}_0 \cdot \hat{\boldsymbol{C}}_0 &= \frac{k_2 A_0}{k_3}\sin\varphi \\
\boldsymbol{k}_1 \cdot \hat{\boldsymbol{C}}_0 &= \frac{k_1 k_2}{k_3}\sin\varphi \\
\boldsymbol{B}_0 \cdot \hat{\boldsymbol{C}}_0 &= \frac{B_0 k_1}{k_3}\sin\varphi \\
\boldsymbol{k}_2 \cdot \hat{\boldsymbol{C}}_0 &= \frac{k_2 k_1}{k_3}\sin\varphi
\end{aligned} \tag{C.86}$$

The wave number magnitudes $k_1 = \frac{\omega_1}{c_L}$, $k_2 = \frac{\omega_1}{c_L}$, $k_3 = \frac{\omega_1 - \omega_2}{c_S}$, and the dot products from the equations listed above can be plugged into the amplitude from Equation C.66. After some algebra,

$$Amplitude = \frac{A_0 B_0}{8\pi\rho_0|\boldsymbol{r}|}\left(\frac{\omega_1\omega_2\left(\omega_1+\omega_2\right)}{c_S c_L^4}\right) V \cos\varphi\sin\varphi\left[2C_1 + C_2 + C_3\right] \tag{C.87}$$

This amplitude expression agrees with that published by Korneev et. al [30].

Interaction of $L(\omega_1) + S_{\parallel}(\omega_2) \rightarrow L(\omega_1 + \omega_2)$

Now, the case where a dilatational wave interacts with a shear wave to produce a dilatational wave with a sum frequency is considered. The shear wave is polarized in the $\boldsymbol{k}_1 - \boldsymbol{k}_2$ plane. It was shown previously that the case where $L(\omega_1) + S_{\perp}(\omega_2) \rightarrow L(\omega_1 + \omega_1)$ fails the polarization condition. Referring to Figure C.7, the dot products are,

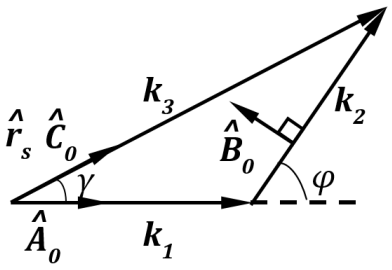

Figure C.7: Geometry of a dilatational wave $\boldsymbol{k}_1$ and shear wave $\boldsymbol{k}_2$ polarized in the $\boldsymbol{k}_1 - \boldsymbol{k}_2$ plane, which interact to produce a scattered dilatational wave $\boldsymbol{k}_3$. The geometry shown is for the sum frequency ($\omega_3 = \omega_1 + \omega_2$) case. The amplitude vectors $\boldsymbol{A}_0$, $\boldsymbol{B}_0$, and $\boldsymbol{C}_0$, are the unit vectors pointed in the direction of the particle oscillation, *i.e.*, wave polarization.

$$\begin{gathered}
\boldsymbol{A}_0 \cdot \boldsymbol{k}_1 = A_0 k_1, \quad \boldsymbol{B}_0 \cdot \boldsymbol{k}_2 = 0 \\
\boldsymbol{A}_0 \cdot \boldsymbol{k}_2 = A_0 k_2 \cos\varphi \\
\boldsymbol{k}_1 \cdot \boldsymbol{B}_0 = k_1 B_0 \cos\left(\frac{\pi}{2} + \varphi\right) = -k_1 B_0 \sin\varphi \\
\boldsymbol{A}_0 \cdot \boldsymbol{B}_0 = -A_0 B_0 \sin\varphi
\end{gathered} \tag{C.88}$$

The dot products defined above are in addition to those in Equations C.47 and C.48. The scattered wave direction vector is,

$$\hat{\boldsymbol{r}}_s = (\boldsymbol{k}_1 + \boldsymbol{k}_2)\frac{1}{k_3} \tag{C.89}$$

where $k_1 = \frac{\omega_1}{c_L}$, $k_2 = \frac{\omega_2}{c_S}$, and $k_3 = \frac{\omega_1 + \omega_2}{c_L}$. The dot products with the scattered wave direction vector $\hat{\boldsymbol{r}}_s$ are,

$$\begin{gathered}
\hat{\boldsymbol{r}}_s \cdot \hat{\boldsymbol{C}}_0 = 1 \\
\hat{\boldsymbol{r}}_s \cdot \boldsymbol{k}_1 = (k_1^2 + k_1 k_2 \cos\varphi)\frac{1}{k_3} \\
\hat{\boldsymbol{r}}_s \cdot \boldsymbol{k}_2 = (k_1 k_2 \cos\varphi + k_2^2)\frac{1}{k_3} \\
\hat{\boldsymbol{r}}_s \cdot \boldsymbol{B}_0 = -\frac{k_1 B_0}{k_3}\sin\varphi \\
\hat{\boldsymbol{r}}_s \cdot \boldsymbol{A}_0 = (A_0 k_1 + A_0 k_2 \cos\varphi)\frac{1}{k_3}
\end{gathered} \tag{C.90}$$

From Equation C.66,

$$\begin{aligned}
Amplitude = \frac{A_0 B_0}{8\pi\rho_0 |\boldsymbol{r}|}\left(\frac{\omega_1\omega_2}{\omega_1+\omega_2}\right)\left(\frac{1}{c_L^4 c_S^3}\right) V \sin\varphi \\
\times \left[C_1(2\beta + 3d) + C_2\beta + C_3(\beta + d) + C_5 d\right]
\end{aligned} \tag{C.91}$$

where,

$$\begin{aligned} \beta &= \alpha \cos\varphi + 2d\cos^2\varphi \\ \alpha &= 2c_S^2\omega_1^2 + c_L^2\omega_2^2 \\ d &= c_L c_S \omega_1 \omega_2 \end{aligned} \tag{C.92}$$

This expression agrees with that published by Korneev [30].

Interaction of $L(\omega_1) + S_{\|}(\omega_2) \rightarrow L(\omega_1 - \omega_2)$

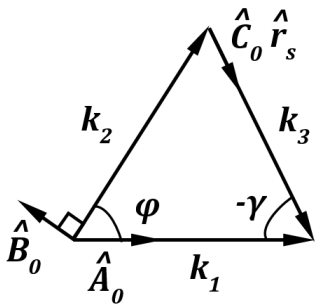

Figure C.8: Geometry of a dilatational wave $\boldsymbol{k}_1$ and shear wave $\boldsymbol{k}_2$ polarized in the $\boldsymbol{k}_1 - \boldsymbol{k}_2$ plane, which interact to produce a scattered dilatational wave $\boldsymbol{k}_3$. The geometry shown is for the difference frequency ($\omega_3 = \omega_1 - \omega_2$) case. The amplitude vectors $\boldsymbol{A}_0$, $\boldsymbol{B}_0$, and $\boldsymbol{C}_0$, are the unit vectors pointed in the direction of the particle oscillation, *i.e.*, wave polarization.

The case is now considered where one dilatational wave interacts with a shear wave polarized in the $\boldsymbol{k}_1 - \boldsymbol{k}_2$ plane to generate a dilatational wave with a difference frequency. See Figure C.8. From the resonance condition,

$$\hat{\boldsymbol{r}}_s = (\boldsymbol{k}_1 - \boldsymbol{k}_2)\left(\frac{1}{k_3}\right) \tag{C.93}$$

In addition to the dot products in Equations C.47 and C.49, the dot products are,

$$\begin{aligned} \boldsymbol{A}_0 \cdot \boldsymbol{k}_1 &= A_0 k_1, \quad \boldsymbol{B}_0 \cdot \boldsymbol{k}_2 = 0 \\ \boldsymbol{A}_0 \cdot \boldsymbol{k}_2 &= A_0 k_2 \cos\varphi, \quad \boldsymbol{B}_0 \cdot \boldsymbol{k}_1 = -B_0 k_1 \sin\varphi \\ \boldsymbol{A}_0 \cdot \boldsymbol{B}_0 &= -A_0 B_0 \sin\varphi \end{aligned} \tag{C.94}$$

where $k_1 = \frac{\omega_1}{c_L}$, $k_2 = \frac{\omega_2}{c_S}$, and $k_3 = \frac{\omega_1 - \omega_2}{c_L}$. The amplitude corresponds to the second expression in Equation C.66. Since $\hat{\boldsymbol{r}}_s \cdot \hat{\boldsymbol{C}}_0 = 1$, the amplitude is proportional to $\boldsymbol{I}^- \cdot \hat{\boldsymbol{r}}_s$. Using Equation C.93,

the dot products with $\hat{\boldsymbol{r}}_s$ are,

$$\begin{aligned}
\hat{\boldsymbol{r}}_s \cdot \boldsymbol{k}_1 &= (k_1^2 - k_1 k_2 \cos\varphi)\frac{1}{k_3} \\
\hat{\boldsymbol{r}}_s \cdot \boldsymbol{k}_2 &= (k_1 k_2 \cos\varphi - k_2^2)\left(\frac{1}{k_3}\right) \\
\hat{\boldsymbol{r}}_s \cdot \boldsymbol{A}_0 &= (A_0 k_1 - A_0 k_2 \cos\varphi)\frac{1}{k_3} \\
\hat{\boldsymbol{r}}_s \cdot \boldsymbol{B}_0 &= -\frac{B_0 k_1}{k_3}\sin\varphi
\end{aligned} \tag{C.95}$$

Using the dot products defined above yields an amplitude of,

$$\begin{aligned}
\mathit{Amplitude} = \frac{-A_0 B_0}{8\pi\rho_0|\boldsymbol{r}|}\left(\frac{\omega_1\omega_2}{\omega_1-\omega_2}\right)\left(\frac{1}{c_L^4 c_S^3}\right) V \sin\varphi \\
\times \left[C_1(2\beta - 3d) + C_2\beta + C_3(\beta - d) - dC_5\right]
\end{aligned} \tag{C.96}$$

where,

$$\begin{aligned}
d &= c_L c_S \omega_1 \omega_2 \\
\beta &= \alpha\cos\varphi - 2d\cos^2\varphi \\
\alpha &= 2c_S^2\omega_1^2 + c_L^2\omega_2^2
\end{aligned} \tag{C.97}$$

This expression does not agree with that presented by Korneev [30].

Interaction of $L(\omega_1) + S_{\parallel}(\omega_2) \rightarrow S_{\parallel}(\omega_1 - \omega_2)$

Now the case is considered where a dilatational wave with frequency ω_1 and shear-horizontal wave with frequency ω_2 interact to product a shear-horizontal scattered wave with a difference frequency. See Figure C.9. In addition to Equations C.47 and C.49, the dot products are,

$$\begin{aligned}
\boldsymbol{A}_0 \cdot \boldsymbol{k}_1 = A_0 k_1, \quad \boldsymbol{B}_0 \cdot \boldsymbol{k}_2 = 0 \\
\boldsymbol{A}_0 \cdot \boldsymbol{k}_2 = A_0 k_2 \cos\varphi, \quad \boldsymbol{B}_0 \cdot \boldsymbol{k}_1 = -Bk_1 \sin\varphi
\end{aligned} \tag{C.98}$$

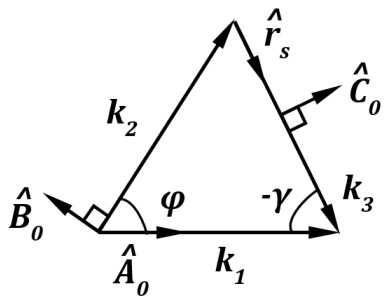

Figure C.9: Geometry of a dilatational wave $\boldsymbol{k}_1$ and shear wave $\boldsymbol{k}_2$ polarized in the $\boldsymbol{k}_1 - \boldsymbol{k}_2$ plane, which interact to produce a scattered shear wave $\boldsymbol{k}_3$ polarized in the $\boldsymbol{k}_1 - \boldsymbol{k}_2$ plane. The geometry shown is for the difference frequency ($\omega_3 = \omega_1 - \omega_2$) case. The amplitude vectors $\boldsymbol{A}_0$, $\boldsymbol{B}_0$, and $\boldsymbol{C}_0$, are the unit vectors pointed in the direction of the particle oscillation, *i.e.*, wave polarization.

The amplitude corresponds to the fourth expression in Equation C.66. Since $\hat{\boldsymbol{C}}_0 \cdot \hat{\boldsymbol{r}}_s = 0$, the amplitude is proportional to $\boldsymbol{I}^- \cdot \hat{\boldsymbol{C}}_0$. The dot products with $\hat{\boldsymbol{C}}_0$ are,

$$\begin{aligned}
\hat{\boldsymbol{C}}_0 \cdot \boldsymbol{k}_1 &= -k_1 \sin\gamma \\
\hat{\boldsymbol{C}}_0 \cdot \boldsymbol{k}_2 &= k_2 \sin(\varphi - \gamma) \\
\hat{\boldsymbol{C}}_0 \cdot \boldsymbol{A}_0 &= -A_0 \sin\gamma \\
\hat{\boldsymbol{C}}_0 \cdot \boldsymbol{B}_0 &= B_0 \cos(\varphi - \gamma)
\end{aligned} \tag{C.99}$$

The following trigonometric identities are useful,

$$\begin{aligned}
\sin(\varphi \pm \gamma) &= \sin\varphi\cos\gamma \pm \cos\varphi\sin\gamma \\
\cos(\varphi \pm \gamma) &= \cos\varphi\cos\gamma \mp \sin\varphi\sin\gamma
\end{aligned} \tag{C.100}$$

Making use of the above trigonometric identities and the geometric relationships from Equation C.49,

$$\begin{aligned}
\hat{\boldsymbol{C}}_0 \cdot \boldsymbol{k}_1 &= \frac{k_1 k_2}{k_3} \sin\varphi \\
\hat{\boldsymbol{C}}_0 \cdot \boldsymbol{k}_2 &= \frac{k_2 k_1}{k_3} \sin\varphi \\
\hat{\boldsymbol{C}}_0 \cdot \boldsymbol{A}_0 &= \frac{A_0 k_2}{k_3} \sin\varphi \\
\hat{\boldsymbol{C}}_0 \cdot \boldsymbol{B}_0 &= (B_0 k_1 \cos\varphi - B_0 k_2)\frac{1}{k_3}
\end{aligned} \tag{C.101}$$

Using the dot products defined above and the magnitudes $k_1 = \frac{\omega_1}{c_L}$, $k_2 = \frac{\omega_2}{c_S}$, and $k_3 = \frac{\omega_1 - \omega_2}{c_S}$ yields an amplitude of,

$$\begin{aligned} Amplitude = -\frac{A_0 B_0}{8\pi\rho_0|\boldsymbol{r}|}\left(\frac{\omega_1\omega_2}{\omega_1-\omega_2}\right)\left(\frac{1}{c_L^3 c_S^4}\right) V\left[-C_1(2c_L^2\omega_2^2 - c_S^2\omega_1^2 - d\cos\varphi - 2\alpha)\right. \\ \left. +C_2\alpha + C_3(\omega_1^2 c_S^2 \sin^2\varphi) + C_5(d\cos\varphi - c_L^2\omega_2^2)\right] \end{aligned} \tag{C.102}$$

where,

$$\begin{aligned} d &= c_L c_S \omega_1 \omega_2 \\ \alpha &= (d - c_S^2\omega_1^2\cos\varphi)\cos\varphi \end{aligned} \tag{C.103}$$

The expression presented here differs from the expression in Korneev. In particular, Korneev's expression is scaled by a factor of $\frac{c_L^2}{c_S^2}$ with respect to the expression above.

Interaction of $S_{\|}(\omega_1) + L(\omega_2) \rightarrow L(\omega_1 + \omega_2)$

Now the case is considered where a shear-horizontal wave with frequency ω_1 and a dilatational wave with frequency ω_2 interact to product a dilatational scattered wave with a sum frequency. See Figure C.10. In addition to the relations in Equations C.47 and C.48, the dot products are,

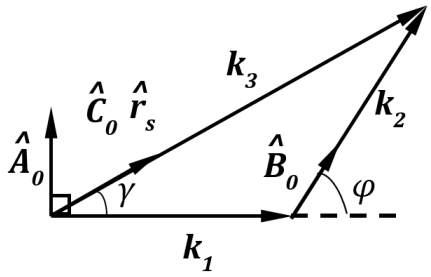

Figure C.10: Geometry of a shear wave $\boldsymbol{k}_1$ polarized in the $\boldsymbol{k}_1 - \boldsymbol{k}_2$ plane and a dilatational wave $\boldsymbol{k}_2$, which interact to produce a scattered dilatational wave $\boldsymbol{k}_3$. The geometry shown is for the sum frequency ($\omega_3 = \omega_1 + \omega_2$) case. The amplitude vectors $\boldsymbol{A}_0$, $\boldsymbol{B}_0$, and $\boldsymbol{C}_0$, are the unit vectors pointed in the direction of the particle oscillation, *i.e.*, wave polarization.

$$\begin{aligned} \boldsymbol{A}_0 \cdot \boldsymbol{k}_1 = 0, \quad \boldsymbol{B}_0 \cdot \boldsymbol{k}_2 = B_0 k_2 \\ \boldsymbol{A}_0 \cdot \boldsymbol{k}_2 = A_0 k_2 \sin\varphi, \quad \boldsymbol{B}_0 \cdot \boldsymbol{k}_1 = B k_1 \cos\varphi \end{aligned} \tag{C.104}$$

From resonance,

$$\hat{\boldsymbol{r}}_s = \frac{\boldsymbol{k}_1 + \boldsymbol{k}_2}{k_3} \tag{C.105}$$

with the magnitudes $k_1 = \frac{\omega_1}{c_S}$, $k_2 = \frac{\omega_2}{c_L}$, and $k_3 = \frac{\omega_1+\omega_2}{c_L}$. The amplitude corresponds to the first term in Equation C.66. Since $\hat{\boldsymbol{r}}_s \cdot \hat{\boldsymbol{C}}_0 = 1$, the amplitude is proportional to $\boldsymbol{I}^+ \cdot \hat{\boldsymbol{r}}_s$. The dot products with $\hat{\boldsymbol{r}}_s$ are,

$$\begin{aligned} \hat{\boldsymbol{r}}_s \cdot \boldsymbol{k}_1 &= (k_1^2 + k_1 k_2 \cos\varphi)\frac{1}{k_3} \\ \hat{\boldsymbol{r}}_s \cdot \boldsymbol{k}_2 &= (k_1 k_2 \cos\varphi + k_2^2)\frac{1}{k_3} \\ \hat{\boldsymbol{r}}_s \cdot \boldsymbol{A}_0 &= \frac{A_0 k_2}{k_3}\sin\varphi \\ \hat{\boldsymbol{r}}_s \cdot \boldsymbol{B}_0 &= (B_0 k_1 \cos\varphi + B_0 k_2)\frac{1}{k_3} \end{aligned} \tag{C.106}$$

Thus,

$$\begin{aligned} \mathit{Amplitude} = \frac{-A_0 B_0}{8\pi\rho_0|\boldsymbol{r}|}\left(\frac{\omega_1\omega_2}{\omega_1+\omega_2}\right)\left(\frac{1}{c_L^4 c_S^3}\right) V \sin\varphi \\ \times \left[C_1(2\alpha + 3d + 2d\cos^2\varphi) + \alpha C_2 + C_3(\alpha + d) + dC_5\right] \end{aligned} \tag{C.107}$$

where,

$$\begin{aligned} d &= c_S c_L \omega_1 \omega_2 \\ \alpha &= (c_L^2\omega_1^2 + 2c_S^2\omega_2^2 + 2d\cos\varphi)\cos\varphi \end{aligned} \tag{C.108}$$

The above expression agrees with that published in Korneev [30].

C.4 Collinear Wave-Mixing

Recall that for the non-collinear wave-mixing, the condition $-1 < \cos\varphi < 1$ was set so that the interactions were non-collinear. A special case can now be considered by letting $\cos\varphi = \pm 1$ so that the primary interacting waves are collinear. Note, $\cos\varphi = -1$ indicates a collision of $\boldsymbol{k}_1$ and $\boldsymbol{k}_2$, *i.e.*, propagating in opposite directions. With this new collinear condition, it is necessary to check the resonance and polarization conditions for each case in the same manner as was done in the non-collinear cases. The results will be summarized in Tables C.2, C.3, and C.4. Since this process was heavily detailed in the previous section, the results here will be presented in a more succinct manner to avoid repetitiveness. For the following discussion, reference will be made to the resonant conditions in Equation C.42. The term "collision" will be used to describe the cases where the primary waves are propagated in opposite directions. Note, only the amplitudes for the cases which were not already treated in the non-collinear section will be presented in this section.

The amplitudes from the analogous non-collinear cases are still applicable for the collinear cases, because no restrictions were made on $\cos\varphi$ during the amplitude calculations. Unlike the non-collinear cases, however, not all of the collinear cases will necessarily have ranges for the frequency domain. Rather, in some cases, since the interaction angle is a discrete value *i.e.*, $\cos\varphi = \pm 1$, there will be an expression, rather than a range, for the valid frequency ratio.

Prior to examining the various interaction cases, it is useful to discuss the general nature of collinear wave mixing. Recall that for wave-mixing to occur, the conditions in Equations C.16 and C.17 must be satisfied. They are repeated here for readability.

$$\boldsymbol{k}_3 = \boldsymbol{k}_1 \pm \boldsymbol{k}_2$$

$$\omega_3 = \omega_1 \pm \omega_2$$

Squaring both sides of the first equation, using the relation $k_i = \frac{\omega_i}{c_i}$, and dividing by ω_1^2, after some simple algebra yields,

$$\left(\frac{\omega_2}{\omega_1}\right)^2 [c_3^{-2} - c_2^{-2}] \pm 2\left(\frac{\omega_2}{\omega_1}\right)[c_3^{-2} - c_1^{-1}c_2^{-1}\cos\varphi] + [c_3^{-2} - c_1^{-2}] = 0 \tag{C.109}$$

Consider the interaction between two waves of the same type. Then, for an isotropic medium $c_1 = c_2 = c$ so that,

$$\left(\frac{\omega_2}{\omega_1}\right)^2 [c_3^{-2} - c^{-2}] \pm 2\left(\frac{\omega_2}{\omega_1}\right)[c_3^{-2} - c^{-2}\cos\varphi] + [c_3^{-2} - c^{-2}] = 0 \tag{C.110}$$

If the waves are propagating collinearly in the same direction, then $\cos\varphi = 1$, and

$$\left(\frac{\omega_2}{\omega_1} \pm 1\right)^2 [c_3^{-2} - c^{-2}] = 0 \tag{C.111}$$

Since by definition $\omega_1 > \omega_2$, then it must be true that $c_3 = c$. Thus, if the two primary waves of the same type are propagating collinearly in the same direction, then they may only produce a third wave of the same type. This is an important conclusion which highlights one of the advantages of the *non*-collinear wave-mixing. Namely, that in non-collinear wave-mixing there is modal separation.

Now consider the case where two primary waves of the same type in an isotropic medium collide collinearly such that $\cos\varphi = -1$. Now Equation C.110 becomes,

$$\left(\frac{\omega_2}{\omega_1}\right)^2 [c_3^{-2} - c^{-2}] \pm 2\left(\frac{\omega_2}{\omega_1}\right)[c_3^{-2} + c^{-2}] + [c_3^{-2} - c^{-2}] = 0 \tag{C.112}$$

Imposing the conditions that $0 < \frac{\omega_2}{\omega_1} < 1$, $c > 0$, and $c_3 > 0$ yields,

$$c_3 = \frac{c(\omega_1 \pm \omega_2)}{\omega_1 \mp \omega_2} \tag{C.113}$$

The above expression is true over a wide range of frequencies. Thus, for the case where two primary waves of the same type collide collinearly and interact, the resulting scattered wave does not necessarily have to be of the same type.

In the above analysis, the condition that the medium was non-dispersive was inherently imposed, because the velocities were assumed to be independent of the frequency. This is important to keep in mind, because in materials where the velocity is a function of the frequency, the condition that $c_1 = c_2$ will not necessarily be true if the primary waves have different frequencies. This can be shown by performing a similar analysis as the previous two scenarios. For example, two primary waves of the same type are propagated such that they interact collinearly in a dispersive medium. The dispersion present is such that the velocity increases with increasing frequency. Therefore,

$$\begin{gathered} c_1(\omega_1) \geq c_2(\omega_2) \\ \Rightarrow c_3 = \frac{c_1 c_2(\omega + 1 + \omega_2)}{\omega_2 c_1 + \omega_1 c_2} \end{gathered} \tag{C.114}$$

The above expression for c_3 is true over a range of frequencies and is not necessarily equal to c_1 or c_2. Therefore, the scattered wave does not necessarily have to be of the same type as the two primary waves in a dispersive medium. A similar analysis could be performed for materials with other "real" world complexities, such as anisotropy, inhomogeneities, etc.

Collinear Interaction of $L(\omega_1) + L(\omega_2)$

First, the case is considered where two dilatational waves are propagated in the same direction so that,

$$\begin{gathered} \cos\varphi = 1 \\ \boldsymbol{k}_1 = \frac{\omega_1}{c_L}\hat{\boldsymbol{k}}_1, \quad \boldsymbol{k}_2 = \frac{\omega_2}{c_L}\hat{\boldsymbol{k}}_2 \\ \boldsymbol{k}_1 \cdot \boldsymbol{k}_2 = k_1 k_2 \end{gathered} \tag{C.115}$$

All four resonance conditions from C.42 must be checked. For the first resonance condition,

$$\begin{aligned} k_3 &= \frac{\omega_1 + \omega_2}{c_L} \\ \hat{\boldsymbol{r}}_s &= (\boldsymbol{k}_1 + \boldsymbol{k}_2)\frac{1}{k_3} \end{aligned}$$

which yields,

$$k_3 = \frac{\omega_1 + \omega_2}{c_L} = \frac{\omega_1^2}{c_L^2} + \frac{\omega_2^2}{c_L^2} + \frac{2\omega_1\omega_2}{c_L^2}$$

Thus, the first resonance condition is satisfied. A similar check for the other three resonance conditions yield that the second resonance condition is also satisfied; however, the third and fourth resonance conditions are not satisfied. The polarization conditions should then be checked for the two cases where the resonance conditions are satisfied. For the first resonant condition, the amplitude corresponds with the first expression in Equation C.66. Since $\hat{\boldsymbol{r}}_s \cdot \hat{\boldsymbol{C}}_0 = 1$, the amplitude is proportional to $\boldsymbol{I}^+ \cdot \hat{\boldsymbol{r}}_s$, where,

$$\hat{\boldsymbol{r}}_s = (\boldsymbol{k}_1 + \boldsymbol{k}_2)\frac{1}{k_3}$$

The relevant dot products are then,

$$\begin{gathered}
\boldsymbol{A}_0 \cdot \boldsymbol{k}_1 = A_0 k_1, \quad \boldsymbol{B}_0 \cdot \boldsymbol{k}_2 = B_0 k_2 \\
\boldsymbol{A}_0 \cdot \boldsymbol{k}_2 = A_0 k_2, \quad \boldsymbol{B}_0 \cdot \boldsymbol{k}_1 = B_0 k_1 \\
\boldsymbol{A}_0 \cdot \boldsymbol{B}_0 = 0 \\
\hat{\boldsymbol{r}}_s \cdot \boldsymbol{k}_1 = (k_1^2 + k_1 k_2)\frac{1}{k_3} \\
\hat{\boldsymbol{r}}_s \cdot \boldsymbol{k}_1 = (k_1 k_2 + k_2^2)\frac{1}{k_3} \\
\hat{\boldsymbol{r}}_s \cdot \boldsymbol{A}_0 = (A_0 k_1 + A_0 k_2)\frac{1}{k_3} \\
\hat{\boldsymbol{r}}_s \cdot \boldsymbol{B}_0 = (B_0 k_1 + B_0 k_2)\frac{1}{k_3}
\end{gathered} \tag{C.116}$$

Thus, the corresponding amplitude for the first resonance condition is,

$$Amplitude = -\frac{A_0 B_0}{8\pi\rho_0}\left(\frac{1}{c_L^5}\right)\omega_1\omega_2\left(\omega_1+\omega_2\right)\left[4C_1+2C_2+2C_3+C_4+C_5\right] \tag{C.117}$$

The direction of propagation for the scattered wave can be found by solving for the angle γ between $\boldsymbol{k}_1$ and $\boldsymbol{k}_3$ as,

$$\begin{gathered}
\boldsymbol{k}_2 = \boldsymbol{k}_3 - \boldsymbol{k}_1 \\
\Rightarrow \left(\frac{\omega_2}{c_L}\right)^2 = \left(\frac{\omega_1+\omega_2}{c_L}\right)^2 + \left(\frac{\omega_1}{c_L}\right)^2 - 2\left(\frac{\omega_1}{c_L}\right)\left(\frac{\omega_1+\omega_2}{c_L}\right)\cos\gamma \\
\Rightarrow \cos\gamma = 1
\end{gathered}$$

This result reveals that for the case of two dilatational waves propagating in the same direction, it is possible for them to interact and produce a third dilatational wave with a sum frequency which propagates in the same direction as the primary waves. Following the same steps as for the first resonance condition, the amplitude for the second resonant case is,

$$Amplitude = \frac{A_0 B_0}{8\pi\rho_0}\left(\frac{1}{c_L^5}\right)\omega_1\omega_2\left(\omega_1-\omega_2\right)\left[4C_1+2C_2+2C_3+C_4+C_5\right] \tag{C.118}$$

Similar to the first resonant condition, $\cos\gamma$ is found to yield a propagation direction in the same direction as the primary waves.

Recall, that for non-collinear wave-mixing, *i.e.*, $-1 < \cos\varphi < 1$, this interaction failed the resonance condition. Thus, two dilatational waves can only interact to produce a third dilatational wave (with sum or difference frequency) if they are propagating collinearly. This illustrates the importance of determining whether or not the various collinear cases satisfy the resonant and polarization conditions separately from the non-collinear cases.

Collision of $L(\omega_1) + L(\omega_2)$

Now, consider the case where $L(\omega_1)$ and $L(\omega_2)$ propagate in opposite directions such that they collide, so that,

$$\begin{aligned} \cos\varphi &= -1 \\ \boldsymbol{k}_1 \cdot \boldsymbol{k}_2 &= -k_1 k_2 \end{aligned} \tag{C.119}$$

For this case, only the fourth resonant condition, *i.e.*, scattered shear wave with a difference frequency, is satisfied. To keep the system physically realizable $c_S < c_L$, and by definition $\omega_2 < \omega_1$, so that from the fourth resonant condition,

$$\begin{aligned} \left(\frac{\omega_1 - \omega_2}{c_S}\right)^2 &= \left(\frac{\omega_1}{c_L}\right)^2 + \left(\frac{\omega_2}{c_L}\right)^2 + 2\frac{\omega_1\omega_2}{c_L^2} \\ \Rightarrow \frac{\omega_1}{\omega_2} &= \frac{c_L - c_S}{c_L + c_S} \end{aligned} \tag{C.120}$$

The amplitude of this scattered wave corresponds to the fourth expression in Equation C.66. Since $\hat{\boldsymbol{C}}_0 \cdot \hat{\boldsymbol{r}}_s = 0$, the amplitude is proportional to $\boldsymbol{I}^- \cdot \hat{\boldsymbol{C}}_0$. When the shear wave is polarized out of the $\boldsymbol{k}_1 - \boldsymbol{k}_2$ plane, $\hat{\boldsymbol{C}}_0$ is perpendicular to the primary wave number vectors and their corresponding amplitude vectors and consequently fails the polarization condition. However, when the shear wave is polarized in $\boldsymbol{k}_1 - \boldsymbol{k}_2$ plane, its direction is such that it's not necessarily collinear with $\boldsymbol{k}_1$ and $\boldsymbol{k}_2$,

$$\cos\gamma = \frac{1}{2c_L c_S \omega_1}\left(c_L^2(\omega_1 - \omega_2) + c_S^2(\omega_1 + \omega_2)\right) \tag{C.121}$$

In order to be physically realizable, the above equation must be $-1 < \cos\gamma \leq 1$. In other words, the case where $\cos\gamma = -1$ is not possible. The amplitude for this case was already determined in the non-collinear section. See Case 1 in Table C.2.

Collinear Interaction of $L(\omega_1) + S(\omega_2)$

For the case where a $L(\omega_1)$ and $S(\omega_2)$ propagate collinearly, only the second resonant condition (scattered wave of $L(\omega_1 - \omega_2)$ is satisfied. Vector algebra can be used to determine $\cos\gamma$ as follows,

$$\begin{aligned}\left(\frac{\omega_2}{c_S}\right)^2 &= \left(\frac{\omega_1}{c_L}\right)^2 + \left(\frac{\omega_1-\omega_2}{c_L}\right)^2 - 2\frac{\omega_1(\omega_1-\omega_2)}{c_L^2}\cos\gamma \\ \Rightarrow \cos\gamma &= \frac{c_S^2(2\omega_1^2 - 2\omega_1\omega_2 + \omega_2^2) - c_L^2\omega_2^2}{2c_S^2\omega_1(\omega_1-\omega_2)}\end{aligned} \tag{C.122}$$

In order for the system to be physically realizable *i.e.*, $c_s < c_L$, then $-1 \leq \cos\gamma < 1$ must be true. Thus, the scattered dilatational wave has the possibility of propagating in a direction opposite to the primary waves or even at an angle; however, it cannot propagate in the same direction as the primary waves. This is true for shear waves polarized both in and out of the plane. The amplitude for this case corresponds to the second amplitude expression Equation C.66. Since $\hat{\boldsymbol{r}}_s \cdot \hat{\boldsymbol{C}}_0 = 1$, the amplitude is proportional to $\boldsymbol{I}^- \cdot \hat{\boldsymbol{r}}_s$. The relevant dot products (whether the shear wave is polarized in or out of the plane) are then,

$$\begin{aligned}\boldsymbol{A}_0 \cdot \boldsymbol{k}_1 &= k_1 A_0 \\ \boldsymbol{B}_0 \cdot \boldsymbol{k}_2 &= k_2 B_0 \\ \boldsymbol{A}_0 \cdot \boldsymbol{k}_2 = \boldsymbol{B}_0 \cdot \boldsymbol{k}_1 &= \boldsymbol{B}_0 \cdot \boldsymbol{A}_0 = 0 \\ \hat{\boldsymbol{r}}_s \cdot \boldsymbol{k}_1 &= (k_1^2 - k_1 k_2)\frac{1}{k_3} \\ \hat{\boldsymbol{r}}_s \cdot \boldsymbol{k}_2 &= (k_1 k_2 - k_2^2)\frac{1}{k_3} \\ \hat{\boldsymbol{r}}_s \cdot \boldsymbol{A}_0 &= (A_0 k_1 - A_0 k_2)\frac{1}{k_3} \\ \hat{\boldsymbol{r}}_s \cdot \boldsymbol{B}_0 &= 0\end{aligned} \tag{C.123}$$

so that the resulting amplitude is,

$$Amplitude = -\frac{A_0 B_0 V}{8\pi\rho_0|\boldsymbol{r}|}\left(\frac{\omega_1\omega_2}{\omega_1-\omega_2}\right)\left(\frac{1}{c_L^4 c_S^3}\right)(c_S\omega_1 - c_L\omega_2)^2[C_1 + C_2] \tag{C.124}$$

Of particular interest might be the case where the scattered wave propagates in a direction opposite to that of the primary waves. For this case,

$$\begin{gathered}\cos\gamma = -1 \\ \Rightarrow \left(\frac{\omega_2}{c_S}\right)^2 = \left(\frac{\omega_1}{c_L}\right)^2 + \left(\frac{\omega_1-\omega_2}{c_L}\right)^2 + 2\frac{\omega_1(\omega_1-\omega_2)}{c_L^2}\end{gathered} \tag{C.125}$$

Solving for $\frac{\omega_2}{\omega_1}$, it is seen that the above interaction will only take place for,

$$\frac{\omega_2}{\omega_1} = \frac{2c_S}{c_L + c_T} \tag{C.126}$$

This case is particularly interesting, because it implies that a pulse-echo type experimental set-up could be employed with the sending/receiving sensor(s) mounted on one side. Since shear waves travel slower than dilatational waves, the system could be set up in the following manner: the shear wave $S(\omega_2)$ is generated, and a dilatational wave $L(\omega_1)$ is generated after a delay time. The delay time corresponds to the difference in travel time of the shear and dilatational wave to interact at a predetermined location. The dilatational wave will "catch up" to the shear wave, interact, and generate a scattered dilatational wave $L(\omega_1 - \omega_2)$, which propagates in the opposite direction. The scattered wave can then be received by the same transducer used to generate the dilatational primary wave. The delay time t_{delay} can be determined for the chosen interaction distance $d_{interaction}$,

$$t_{delay} = d_{interaction}\left(\frac{1}{c_S} - \frac{1}{c_L}\right) \tag{C.127}$$

It is clear from the above equation that a scanning method can be used, where the delay time can be varied to scan along the depth of the specimen.

Typically, the primary waves are sinusoidal pulse trains in order to have a large volume of interaction. As the scattered wave is generated and propagated back ($\gamma = 180°$), it is possible that a portion of one or both of the primary wave pulse trains are still propagating in the forward direction ($\gamma = 0°$). The scattered dilatational wave $L(\omega_1 - \omega_2)$ will then collide with $L(\omega_1)$ and/or $S(\omega_2)$. Collision between two dilatational waves can produce a shear wave with a difference frequency. Collision between a dilatational wave and a shear wave (with a lower frequency) can produce a

shear wave with a difference frequency. If $\frac{\omega_2}{\omega_1} > 0.5$, then the collision between $L(\omega_1 - \omega_2)$ and $S(\omega_2)$ will not interact, because $\omega_2 > \omega_1 - \omega_2$. A collision between $L(\omega_1)$ and $L(\omega_1 - \omega_2)$ may result in a scattered shear wave with a difference frequency, *i.e.*, $S(\omega_2)$. This is noticeably the same frequency as the primary wave. In practice, filters are used to filter out the primary waves; thus, implementing a filter would get rid of any effects from waves resulting from collision. However, the energy from this interaction will result in a slightly diminished amplitude of the received scattered wave of interest $L(\omega_1 - \omega_2)$.

Collision of $L(\omega_1) + S(\omega_2)$

For the case where $L(\omega_1)$ and $S(\omega_2)$ propagate in opposite directions, the first and the fourth resonance conditions are satisfied; however, the first condition fails the polarization condition. For the fourth resonance condition, the amplitude is proportional to $\boldsymbol{I}^- \cdot \hat{\boldsymbol{C}}_0$. If the shear wave is polarized out of the plane, then $\hat{\boldsymbol{C}}_0 \cdot \boldsymbol{k}_1 = \hat{\boldsymbol{C}}_0 \cdot \boldsymbol{k}_2 = \hat{\boldsymbol{C}}_0 \cdot \boldsymbol{A}_0 = \hat{\boldsymbol{C}}_0 \cdot \boldsymbol{B}_0 = 0$, and the polarization condition is not satisfied. If the shear wave is polarized in the plane, the relevant dot products are then,

$$\begin{gathered} \boldsymbol{k}_1 \cdot \boldsymbol{A}_0 = A_0 k_1 \\ \boldsymbol{k}_2 \cdot \boldsymbol{B}_0 = \boldsymbol{k}_1 \cdot \boldsymbol{B}_0 = 0 \\ \boldsymbol{k}_2 \cdot \boldsymbol{A}_0 = -A_0 k_2 \\ \boldsymbol{A}_0 \cdot \boldsymbol{B}_0 = 0 \end{gathered} \tag{C.128}$$

which yield a non-zero amplitude as follows,

$$\textit{Amplitude} = \left(\frac{A_0 B_0}{8\pi\rho_0 |\boldsymbol{r}|}\right) V \left(\frac{1}{c_L^4 c_S^3}\right) \left(\frac{\omega_1 \omega_2}{\omega_1 - \omega_2}\right) (c_S\omega_1 - c_L\omega_2)^2 (C_1 + C_2) \tag{C.129}$$

The direction of propagation for the scattered wave is then,

$$\begin{gathered} \left(\frac{\omega_2}{c_S}\right)^2 = \left(\frac{\omega_1}{c_L}\right)^2 + \left(\frac{\omega_1 - \omega_2}{c_S}\right)^2 - 2\left(\frac{\omega_1}{c_L}\right)\left(\frac{\omega_1 - \omega_2}{c_S}\right)\cos\gamma \\ \Rightarrow \cos\gamma = \frac{c_L^2\omega_1 + c_S^2\omega_1 - 2c_L^2\omega_2}{2c_L c_S(\omega_1 - \omega_2)} \end{gathered} \tag{C.130}$$

The expression for $\cos\gamma$ is true for $-1 \leq \cos\gamma \leq 1$; however, it should always be verified that the expression meets the conditions $0 < \omega_2 < \omega_1$ and $0 < c_S < c_L$.

Collinear Interaction and Collision of $S(\omega_1) + L(\omega_2)$

For a shear wave with frequency ω_1 propagating collinearly with a dilatational wave with frequency ω_2, none of the resonant conditions are satisfied. Therefore, it is concluded that interaction is not possible and the cases where they collide must be checked.

If the two waves collide, only the first resonant condition is satisfied. Since $\hat{\boldsymbol{r}}_s \cdot \hat{\boldsymbol{C}}_0 = 1$, the amplitude is proportional to $\boldsymbol{I}^+ \cdot \hat{\boldsymbol{r}}_s$. For the shear wave polarized either in or out of the plane, the relevant dot products are,

$$\begin{gathered}
\boldsymbol{k}_1 \cdot \boldsymbol{A}_0 = \boldsymbol{k}_2 \cdot \boldsymbol{A}_0 = 0 \\
\boldsymbol{A}_0 \cdot \boldsymbol{B}_0 = 0 \\
\boldsymbol{k}_2 \cdot \boldsymbol{B}_0 = B_0 k_2, \quad \boldsymbol{k}_1 \cdot \boldsymbol{B}_0 = -B_0 k_1 \\
\boldsymbol{A}_0 \cdot \hat{\boldsymbol{r}}_s = 0 \\
\boldsymbol{B}_0 \cdot \hat{\boldsymbol{r}}_s = (B_0 k_2 - B_0 k_1)\frac{1}{k_3} \\
\boldsymbol{k}_1 \cdot \hat{\boldsymbol{r}}_s = (k_1^2 - k_1 k_2)\frac{1}{k_3} \\
\boldsymbol{k}_2 \cdot \hat{\boldsymbol{r}}_s = (k_2^2 - k_1 k_2)\frac{1}{k_3}
\end{gathered} \tag{C.131}$$

Plugging the dot products into C.23 and dotting it with $\hat{\boldsymbol{C}}_0$ yields an amplitude of zero. Thus, the polarization condition fails and no interaction will take place.

Collinear Interaction and Collision of $S(\omega_1) + S(\omega_2)$

When two shear waves are propagated collinearly, the third and fourth resonant conditions are satisfied. It is therefore necessary to check these two cases to determine if polarization conditions are met. For both cases, it can be determined that the direction of propagation is same as the primary wave vectors, *i.e.*, $\cos\gamma = 1$. Since $\hat{\boldsymbol{r}}_s \cdot \hat{\boldsymbol{C}}_0 = 0$, the amplitudes for both cases are proportional to $\boldsymbol{I} \cdot \hat{\boldsymbol{C}}_0$. If the shear waves are polarized in the $\boldsymbol{k}_1 - \boldsymbol{k}_2$ plane, the relevant dot

products for both cases are,

$$\begin{gathered}\boldsymbol{A}_0 \cdot \boldsymbol{k}_1 = \boldsymbol{A}_0 \cdot \boldsymbol{k}_2 = \boldsymbol{B}_0 \cdot \boldsymbol{k}_1 = \boldsymbol{B}_0 \cdot \boldsymbol{k}_2 = 0 \\ \boldsymbol{A}_0 \cdot \boldsymbol{B}_0 = A_0 B_0 \\ \hat{\boldsymbol{C}}_0 \cdot \boldsymbol{A}_0 = A_0, \quad \hat{\boldsymbol{C}}_0 \cdot \boldsymbol{B}_0 = B_0 \\ \hat{\boldsymbol{C}}_0 \cdot \boldsymbol{k}_1 = \hat{\boldsymbol{C}}_0 \cdot \boldsymbol{k}_2 = 0\end{gathered} \tag{C.132}$$

which yield an amplitude of zero, *i.e*, the polarization conditions fail. The same is true for the case where the shear waves are polarized out of the $\boldsymbol{k}_1 - \boldsymbol{k}_2$ plane. Since none of the resonant and polarization conditions are satisfied, it is concluded that shear waves propagated collinearly will not interact.

For the case where the two shear waves collide, only the first resonant condition is satisfied; however, it fails the polarization condition. So, the collision of two shear waves will not produce a scattered wave.

C.5 General Form of the Amplitude Expression

In order to understand the roles of the various acoustic parameters on the amplitude of the scattered wave, it is worthwhile to spend some time bringing the amplitude expressions into the same general form. The general form of the amplitude expressions can be written as,

$$\textit{Amplitude} = -\left(\frac{A_0 B_0}{8\pi\rho_0 |\boldsymbol{r}|} V\right)\left(\frac{\omega_1^3}{c_3^5}\right)\left[c_1 C_1 + c_2 C_2 + c_3 C_3 + c_4 C_4 + c_5 C_5\right] \tag{C.133}$$

where the c_i terms are non-dimensional coefficients, and the C_i terms are made up of the material elastic constants (see Equation C.64). The amplitudes found in the previous two sections can all be manipulated such that they fit this form. This can be done by algebraically rearranging the amplitude expressions found in the previous two sections and introducing the non-dimensional terms,

$$\begin{aligned} a &= \frac{\omega_2}{\omega_1} \\ c &= \frac{c_S}{c_L} \end{aligned} \tag{C.134}$$

The notation used for the above ratios is the same as that used by Jones and Kobett [27] and Johnson and Shankland [32, 33]. This was done for all of the amplitude expressions for both the collinear and non-collinear cases. The amplitude expressions are written in this general form in Table C.2 on page 201.

C.6 Strong Scattered Wave

When designing an experimental set-up to detect a nonlinear scattered wave via non-collinear wave mixing, some steps can be taken in order to maximize the amplitude of the scattered wave to aid detection efforts. Recall that all of the amplitude expressions can be written such that they are of a similar form (see Equation C.133), which is a linear combination of the coefficients C_1, C_2, C_3, C_4, and C_5 preceded by the term $\left(-\frac{A_0 B_0}{8\pi\rho_0|\boldsymbol{r}|c_3^5}\right) V\omega_1^3$. The amplitude of the scattered wave will be proportional the size of the volume of interaction V, the product of the amplitude of the primary waves A_0B_0, and the primary wave $\boldsymbol{k}_1$ frequency ω_1 cubed. Thus, a large interaction region, high primary wave input voltage, and high primary wave frequencies will all yield a higher scattered wave amplitude. Of course, in highly attenuative material, it is important to consider that attenuation generally increases with increasing frequency, and thus is a counteracting affect.

The amplitude expressions are also a function of the material constants (Lamé's constants and the TOECs), frequency ratio, and velocity ratio. If the material constants are known (hence, the velocity ratio is known), then it is worthwhile to plot amplitude expression as a function of the frequency ratio. In doing so, one can determine for which frequency ratio the maximum scattered wave amplitude can be generated, and the proper testing set-up can be implemented. Furthermore, some of the amplitude expressions contain zeros, which would place an additional constraint on the experimental set-up, as the polarization condition is unsatisfied at these points. The zero points can (and should) be determined even if the material constants are unknown.

C.6.1 Numerical Example

Korneev [30] provided numerical results for the interaction angle ϕ, scattered wave angle γ, and amplitude coefficient (see expressions in Table C.2, page 201) for values belonging to polyvinyl

chloride. For comparison, the same set of elastic constants will be used here. The values they used were,

$$\lambda = 3.64 \text{ GPa}, \quad \mu = 1.83 \text{ GPa}$$

$$A = -15.86 \text{ GPa}, \quad B = -12.95 \text{ GPa}, \quad C = -20.48 \text{ GPa}$$

$$\rho_0 = 1350 \frac{\text{kg}}{\text{m}^3}$$

$$\omega_1 = 2\pi \times 1 \text{ MHz}$$

Using these values, the interaction angle can be found from the expressions in Table C.1 (page 200). Then, the amplitude can be found as a function of the frequency ratio using the expressions from Table C.2 (page 201). It should be mentioned that Korneev plotted the results corresponding to the approximation that the TOECs were much larger than Lamé's constants so that Lamé's constants could be neglected. While this approximation is fine for the majority of the cases, it does have the potential to significantly alter the shape of the amplitude plot. Such is the case for Cases 2 and 3, where $L(\omega_1) + S_{\|}(\omega_2) \rightarrow L(\omega_1 \pm \omega_2)$. Refer to Figures C.11 through C.15, which contain the interaction angles, scattered wave angle, and amplitudes as a function of the frequency ratio for the values above.

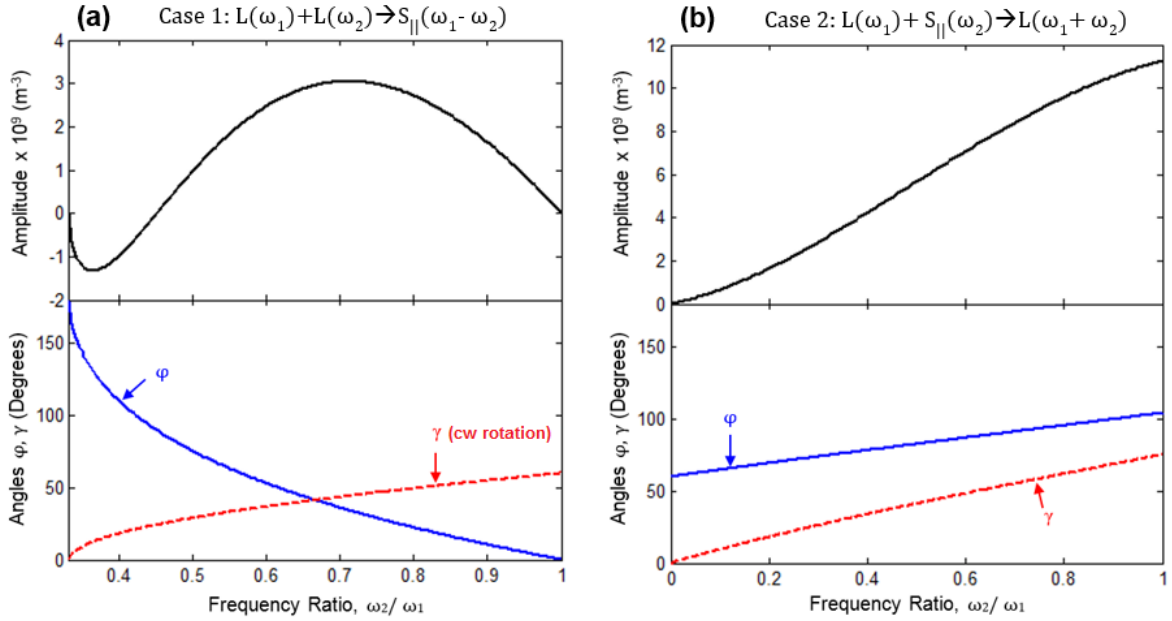

Figure C.11: Numerical results for (a) Case 1 and (b) Case 2 as a function of the frequency ratio $\frac{\omega_2}{\omega_1}$ using the expression from Table C.2. The angle between the primary waves is φ, and the resulting scattered wave angle is γ.

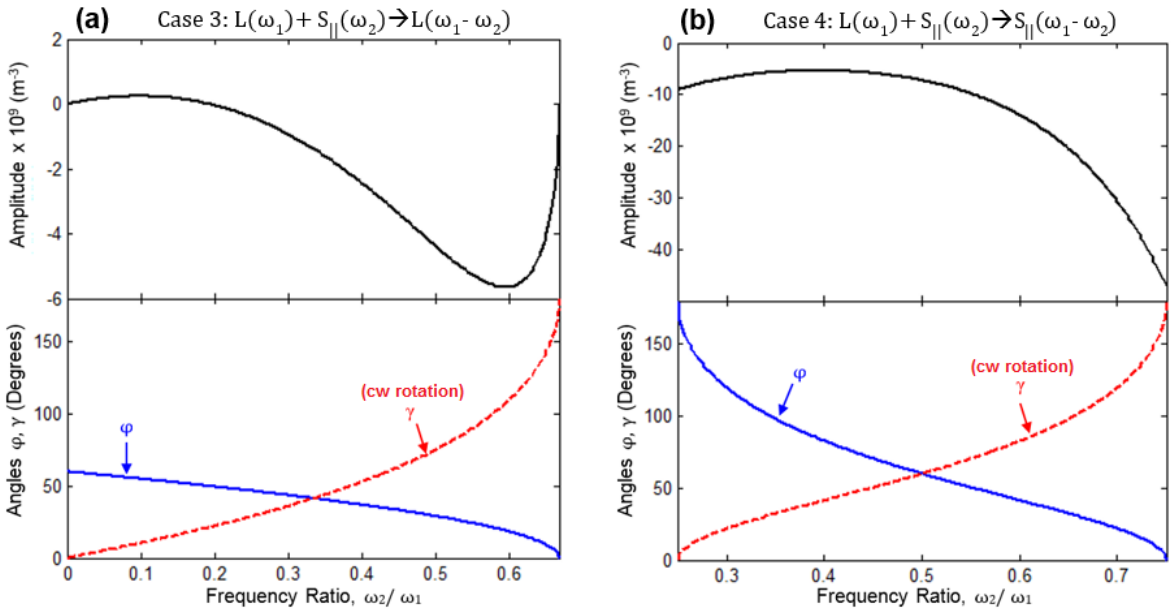

Figure C.12: Numerical results for (a) Case 3 and (b) Case 4 as a function of the frequency ratio $\frac{\omega_2}{\omega_1}$ using the expression from Table C.2. The angle between the primary waves is φ, and the resulting scattered wave angle is γ.

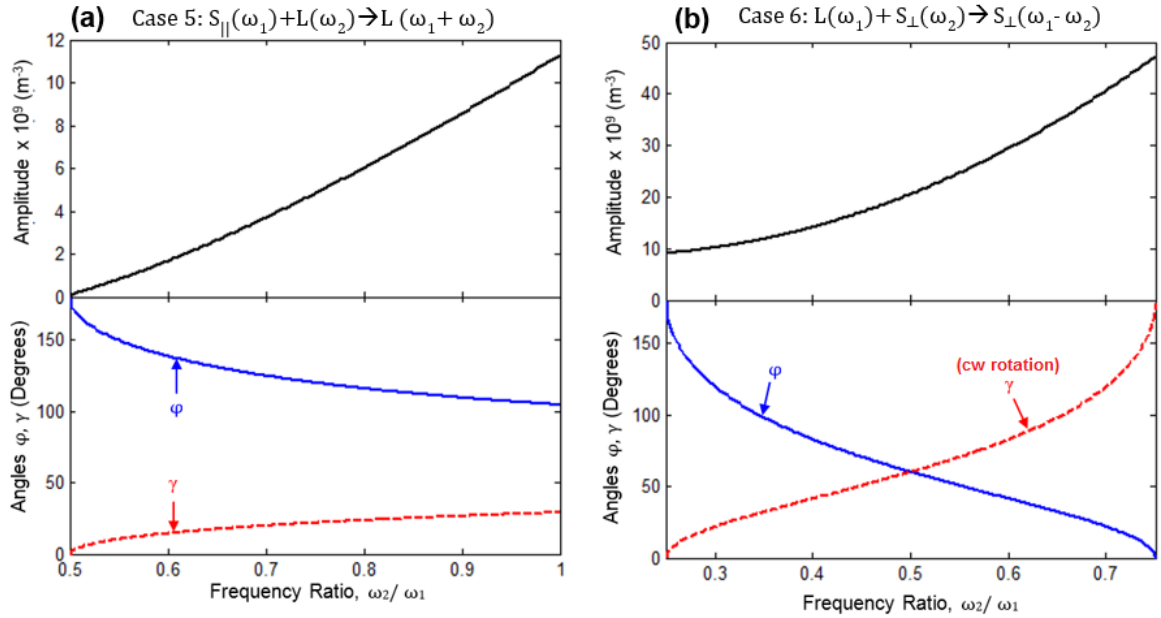

Figure C.13: Numerical results for (a) Case 5 and (b) Case 6 as a function of the frequency ratio $\frac{\omega_2}{\omega_1}$ using the expression from Table C.2. The angle between the primary waves is φ, and the resulting scattered wave angle is γ.

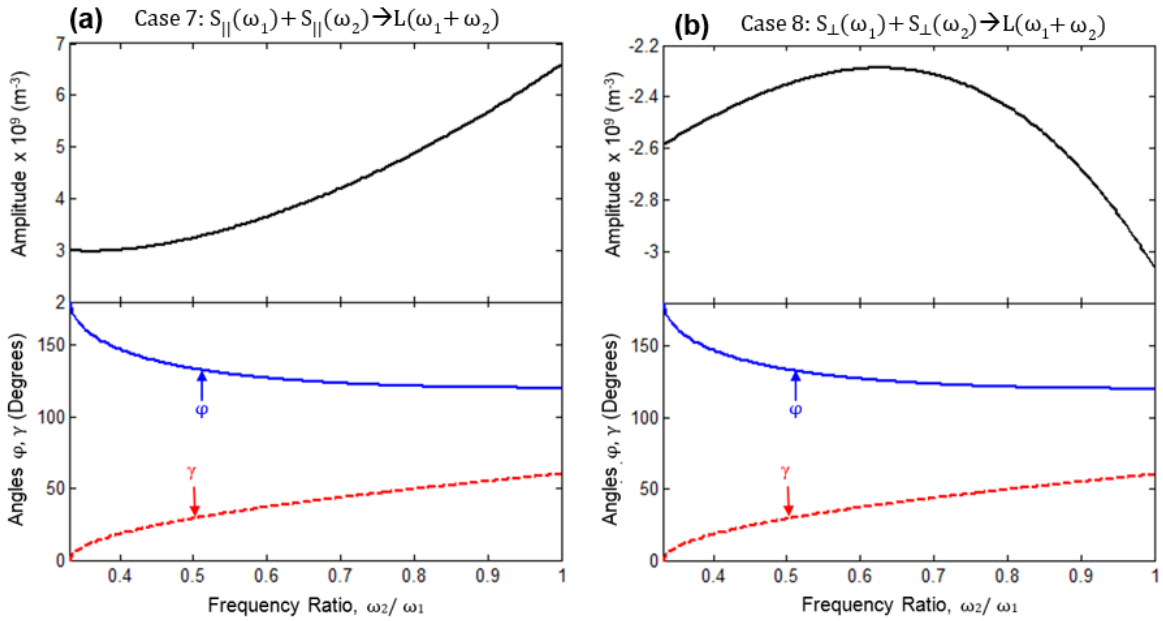

Figure C.14: Numerical results for (a) Case 7 and (b) Case 8 as a function of the frequency ratio $\frac{\omega_2}{\omega_1}$ using the expression from Table C.2. The angle between the primary waves is φ, and the resulting scattered wave angle is γ.

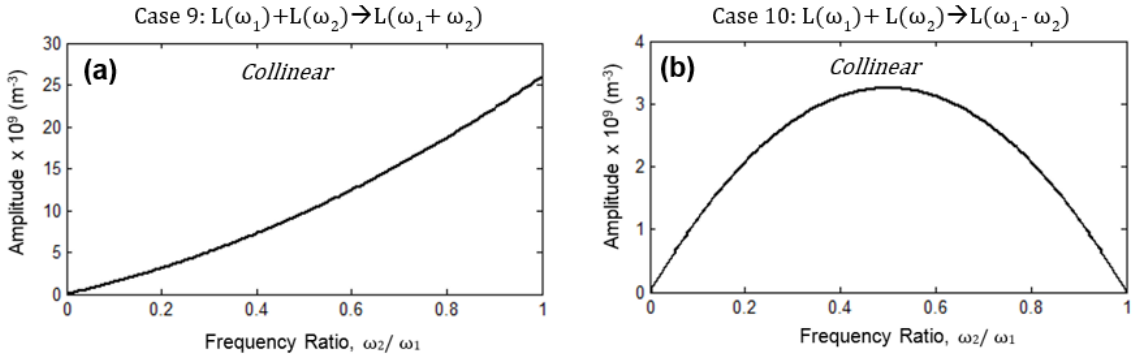

Figure C.15: Numerical results for amplitude (top) for Case 10: $(L(\omega_1) + L(\omega_2) \rightarrow L(\omega_1 - \omega_2))$ as a function of the frequency ratio $\frac{\omega_2}{\omega_1}$ using the expression from Table C.2. The primary waves are collinear, $\cos\varphi = 1$, and the resulting scattered wave angle is $\cos\gamma = 1$.

C.6.2 Selection Criteria for the Received Nonlinear Scattered Wave

Johnson and Shankland [32, 33] reported waves of mixed frequencies as a result of nonlinear interaction in crystalline rock. In order to confirm that the nonlinear wave originated from the nonlinear interaction between bulk waves in the rock, and not from the testing apparatus, they proposed three selection criteria: 1. *Frequency criterion:* the frequency of the observed nonlinear signal must match that predicted by theory, 2. *Amplitude criterion:* the amplitude of the nonlinear

signal must be proportional to the product of the primary waves, and 3. *Directionality criterion:* the trajectory of the nonlinear wave must match that predicted by theory. The first criterion is of course based on $\omega_3 = \omega_1 \pm \omega_2$. The second criterion is based on the general form that the amplitude expressions take (see Table C.2). The third criterion is based on the direction found for γ (see Table C.1). Recall, one of the advantages of using the non-collinear wave mixing technique is the time-separation between the primary and nonlinear scattered waves. Thus, in addition to the three criteria, a *time-of-flight criterion* can be used, assuming a straight ray path for all traveling waves. In practice, it is essential to verify all measurements against these criteria. Systems inherently contain nonlinearities, which if not accounted for, can complicate the results and cause an erroneous analysis of the data.

Table C.1: Non-collinear interaction cases which satisfy the resonance conditions, where φ and γ are defined in Figure C.3.

Primary Waves	**Nonlinear Scattered Wave**	$\cos\varphi$***	$\tan\gamma$	**Valid Frequency Range***	
				Lower	**Upper**
$\boldsymbol{L}(\omega_1)$ $\boldsymbol{L}(\omega_2)$	$\boldsymbol{S}(\omega_1-\omega_2)$	$\frac{c_L^2}{c_S^2}+\frac{1}{2}\left(1-\frac{c_L^2}{c_S^2}\right)\left(\frac{\omega_1}{\omega_2}+\frac{\omega_2}{\omega_1}\right)$	$\frac{-\omega_2\sin\varphi}{\omega_1-\omega_2\cos\varphi}$	$\frac{c_L-c_S}{c_L+c_S}$	1
$\boldsymbol{L}(\omega_1)$ $\boldsymbol{S}(\omega_2)$**	$\boldsymbol{L}(\omega_1+\omega_2)$	$\frac{c_S}{c_L}+\frac{1}{2}\frac{\omega_2}{\omega_1}\left(\frac{c_S}{c_L}-\frac{c_L}{c_S}\right)$	$\frac{c_L\omega_2\sin\varphi}{c_S\omega_1+c_L\omega_2\cos\varphi}$	0	$\begin{cases}\frac{2c_S}{c_L-c_S} & \text{for } 0<\frac{c_S}{c_L}\leq\frac{1}{3}\\ 1 & \text{for } \frac{1}{3}<\frac{c_S}{c_L}<1\end{cases}$
	$\boldsymbol{L}(\omega_1-\omega_2)$	$\frac{c_S}{c_L}-\frac{1}{2}\frac{\omega_2}{\omega_1}\left(\frac{c_S}{c_L}-\frac{c_L}{c_S}\right)$	$\frac{-c_L\omega_2\sin\varphi}{c_S\omega_1-c_L\omega_2\cos\varphi}$	0	$\frac{2c_S}{c_L+c_S}$
	$\boldsymbol{S}(\omega_1-\omega_2)$	$\frac{c_L}{c_S}-\frac{1}{2}\frac{\omega_1}{\omega_2}\left(\frac{c_L}{c_S}-\frac{c_S}{c_L}\right)$	$\frac{-c_L\omega_2\sin\varphi}{c_S\omega_1-c_L\omega_2\cos\varphi}$	$\frac{c_L-c_S}{2c_L}$	$\frac{c_L+c_S}{2c_L}$
$\boldsymbol{S}(\omega_1)$ $\boldsymbol{L}(\omega_2)$**	$\boldsymbol{L}(\omega_1+\omega_2)$	$\frac{c_S}{c_L}+\frac{1}{2}\frac{\omega_1}{\omega_2}\left(\frac{c_S}{c_L}-\frac{c_L}{c_S}\right)$	$\frac{c_S\omega_2\sin\varphi}{c_L\omega_1+c_S\omega_2\cos\varphi}$	$\frac{c_L-c_S}{2c_S}$	$\begin{cases}1 \text{ for } \frac{1}{3}<\frac{c_S}{c_L}<1\\ \text{Otherwise not satisfied}\end{cases}$
$\boldsymbol{S}(\omega_1)$ $\boldsymbol{S}(\omega_2)$	$\boldsymbol{L}(\omega_1+\omega_2)$	$\frac{c_S^2}{c_L^2}+\frac{1}{2}\left(\frac{\omega_1}{\omega_2}+\frac{\omega_2}{\omega_1}\right)\left(\frac{c_S^2}{c_L^2}-1\right)$	$\frac{\omega_2\sin\varphi}{\omega_1+\omega_2\cos\varphi}$	$\frac{c_L-c_S}{c_S+c_L}$	1

* In order to be physically realizable, the velocities and frequencies are defined such that $c_S < c_L$ and $\omega_2 < \omega_1$; thus, $0 < \frac{c_S}{c_L} < 1$ unless otherwise noted.

** Not all shear wave polarizations satisfy the polarization conditions.

*** These values are for non-collinear wave-mixing, $-1 < \cos\varphi < 1$

Table C.2: Amplitude expressions for cases which satisfy both the resonance polarization conditions, where φ and γ are defined in Figure C.3.

Case	Primary Waves	Nonlinear Scattered Wave	Amplitude Expression *
1	$L(\omega_1) + L(\omega_2)$	$S_{\parallel}(\omega_1 - \omega_2)$	$D\left(\frac{\omega_1^3}{c_S^5}\right) ac^4(1+a)\cos\varphi\sin\varphi\,[2C_1 + C_2 + C_3]$
2	$L(\omega_1) + S_{\parallel}(\omega_2)$	$L(\omega_1 + \omega_2)$	$D\left(\frac{\omega_1^3}{c_L^5}\right)\frac{a}{c^3(1+a)}\sin\varphi\,[C_1(3ac+2\beta) + C_2\beta + C_3(ac+\beta) + C_5 ac]$ where, $\beta = (2c^2 + a^2)\cos\varphi + 2ac\cos^2\varphi$
3		$L(\omega_1 - \omega_2)$	$D\left(\frac{\omega_1^3}{c_L^5}\right)\frac{a}{c^3(1-a)}\sin\varphi\,[C_1(2\beta - 3ac) + C_2\beta + C_3(\beta - ac) - C_5 ac]$ where, $\beta = (2c^2 + a^2)\cos\varphi - 2ac\cos^2\varphi$
4		$S_{\parallel}(\omega_1 - \omega_2)$	$D\left(\frac{\omega_1^3}{c_S^5}\right)\frac{ac}{1-a}\left[-C_1(a^2 - c^2 - 2\beta - d) + C_2\beta + C_3 c^2\sin^2\varphi + C_5 d\right]$ where, $d = ac\cos\varphi - a^2$; $\beta = (ac - c^2\cos\varphi)\cos\varphi$
5	$S_{\parallel}(\omega_1) + L(\omega_2)$	$L(\omega_1 + \omega_2)$	$D\left(\frac{\omega_1^3}{c_L^5}\right)\frac{a}{c^3(1+a)}\sin\varphi\left[C_1(3ac + 2ac\cos^2\varphi + 2\beta) + C_2\beta + C_3(ac+\beta) + C_5 ac\right]$ where, $\beta = (1 + 2a^2c^2 + 2ac\cos\varphi)\cos\varphi$
6	$L(\omega_1) + S_{\perp}(\omega_2)$	$S_{\perp}(\omega_1 - \omega_2)$	$D\left(\frac{\omega_1^3}{c_S^5}\right) ac\left[C_1(2a\cos^2\varphi - c\cos\varphi) - C_2 c\cos\varphi + C_5 a\right]$
7	$S_{\parallel}(\omega_1) + S_{\parallel}(\omega_2)$	$L(\omega_1 + \omega_2)$	$D\left(\frac{\omega_1^3}{c_L^5}\right)\frac{a}{c^4(1+a)}(1 + a^2 + 2a\cos\varphi)\left[C_1\cos(2\varphi) + C_2\cos^2\varphi - C_3\sin^2\varphi\right]$
8	$S_{\perp}(\omega_1) + S_{\perp}(\omega_2)$	$L(\omega_1 + \omega_2)$	$D\left(\frac{\omega_1^3}{c_L^5}\right)\frac{a}{c^4(1+a)}\left[C_1(2a + (1+a^2)\cos\varphi) + C_2(1 + a^2 + 2a\cos\varphi)\cos\varphi\right]$
9**	$L(\omega_1) + L(\omega_2)$	$L(\omega_1 + \omega_2)$	$D\left(\frac{\omega_1^3}{c_L^5}\right) a(1+a)\,[4C_1 + 2C_2 + 2C_3 + C_4 + C_5]$
10**		$L(\omega_1 - \omega_2)$	$D\left(\frac{\omega_1^3}{c_L^5}\right) a(1-a)\,[4C_1 + 2C_2 + 2C_3 + C_4 + C_5]$
11**	$L(\omega_1) + S_{\parallel/\perp}(\omega_2)$	$L(\omega_1 - \omega_2)$	$D\left(\frac{\omega_1^3}{c_L^5}\right)\frac{a}{c^3(a-1)}(c^2 - 2ac + a^2)\,[C_1 + C_2]$

* Note: $D = -\dfrac{A_0 B_0}{8\pi\rho_0|\boldsymbol{r}|}V$; $\quad a = \dfrac{\omega_2}{\omega_1}$; $\quad c = \dfrac{c_S}{c_L}$

** Only collinear interaction *i.e.*, $\cos\varphi = 1$, is possible

Table C.3: Collinear interaction cases which satisfy both the resonance and polarization conditions, where φ is the angle between primary waves $\boldsymbol{k}_1$ and $\boldsymbol{k}_2$ and γ is the angle between $\boldsymbol{k}_1$ and $\boldsymbol{k}_3$.

Primary Waves	**Nonlinear Scattered Wave**	$\cos\varphi$**	$\cos\gamma$**	**Valid Frequency Range***
$\boldsymbol{L}(\omega_1)$ $\boldsymbol{L}(\omega_2)$	$\boldsymbol{L}(\omega_1+\omega_2)$	1	1	$0<\frac{\omega_2}{\omega_1}<1$
	$\boldsymbol{L}(\omega_1-\omega_2)$	1	1	$0<\frac{\omega_2}{\omega_1}<1$
	$\boldsymbol{S}(\omega_1-\omega_2)$	-1	$\frac{c_L^2(\omega_1-\omega_2)+c_S^2(\omega_1+\omega_2)}{2c_Lc_S\omega_1}$	$\frac{\omega_2}{\omega_1}=\frac{c_L-c_S}{c_L+c_S}$
$\boldsymbol{L}(\omega_1)$ $\boldsymbol{S}_\perp(\omega_2)$	$\boldsymbol{L}(\omega_1-\omega_2)$	1	$\frac{c_S^2(2\omega_1^2-2\omega_1\omega_2+\omega_2^2)-c_L^2\omega_2^2}{2c_S^2\omega_1(\omega_1-\omega_2)}$	$\frac{\omega_2}{\omega_1}=\frac{2c_S}{c_L+c_S}$
$\boldsymbol{L}(\omega_1)$ $\boldsymbol{S}_\parallel(\omega_2)$	$\boldsymbol{L}(\omega_1-\omega_2)$	1	$\frac{c_S^2(2\omega_1^2-2\omega_1\omega_2+\omega_2^2)-c_L^2\omega_2^2}{2c_S^2\omega_1(\omega_1-\omega_2)}$	$\frac{\omega_2}{\omega_1}=\frac{2c_S}{c_L+c_S}$
	$\boldsymbol{S}_\parallel(\omega_1-\omega_2)$	-1	$\frac{c_L^2\omega_1+c_S^2\omega_1-2c_L^2\omega_2}{2c_Lc_S(\omega_1-\omega_2)}$	$\frac{\omega_2}{\omega_1}=\frac{c_L^2-c_S^2}{2c_L(c_L+c_S)}$

* In order to be physically realizable, the velocities and frequencies are defined such that $c_S<c_L$ and $\omega_2<\omega_1$; thus, $0<\frac{c_S}{c_L}<1$ unless otherwise noted.

** These values are for collinear wave-mixing, where $\cos x=1$ indicates propagation in the same direction and $\cos x=-1$ indicates propagation in the opposite direction *i.e*,collision.

Table C.4: Collinear interaction cases which satisfy both the resonance and polarization conditions, where φ is the angle between primary waves $\boldsymbol{k}_1$ and $\boldsymbol{k}_2$ and γ is the angle between $\boldsymbol{k}_1$ and $\boldsymbol{k}_3$.

Primary Waves	**Nonlinear Scattered Wave**					
	$\omega_3=\omega_1+\omega_2$			$\omega_3=\omega_1-\omega_2$		
	$\boldsymbol{L}$	$\boldsymbol{S}_\parallel$	$\boldsymbol{S}_\perp$	$\boldsymbol{L}$	$\boldsymbol{S}_\parallel$	$\boldsymbol{S}_\perp$
$\boldsymbol{L}(\omega_1)$ $\boldsymbol{L}(\omega_2)$	→	×	×	→	← ✓	0
$\boldsymbol{L}(\omega_1)$ $\boldsymbol{S}_\parallel(\omega_2)$	✓	×	×	→ ✓	✓	0
$\boldsymbol{L}(\omega_1)$ $\boldsymbol{S}_\perp(\omega_2)$	0	×	×	0	0	✓
$\boldsymbol{S}_\parallel(\omega_1)$ $\boldsymbol{L}(\omega_2)$	✓	×	×	×	×	×
$\boldsymbol{S}_\perp(\omega_1)$ $\boldsymbol{L}(\omega_2)$	0	×	×	×	×	×
$\boldsymbol{S}_\parallel(\omega_1)$ $\boldsymbol{S}_\parallel(\omega_2)$	✓	×	×	×	×	×
$\boldsymbol{S}_\perp(\omega_1)$ $\boldsymbol{S}_\perp(\omega_2)$	✓	×	×	×	×	×
$\boldsymbol{S}_{\parallel/\perp}(\omega_1)$ $\boldsymbol{S}_{\perp/\parallel}(\omega_2)$	0	×	×	×	×	×

✓ Satisfies both resonance and polarization conditions
→/← Collinear/collision interaction possible
×/0 Does not satisfy resonance/polarization conditions

Appendix D
Harmonic Generation and the Self-Interaction of Plane Elastic Waves

For completeness, the nonlinearities which manifest from propagation of a single acoustic wave, termed "self-interaction," through a nonlinear medium will now be discussed. While self-interaction of acoustic waves was not directly utilized for the investigations presented in this manuscript, for the reader who wishes to have a more conceptual understanding of nonlinear acoustics, a good discussion on harmonic generation is warranted.

Consider the case where a single, monochromatic sinusoidal wave is transmitted at time $t_0 = t = 0$ into a linear, elastic, isotropic, non-dispersive medium. If there is no attenuation, at a much later time $t_1 >> t_0$, the wave will look exactly the same as it did at t_0. In other words, a wave which propagates through a linear, elastic medium will retain its shape. If the same wave is now propagated through a nonlinear elastic medium, distortion will occur. This distortion arises from self-interaction of the wave and can give rise to the presence of harmonics.

Self-interaction of elastic waves is *not* the same as collinear wave mixing. Collinear wave mixing involves the interaction between two or more waves propagating in the same direction; whereas, self-interaction refers to the interaction of a wave with itself to generate a second wave. Collinear wave-mixing was treated in Section C.4. Here, self-interaction will be treated separately than harmonic generation; however, it should be emphasized that these two nonlinear manifestations are not necessarily independent phenomena. Self-interaction simply describes the generation of at least one other wave, which may be a harmonic of the same type. Thus, harmonic waves are a special case of self-interaction in solid media. In this chapter, harmonic generation will be discussed first for the case of wave propagation in fluid media, followed by a discussion on the more general self-interaction phenomenon in solids. Harmonic generation is discussed in fluids, rather than solids, because the derivation is relatively straightforward, and the implications of the resulting equation can be extended to solids, which will be shown.

D.1 Harmonic Generation

Please refer to Appendix B for the fundamentals of linear acoustics. The following derivations can be found in many acoustic textbooks. The reader is referred to references [11, 49, 81, 84].

Wave propagation in fluids is governed by the behavior of the particle velocity, pressure, and density as a function of time and location. Once functions for these parameters are established for the appropriate initial and boundary conditions, the wave motion can be determined. Three equations are used to determine the governing wave equations: 1. an equation of motion, which characterizes the particle velocity in terms of pressure and density, 2. a continuity equation, which is expresses the conservation of mass, and 3. an equation of state, which relates the pressure and density. This derivation will begin with the equation of state,

$$\begin{aligned} P = P(\rho) = P_0 + p \\ \rho = \rho_0 + \rho' \end{aligned} \tag{D.1}$$

where ρ is the acoustic density, p is the acoustic pressure, P is the instantaneous pressure, ρ' is the perturbed density, and the parameters with the subscript "0" denote ambient terms. The instantaneous pressure can be expanded in a Taylor series about ρ_0 as,

$$\begin{aligned} P = P(\rho_0) + \rho' P'(\rho_0) + \frac{1}{2}\rho'^2 P''(\rho_0) + H.O.T. \\ \Rightarrow p = \rho' P'(\rho_0) + \frac{1}{2}\rho'^2 P''(\rho_0) + H.O.T. \end{aligned} \tag{D.2}$$

Truncating terms higher than the second order and rewriting yields,

$$p \approx As + \frac{B}{2}s^2 \tag{D.3}$$

where,

$$\begin{aligned} A = \rho_0 P'(\rho_0) = \rho_0 c_0^2 \\ B = \rho_0^2 P''(\rho_0) \\ s = \frac{\rho - \rho_0}{\rho_0} \end{aligned} \tag{D.4}$$

Note, s is the condensation. The parameter of nonlinearity is the ratio of the coefficients preceding the condensation terms as follows,

$$\frac{B}{A} = \frac{\rho_0}{c_0^2}\left(\frac{\partial^2 P}{\partial \rho_0^2}\right)_{\rho_0} \tag{D.5}$$

The following relation can be obtained from the conservation of mass,

$$\frac{\rho}{\rho_0} = \frac{1}{(1+\nabla u)} \tag{D.6}$$

The above equation can be algebraically manipulated to obtain,

$$\frac{\nabla u}{1+\nabla u} = -\frac{\rho - \rho_0}{\rho_0} \tag{D.7}$$

For small pressure waves and displacements, the following approximation can be made for propagation along the x-axis,

$$s \approx -\frac{\partial u}{\partial x}\left(1 - \frac{\partial u}{\partial x}\right) \tag{D.8}$$

Plugging the condensation approximation into Equation D.3 and truncating terms higher than the second order yields,

$$p \approx -A\left[\frac{\partial u}{\partial x} + \beta_n\left(\frac{\partial u}{\partial x}\right)^2\right] \tag{D.9}$$

where β_n is the Beyer parameter[1] defined by,

$$\beta_n = 1 + \frac{B}{2A} \tag{D.10}$$

From the 1-D Euler's equation,

$$-\frac{\partial p}{\partial x} = \rho_0 \frac{\partial^2 u}{\partial t^2} \tag{D.11}$$

So that using the above equation with Equations D.9 and D.3 yields,

$$\frac{\partial^2 u}{\partial t^2} - c_0^2 \frac{\partial^2 u}{\partial x^2} = -2\beta_n \frac{\partial^2 u}{\partial x^2}\frac{\partial u}{\partial x} \tag{D.12}$$

[1]This parameter β_n is *not* the same as the nonlinear wave generation parameter $\frac{\beta}{\beta_0}$ (introduced in Chapter 3 and used throughout the manuscript). In fact, the Greek letter "β" was chosen to instill a sense of familiarity. In this manuscript, the Beyer parameter will always have the subscript "n" to distinguish it from the nonlinear wave generation parameter from Chapter 3.

The above equation is the 1-D nonlinear wave equation. So far, the analysis has been restricted to liquids; thus, the nonlinearity parameter defined in Equation D.10 is *only* true for liquids. In solids, a 1-D nonlinear equation can be shown to be of the same form as Equation D.12, where the only differences are in the definitions of the constants c_0 and β_n. For the details on this derivation, the reader is referred to Breazeale [120]. For an isotropic, homogeneous, solid material, the constants from Equation D.12 are,

$$\begin{aligned} \beta_n|_{solid} &= -\left(\frac{4C_1 + 2C_2 + C_3 + 2C_4 + C_5}{\rho_0} + 3\right) \\ c_0|_{solid} &= -\sqrt{\frac{\lambda + 2\mu}{\rho_0}} \end{aligned} \tag{D.13}$$

where, C_1 through C_5 are defined in Equation C.64, and c_0 is now the bulk dilatational velocity.

Equation D.12 can be rearranged to the following form,

$$\frac{\partial^2 u}{\partial t^2} = c_0^2 \left[1 - 2\beta_n \frac{\partial u}{\partial x}\right] \frac{\partial^2 u}{\partial x^2} \tag{D.14}$$

Now, the nonlinear wave equation has a similar form to the linear 1-D wave equation (see Equation B.28, Appendix B) with the notable difference being the presence of the Beyer parameter β_n. Clearly, if $\beta_n = 0$, the linear 1-D wave equation is recovered. As the wave propagates through the nonlinear medium, the nonlinearities have therefore effectively changed the velocity of the wave to be of the form,

$$c(p) = c_0 \sqrt{1 - 2\beta_n \frac{\partial u}{\partial x}} \tag{D.15}$$

Now, the speed of the wave is a function of the pressure of the wave. Some approximations can now be made to express this equation in a more convenient manner. Equation D.9 can be satisfied (up to the second order in p) for,

$$\frac{\partial u}{\partial x} = -\frac{p}{A} + \beta_n \left(\frac{p}{A}\right)^2 \tag{D.16}$$

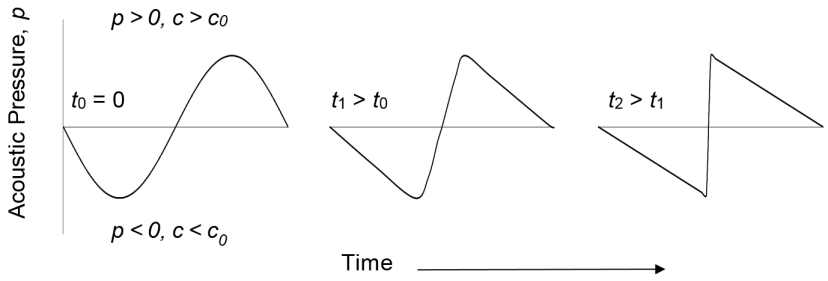

Figure D.1: Schematic showing an acoustic wave at three different snapshots in time t_0, t_1, and t_2 as it propagates through a nonlinear elastic medium and suffers distortion. At t_2, a sawtooth wave is formed, which is known as a shock formation.

Plugging this into Equation D.15 yields,

$$\begin{aligned} c(p) &\approx c_0 \sqrt{1 + \frac{2p\beta_n}{A} - 2\left(\frac{p\beta_n}{A}\right)^2} \\ &\approx c_0 \left[1 + \frac{p\beta_n}{A}\right] \end{aligned} \tag{D.17}$$

Equation D.17 provides insight into how the wave distortion will occur. Since the speed of the wave depends on the pressure of the wave, the compressional ($p > 0$) and rarefactional ($p < 0$) portions of the wave will move at different speeds. Particularly, the compressional portions of the wave will have a wave speed $c(p) > c_0$, and the rarefactional portions of the wave will have a wave speed $c(p) < c_0$. This nonuniform movement will cause distortion of the wave shape. This is best illustrated visually. Refer to Figure D.1, which contains a schematic of the pressure wave as it propagates and undergoes distortion at different snapshots in time. Initially at time $t_0 = 0$, the wave is a simple monochromatic sine wave. As the wave propagates through the nonlinear medium, a snapshot at time $t = t_1 > t_0$ shows that it begins to suffer a slight distortion as the peaks move quicker (and thus arrive earlier in time) than the troughs. Eventually, at time $t = t_2 > t_1$, the peaks "catch up" with the troughs. The point at which this occurs is known as a shock formation, and the wave is a sawtooth wave. These distortion effects are stronger for higher amplitudes.

Clearly, the frequency domain of the undistorted monochromatic sine wave will be different than the frequency domain of the distorted wave. In fact, the differences between the frequency domains of these two waves is the presence of harmonics in the distorted waveform. This can be conceptually realized by noting that although the wave changes shape as it suffers distortion, the points where

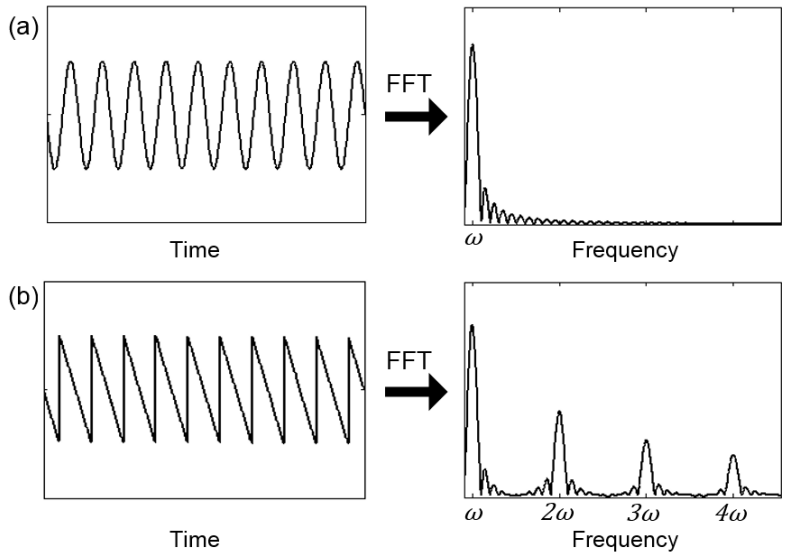

Figure D.2: The time-domains (left) and frequency-domains (right) of a (a) monochromatic sine wave pulse with a frequency of ω, and a (b) sawtooth wave. The distortion of the sinusoidal wave into a sawtooth wave results in higher order harmonics.

$p = 0$ retain the original velocity c_0 (see Equation D.17). Thus, the zero-crossing points remain the same, and the higher frequencies that are introduced must be integer multiple harmonics. Figure D.2 shows the time-domain and corresponding frequency domain of a monochromatic sine wave and a sawtooth wave. The frequency domain was found by taking the fast fourier transform (FFT) of the signal. As expected, the frequency domain for the monochromatic sine wave contains a single peak at the wave's fundamental frequency; whereas, the frequency domain for the sawtooth wave contains peaks at the fundamental frequency as well as the higher-order harmonics.

D.2 Self-Interaction of Plane Waves

The more general case of self-interaction of acoustic waves in a nonlinear elastic solid medium will now be discussed. Gol'dberg [95] was the first to carry out the derivation for the nonlinear equation of motion in the manner proposed by Landau and Lifshitz [26]. In doing so, he considered the implications of these equations on wave propagation. The following discussion will closely follow Gol'dberg's discussion.

The nonlinear equations of motion are presented in Equation C.15. Gol'dberg considered the special case of plane waves propagating in the x_1 direction such that,

$$\boldsymbol{u}(x_1,t) = u_1(x_1,t)\hat{\boldsymbol{\imath}} + u_2(x_1,t)\hat{\boldsymbol{\jmath}} + u_3(x_1,t)\hat{\boldsymbol{k}} \tag{D.18}$$

Where $\hat{\boldsymbol{\imath}}$, $\hat{\boldsymbol{\jmath}}$, and $\hat{\boldsymbol{k}}$, are unit vectors in the x_1, x_2, and x_3 directions, respectively. Note that the displacement components are only a function of time t and the direction of propagation x_1. The equations of motion from C.15 are then reduced to,

$$\begin{aligned}
\rho_0\frac{\partial^2 u_1}{\partial t^2} - (\lambda+2\mu)\frac{\partial^2 u_1}{\partial x_1^2} &= \alpha\frac{\partial^2 u_1}{\partial x_1^2}\cdot\frac{\partial u_1}{\partial x_1} + \beta\left[\frac{\partial^2 u_2}{\partial x_1^2}\cdot\frac{\partial u_2}{\partial x_1} + \frac{\partial^2 u_3}{\partial x_1^2}\cdot\frac{\partial u_3}{\partial x_1}\right] \\
\rho_0\frac{\partial^2 u_2}{\partial t^2} - \mu\frac{\partial^2 u_2}{\partial x_1^2} &= \beta\left[\frac{\partial^2 u_2}{\partial x_1^2}\cdot\frac{\partial u_1}{\partial x_1} + \frac{\partial^2 u_1}{\partial x_1^2}\cdot\frac{\partial u_2}{\partial x_1}\right] \\
\rho_0\frac{\partial^2 u_3}{\partial t^2} - \mu\frac{\partial^2 u_3}{\partial x_1^2} &= \beta\left[\frac{\partial^2 u_3}{\partial x_1^2}\cdot\frac{\partial u_1}{\partial x_1} + \frac{\partial^2 u_1}{\partial x_1^2}\cdot\frac{\partial u_3}{\partial x_1}\right]
\end{aligned} \tag{D.19}$$

where,

$$\begin{aligned}
\alpha &= 4C_1 + 2C_2 + C_3 + 2C_4 + C_5 \\
\beta &= C_1 + C_2
\end{aligned} \tag{D.20}$$

and the constants C_1 through C_5 are the same as were defined in Equation C.64. As noted by Gol'dberg, the above equations are different than those that arise from the linear approximation in that the dilatational and shear waves do not necessarily propagate independently of one another as they do in the linear case. Interaction can occur, which of course, was treated in Section C.4. Gol'dberg specifically considered self-interaction by way of an example. Recall that self-interaction of the primary waves manifested via the terms $\boldsymbol{I}^{(\omega_1)}$ and $\boldsymbol{I}^{(\omega_2)}$ in Equation C.22, however, was neglected such that only interactions between the two primary waves were considered.

D.2.1 Propagation of a Single Shear Wave

Gol'dberg considered a case where a single shear wave polarized in the x_2 propagates in the x_1 direction,

$$\begin{aligned}
u_1 = u_3 &= 0 \\
u_2 &\neq 0
\end{aligned} \tag{D.21}$$

Plugging these values into Equations D.19 yields,

$$\begin{gathered}\beta\left[\frac{\partial^2 u_2}{\partial x_1^2}\cdot\frac{\partial u_2}{\partial x_1}\right]=0\Rightarrow\frac{\partial^2 u_2}{\partial x_1^2}\cdot\frac{\partial u_2}{\partial x_1}=0\\ \rho_0\frac{\partial^2 u_2}{\partial t^2}-\mu\frac{\partial^2 u_2}{\partial x_1^2}=0\end{gathered}\tag{D.22}$$

However, the first equation cannot be true; therefore, a single shear wave does not satisfy the equations. In fact, in order to satisfy the equations of motion from Equation D.19, a dilatational wave must also exist. Another important implication of these results is the fact that a single shear wave will not generate harmonics for materials nonlinear in strain to the second-order.

D.2.2 Propagation of a Single Dilatational Wave

If, instead, a single dilatational wave is considered,

$$\begin{gathered}u_2=u_3=0\\ u_1\neq 0\\ \Rightarrow\rho_0\frac{\partial^2 u_1}{\partial t^2}-(\lambda+2\mu)\frac{\partial^2 u_1}{\partial x_1^2}=\alpha\frac{\partial^2 u_1}{\partial x_1^2}\cdot\frac{\partial u_1}{\partial x_1}\end{gathered}\tag{D.23}$$

The above equation is the same as 1-D nonlinear wave equation from Equation D.12. This example illustrates that self-interaction is the basis of harmonic generation in solids. Self-interaction was also evident in Equation C.22 from the following terms,

$$\begin{gathered}\boldsymbol{I}^{(\omega_1)}\sin[(2\omega_1 t-2\boldsymbol{k}_1\cdot\boldsymbol{r})]\\ \boldsymbol{I}^{(\omega_2)}\sin[(2\omega_2 t-2\boldsymbol{k}_2\cdot\boldsymbol{r})]\end{gathered}\tag{D.24}$$

At the time, however, these terms were neglected. It is now noted that these terms generate waves with twice the frequency, which propagate in the same direction as the primary wave. Thus, these terms correspond to harmonics generated by the primary wave.

Appendix E
Detection of Shear-Horizontal Waves at the Surface

In many non-destructive testing applications, it is necessary to perform measurements in a one-sided configuration, where all of the sensors are mounted on the same surface. One obvious example is for the case of the work performed in this manuscript, which involves the assessment of asphalt pavements. In pavements, there is only access to one side: the surface. Taking a core of the pavement for the purposes of characterization is destructive, and thus by definition, is not a non-destructive test. Therefore, if a non-destructive method such as non-collinear wave-mixing is to be utilized, both the sending transducers and receiving transducer should be mounted on one side.

Clearly, the scattered wave which results from the interaction between the two primary waves for one-sided non-collinear wave mixing should be detectable at the surface. Detectability is directly dependent on the amplitude and direction of the displacement at the surface, as well as the polarization of the crystal in the sensor itself (for piezoelectric transducers). A dilatational transducer will readily record displacements which are normal to the surface; whereas shear transducers will detect waves at the surface which are polarized in the same direction as the transducer's crystal. Hence, if a wave propagates at the surface such that its polarization is parallel to the surface, it can be detected as long as the receiving shear polarized transducer is oriented appropriately. A wave of this type will be referred to as a shear-horizontal surface wave. Shear-horizontal (SH) surface waves propagate along the surface and have a polarization orthogonal to the normal surface vector,*i.e.*, in the plane of the surface.

Traditional linear elastic theory, however, does not support the propagation of such shear-horizontal polarized waves on a flat, smooth surface of an isotropic semi-infinite medium [84]. Rather, SH waves do not exist according to linear elasticity, because they are unstable. Deviations from the aforementioned conditions (planar, isotropic, homogenous, etc.) can allow for the existence of surface shear-horizontal polarized waves. These deviations have been termed "perturbations," whereby the boundary conditions are altered enough to allow for SH waves. Maugin [51]

provides an excellent, in-depth discussion on various conditions which allow SH waves to at the surface. This discussion will draw primarily from Maugin's work. The reader is encouraged to read the section on surface waves in Appendix B prior to this section for prerequisite knowledge. First, it will be shown that SH waves do not exist in classical linear elastic theory. Then, some perturbation methods will be discussed. Finally, the importance of SH surface waves to the current study will be discussed [50, 121].

E.1 SH Waves in Traditional Linear Elastic Theory

As stated above, SH surface waves are not supported in classical linear elasticity theory. This was shown in Appendix B. See Equation B.48. Here it will be revisited in the context of the existence of SH surface waves. Recall that the problem was formulated as a surface wave polarized as a shear horizontal wave which propagates along the surface $x_3 = 0$ of a semi-infinite medium with a half-space $x_3 > 0$. From the assumed form of the displacement field and traction free boundary condition, the problem was formulated and is restated here [51],

$$\begin{aligned} \frac{\mathrm{d}^2 f(x_3)}{\mathrm{d}x_3^2} &= \left(k^2 - \frac{\omega^2}{c^2}\right) f(x_3) \\ \left[\frac{\mathrm{d}f(x_3)}{\mathrm{d}x_3}\right]_{x_3=0} &= 0 \end{aligned} \tag{E.1}$$

where the $f(x_3)$ is the amplitude function, which is only a function of the coordinate x_3. The solution of this Equation is,

$$f(x_3) = A \exp\left(x_3 \sqrt{k_T^2 - k^2}\right) \tag{E.2}$$

From the traction free boundary condition,

$$A\sqrt{k_T^2 - k^2} = 0 \tag{E.3}$$

In order for a wave to exist, it must have a non-zero amplitude $A \neq 0$. Therefore, to satisfy the traction free boundary condition, the following must be true,

$$\begin{aligned} \sqrt{k_T^2 - k^2} &= \sqrt{\frac{\omega^2}{c_S^2} - k} = 0 \\ &\Rightarrow \omega = k c_S \end{aligned} \tag{E.4}$$

This, however, corresponds to a bulk shear wave which skims the surface, not a surface wave. In fact, it is the second expression in Equation E.1 arising from the traction free boundary condition that inhibits the propagation of SH surface waves. If SH surface waves are to exist, the boundary condition must be perturbed enough to allow for $\left[\frac{\mathrm{d}f(x_3)}{\mathrm{d}x_3}\right]_{x_3=0} \neq 0$.

E.2 Perturbation Methods

Perturbation methods operate on the theory that bulk shear waves propagating very close to the surface ("surface skimming" bulk waves) are converted to SH polarized surface waves by perturbing the boundary conditions [53]. Here, the focus will be limited to mechanical-type perturbations, where the boundary conditions themselves are altered. There are, however, other "nonmechanical" type perturbation methods, where the interaction with other fields, such as electric and magnetic fields, allow for the existence of a SH surface wave.

E.2.1 Love Waves

In 1911, Love [122] considered the propagation of SH waves in a semi-infinite half-space overlaid by a thin solid layer. The motivation arose from the observation that SH surface waves existed during seismic events (earthquakes), even though they were predicted not to exist in linear elasticity. Love hypothesized that these waves were a consequence of the inhomogeneous construction of the earth's mantle. He modeled this inhomogeneous structure by considering a superficial layer, which would have the effect of "trapping" the SH waves and propagating them via multiple reflections in the layer. Thus, the thin layer acts as a waveguide and changes the boundary conditions. What was once the traction free surface, is now the interface between the substrate and superficial layer. Now, rather than traction free boundary conditions, continuity of displacement and traction must

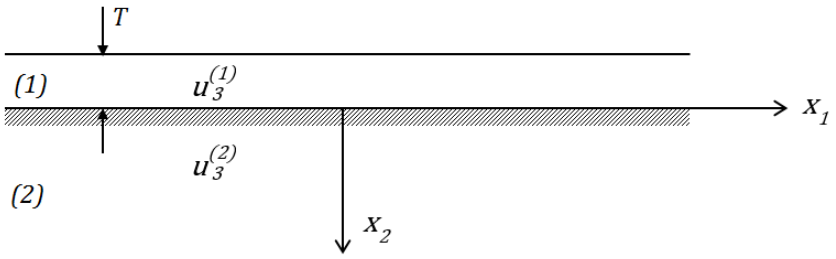

Figure E.1: Superficial layer of thickness T rigidly bonded to a semi-infinite bulk isotropic medium.

be satisfied at the interface.

Now the problem will be formulated as a SH wave propagating in the thin layer of thickness T, which is rigidly adhered to a semi-infinite isotropic medium. Please refer to [84] for an excellent discussion on this topic. The interface between the two layers is at $x_2 = 0$, so that the top of the superficial layer is at $x_2 = -T$. See Figure E.1. Considering only the displacements in the x_3 direction,

$$\begin{aligned} u_3^{(1)} &= u_3^{(1)}(x_1, x_2, t), \quad u_1^{(1)} = u_2^{(1)} = 0 \\ u_3^{(2)} &= u_3^{(2)}(x_1, x_2, t), \quad u_1^{(2)} = u_2^{(2)} = 0 \end{aligned} \tag{E.5}$$

where the superscripts (1) and (2) denote the superficial layer and substrate, respectively. The equations of motion are,

$$\begin{aligned} \nabla^2 u_3^{(1)} &= \left(c_S^{(1)}\right)^{-2} \frac{\partial^2 u_3^{(1)}}{\partial t^2} \\ \nabla^2 u_3^{(2)} &= \left(c_S^{(2)}\right)^{-2} \frac{\partial^2 u_3^{(2)}}{\partial t^2} \end{aligned} \tag{E.6}$$

The boundary conditions are such that there should be continuity at the interface of the two layers and the superficial layer should have a traction free surface as follows,

$$\begin{aligned} \tau_{23}^{(1)} &= 0 \quad \text{for } x_2 = -T \\ \tau_{23}^{(1)} = \tau_{23}^{(2)}, &\quad u_3^{(1)} = u_3^{(2)} \quad \text{for } x_2 = 0 \end{aligned} \tag{E.7}$$

where the shear components of the stress tensor have been replaced with the more familiar τ notation for shear stress components. The solutions take the form,

$$\begin{aligned} u_3^{(1)} &= U(x_2)^{(1)} e^{i(kx_1 - ct)} \\ u_3^{(2)} &= U(x_2)^{(2)} e^{i(kx_1 - ct)} \end{aligned} \tag{E.8}$$

To obtain,

$$\begin{aligned} \frac{\mathrm{d}^2 U^{(1)}}{\mathrm{d}x_2^2} + \left(\beta^{(1)}\right)^2 U^{(1)} &= 0 \\ \frac{\mathrm{d}^2 U^{(2)}}{\mathrm{d}x_2^2} - \left(\beta^{(2)}\right)^2 U^{(2)} &= 0 \end{aligned} \tag{E.9}$$

where,

$$\left(\beta^{(n)}\right)^2 = k^2 \left(\frac{c^2}{\left(c_S^{(n)}\right)^2} - 1 \right) \tag{E.10}$$

The solutions are then,

$$\begin{aligned} u_3^{(1)} &= A_1 e^{i(kx_1 - \beta^{(1)} x_2 - \omega t)} + A_2 e^{i(kx_1 + \beta^{(1)} x_2 - \omega t)} \\ u_3^{(2)} &= B_1 e^{i(kx_1 - \beta^{(2)} x_2 - \omega t)} \end{aligned} \tag{E.11}$$

This represents plane waves propagating back and forth within the layer. A few important observations should be made. In order for the above to be possible, the superficial layer should have a shear wave speed smaller than that of the substrate below. Also, since the thin layer is acting as a waveguide, there are multiple modes and dispersion. As the wavelength becomes large with respect to the thickness T of the top layer, the velocity of the wave propagating in the top layer approaches that of the velocity in the substrate.

E.2.2 Inhomogeneous Substrate

A natural extension to the boundary conditions imposed in the derivation of Love waves is to consider the case where the substrate has properties which vary with depth [50, 52, 123–126]. Now, rather than a discontinuity in material properties as was the case for the generation of Love waves, the material properties gradually vary with depth in a continuous (smooth) manner. This was first explored by Bhattacharya [123] in 1970. For the case where the shear modulus μ varies with depth

x_2, the problem can be reformulated [53] as shown below,

$$\begin{aligned} \nabla^2 u_i + \frac{\partial\left(\mu u_i\right)}{\partial x_2} &= c_S^{-2}\frac{\partial^2 u_i}{\partial t^2} \\ \left[\frac{\mathrm{d}u_i}{\mathrm{d}x_2}\right]_{x_2=0} &= 0 \end{aligned} \tag{E.12}$$

Notice that now the field equation, rather than the boundary condition, is perturbed. This system supports the propagation of surface SH waves.

E.2.3 Deviations from a Flat Surface

The last two cases involved deviations from the homogeneous condition via perturbing the boundary condition or field equations. Here, the deviation from a smooth, flat surface is considered. One obvious deviation from a flat surface is that of a curved surface. The reader is referred to Viktorov [127], who provides a comprehensive review on the work done on surface waves on curved surfaces. The principle idea is that an analogy can be drawn between a wave propagating around the circumference of a cylinder and Love waves. For both scenarios, the waves exhibit the characteristic that the velocity increases with increasing distance from the surface into the depth. Furthermore, waves propagating along cylinders exhibit dispersion, because there is a characteristic length, *i.e.*, the radius, associated with the geometry. Thus, like the case of the Love waves, the curved surface can support the existence of SH surface waves.

Another type of deviation from idealized conditions is that from a smooth surface. Various types of this "un-smooth" nature have been considered [53], including periodic grating [128], grooves [51], and a randomly rough surface [129, 130]. For these cases, the direction of the surface unit normal vector is perturbed. For the idealized smooth case, the surface unit normal vector points in the $-x_2$ direction. See Figure E.1. Under perturbed conditions, the surface unit normal vector does not always point in the $-x_2$ direction; rather, it is a function of x_1 and possibly x_3. For the case where the surface only varies along x_1, the free surface is now at $x_2 = \zeta(x_1)$, where ζ is some function describing the roughness. For the case of one-dimensional gratings, the boundary condition is [53],

$$\left[\frac{\mathrm{d}u_i}{\mathrm{d}x_2} - \frac{\partial\zeta}{\partial x_1}\frac{\partial u_i}{\partial x_1}\right]_{x_2=\zeta(x_1)} = 0 \tag{E.13}$$

In 1979, Auld and Yeh [128] performed a theoretical study on SH wave propagation on a corrugated surface. They found that presence of the gratings have the capability of supporting surface SH waves. They also reported that the corrugated surface has the effect of a stop band filter with a bandwidth proportional to the teeth height. Duparc and Maradudin [129] recognized that a randomly rough surface can be regarded as the superposition of an infinite number of randomly oriented diffraction gratings with varying periods and amplitudes. The randomly rough surface is observed in "real" materials, where even the most carefully prepared specimen will contain at least a small degree of roughness on some scale.

E.3 Applicability to Current Study

For the current study, the motivation behind understanding the conditions under which the existence of SH surface waves are possible arises from Case 1 of the non-collinear wave mixing cases (see Table C.2) via the use of subsurface waves. Refer to the experimental set-up used in Chapter 4, where subsurface waves were interacted to enable a completely one-sided testing set-up. Subsurface waves are generated through the use of transducers mounted on angle wedges set to an angle close to the first critical refracted angle so that they propagate close and parallel to the surface. Recall that the primary waves consist of two dilatational subsurface waves, which interact to produce a scattered shear wave. The scattered shear wave is polarized in the plane parallel to the surface and is therefore an SH wave. It was shown in the previous subsections that perturbations in the boundary conditions can result in the capability of supporting the propagation of an SH surface wave. Asphalt concrete is a highly complex material. As such, the boundary conditions are highly perturbed when compared to those of the idealized flat, smooth, isotropic, homogeneous medium. In fact, the mode conversion resulting from the scattering effects is so great that a wave of any polarization can be detected at the surface (as long as it is close to the surface).

To test this hypothesis, a small study was performed. A shear polarized transducer was incidentally mounted to the small face of a prismatic asphalt concrete specimen so that it generated an SH wave close to the surface. A receiving transducer was placed on the surface corresponding to the largest face of the specimen. It was observed that a signal was detectable whether a dilatational

transducer or shear transducer was used. This indicated that the high presence of scattering causes mode conversion. Furthermore, based on the perturbation methods presented in the previous subsections, asphalt concrete should be able to support the propagation of a SH surface wave; however, the high amount of scattering induced mode conversion will result in a highly complex displacement field. For this reason, a dilatational transducer can be used as the receiving transducer in a one-sided configuration.

An isotropic material, such as steel, however, might pose some difficulty if the geometry is such that it fits the idealized flat, smooth conditions. For the case of a steel, if it was desired to propagate a surface SH wave, one of the perturbation methods above would have to be utilized. One of the most easily implemented might be to rigidly adhere a superficial layer to the surface of the steel specimen so that the propagation of a Love wave is possible.

Appendix F
Pulse-Inversion Technique for Non-Collinear Wave Mixing

One way to extract the nonlinear scattered wave from the time domain difference signal and improve the signal-to-noise ratio, is to use the pulse-inversion technique. This technique relies on the fact that a 180° phase shift in the primary waves will correspond to a 360° or 0° phase shift in the nonlinear scattered wave (for sum and different waves, respectively). The pulse-inversion technique is often implemented in harmonic generation applications [131] and has also been implemented in collinear wave-mixing [132] applications; however, it has yet to be implemented in non-collinear wave-mixing. In addition to filtering the data, the pulse-inversion technique has the potential to improve quality of the received scattered wave signal. The pulse-inversion technique, with its applications in non-collinear wave mixing, will now be explained in further detail.

F.1 Theory

Consider the non-collinear wave interaction (see Appendix C) of two waves, termed primary waves, which have amplitudes written as,

$$\begin{aligned} y_1(\boldsymbol{r},t) &= A_1 \sin\left[(\boldsymbol{k}_1\boldsymbol{r} - \omega_1 t + \phi_1)\right] \\ y_2(\boldsymbol{r},t) &= A_2 \sin\left[(\boldsymbol{k}_2\boldsymbol{r} - \omega_2 t + \phi_2)\right] \end{aligned} \tag{F.1}$$

where k is the wave vector, r is the displacement vector, ω is the circular frequency, t is time, and ϕ is the phase. The subscripts "1" and "2" denote the first and second primary wave, respectively. The third scattered wave, which results from interaction, has an amplitude written as follows,

$$y_3(\boldsymbol{r},t) = A_1 A_2 \sin[(\boldsymbol{k}_1 \pm \boldsymbol{k}_2)\cdot\boldsymbol{r} - (\omega_1 \pm \omega_2)t + \phi_3] \tag{F.2}$$

where the plus or minus terms are positive for sum frequency cases and negative for difference frequency cases. At the nodes, the sin argument is zero, and expressions for the primary wave

phases can be found as,

$$\begin{aligned} \phi_1 &= \omega_1 t - \boldsymbol{k}_1 \cdot \boldsymbol{r} \\ \phi_2 &= \omega_2 t - \boldsymbol{k}_2 \cdot \boldsymbol{r} \end{aligned} \tag{F.3}$$

Similarly for the nonlinear scattered wave,

$$\phi_3 = (\omega_1 \pm \omega_2)t - (\boldsymbol{k}_1 \pm \boldsymbol{k}_2) \cdot \boldsymbol{r} \tag{F.4}$$

which, from the expressions in Equation F.3, is equivalent to,

$$\phi_3 = \phi_1 \pm \phi_2 \tag{F.5}$$

In terms of phase difference (shift),

$$\Delta\phi_3 = \Delta\phi_1 \pm \Delta\phi_2 \tag{F.6}$$

Thus, for a 180° phase shift for the primary waves,

$$\Delta\phi_1 = \Delta\phi_2 = 180^\circ \tag{F.7}$$

$$\therefore \Delta\phi_3 = \begin{cases} 0^\circ & \text{difference frequency} \\ 360^\circ & \text{sum frequency} \end{cases} \tag{F.8}$$

A 180° phase difference corresponds to an out-of-phase wave, whereas 0° and 360° are in-phase.

F.2 Implementation

The data collection scheme would be as follows: 1. Collect time record of interaction between two primary waves, 2. Invert pulses of two primary waves and collect time record, 3. Add records from Steps 1 and 2. Since signals shifted 180° will cancel each other out, the resulting signal from Step 3 would solely consist of the nonlinear scattered wave.

To implement this method, the amplitude-inverting equipment must be precise. In other words, the 0°-phase and 180°-phase signals must be nearly identical mirror images (about the time axis) of each other. If the amplitudes are not perfectly inverted, there will be residue of the primary waves, and filtering will still be required. Relatedly, there should be no time delay between the two signals. A check should be performed on measurements of the output signal and the inverted output signal of the equipment to verify that they do indeed cancel, or nearly cancel, when summed.